

**CHEMICAL REACTIONS IN A SCRAMJET COMBUSTOR
AND
TWO-DIMENSIONAL NOZZLES**

**Thesis by
Moon-Tai Yeung**

**In Partial Fulfillment of the Requirements
for the Degree of
Aeronautical Engineer**

**California Institute of Technology
Pasadena, California**

1993

(Submitted October 6, 1992)

Acknowledgement

Most of all, I wish to thank my committee members, Prof. E. Zukoski, Prof. T. Kubota, and Prof. A. Leonard, for being extremely patient with my research. I especially thank Prof. Zukoski and Prof. Kubota for their continuous support and invaluable technical advice throughout the program. I would also like to thank Prof. J. Kerrebrock who, during his visit from MIT, helped me shape and provided me with the grounds for my research. I am also indebted to Prof. S. Serdengecti who supplied me with the result from his “SCRAMJET” program. This information and his valuable suggestions allowed me to construct some of the case studies in my work and helped me validate the corresponding results.

Abstract

Finite-rate chemistry of hydrogen-air combustion is to be investigated numerically in a one-dimensional constant pressure SCRAMJET combustor and two-dimensional nozzles. Detailed reaction mechanisms and temperature dependent thermodynamics are to be used in the models. The aspects of interest include the combustion characteristics at different fuel-air ratios, pressures and initial temperatures in the combustor. Methods for enhancing the combustion rate in the combustor is to be studied also. The effect of expansion rate on the hydrogen-air reactions is the prime focus of the nozzle calculation. The results from different inlet conditions and wall geometries are to be analyzed.

A computer model for a one-dimensional (channel-flow) combustor is constructed based on the chemical kinetics subroutine library CHEMKIN. Subsequent calculations show that the initial temperature is the most important parameter in the combustor. It is further discovered that certain reaction steps are responsible for the initial delay exhibited in all hydrogen-air combustion processes. Low temperature behavior is studied extensively and augmentation methods are developed. The introduction of a small percentage of the hydrogen radical into the initial mixture is found to be the most effective in reducing the reaction delay. The combustor pressure enters the overall reaction process in a linear manner. The calculations over five combustor pressures show that the initial delay in hydrogen-air reaction and the following period of explosion are proportional to the combustor pressure raised to certain powers.

The nozzle model is two-dimensional, steady and inviscid with no conductivity and diffusivity. Two schemes are developed to handle the boundary conditions. One is based on pure numerical interpolation/extrapolation methods while the other imposes analytical supersonic characteristic equations. The former scheme is found to be more efficient while the latter is more accurate. In analysing the response of the combustion product to an expansion, it is found that the formation of water is favoured by an expansion. A closer examination reveals that the behavior can be attributed to the abundance of free radicals in the nozzle inlet composition. Freezing is not clearly observed except for the NO_x species.

Table of Contents

Acknowledgement	ii
Abstract	iii
Table of Contents	iv
1. Computational Chemical Kinetics	1
1.1 Introduction	1
1.2 Classification of Chemistry	2
1.3 Components of a Chemical System	3
1.3.1 Species	3
1.3.2 Reaction Mechanisms	4
1.3.3 Thermodynamic Properties	7
1.4 Selection of Species, Reactions, Rates and Thermodynamic Properties	8
1.4.1 Selection of Species	8
1.4.2 Selection of Reaction Mechanisms and Rate Coefficients	10
1.4.3 Selection of Thermodynamic Properties	11
1.5 Construction of a Chemical Model	12

2. Finite-Rate Chemical Reaction in a Static Homogeneous Medium	13
2.1 Introduction	13
2.2 Model	14
2.3 Formulation	16
2.3.1 State Equation	17
2.3.2 Rate Equation	18
2.3.3 Energy Equation	19
2.4 Summary of Static Model	21
3. Finite-Rate Reaction in a 1-D Constant Pressure Combustor	23
Part I: Setup	
3.1 Background	23
3.2 Model	24
3.3 Governing Equations	25
3.4 Survey of Kinetic Data for a Hydrogen-Air System	28
3.5 Estimation of Initial Conditions and Combustor Pressure	30
3.6 Basic Constraints on Calculation	33
3.6.1 Combustor input conditions	33
3.6.2 Accuracy	34
3.6.3 Reduced kinetic data set	35
3.7 Parametric Studies	37

4. Finite-Rate Reaction in a 1-D Constant Pressure Combustor	39
Part II: Parametric Studies	
4.1 Introduction	39
4.2 The Reference Case	41
4.3 Variation of Equivalence Ratio	51
4.3.1 Start-up behavior	52
4.3.2 Fast-rise behavior	53
4.3.3 Conditions at chemical equilibrium	53
4.4 Variation of Initial Temperature	56
4.4.1 Start-up behavior	56
4.4.2 Low temperature behavior	63
4.4.3 Explosive rise behavior	65
4.4.4 Conditions at chemical equilibrium	67
4.5 Variation of Pressure	76
4.5.1 Start-up behavior	77
4.5.2 Fast-rise behavior	80
4.5.3 Scaling with pressure: Mole fraction	80
4.5.4 Scaling with pressure: Heat release and Temperature	84
4.5.5 Conditions at chemical equilibrium	86
4.6 Discussion	94

5. Finite-Rate Chemical Reaction in a Combustor	96
Part III: Special Combustor Conditions	
5.1 Introduction	96
5.2 Hydrogen Radical in Initial Composition	97
5.3 Fluctuating Pressure Boundary Condition	100
5.4 Explanation	105
6. Reacting Flow in a Two-Dimensional Expansion Nozzle	106
Part I: Formulation	
6.1 Background	106
6.2 Model	107
6.3 Multi-Component Flow Problem	109
6.3.1 Rate equation	110
6.3.2 State equation	111
6.3.3 Continuity equation	111
6.3.4 Momentum equations	112
6.3.5 Energy equation	112
6.4 Coordinate Transformation — the <i>Von Mises</i> transformation	113
6.5 Transformed Governing Equations	119
6.5.1 Singular conditions	121
6.6 Numerical Implementation	122
6.7 Determination of P'_j and θ'_j — The Interpolation/ Extrapolation Method ..	125
6.8 Summary of implementation procedures	130

7. Reacting Flow in a Two-Dimensional Expansion Nozzle	132
Part II: Numerical Results	
7.1 Introduction	132
7.2 System Description	133
7.2.1 Inlet conditions	133
7.2.2 Wall geometry	134
7.2.3 Nozzle dimensions	138
7.3 Setup of Preliminary Calculations	139
7.4 Case 1: Inlet Mach number of a step-like <i>hyperbolic tangent</i> profile	141
7.5 Case 2: Uniform inlet conditions and a R_t of $0.8 m$ (<i>i.e.</i> $800 L_x$)	146
7.6 Case 3: Uniform inlet conditions and a R_t of $0.1 m$	151
7.7 Case 4: Uniform inlet conditions and R_t 's of $0.2 m$ and $0.4 m$	152
7.8 Evaluation of the Numerical Scheme	155
7.8.1 Comments on the interpolation/extrapolation approach	155
7.8.2 Limitation	157
8. Reacting Flow in a Two-Dimensional Expansion Nozzle	158
Part III: Characteristic Boundary Condition	
8.1 Introduction	158
8.2 Characteristics Solution at Wall Boundaries — Simple Wave Solution	158
8.3 Characteristics Solution at Wall Boundaries — General Approach	162
8.4 Accuracy of General Characteristic Treatment	166

8.5	Finite-rate Chemistry Calculations	168
8.6	Case 1: A P_{inlet} of 1.0 atm and R_t of 0.8 m (i.e. 800 L_x)	170
8.6.1	Species response to expansion	170
8.7	Case 2: A P_{inlet} of 1.0 atm and R_t of 0.1 m (i.e. 100 L_x)	179
8.8	Case 3: A P_{inlet} of 1.0 atm and R_t of 0.001 m (i.e. L_x)	186
8.9	Case 4: A P_{inlet} of 0.1 atm and R_t of 0.1 m (i.e. 100 L_x)	193
8.10	Case 5: A P_{inlet} of 0.1 atm and R_t of 0.001 m (i.e. L_x)	199
8.11	Discussion	204
9.	Recommendation for Future Work	208
9.1	Chemical Kinetics	208
9.2	Numerical	209
I.	Thermodynamic Equations for a Calorically Imperfect Gas	211
I.1	The Absolute Entropy	211
I.2	The frozen Speed of Sound	212
II.	A One-Dimensional Diffuser Model	215
III.	Kinetic Data for Hydrogen-Air Reactions	218
III.1	Compiled Kinetic Data	218
III.2	References for Kinetic Data	224

IV. Governing Equations for a Two-Dimensional Nozzle	225
References	228

CHAPTER 1

Computational Chemical Kinetics**1.1 Introduction**

The most efficient approach to model a multi-component chemical system is by numerical means. This is often the only approach when a more accurate representation is desired. That is, when the chemical species are calorically imperfect and the reactions are of finite-rate with temperature dependent rate coefficients. The work to be presented is primarily focused in this area.

A chemical system consists of a set of species at a certain composition and state which are governed by chemical kinetics and the laws of thermodynamics and material transport. The part involving physical dynamics is discussed in later chapters with specific applications. In this chapter, the chemical kinetics part is described. The subjects to be introduced are the basic type of chemical kinetics, the essential building blocks of a chemical system and the making and selection of those blocks. Some fine points regarding the computational aspect of chemical kinetics are also discussed.

1.2 Classification of Chemistry

There are three basic types of chemistry: *frozen*, *finite-rate* and *equilibrium*. In a situation where the production and destruction rates of a chemical species are identically zero, its mass weighted composition or mass fraction would remain constant in time along its path of motion. This type of chemistry is therefore known as *frozen*. On the other hand, a species can be *chemically reactive* if the reactions it involves have non-zero rates. In the reacting case, the change in the mass fraction of a species may be governed by either *finite-rate* reactions or *equilibrium* reactions. As the term literally implies, finite-rate reactions refer to those with finite but non-zero rates. Rates are not necessarily concerned in an equilibrium reaction except that the creation and destruction rates must be equal; instead, the appropriate equilibrium criteria* can be imposed. Inherently, all systems in nature are governed by finite rate processes; however, many systems may be considered either frozen or at equilibrium under the conditions of an investigation. It is often useful to analyze those two cases in addition to the finite-rate process since they are simpler mathematically and less expensive computationally. Their results can provide valuable insight to the behavior of their finite-rate correspondence.

A chemical system may be modelled by either one of the three types of chemistry or any combination of them. The current work is only concerned with having one type of chemistry at a time. In particular, finite-rate chemistry is to be considered substantially since it is the most general of all. Either the frozen or the equilibrium situation can be taken as the limiting case when the reactions rates approach zero or infinity. Since no reaction is needed in a frozen system, its chemical state is sufficiently described by specifying the initial composition. The evolution afterwards can be computed using species conservation. This is not true in general for the reacting case. Species are created and destroyed in time according to a set of reactions. Therefore, it is necessary to specify the reaction steps and their rates. The knowledge of this information and the thermodynamic properties of each species then allow the construction of a reacting model.

* For instance, see Rossini,^[12] chapter 16 for some of the equilibrium criteria.

1.3 Components of a Chemical System

The three building blocks of a kinetic model have been briefly mentioned. In short, a chemical system is characterized by its species set, reaction set and thermodynamic properties. The last of which consists of the properties of all individual species since they are the fundamental units determining the overall system properties. Various descriptions are given in literatures under different contexts. The three components are again described in the following sections to improve the clarity of the formulations presented in this work.

1.3.1 Species

Species are generally distinguished by their elemental constituents. There are molecular, atomic and ionic species which may be either inert, catalytic or chemically active. Free electron and photon are also considered as distinct species because of their role in some chemical reactions. By way of example, standard dry air at 5000 K and 0.1 atm would contain approximately 19 species^[3] with the following equilibrium composition:

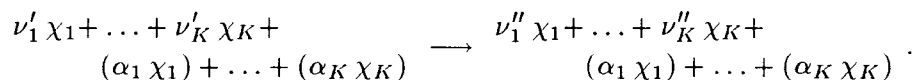
	equilibrium		equilibrium
species	mole fraction	species	mole fraction
1. N ₂	5.765×10^{-1}	11. N	8.270×10^{-2}
2. O ₂	2.065×10^{-4}	12. O	3.271×10^{-1}
3. CO ₂	4.655×10^{-8}	13. CO	2.614×10^{-4}
4. Ar	7.424×10^{-3}	14. N ₂ ⁺	4.820×10^{-8}
5. Ne	2.385×10^{-5}	15. O ₂ ⁺	1.466×10^{-8}
6. NO	5.618×10^{-3}	16. N ⁺	6.568×10^{-8}
7. NO ₂	1.327×10^{-8}	17. O ⁺	4.495×10^{-7}
8. N ₂ O	4.203×10^{-8}	18. NO ⁺	7.814×10^{-5}
9. C	9.031×10^{-7}	19. O ⁻	4.114×10^{-8}
10. e ⁻	7.868×10^{-5}		

The status of a species in a system is given by its composition. Composition may be expressed in terms of molar concentration (C), mole fraction (X) or mass fraction (Y). In the above list, the equilibrium mole fractions are shown. For computational purpose, mass fraction is often the preferred unit since its use may very often simplify a problem. For instance, if a species is not an active participant in any reaction (*i.e.* an inert or a frozen species), its mass fraction would remain constant in time under any circumstance. This is not true with C and X since they vary as the compositions of other species vary or as the density varies.

Regardless of the type of chemistry, frozen or chemically reacting, a set of species must be defined in order to build a system. The properties and composition of the individual species then determine the overall behavior of a system. In terms of chemical kinetics, each species has its own role in a chemical reaction, its own thermodynamic properties, its own atomic or molecular weight, and the list goes on. More importantly, the species set constitutes a factor in determining the possible chemical processes in a system. Chemical species also have their bearing in physical dynamics; transport properties such as diffusivity and viscosity are species dependent. This, however, is beyond the scope of this work.

1.3.2 Reaction Mechanisms

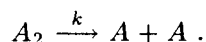
The change in species composition in a reacting system is generally the result of many elementary reaction steps or mechanisms. They are distinguished by their reactants, products and rate coefficients. Each reaction step has the form



A species, reactant or product, is denoted by χ . In this system, there is a total of K species. The number of one species participating as the reactant and the product is indicated by the stoichiometric coefficients ν' and ν'' respectively. They are integers and may be zero if a species does not take part. The other coefficient, α , which appears identically on both sides of the reaction is the enhanced factor for a third body. More information regarding a third body is provided shortly. The factor is the result of statistics and may not be an integer.

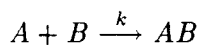
The *general* mechanism given above is useful in a computational model. But the more concise mechanism is necessary to help understand the behavior of a chemical system and to analyze the computational result.** In nature, there are only three types of elementary steps ranging from order 1 to 3. They are determined by the order of kinetics they obey.

1. First Order Reaction. A 1st order reaction has one reactant and obeys first order kinetic. An example is a dissociation:

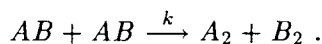


** Some kinetic properties are studied in chapter 4.

2. Second Order Reaction. These include

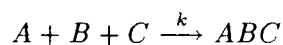


or

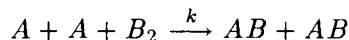


A 2nd order reaction is bimolecular and obeys second order kinetics. Note that bimolecular processes are slow and may affect the overall progress rate of a system. The slowest step would then constitute the *rate-determining* step.

3. Third Order Reaction. Similarly, a 3rd order reaction is termolecular; examples are

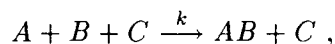


or

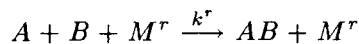


and so on.

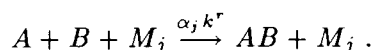
Frequently, a third body is involved; that is,



where C is known as the third body since its chemical constituent is not altered. Generally, any species in a system may act as a third body. This results in a set of such reactions with a different rate coefficient, k , in each case. However, it is often true that most species have the same effect as a third body and result in the same rate coefficient. A set of third body reactions are conventionally defined with respect to a reference case

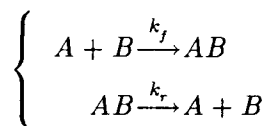


such that for any third body M_j in the species set,

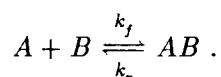


In other words, their reaction rates are the products of the enhanced factors α_j and the reference rate.

The above reactions have been described as *irreversible* steps; most chemical systems involved a combination of these steps or *reversible* reactions. For example, the reaction pair



is collectively called a reversible reaction and represented by



Two rates are involved, a forward rate coefficient k_f and a reverse rate coefficient k_r . To prevent confusion, reference to any reaction in this report always implies an irreversible step or the forward step in a reversible one. When chemical equilibrium is concerned, reversible reactions are always implied.

The rate coefficient, k , k_f or k_r in each of the above reactions is the key to a finite-rate process. It is reaction specific and may depend on temperature and pressure. The most commonly used model of the rate coefficient is given by the Arrhenius equation which has the form

$$k(T) = AT^\beta \exp\left(-\frac{E_a}{R_u T}\right) , \quad (1.3.2)$$

where A , β and E_a are reaction specific constants and R_u is the universal gas constant. The equation only emphasizes the effect of temperature[†] and contains a Boltzmann factor, $\exp\left(-\frac{E_a}{R_u T}\right)$, which was introduced by Svante Arrhenius (1859–1927) in 1889. The Arrhenius' formulation claims that the reactants of a reaction must have an energy greater than the level E_a in order to participate in the reaction. E_a is therefore called the *activation energy*. The probability of a species having a thermo-energy greater than E_a is reflected in the Boltzmann factor. The temperature exponent, β , reflects the contribution of particle collision to the reaction rate. In an equilibrium process, an equilibrium constant may be used in place of a reaction rate.

[†] There are other rate expressions formulated for special purposes; some can be pressure dependent.

1.3.3 Thermodynamic Properties

Underlying the overall behavior of a chemical system are the thermodynamic properties of its species. For instance, the feasibility of a reaction is determined by the chemical potentials of its participants; the system energy state is determined by an average enthalpy (*c.f.* section 2.3.3, equation 2.3.3.1) and so on. There is a large number of thermodynamic properties quantified for various purposes. They are related through the laws of thermodynamic and it is often sufficient to define a small fundamental set only. There is no best known theoretical method to predict the properties of all species under all conditions. The fundamental properties refer to those that are directly measured in or readily deducible from experiments.

The fundamental properties can be found in many handbooks. To comply with most of the commonly used databases, including the JANAF thermochemical tables,^[1] three standard state properties are to be defined for a species:

1. the standard state specific heat at constant pressure $C_p(T)$,
2. the standard state enthalpy $h^\circ(T)$, and heat of formation $\Delta h_f^\circ(T)$, and,
3. the standard state entropy $S^\circ(T)$.

Other quantities such as the absolute entropy, internal energy, chemical affinity are furnished by the corresponding thermodynamic laws. A note on the absolute entropy is given in appendix I because of its role in supersonic flows.

The three selected standard state properties are functions of temperature. They are acquired experimentally at discrete temperatures and are tabulated as such in the databases. Standard state refers to a pressure of one atmosphere, but the range of temperature at which data are given varies from species to species. In the JANAF tables, the temperature range is $200\text{ K} - 5000\text{ K}$ for most gaseous species.

The caloric imperfection aspect of a chemical system is reflected in the temperature dependence of C_p° . It may be assumed otherwise if the temperature in a system is not expected to change very much. But this is often a bad assumption in combustion problems. For the hydrogen-air system to be considered, the specific heat[‡] varies over 20% during the course of combustion.

[‡] Mass weighted specific heat at constant pressure $\bar{C}_p \equiv \sum_{k=1}^K C_{pk} Y_k$; see chapter 3 for its origin.

In a practical application, such as computer modelling, the properties are desired over a continuous temperature range. This is accomplished by interpolating or fitting the data tabulated at discrete temperatures. In the NASA combustion database,^[2] fourth order polynomials are used for C_p° over two temperature ranges (*e.g.* 200 K – 1000 K and 1000 K – 5000 K). Each of the polynomials has the form:

$$\frac{C_p(T)}{R_u} = a_1 + a_2T + a_3T^2 + a_4T^3 + a_5T^4 . \quad (1.3.3a)$$

Since h° and S° are related to C_p through differential thermodynamic laws, their polynomials over the same temperature range are

$$\frac{h(T)}{R_uT} = a_1 + \frac{a_2}{2}T + \frac{a_3}{3}T^2 + \frac{a_4}{4}T^3 + \frac{a_5}{5}T^4 + \frac{a_6}{T} \quad \text{and} \quad (1.3.3b)$$

$$\frac{S^\circ(T)}{R_uT} = a_1 \log T + a_2T + \frac{a_3}{2}T^2 + \frac{a_4}{3}T^3 + \frac{a_5}{4}T^4 + a_7 . \quad (1.3.3c)$$

Note that the heat of formation is included in the expression for enthalpy. The temperature range in which a fit is valid is very important. Since each polynomial has a fourth order terms, attempts to use a fit beyond its specified range may lead to a disastrous result.

1.4 Selection of Species, Reactions, Rates and Thermodynamic Properties

As in the modelling of any problem, it is not possible to build a chemical system that represents the actual physical system exactly. The information for the three building blocks in a chemical system – species set, reaction mechanisms and thermodynamic properties – must be carefully selected in order to form a model that is both accurate and manageable.

1.4.1 Selection of Species

The species set in a non-reacting or frozen system is fixed. Since no new species is created nor any existing one is destroyed by chemical reaction, the species set at all times is identical to the initial one plus any that is added *externally* during the course of evolution.

Species selection is primarily needed in a reacting system to limit the size of the set. Selecting only the *relevant* species can improve the efficiency of a calculation and allow more detailed analyses. Due to the presence of chemical reaction, a species set may include a substantial number of new species in addition to the ones specified initially and the ones added externally. A complete species set can be derived from the more fundamental unit, the element since there is rarely any doubt as to what elements a system contains. The element set can be regarded as the root of a combination tree whose leaves comprise the species set. It is clear that the number of species derived this way grows exponentially with the number of elements. For example, a simple system of pure hydrogen and oxygen may contain 8 neutral species of the form H_xO_y where x and y range from 0 to 2 (*c.f.* table III.a).

To select the *relevant* species, one must consider the reaction mechanisms, the physical conditions of the system and the desired accuracy of the chemical model. Clearly, a species is relevant only when it is involved in known reactions (presumably those found in experiments). The physical conditions, primarily temperature and pressure, determine how probable a new species may participate in chemical reactions. Finally, the desired accuracy determines how low a probability can be ignored.

The probability of a species' participation in chemical reactions is given by its rate equation which partially depends on physical conditions. There are two major factors in a rate equation – the rate coefficient and the species concentration. Recall from section 1.3.2 the Arrhenius rate coefficient,

$$k(T) = AT^\beta \exp\left(-\frac{E_a}{R_u T}\right),$$

which depends on temperature only. The probability of a species having an energy large enough to participate in a reaction (*i.e.* $> E_a$ of that reaction) is given by the Boltzmann factor $\exp\left(-\frac{E_a}{R_u T}\right)$. Since it is a strong function of temperature, the contribution of temperature follows. The exponent, β , is usually a small number and has much weaker effect. The other factor in a rate equation, the species concentration, models the contribution of the particle collision frequency to the chemical production rate. It is only affected by physical conditions when gaseous species are concerned. The gas law is a measure of their effects. In conclusion, a new species may be eliminated if its probability of participating in any reaction is small compared to the desired accuracy.

In section 1.3.1, a list of species and equilibrium composition was given at 5000 *K* and 0.1 *atm* for a dry air which contains the elements N, O, C, Ar and Ne. With the same accuracy, the list becomes:^[3]

	equilibrium species	mole fraction		equilibrium species	mole fraction
1.	N ₂	7.760×10^{-1}	11.	N	4.621×10^{-9}
2.	O ₂	2.043×10^{-1}	12.	O	1.755×10^{-3}
3.	CO ₂	3.243×10^{-4}	13.	CO	5.393×10^{-6}
4.	Ar	9.332×10^{-3}	14.	N ₂ ⁺	—
5.	Ne	2.997×10^{-5}	15.	O ₂ ⁺	—
6.	NO	8.248×10^{-3}	16.	N ⁺	—
7.	NO ₂	2.581×10^{-6}	17.	O ⁺	—
8.	N ₂ O	5.677×10^{-8}	18.	NO ⁺	—
9.	C	—	19.	O ⁻	—
10.	e ⁻	—			

at 2000 K and the same pressure. The relevant set now contains 11 species only.

1.4.2 Selection of Reaction Mechanisms and Rate Coefficients

Reaction mechanisms are selected in the same way as species. First of all, no reactions are involved in a frozen system. In the reacting case, their selection is based on the species set, the physical conditions and the desired accuracy of the model. A complete reaction set includes all the known steps or mechanisms relating the components of the entire species set. A rate equation can be written for each step and the probability of its occurrence can be estimated. Then the improbable ones can be eliminated according to the desired accuracy.

The reaction rate must be known for each step in the reaction set. It is often necessary to select a rate since different rates might be given for the same step by different literatures. The Arrhenius rate coefficient of a step is given in equation 1.3.2. It is a function of temperature and contains three parameters:

1. the pre-exponent constant A ,
2. the temperature exponent β , and
3. the activation energy E_a .

These parameters are deduced by fitting the Arrhenius equation to experimentally obtained kinetic data. Due to the nonlinearity of the Arrhenius expression, two slightly different sets of kinetic data may produce significantly different sets of constants, though they may

represent the same $k(T)$ closely over a small temperature range. Thus, it is best to select the reaction rates that are deduced from a consistent set of experiments performed over the same temperature range. As this is not always possible, combination of rates (obtained from different experiments using different methods over different temperature ranges ...) may also be used provided that set produced *good* results. A common practice is to extract the *entire* set of rates from a source where study of the same or a larger chemical system has been performed with validated results.[‡]

The equilibrium constant for a reversible reaction also depends on temperature. Unlike the rate coefficient, it can be theoretically predicted according to the thermodynamic properties of the species involved. No selection is necessary. However, there are instances when such predictions fail due to the lack of accuracy in the thermodynamic properties. Experimental values must then be used and the same criteria for selecting rate coefficients apply.

1.4.3 Selection of Thermodynamic Properties

With the species set determined, the selection of thermodynamic data only amounts to finding the right numbers. Thermodynamic properties are also determined experimentally. However, they are more consistent than the rate coefficients since they are less sensitive to experimental conditions and are much weaker functions of temperature. For example, the specific heat at constant pressure for $\text{H}_2\text{O}_{(\text{gas})}$ normalized by the universal gas constant can be fitted by the fourth order polynomial

$$\frac{C_p(T)}{R_u} = .2717 + .2945 \times 10^{-2} T - .8022 \times 10^{-6} T^2 + .1023 \times 10^{-9} T^3 - .4847 \times 10^{-14} T^4$$

over the temperature range 1000 K – 5000 K. The magnitude of the coefficients reflect the weak dependence in temperature. Therefore, it is acceptable to select data from any source or any combination of sources as long as they are consistently defined for all species. The JANAF thermochemical tables is often the most complete source. Others include the NASA combustion database and the STANJAN database. In addition, data of rare species or over extended temperature range may sometimes be found in specific papers.

[‡] From a private communication with Dr. Robert J. Kee, co-author of CHEMKIN.^[6]

Consistency of thermodynamic properties among species is important especially for non-absolute quantities such as enthalpy. As in the JANAF thermochemical tables, the enthalpy of compounds are not consistent with that of their standard composing elements. That is,

$$\sum_{\substack{\text{standard} \\ \text{elements}}} \nu'_j h_j(T) + \Delta h_{f, \text{compound}}(T) = [\nu'' h(T)]_{\text{compound}} \quad (1.4.3)$$

is not satisfied which would lead to an erroneous result in energy consideration. The equation is based on the fact that the heat of formation $\Delta h_f(T)$ is absolute and that Δh_f 's for the standard elements are zero. The symbols ν'_j and ν'' are the stoichiometric coefficients of the standard elements and compound respectively. No such problem is presented in the NASA combustion database.

1.5 Construction of a Chemical Model

The kinetic part of a chemical system has been described. To construct a model suitable for any application requires additional considerations. Firstly, a state equation must be supplied. Then dynamical conditions governing the species transport must be considered. Finally, an energy equation balancing the transfer of kinetic energy, work done, heat loss, heat of reaction, and so on must be included. As in any other fields of study, simplifications are often necessary. Some simplified models are constructed and analyzed in later chapters.

CHAPTER 2

Finite-Rate Chemical Reaction in a Static Homogeneous Medium**2.1 Introduction**

Among the three types of chemical systems, namely, frozen, finite-rate and equilibrium, it is best to study the finite-rate process since the other two may be reduced from this study with minor modification. The frozen case is obtained by setting all reaction rates to zero while the equilibrium case is obtained by replacing the finite-rate *rate equations** by the law of mass action.**

Before engaging in the calculation of chemical reaction in complicated gas dynamical systems, it is instructional to first study another class of problems. That is, the problems of chemical reaction in static homogeneous media. The results of these problems, for example, species composition, pressure, adiabatic temperature, and so on are useful guidelines for the dynamical problems. Since the static problems are considerably simpler than their dynamical counter parts, it is then possible to study the various effects of chemical reaction in a system for wide ranges of initial conditions and boundary conditions inexpensively. In addition, the study of these problems is extremely valuable for the selection of species and reaction mechanisms discussed in section 1.4. Some dynamical problems may actually be reduced to static ones. Such cases include most one-dimensional problems where the convection rate is constant or slowly varying with respect to the chemistry. Candidates are one-dimensional diffuser, combustor and nozzle.

A chemically reacting system is described by the species present, their thermodynamic properties, and their interactions specified in the reaction mechanisms. Given the complete description, with the initial conditions and boundary conditions specified, the evolution of the system can be solved. However, for a system with more than two active species and two reaction steps, calculation becomes complicated and to obtain analytic solutions is,

* See section 2.3 and 2.3.1 for description.

** See Penner (1955) for details. Some equilibrium results are presented in chapter 4 as supplements to the finite-rate calculations.

if not impossible, extremely difficult. This will become clear as the governing equations are described in the following section. Procedures for asymptotic approximation such as the induction stage analysis are very accurate under special circumstances. An illustration is given by Mikolaitis.^[10] A disadvantage of these procedures is that they require precise understanding of the particular chemistry involved. In other words, they are problem dependent. In the present research, numerical approach is used to solve the exact governing equations for the complete system at all times; thus, eliminating the trouble of being problem dependent.

A numerical package, CHEMKIN,^[6] designed for handling gas phase chemical kinetic is used to aid the calculations.[†] It conveniently provides various thermodynamic quantities and chemical production rates at a given state for a prescribed system. Finally, the solutions of the finite-rate problems are accomplished by the numerical integration of the governing equations in time.

2.2 Model

Consider a homogeneous mixture in a container that is stationary in space. Its physical properties such as density, pressure, temperature and composition, however, may change with time due to mass addition, external work and chemical reaction. Schematically, the system may be viewed as:

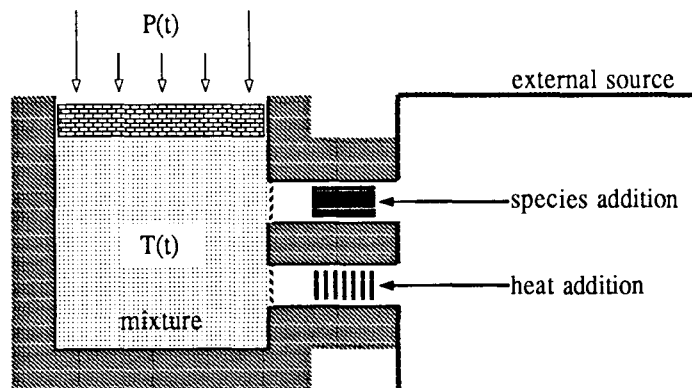


FIG. 2.2.1a Container model of a static system.

For future convenience, let $\dot{\omega}_k^a$ and \dot{Q}^a denote the rate of addition of the k^{th} species and the rate of heat addition respectively, where the superscript 'a' designates addition from external source. Note that these quantities constitute part of the boundary conditions.

[†] A comprehensive description of the code can be found in the CHEMKIN manual (1980) and (1989).

The container model may also be applied to a dynamical system when a volume of mixture is being followed along a particle path:

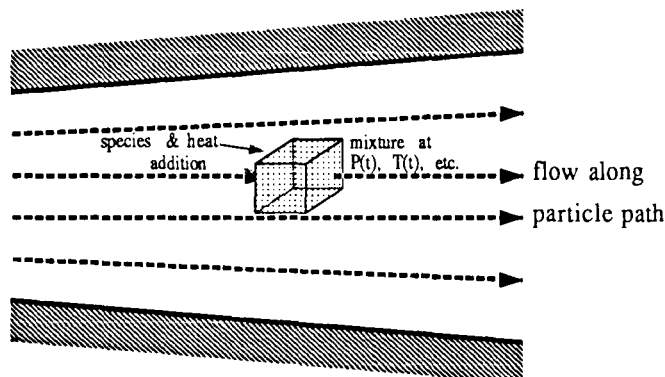


FIG. 2.2.1b Static model applied to a dynamical system.

In this case, the volume of the container approaches an infinitesimal point and the quantities $\dot{\omega}_k^a$ and \dot{Q}^a become dependent upon the conditions of the neighboring points. Kinetic energy must also be introduced due to the particle motion. Thus, the static model only applies when all the neighboring points have the same $\dot{\omega}_k^a$ and \dot{Q}^a at all times* and when the kinetic energy is constant, which is generally true for the one-dimensional problems mentioned in the previous section. Modeling of a dynamical system is quite different. The study of a special case in the dynamical problem is presented in chapter 6 where the differences will become obvious.

In summary, the essential assumptions embedded in the model are:

- i) mixture is homogeneous,
- ii) mixture is at thermal equilibrium,
- iii) no net transport and heat dissipation, and
- iv) all species are in gas phase.

The last item is added to simplify the problem. Mixed phases enhances the difficulties in handling the chemistry.

* Note that $\dot{\omega}_k^a$ and \dot{Q}^a must be identically zero in this case.

1.6 Formulation

The static chemical system specified above can be described completely by the species composition and two state variables. Admissible variables for the numerical tool CHEMKIN include either molar concentration, mole fraction or mass fraction for composition and temperature and either pressure or density for state. Mass fraction is the natural choice for representing composition since it is related directly to the conservation equations and is used in the evaluation of important quantities such as the frozen speed of sound, absolute entropy, enthalpy, and other mass average quantities. For the state variables, it is best to choose the variables that confer with the initial and boundary conditions. For a wide range of problems, temperature and pressure are usually applicable.

In a system with K distinct species, the variable set describing it may be written as

$$(Y_k, T, P) \quad \text{for } k = 1, K, \quad (2.3.1)$$

where Y_k , P and T are the mass fraction of the k^{th} species, the pressure and the temperature respectively and they are functions of time. The *rate law* governing the chemistry in a finite-rate process is fundamentally defined in terms of the number densities (or molar concentrations) rather than the mass fractions of the species. A definition of mass fraction in terms of molar concentrations is

$$Y_k = \frac{C_k m_k}{\sum_{j=1}^K C_j m_j}, \quad (2.3.2)$$

where C_k and m_k are the molar concentration and molar mass of the k^{th} species respectively.

The evolution of a static chemical system are governed by three types of equation:

- 1) the state equation,
- 2) the rate equation, and
- 3) the energy equation.

They are individually described in the following sections.

2.3.1 State Equation

The use of temperature and pressure as the state variables and the assumption of a homogeneous gaseous system imply that a gas law should be chosen as the state equation. The *perfect* gas law is often a good approximation except under extreme temperature and pressure. These conditions are sometimes encountered in reacting problems. The *real* gas effects can be incorporated into the perfect gas law through a correction called the *compressibility factor* Z :

$$\bar{m} \frac{P}{\rho R_u T} = Z ,$$

where R_u stands for the universal gas constant in molar units, \bar{m} is the average molar mass of the mixture defined by

$$\bar{m} = \frac{1}{\sum_{j=1}^K \frac{Y_j}{m_j}}$$

and Z is given by

$$Z = 1 + \Delta_1 + \Delta_2 + \dots .$$

The first correction Δ_1 is due to the limiting-law Debye-Hückel effect; the next correction Δ_2 is due to the second virial effect for pair interactions; the remaining are due to higher order virial effects. These corrections are important when ionic species are abundant. In addition to the gas law, these corrections also apply to the thermodynamic properties and equilibrium behavior[‡] of a system. They are generally functions of temperature, species concentrations, and interaction coefficients among the species. Application of these corrections is often limited by the availability of the interaction coefficients; hence, no such consideration is made and the gas law for a mixture of perfect gas is adopted (*i.e.* $Z \approx 1$) is used in this work:

$$P = \rho \frac{R_u}{\bar{m}} T \tag{2.3.1.1a}$$

or

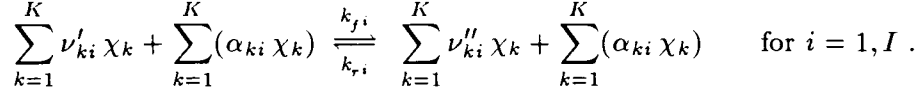
$$\rho = \bar{m} \frac{P}{R_u T} . \tag{2.3.1.1b}$$

Furthermore, the analysis of a chemical system is restricted to the temperature ranges in which thermodynamic properties are available, particularly within $\sim 200 \text{ K}$ to 5000 K where the departure from perfect gas is small. The formulation in CHEMKIN also assumes the perfect gas law for the above reasons.

[‡] A more detail discussion on this subject is given by Woolley (1958).

2.3.2 Rate Equation

Rate equations are derived based on the reaction mechanisms and the rate law. Consider a set I elementary reaction steps, each written in the general form



The variables used here are in accordance with the description given in section 1.3.2 for the reaction mechanisms: χ_k is the symbolic representation of the k^{th} species and ν'_{ki} and ν''_{ki} are the corresponding stoichiometric coefficients in the i^{th} reaction. The second sum which appears identically on both sides of the reactions are the third body terms. The numbers, α_{ki} , are the enhanced third body coefficients and need not be integers. Without loss of generality, each of the reactions is assumed reversible, designated by a forward rate, $k_{f,i}$, and a reverse rate, $k_{r,i}$. An irreversible reaction is represented by one with either $k_{f,i}$ or $k_{r,i}$ identically equal to zero.

Given the reaction rates in units of molar concentration, the contribution of the forward step in the i^{th} reaction to the chemical production rate of the k^{th} species is given by the respective difference between the creation and destruction rates:

$$(\dot{\omega}_{ki})_f = (\nu''_{ki} - \nu'_{ki}) k_{f,i} \left(\sum_{j=1}^K \alpha_{ji} C_j \right) \prod_{j=1}^K C_j^{\nu'_{ji}} . \quad (2.3.2.1a)$$

Similarly, the contribution of the reverse step is

$$(\dot{\omega}_{ki})_r = (\nu'_{ki} - \nu''_{ki}) k_{r,i} \left(\sum_{j=1}^K \alpha_{ji} C_j \right) \prod_{j=1}^K C_j^{\nu''_{ji}} . \quad (2.3.2.1b)$$

The chemical production rate $\dot{\omega}$ is also known as the rate of progress variable. Written here in terms of molar concentration, it has the unit of moles per unit volume per unit time or, in metric units, *molar per second*. The overall chemical production rate of the k^{th} species is the sum of the above two contributions:

$$\dot{\omega}_k = \sum_{i=1}^I ((\dot{\omega}_{ki})_f + (\dot{\omega}_{ki})_r) ;$$

that is,

$$\dot{\omega}_k = \sum_{i=1}^I (\nu''_{ki} - \nu'_{ki}) \left(\sum_{j=1}^K \alpha_{ji} C_j \right) \left[k_{f,i} \prod_{j=1}^K C_j^{\nu'_{ji}} - k_{r,i} \prod_{j=1}^K C_j^{\nu''_{ji}} \right] . \quad (2.3.2.2)$$

The rate of change of mass fraction can then be derived from mass conservation. Taking into account the external mass addition $\dot{\omega}_k^a$ defined for the model, the rate equation for mass fraction is given by

$$\frac{dY_k}{dt} = \frac{m_k}{\rho} (\dot{\omega}_k + \dot{\omega}_k^a) ; \quad (2.3.2.3a)$$

and in terms of temperature and pressure,

$$\frac{dY_k}{dt} = \frac{m_k R_u T}{\bar{m} P} (\dot{\omega}_k + \dot{\omega}_k^a) . \quad (2.3.2.3b)$$

The molar concentration in the chemical production rate equations may be expressed in terms of the selected variable set, (Y_k, T, P) . First, note that the mass density can take the form

$$\rho = \sum_{j=1}^K C_j m_j ;$$

then, with equation 2.3.2 and the state equation 2.3.1.1a,

$$C_k \longrightarrow C_k(Y_k, T, P) = \frac{\bar{m}}{m_k} \frac{P}{R_u T} Y_k . \quad (2.3.2.4)$$

Note again that all variables in the finite rate process are functions of time. That is,

$$Y_k = Y_k(t) ,$$

$$T = T(t) ,$$

$$P = P(t) ,$$

and so on.

2.3.3 Energy Equation

While common *total* or *stagnation* quantities such as that for temperature and pressure become less meaningful in a calorically imperfect medium, one must resort to a more fundamental measurement, the specific enthalpy. The specific enthalpy per unit mass of a mixture is defined by

$$\bar{h} = \sum_{k=1}^K h_k Y_k , \quad (2.3.3.1)$$

where $h_k(T)$ is the standard state enthalpy in mass unit for the k^{th} species. In terms of the specific heat at constant pressure C_{pk} ,

$$\frac{dh_k(T)}{dT} = C_{pk}(T) \quad (2.3.3.2a)$$

or

$$h_k(T) = \int_{T_r}^T C_{pk}(T) dT + \Delta h_{fk}^r . \quad (2.3.3.2b)$$

The last term, Δh_{fk}^r , in the second equation is a constant of integration which may be recognized as the heat of formation at the reference temperature T_r . Conventionally, T_r is taken to be the standard temperature of 298.15 K.

According to the first law of thermodynamic, the change in energy of a system must be balanced by the changes due to heat transfer and work done, namely,

$$dE = dQ - dW \quad (2.3.3.3)$$

which is the conservation of energy. E , Q and W are the total energy, heat transfer and work done respectively. The sign conventions are such that Q is positive when heat is transferred *into* the system and W is positive when work is done *by* the system.

In case of a static system, no kinetic or potential energy is involved. Therefore, the total energy must equal the internal energy. Let e denote the specific internal energy defined by

$$e = \bar{h} - \frac{P}{\rho} .$$

Then

$$dE = de = d\left(\bar{h} - \frac{P}{\rho}\right) .$$

The conservation of energy in equation 2.3.3.3 implies that

$$d\left(\bar{h} - \frac{P}{\rho}\right) = dQ - P d\left(\frac{1}{\rho}\right)$$

or

$$d\bar{h} - \frac{1}{\rho} dP = dQ \quad (2.3.3.4)$$

where the relation

$$dW = P d\left(\frac{1}{\rho}\right)$$

has been used. According to the definition of \dot{Q}^a for the model,

$$\frac{dQ}{dt} \equiv \dot{Q}^a .$$

Equation 2.3.3.4 then becomes

$$\frac{d\bar{h}}{dt} - \frac{1}{\rho} \frac{dP}{dt} = \dot{Q}^a .$$

Using equation 2.3.3.1 and the fact that

$$\frac{dh_k}{dt} = \frac{dh_k}{dT} \frac{dT}{dt} = C_{pk} \frac{dT}{dt} ,$$

the energy equation is obtained:

$$\sum_{k=1}^K h_k \frac{dY_k}{dt} + \left(\sum_{k=1}^K C_{pk} Y_k \right) \frac{dT}{dt} - \frac{1}{\rho} \frac{dP}{dt} = \dot{Q}^a . \quad (2.3.3.5)$$

2.4 Summary of Static Model

The set of equations governing a static chemical system is summarized as follows:

$$\frac{dY_k}{dt} = \frac{m_k}{\rho} (\dot{\omega}_k + \dot{\omega}_k^a) \quad \text{for } k = 1, K, \quad (2.4.1)$$

$$\sum_{k=1}^K h_k \frac{dY_k}{dt} + \bar{C}_p \frac{dT}{dt} - \frac{1}{\rho} \frac{dP}{dt} = \dot{Q}^a, \quad (2.4.2)$$

and for a mixture of perfect gas,

$$P = \rho \frac{R_u}{\bar{m}} T. \quad (2.4.3)$$

The chemical production rates are given by

$$\dot{\omega}_k = \sum_{i=1}^I (\nu''_{ki} - \nu'_{ki}) \left(\sum_{j=1}^K \alpha_{ji} C_j \right) \left[k_{fi} \prod_{j=1}^K C_j^{\nu'_{ji}} - k_{ri} \prod_{j=1}^K C_j^{\nu''_{ji}} \right] \quad \text{for } k = 1, K \quad (2.4.4)$$

for the reactions

$$\sum_{k=1}^K \nu'_{ki} \chi_k + \sum_{k=1}^K \alpha_{ki} \chi_k \xrightleftharpoons[k_{r,i}]{k_{f,i}} \sum_{k=1}^K \nu''_{ki} \chi_k + \sum_{k=1}^K \alpha_{ki} \chi_k \quad \text{for } i = 1, I.$$

Concentrations are given in terms of (Y_k, T, P) by

$$C_k = \rho \frac{Y_k}{m_k}. \quad (2.4.5)$$

In equation 2.4.2, the mass-weighted average specific heat at constant pressure \bar{C}_p is introduced. It is defined by

$$\bar{C}_p(Y_k, T) = \sum_{k=1}^K C_{pk}(T) Y_k. \quad (2.4.6)$$

The importance of thermodynamic properties has been mentioned in section 1.3.3. Without over stretching this point, they enter the problem through $h_k(T)$ and $\bar{C}_p(Y_k, T)$ in equation 2.4.2.

The equations shown above are derived explicitly in terms of Y_k, T and P . Sometimes, it is desirable to write equations in terms of mole fractions and other state variables depending on the nature of the initial and boundary conditions. Transformation to other composition variables can be accomplished via simple conversion formulae. The use of other state variables aside from density is usually more difficult, as can be seen from the expression for absolute entropy given in appendix I.

If ρ is eliminated from the equations, the governing set then consists of equation 2.4.1 and equation 2.4.2. These are $K + 1$ equations for $K + 2$ unknowns (Y_k, T, P). Therefore, one more boundary condition must be specified in addition to $\dot{\omega}_k^a$ and \dot{Q}^a . Some common conditions are *isobaric*, *isothermal* and *isentropic* which correspond to constant pressure, constant temperature and constant entropy respectively. A practical application of the isobaric system is presented in the following chapter for a combustor. A near isentropic condition is used to model a one-dimensional diffuser in appendix II.

CHAPTER 3

Finite-Rate Reaction in a 1-D Constant Pressure Combustor

Part I: Setup

3.1 Background

In view of the growing interest in hypersonic or transatmospheric vehicles, especially in the air-breathing NASP (National AeroSpace Plane), preliminary overall vehicle analyses have been performed* while studies on more detailed fluid dynamical models are being conducted by CFD (Computational Fluid Mechanics) researchers. This research attempts to construct intermediate models that would provide useful vehicle performance information efficiently. Calculations are based upon the preliminary analyses; the results may be used as the inputs for more detailed studies. Emphasis is placed on the finite-rate combustion process since it is the principal energy source of vehicle propulsion.

Due to the many advantages of hydrogen fuel,** it has been selected as the chemical propellant for the NASP. Effort is made here to determine the combustion characteristics of a hydrogen-air mixture. A constant pressure adiabatic environment is chosen for the working model to simulate the conditions in a SCRAMJET (supersonic ramjet) combustion chamber. Numerical calculations are conducted to study the effects of *fuel-air ratio* (initial composition), *initial temperature* and *combustor pressure* on the combustion efficiency and some intrinsic chemical time scales. Attempts are also made to deduce the essential species and reactions steps in the combustion process.

The equations summarized in section 2.4. may be applied to the combustion calculations. Imposing the constant pressure condition, the equations reduce to a set of ordinary differential equations which can be integrated numerically in time. The reduced equation set is shown in section 3.3. It is clear from the governing equations that the chemistry may be handled independently from the integration. This is generally true for many problems

* For example, see Ikawa.[5]

** The advantages of *hydrogen* include being light, non-corrosive, and having high combustion heat release, high specific heat for cooling, clean products, etc.

involving chemical reaction, including the two-dimensional supersonic reacting nozzle problem illustrated in chapter. Since a numerical approach is to be used, a numerical package is chosen to handle the chemistry. In particular, the gas-phase chemical kinetic subroutine library CHEMKIN^[5] is used. The original version of CHEMKIN* has been reviewed and tested extensively over the past ten years and its reliability has been well proven; thus, the possibility of any error introduced by poorly handled chemistry is eliminated in the present work.**

In order to achieve the highest possible accuracy, the equations are integrated concurrently; in other words, the rate equations are marched along with the energy equation at each time step. Since the derivatives in the rate equations can be many order higher than that in the energy equation, the system of equations is inherently *stiff*. An ordinary differential equation solver LSODE^[4] specially designed for handling a stiff set of equations is therefore used.

2.5 Model

At this point, it is best to reiterate the four basic assumptions in the static model described earlier and to state the additional constraints in this model:

- i) mixture is homogeneous,
- ii) mixture is at thermal equilibrium,
- iii) net motion and dissipative heat loss are neglected,
- iv) all species are in gas phase,
- v) pressure is constant at all time,
- vi) adiabatic conditions are satisfied, and
- vii) species is not added from external.

The last three items pertaining to the present model are designed to approximate the environment in a scramjet combustor. In this point of view, a steady one-dimensional model with area variation best fits this application. The model shown in figure 2.2.1b may be modified for the present purpose:

* A newer version, CHEMKIN-II(1989), is now available.

** Though there is a problem when reactions with rates or equilibrium constants close to a computer's largest or smallest number are involved.

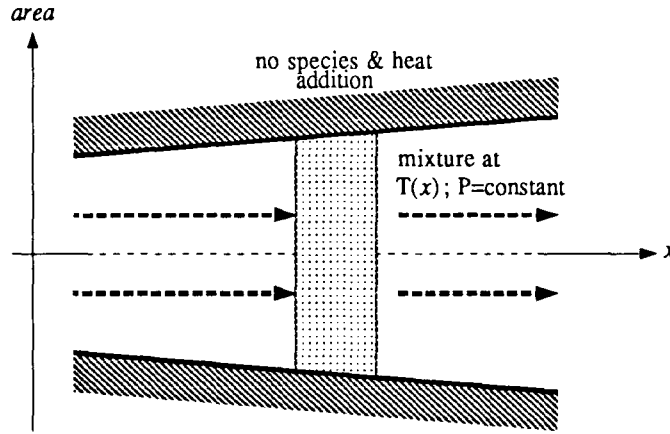


FIG. 3.2.1 One-dimensional scramjet combustor model.

In figure 3.2.1, assumptions (v) to (vii) have been applied. Due to assumption (v), the cross-sectional area must change such that pressure remains constant along the channel. Furthermore, assumptions (vi) and (vii) imply that the conditions

$$\dot{Q}^a \equiv 0 \quad (3.2.1)$$

and

$$\dot{\omega}_k^a \equiv 0 \quad \text{for } k = 1, K \quad (3.2.2)$$

are indeed satisfied. Together with the constant pressure condition,

$$\frac{dP}{dt} \equiv 0, \quad (3.2.3)$$

they allow the application of the equations shown in section 2.4. Subsequent simplification of the governing set is also made possible by conditions 3.2.1, 3.2.2 and assumption (v).

3.3 Governing Equations

The combustion process in a one-dimensional system is to be analyzed. Despite the introduction of a flow speed, the situation may be readily reduced to that of a static case through some simple considerations. In particular, the static model derived in chapter 2 may be used. Let $U(x)$ denote the flow speed along the channel. Momentum conservation implies that

$$U dU + \frac{1}{\rho} dP = 0 \quad (3.3.1)$$

when there is no mass (or species) addition. Since pressure is constant, it immediately follows that

$$U dU = 0$$

or

$$U(x) \longrightarrow U \equiv \text{constant} . \quad (3.3.2)$$

The presence of kinetic energy modifies the energy conservation in a static case by adding the term $\frac{U^2}{2}$ in equation 2.3.3.4; however, U is constant and so

$$dE = de + d\frac{U^2}{2} = de$$

and the following derivation in section 2.3.3 remains unchanged. Furthermore, the steady one-dimensional spatial flow problem may be transformed into a time evolution one through

$$x = U t \longleftrightarrow dx = U dt \quad \text{for } U = \text{constant} .$$

Thus allowing the combustion process to be described by the equations summarized in section 2.4. Since the boundary conditions in equation 3.2.1 to 3.2.3 are time independent, they may be incorporated into the equations directly:

$$\frac{dY_k}{dt} = \frac{m_k}{\rho} \dot{\omega}_k \quad \text{for } k = 1, K , \quad (3.3.3)$$

$$\sum_{k=1}^K h_k \frac{dY_k}{dt} + \bar{C}_p \frac{dT}{dt} = 0 , \quad (3.3.4)$$

and for a mixture of perfect gas,

$$\rho = \bar{m} \frac{P}{R_u T} . \quad (3.3.5)$$

The expressions for the chemical production rates $\dot{\omega}_k(Y_k, T)$ and the mass-weighted average specific heat at constant pressure $\bar{C}_p(Y_k, T)$ are given in section 2.4.

As pressure is constant, it only appears in the equations as a parameter. On the other hand, U decoupled from the governing equations and is neither a variable nor a parameter as far as the reacting system is concerned. The relevant variable set reduces to

$$(Y_k(t), T(t)) \quad \text{for } k = 1, K .$$

Since density ρ is a point function of (Y_k, T) and the parameter P , substituting equation 3.3.3 for ρ in equation 3.3.1 and 3.3.2 results in a set of $K + 1$ ordinary differential equations for the $K + 1$ unknowns $Y_k(t)$ and $T(t)$. A set of $K + 1$ initial conditions is needed to complete the problem. Generally, they are specified through $Y_k(t = 0)$ and one of the state variables at $t = 0$. The solution then defines the evolution of the system: $\rho(t)$ is readily deduced from the state equation; molar concentrations and mole fractions can be obtained from simple conversion formulae; the speed of sound and absolute entropy are given in the equations of appendix I; and so on.

To aid the study of a combustion process, a quantity of interest is the *chemical heat release* ΔH during reaction. In this context, ΔH is positive when heat is generated. It is a derived quantity depending on the two variables in the problem, Y_k and T , and the *heat of formation* which is a thermodynamic property of each species. For the present purpose, it is more convenient to define ΔH using the standard enthalpy instead. Consider the equation of energy conservation in section 2.3.3:

$$\sum_{k=1}^K h_k(T) Y_k(T) = \text{constant} ;$$

it may be evaluated at a reference initial state and an arbitrary state in time such that

$$\sum_{k=1}^K h_k(T_0) Y_k(T_0) = \sum_{k=1}^K h_k(T) Y_k(T) ,$$

where the subscript ‘0’ denotes the initial state. Then the chemical heat release can be extracted by replacing $h_k(T)$ with an equivalent expression:

$$\begin{aligned} \sum_{k=1}^K h_k(T_0) Y_k(T_0) &= \sum_{k=1}^K \left[h_k(T_0) + \int_{T_0}^T C_{pk}(T) dT \right] Y_k(T) \\ &= \sum_{k=1}^K h_k(T_0) Y_k(T) + \text{chemical heat release} \end{aligned}$$

or

$$\Delta H(T) = \sum_{k=1}^K h_k(T_0) [Y_k(T_0) - Y_k(T)] . \quad (3.3.6)$$

Note that ΔH depends explicitly on the reference initial point; different choice of the initial point would lead to a different $\Delta H(T)$. For most applications, it should be chosen as the point where chemical changes begin such that ΔH would represent the chemical energy *available* in the form of heat since the reactions have *initiated*. In an aircraft engine, this may be right after fuel-oxidizer mixing, a spark ignition, a shock induced temperature rise and so on.

Although the equations as written are intended for a finite-rate process, they can be extended to the *frozen* and the *equilibrium* processes. The frozen calculation is trivial in the present model. A frozen system is one defined by $\dot{\omega}_k$ being identically zero for all k . It is then obvious from conditions 3.3.1 and 3.3.2 that Y_k and T would remain unchanged and consequently so would all other quantities. There are two approaches to the equilibrium calculation. The first one is to replace the rate equations by a set of nonlinear algebraic equilibrium conditions (the laws of mass action for instance). Along

with the energy equation, the equilibrium solution can be solved. Note that the equilibrium solution is stationary in time since the boundary conditions are time independent. This allows for a second approach. The finite-rate equations as is may be integrated to infinite time to obtain the equilibrium solution. In practice, a *large time*[‡] is usually sufficient for a close approximation.

3.4 Survey of Kinetic Data for a Hydrogen-Air System

The task here is to select the appropriate species set, reaction set, rate coefficients and thermodynamic data for a hydrogen-air system based on the ranges of conditions selected. As these conditions are described in section 3.6, they are considered non-exceptional in the sense that they had been encountered in many previous calculations and experiments. For this reason, kinetic data may be extracted from various literatures and handbooks. A set of references used for this purpose is listed at the end of this chapter.

In order to make the selection of kinetic data, it is necessary to define the constituents of *air* for the problem at interest. Atmospheric air of the current century (20th) consists of nitrogen, oxygen as well as traces of carbon dioxide, water vapor, several inert gases and numerous unspeakable pollutants. Although the trace species constitute less than 1% of air by mole, their existence cannot be neglected since many chain initiating reactions rely on third bodies such that all possible candidates, particularly inert gases, must be accounted for. According to the results of former works, it is unlikely that any trace species can be as important as a radical such as the hydrogen radical or hydroxide radical which also appears in a trace quantity but is essential and has prominent effects in the combustion process; it is acceptable to assume that the trace species only act as third bodies and do not generate any active or high energy products that may affect the combustion characteristics. Despite that the concentrations of nitrogen and oxygen in air are relatively constant, the exact composition and constituents of the trace species may vary over the atmosphere; hence, only the most abundant inert gas, argon, is included to account for their presence.* This leads to a dry air consisting of only three elements. Its composition at standard temperature

[‡] The time scale is problem dependent.

* Trace species excluding Ar constitute less than 0.04% of air by mole.

and pressure (298 K and 1.0 atm) is listed in table 3.4.

	Species (chemical formula)	Molar Mass m [g/mol]	Mass Fraction Y	Mole Fraction X
1	N ₂	28.0134	7.5530×10^{-1}	7.8090×10^{-1}
2	O ₂	31.9988	2.3146×10^{-1}	2.0950×10^{-1}
3	Ar	39.9480	0.1324×10^{-1}	0.0960×10^{-1}

TABLE 3.4 Composition of Air at STP.

Using the assumed constituents of air and hydrogen as fuel, a total of seven reports are compiled to construct the species set, reaction set and rate coefficients. As a result, a total of 55 reversible reactions, 19 species and 4 elements are collected. The reaction steps together with the rate coefficients are listed in tables III.1a to III.1c of appendix III. The seven references used are also listed in the same appendix.

Although the list in appendix III is already a simplified one since carbon-dioxide has not been included as a constituent of air, it will be further reduced to eliminate the components that are not essential in the present application. This process is described in section 3.6 where the selection of kinetic data from the seven references is also discussed. It is important that the appropriate data be selected since conflicting data are sometimes found in different references for the same reaction. In terms of the rate coefficient of equation 1.3.2, the activation energies are found to be quite consistent amount the references while more dramatic discrepancies are found in the pre-exponent constants and the temperature exponents.

Only two sources, the CHEMKIN^[6] thermodynamic data base and the JANAF^[1] thermochemical tables, are surveyed to obtain the thermodynamic properties. Good agreement is presented by the properties from the two sources. In the JANAF tables, data have been compiled such that inter-consistency among species properties is maintained with minimal discrepancy within the average temperature range (~ 273 K – 5000 K for gaseous species) considered in the tables. However, constants of adjustment must be determined for the species properties before they can be applied to the governing set. Equation 1.4.3 of chapter 1 may be used for this purpose. The CHEMKIN data base, on the other hand, requires no adjustments. It is designed according to the format used by the NASA complex chemical equilibrium code by Gordon and McBride.^[2] Comparison between the CHEMKIN data and some of the adjusted JANAF data shows an overall deviation of less than 0.2% for the species set at interest. Therefore, the CHEMKIN data base will be used in the combustion

calculations for convenience.

3.5 Estimation of Initial Conditions and Combustor Pressure

The initial conditions for the static calculations correspond to the inlet conditions for the scramjet combustor model. Therefore, the components upstream of the combustor must be considered in order to determine practical ranges of initial or inlet conditions. The construction of a simple one-dimensional air-breathing engine consisting of a forebody inlet, a supersonic combustor and an afterbody expansion nozzle is adopted. The conditions defining the individual components are:

1. Diffuser — equilibrium chemistry with fixed kinetic energy efficiency η_{eff} .
2. Combustor — adiabatic and constant pressure.
3. Nozzle — strictly supersonic; other conditions arbitrary.

Air from free-stream is compressed through the diffuser. Fuel-air mixing takes place between the diffuser exit and the combustor inlet. The mixture, assumed to be perfectly mixed and not yet reacting, then enters the combustor where the combustion process *begins* and is to be analyzed. The product is exhausted through the nozzle which is not relevant presently.

In this simple engine, the component that must first be analyzed is the diffuser. An important phenomenon faced by all hypersonic aircraft is the hypersonic viscous interaction at the forebody inlet. The effects of such interaction grossly determine the performance of the diffuser, especially at high flight Mach number and high altitude. To include these effects, one may resort to approximate methods such as the second-order expansion treated by Kubota^[8] for the weak interaction or to highly complicated CFD calculations. Nevertheless, all the losses are integrated into one factor known as the kinetic energy efficiency η_{eff} . It is defined as

$$\begin{aligned} \eta_{\text{eff}} &\equiv \frac{\text{kinetic energy available by expanding diffuser exit flow to ambient pressure}}{\text{kinetic energy of diffuser inlet flow}} \\ &\equiv \frac{U_{\text{eff}}^2}{U_{\infty}^2} . \end{aligned}$$

For a well designed diffuser inlet, η_{eff} is nearly constant over a wide range of flight speed and inlet conditions. Alternatively, a fractional increase in entropy may be defined. This choice is eliminated since it tends to under-estimate the diffuser loss at high flight Mach number while over-estimating the loss at lower values. The choice of frozen or equilibrium chemistry in the diffuser is found to have little effect on its exit conditions. But equilibrium chemistry is chosen since it presents a worse situation where more energy is locked up in NO_x radicals.

A one-dimensional diffuser model is built based on the following constraints:

- i) diffuser inlet conditions are equivalent to ambient conditions which correspond to standard atmospheric conditions;
- ii) diffuser is characterized by an inherent loss, quantified by a kinetic energy efficiency η_{eff} ; and
- iii) diffuser chemistry is equilibrium.

The details are described in appendix II. In short, the model is formulated such that both equilibrium and frozen chemistries can be handled. In this way, the effect of finite-rate reactions on the diffuser exit conditions can be estimated. The used of a fractional entropy loss instead of the kinetic energy efficiency is also incorporated in the model. Findings show that even equilibrium chemistry has little effect on the diffuser exit conditions.

In a scramjet performance analysis by Kerrebrock,^[7] it has been found that an optimum combustor inlet Mach number exists for combustor pressure higher than 0.03 atm and flight Mach number approximately higher than 10 such that the specific impulse of the engine is a maximum for near stoichiometric fuel-air mixture and ideal expansion at the exhaust nozzle. The result is based upon the calculations of a “SCRAMJET” program developed by Serdengecti.^[13] Although equilibrium and frozen chemistries are assumed in deducing the above conclusion, it is rational that such an optimum Mach number also exists for finite-rate chemistry. Detailed arguments are given by Kerrebrock. As a result, the following reference cruise conditions for the diffuser are adopted:

- i) free-stream Mach number, $M_\infty \approx 15$;
- ii) diffuser exit (\sim combustor inlet) Mach number, $M_c \approx 5$;
- iii) diffuser exit (\sim combustor) pressure, $P_c \approx 1.0 \text{ atm}$; and,
- iv) diffuser kinetic energy efficiency, $\eta_{\text{eff}} \approx 0.985$.

Equivalent to imposing a diffuser exit Mach number (condition ii) is to select a flight altitude H . In this case, the corresponding H is $\sim 127,000 \text{ ft}$.

The diffuser exit conditions corresponding to the reference inputs are computed using the model described in Appendix II. Upon fuel-air mixing, the combustor inlet conditions are obtained. Although the state of hydrogen prior to mixing can be very important in determining the final state of the mixture, there is little information pertaining to its prior state that would allow such consideration. Thus, hydrogen is assumed to have the same state as the diffuser exit air. The following reference combustor inlet conditions are then deduced:

	Diffuser Parameters and Inlet Conditions	Combustor Parameters and Inlet Conditions
K.E. Efficiency η_{eff}	0.9850	—
Equivalence Ratio ϕ	—	1.2
Temperature T [K]	2.4695×10^2	1.3570×10^3
Pressure P [atm]	3.3822×10^{-3}	1.0000
Flow Speed U [m/s]	4.7265×10^3	4.3345×10^3
Mach Number M	15	5
Composition Y_{H}	—	0.0000
Y_{H_2}	—	0.3381×10^{-1}
Y_{N}	0.0000	0.0000
Y_{N_2}	7.5530×10^{-1}	7.2947×10^{-1}
Y_{NO}	0.0000	0.0062×10^{-1}
Y_{O}	0.0000	0.0002×10^{-1}
Y_{O_2}	2.3146×10^{-1}	2.2330×10^{-1}
Y_{Ar}	0.1324×10^{-1}	0.1280×10^{-1}

TABLE 3.5 Reference diffuser inlet and combustor inlet conditions.

The *equivalence ratio* ϕ used in the table is a dimensionless number representing the amount of fuel in a fuel-oxidizer mixture. It is defined as

$$\phi \equiv \frac{(\text{Fuel-Oxidizer ratio})}{(\text{Fuel-Oxidizer ratio})_{\text{st}}}$$

where

$$\text{Fuel-Oxidizer ratio} \propto \frac{\text{mass of fuel}}{\text{mass of oxidizer}} \propto \frac{\text{mole of fuel}}{\text{mole of oxidizer}} \propto \dots \text{ etc.}$$

The subscript 'st' stands for the stoichiometric condition where all reactants are ideally consumed.

3.6 Basic Constraints on Calculation

To use the governing equations in section 3.3 requires that the model assumptions in section 3.2 be satisfied; and to implement these equations and perform the actual calculations require that three additional constraints be established. The first one is the range of temperature that may be encountered by the system. Then there is the desired accuracy for the calculations. Finally, a set of kinetic data must be selected to represent the chemical processes. The three constraints are interrelated and must be considered together. For instance, the availability of kinetic data limits the range of temperature that can be studied and their reliability determines the obtainable accuracy on the solutions. Conversely, a limit on the desired accuracy aids in eliminating trace species and, hence, irrelevant reactions. It also determines the acceptable schemes for implementing the governing equations.

3.6.1 Combustor input conditions

Unless a calculation has been performed, it is impossible to know the exact range of temperature that may be encountered even by a constant pressure combustor. Fortunately, experience and previous works serve to provide good estimates on this range if the combustor initial conditions and pressure are known**.

The combustor inlet conditions shown in table 3.4 are believed to produce near optimal engine performance. The remaining task is to vary these parameters over reasonable ranges such that the changes in combustion characteristics can be examined. Three variables, inlet temperature, combustor pressure and equivalence ratio, are selected for this purpose since flow speed or Mach number is irrelevant in the one-dimensional model. The following values are explored:

	Ranges	Values explored
Equivalence Ratio ϕ	0.6–1.4	0.6, 0.8, 1.0*, 1.2, 1.4
Inlet Temperature T_0 [K]	500–2500	500, 1000, 1500*, 2000, 2500
Pressure P_c [atm]	0.1–1.0	0.1, 0.2, 0.5*, 0.7, 1.0

TABLE 3.6.1 Ranges and values of combustor calculation parameters.

** The equilibrium conditions are also good references.

For these ranges of ϕ , T_0 and P_c , the temperature that may be encountered by the combustor is estimated to fall within 500 K and 4000 K. In this way, thermodynamic properties for most species and the kinetic data for most reactions are valid. Note that the values indicated by ‘*’ are selected as the reference conditions for the parametric study in Chapter 4.

3.6.2 Accuracy

The accuracy or allowable error of a variable is defined by its magnitude and two factors — a *relative tolerance* ϵ_r and an *absolute tolerance* ϵ_a . For a variable V , its overall error tolerance defined by

$$\epsilon_V = |V| \epsilon_{Vr} + \epsilon_{Va} .$$

The tolerances, particularly ϵ_{Va} , are variable specific. After several trail calculations, the tolerances for temperature and mass fraction are established; their values are listed in table 3.6.2. The tolerances for ΔH estimated from those of T and Y_k are also shown in the table for reference. Although these values are not needed in the calculations, they indicate how reliable the heat release is quantitatively.

	Relative Tolerance	Absolute Tolerance
Temperature T [K]	1.0×10^{-4}	1.0×10^{-4}
Mass Fraction Y_k	1.0×10^{-4}	1.0×10^{-8}
Heat Release* ΔH [kJ/kg]	1.0×10^{-4}	1.0×10^{-4}

* (see definition in section 3.3)

TABLE 3.6.2 Error tolerances.

Many considerations have been incorporated to determine those tolerances. An overall constraint is that they must be consistently set since all the variables are related.[†] Consider for example the absolute tolerance. An error in the magnitude of a mass fraction (in particular, that of a high energy radical) exceeding 10^{-5} can result in an error in the temperature of $\sim 10^1$ K. It is for this reason that trail calculations have been conducted before setting the tolerances.

[†] That is, $\partial V_i / \partial V_j \neq 0$ for variable i and variable j .

Two other factors which must be considered when setting the tolerances are the capability of the numerical computation and the accuracy of the input data. In the former case, there is a lower limit on the tolerances determined by the computing environment and the numerical schemes. It is often possible to use a highly sophisticated schemes to lower this limit. But this may lead to an unnecessary computational effort which is especially evident when a large number of chemical reactions and species are involved. In the latter case, particular examples are the input kinetic data and thermodynamic properties.

3.6.3 Reduced kinetic data set

It has been known to an experimentalist that the effects of some reaction steps are often dominated by the effects of some others. In other words, their rate coefficients are harder to determine or cannot be determined with precision which may account for the discrepancies among the 7 references shown in table III.1a and III.1c. To check this, a set of 27 reactions most commonly found in the references were selected from the tables. While their rates are already in good agreement, the values from references 3 and 7 are chosen as references since they are the most comprehensive sources. Test runs are performed on the 27 reactions by selecting different rates or adding a new reaction.[‡] The results show that the use of different rates has little effect (*i.e.*, within the accuracy limits) in terms of the heat release. The addition of new reactions[‡] has more noticeable effects, but they do not exceed the accuracy limits. Therefore, the 27 reactions tested are selected for the combustion analysis.

Indicated in table 3.6.3a are the selected reactions along with the rates and enhanced third body coefficients for some species. The coefficients are unity for all other species. There is a total of 13 species and 4 elements. Their chemical formulae and molar masses are shown in table 3.6.3b.

[‡] Including those from table III.1b.

[‡] In the cases where new species arose, their initial concentrations were set to zero in the test runs.

	Reaction Mechanism (reversible steps)	Enhanced Coeff. α	$k_f = AT^\beta \exp\left(-\frac{E_a}{R_u T}\right)$		
			A	β	E_a [cal/mol]
1	$\text{H}_2 + \text{O}_2 \rightleftharpoons \text{OH} + \text{OH}$		1.70×10^{13}	0.0	47780.0
2	$\text{H}_2 + \text{OH} \rightleftharpoons \text{H}_2\text{O} + \text{H}$		1.17×10^9	1.3	3626.0
3	$\text{O}_2 + \text{H} \rightleftharpoons \text{OH} + \text{O}$		5.13×10^{16}	-0.816	16507.0
4	$\text{H}_2 + \text{O} \rightleftharpoons \text{OH} + \text{H}$		1.82×10^{10}	1.0	8826.0
5	$\text{O}_2 + \text{H} + \text{M} \rightleftharpoons \text{HO}_2 + \text{M}$		2.10×10^{18}	-1.0	0.0
	M = H ₂ , H ₂ O	3.3,21			
	M = N ₂ , O ₂	0.0,0.0			
6	$\text{O}_2 + \text{H} + \text{O}_2 \rightleftharpoons \text{HO}_2 + \text{O}_2$		6.76×10^{19}	-1.42	0.0
7	$\text{O}_2 + \text{H} + \text{N}_2 \rightleftharpoons \text{HO}_2 + \text{N}_2$		6.76×10^{19}	-1.42	0.0
8	$\text{OH} + \text{HO}_2 \rightleftharpoons \text{O}_2 + \text{H}_2\text{O}$		5.01×10^{13}	0.0	1000.0
9	$\text{H} + \text{HO}_2 \rightleftharpoons \text{OH} + \text{OH}$		2.51×10^{14}	0.0	1900.0
10	$\text{O} + \text{HO}_2 \rightleftharpoons \text{O}_2 + \text{OH}$		4.79×10^{13}	0.0	1000.0
11	$\text{OH} + \text{OH} \rightleftharpoons \text{H}_2\text{O} + \text{O}$		6.03×10^8	1.3	0.0
12	$\text{H}_2 + \text{M} \rightleftharpoons \text{H} + \text{H} + \text{M}$		2.24×10^{12}	0.5	92600.0
	M = H, H ₂ , H ₂ O	2.0,3.0,6.0			
13	$\text{O}_2 + \text{M} \rightleftharpoons \text{O} + \text{O} + \text{M}$		1.86×10^{11}	0.5	95560.0
14	$\text{H} + \text{HO} + \text{M} \rightleftharpoons \text{H}_2\text{O} + \text{M}$		7.59×10^{23}	-2.6	0.0
	M = H ₂ O	20.0			
15	$\text{H} + \text{HO}_2 \rightleftharpoons \text{H}_2 + \text{O}_2$		2.52×10^{13}	0.0	700.0
16	$\text{HO}_2 + \text{HO}_2 \rightleftharpoons \text{H}_2\text{O}_2 + \text{O}_2$		2.00×10^{12}	0.0	0.0
17	$\text{H}_2\text{O}_2 + \text{M} \rightleftharpoons \text{OH} + \text{OH} + \text{M}$		1.29×10^{17}	0.0	45500.0
18	$\text{H}_2\text{O}_2 + \text{H} \rightleftharpoons \text{H}_2 + \text{HO}_2$		1.59×10^{12}	0.0	3800.0
19	$\text{H}_2\text{O}_2 + \text{OH} \rightleftharpoons \text{H}_2\text{O} + \text{HO}_2$		1.00×10^{13}	0.0	1800.0
20	$\text{N}_2 + \text{M} \rightleftharpoons \text{N} + \text{N} + \text{M}$		3.72×10^{21}	-1.6	224928.0
	M = Ar	0.2			
21	$\text{N}_2 + \text{O} \rightleftharpoons \text{NO} + \text{N}$		1.82×10^{14}	0.0	76241.0
22	$\text{NO} + \text{M} \rightleftharpoons \text{N} + \text{O} + \text{M}$		3.98×10^{20}	-1.5	150000.0
23	$\text{NO} + \text{O} \rightleftharpoons \text{N} + \text{O}_2$		3.80×10^9	1.0	41369.0
24	$\text{NO}_2 + \text{M} \rightleftharpoons \text{NO} + \text{O} + \text{M}$		1.10×10^{16}	0.0	65571.0
25	$\text{NO}_2 + \text{O} \rightleftharpoons \text{NO} + \text{O}_2$		1.00×10^{13}	0.0	596.0
26	$\text{NO}_2 + \text{N} \rightleftharpoons \text{NO} + \text{NO}$		3.98×10^{12}	0.0	0.0
27	$\text{NO}_2 + \text{NO}_2 \rightleftharpoons \text{NO} + \text{NO} + \text{O}_2$		2.00×10^{12}	0.0	26825.0

TABLE 3.6.3a Reduced kinetic data set.

	Species (chemical formula)	Molecular Mass m [g/mol]
1	N	14.0067
2	N ₂	28.0134
3	NO	30.0061
4	NO ₂	46.0055
5	O	15.9994
6	O ₂	31.9988
7	OH	17.0074
8	H	1.00797
9	H ₂	2.01594
10	HO ₂	33.0068
11	H ₂ O	18.0153
12	H ₂ O ₂	34.0147
13	Ar	39.9480

	Element (chemical formula)	Atomic Mass m [g/mol]
1	N	14.0067
2	O	15.9994
3	H	1.00797
4	Ar	39.9480

TABLE 3.6.3b Species and element sets.

The above lists may be sufficient for the present purpose. Other calculations should reconsider these choices depending on their purpose and desired accuracy.

1. Parametric Studies

In chapter 4, effects of equivalence ratio, initial temperature and combustor pressure on the hydrogen-air system will be presented respectively according to the conditions shown in table 3.6.1. In order to reduce the number of calculations while keeping their results practical for engine performance analyses, variation of each parameter is performed by fixing the other two at their reference values. Each reference condition is indicated by an ‘*’ in table 3.6.1. The reference set is

$$\left\{ \begin{array}{l} \phi = 1.0 \\ T_{\text{initial}} = 1500 \text{ K} \\ P_{\text{combustor}} = 0.5 \text{ atm} \end{array} \right.$$

There are several short comings with these choices because the behavior of combustion at the reference is not representative of some cases within the ranges selected in table 3.6.1. The most noticeable effect is found in the temperature study where abrupt change in behavior is observed at a low initial temperature. Some explanations are attempted in

chapter 4. As the reference conditions are selected only after a few trial calculations, the detailed studies to be presented will reveal what the better choices would be. For instance, the equivalence ratio of 1.0 does not result in the highest heat release per unit mass of fuel which is contrary to the common belief that the adiabatic flame temperature is maximum at a ratio of 1.0. Other subtle points together with some interesting findings are discussed in the parametric studies.

CHAPTER 4

Finite-Rate Reaction in a 1-D Constant Pressure Combustor

Part II: Parametric Studies

4.1 Introduction

The calculations described in this chapter include five discrete equivalence ratios, five initial temperatures and five pressures. The three studies are based on T_0 equals 1500 K and P equals 0.5 atm, ϕ equals 1.0 and P equals 0.5 atm, and ϕ equals 1.0 and T_0 equals 1500 K respectively where ϕ , T_0 and P are the equivalence ratio, initial temperature and the pressure.* These conditions are designated as the reference ones. In addition to the equivalence ratio, the exact initial composition is also an essential input for the calculations. It is intentionally chosen that the initial fuel-air mixture be composed of *neither* any radicals *nor* any combustion products. Until the result of the calculations has been analyzed, it is not known what effects the presence of radicals or products would have on the combustion characteristics. This choice seems only reasonable.

Some basic characteristics of hydrogen-air combustion has been well known. In the case where no radical exists initially, there appears to be an initial period of extremely slow chemical activity; this is followed by a sudden increase in activity which is the beginning of a second stage. These two stages are usually called the *start-up* period and the *fast-rise* period in the following analyses. The first one is of particular importance since its duration can vary over many orders of magnitude and is vital information in terms of engine design. The importance of the second one lies on its rate of increase. In most cases, it is desirable to have the highest rate of increase. The eventual approach towards chemical equilibrium may take two paths. The activity may simply increase towards the equilibrium level or it may increase above that level and then turn back. More importantly, the approach can happen gradually or at a very high rate. The results will present examples of these cases. The word 'rise' has been introduced to describe an *activity*. It is also used repeatedly when the results are discussed. Note that a rise in an activity may refer to an increase in the magnitude of its corresponding variable or a decrease.

* This pressure is constant and is equivalent to the combustor pressure P_c used in chapter 6 when an aircraft engine is concerned.

Because of the importance of the first two stages, three quantities are defined and used throughout the analyses: the duration of the initial period, the time when the increased activity begins to slow down, and the maximum rate of increase during the second stage. They are designed to quantify the extents of the start-up and fast-rise periods and the steepness of the rise. The three quantities are not unique in a calculation since each calculation involves many variables such as the evolution of temperature, heat release, a species' composition, and so on and they are defined according to the magnitude of a variable. However, even if a specific activity or variable is selected, the definitions themselves are not unique since many can serve the same purposes. Three conveniently implemented definitions are adopted after some trials and tests. The point at which the rate of rise first begins to slow down is selected as a base for the definitions. It translates to the first inflexion point of the magnitude of a variable in the second stage. The quantities desired are thus defined by:

1. Start-up time — the period from the initial time to the time at which the tangents at the initial point and the inflexion point meets.
2. End of fast-rise — the period from the initial time to the time at the inflexion point.
3. Steepness of rise — the slope at the inflexion point.

In this formulation, it has been assumed that the second stage terminates at the inflexion point. This definition is not consistent with that of the start-up time. A consistent choice would be to use the point at which the tangent at the inflexion point and the asymptote at infinity meet. But the results of some correlation studies have shown that the latter choice is inferior. Yet another alternative makes use of the points of maximum curvature. The first maximum results in a start-up time similar to that obtained from the above definition. The second maximum which presumably indicates the end of fast-rise, however, does not lead to any good correlations either.

In presenting the results, the chemical heat release ΔH is used to indicate the overall progress of combustion in each calculation. As far as engine performance is concerned, the study of ΔH is quite sufficient. Yet some analyses do require the consideration of composition and temperature. They pertain to the basic mechanics of combustion rather than the overall performance. For example, some species are deemed more important due to their roles in the *chain initiating reactions*, *chain branching reactions*, or *rate controlling reactions* and it is by the consideration of composition that these species can be determined. Temperature is important when the reaction rate is at stake. Nevertheless, their continuous evolution is not very important; knowledge of their values at the starting point, start-up time, inflexion point, possible turning points and equilibrium are sufficient for most

analyses. Some of these values are tabulated in the results.

Normalized values of the variables are often used in the results. In this way, cases with different conditions can be compared. Normalization of a variable is achieved using its initial and equilibrium values:

$$\hat{V}(t) \equiv \frac{V(t) - V(0)}{V_{\text{eq}} - V(0)},$$

where $V(t)$ is a time dependent variable and the subscript 'eq' represents the condition at chemical equilibrium. For each study, the equilibrium conditions are tabulated to provide quantitative information on the data presented.

The same length of time is to be calculated in each case unless specific purposes are to be achieved. Depending on the conditions of each calculation, combustion may proceed extremely fast or extremely slow. Nevertheless, the time needed to be calculated is set by the combustor residence time. Based on a combustor length of less than 15 meters, a residence time of less than 4 millisecond is estimated** for all the cases according to the diffuser model mentioned in section 3.5. Progress of combustion is therefore calculated for a period of 10 times the estimated length; that is, up to 0.04 second.

4.2 The Reference Case

Although each calculation involves many variables as well as some derived quantities, not all of them are needed in the analyses. More importantly, focus may shift from variable to variable in different analyses. Therefore, only the results for selected variables are shown in the calculations. Nevertheless, a detailed account is given in this section for the reference case. The time history for some fundamental variables and several quantities of interest to the combustor performance analysis are shown in figure 4.2.1a through figure 4.2.9b. They are presented in both their absolute magnitudes and normalized values.

According to the assumptions in the static model, the fundamental variable set includes the composition and temperature for which the equations are derived in section 3.3. Mass fraction, Y , is chosen to represent the composition. In figures 4.2.1a and 4.2.1b, the evolution of Y_{N_2} , Y_{O_2} , Y_{H_2} , $Y_{\text{H}_2\text{O}}$ and Y_{Ar} are shown. The first figure is for a duration of zero to 0.04 second. The second one is a closer view of the first 0.0002 second where the start-up

** The combustor is one-dimensional and has constant flow speed; *c.f.* sections 3.3 and 3.5.

behavior can be observed. The remaining species are radicals and have smaller population in general. They are presented in two groups. The first group includes the more abundant ones: NO, O, H and OH. Their mass fractions are shown in figures 4.2.2a and 4.2.2b. The other group is of much smaller abundance; it includes N, NO₂, HO₂ and H₂O₂ whose mass fractions are shown in figures 4.2.3a and 4.2.3b. The time history of temperature is given in figure 4.2.4.

Three additional quantities may also be useful for a combustor analysis. The importance of the chemical heat release, ΔH has been mentioned. The other two are the frozen speed of sound, a_f , and the density, ρ . Since the combustor flow speed is decoupled from the problem, knowledge of a_f can help to translate time scale into length scale which is a physical parameter in an engine. The density can provide an estimate on the channel area in the proposed one-dimensional combustor. These three quantities are shown in figures 4.2.5a, 4.2.6 and 4.2.7 respectively. The start-up behavior of ΔH is shown in figure 4.2.5b. The other two exhibit very similar initial behavior and hence are not shown.

The above results are plotted again with a normalized coordinate. The normalized mass fractions, \hat{Y} , of N₂, O₂, H₂, H₂O and Ar are plotted in figures 4.2.8a and 4.2.8b for long and short time scales. However, those of the radicals are not plotted because their initial values are zero and their normalized curves would resemble the former ones except for a multiplicative factor. \hat{T} , $\hat{\Delta H}$, \hat{a}_f and $\hat{\rho}$ are plotted together due to their similarity. They appear very close in the larger time scale of figure 4.2.9a; only in the magnified scale of figure 4.2.9b can they be distinguished.

Some basic characteristics of hydrogen-air combustion can be observed in the plots. Examples include the initial delay and fast-rise, excessive build-up of some radicals during fast-rise, similarity between normalized temperature and heat release, and so on. These characteristics together with other specific features are described at length in the following sections.

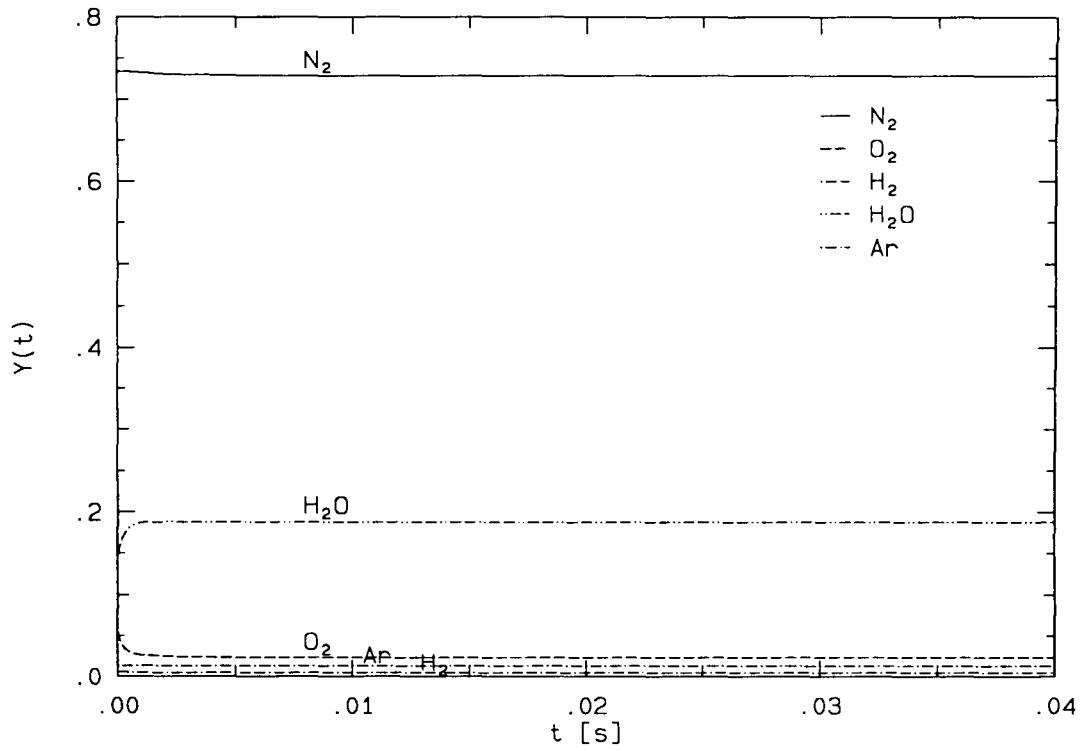


FIG. 4.2.1a Mass fraction of five species.

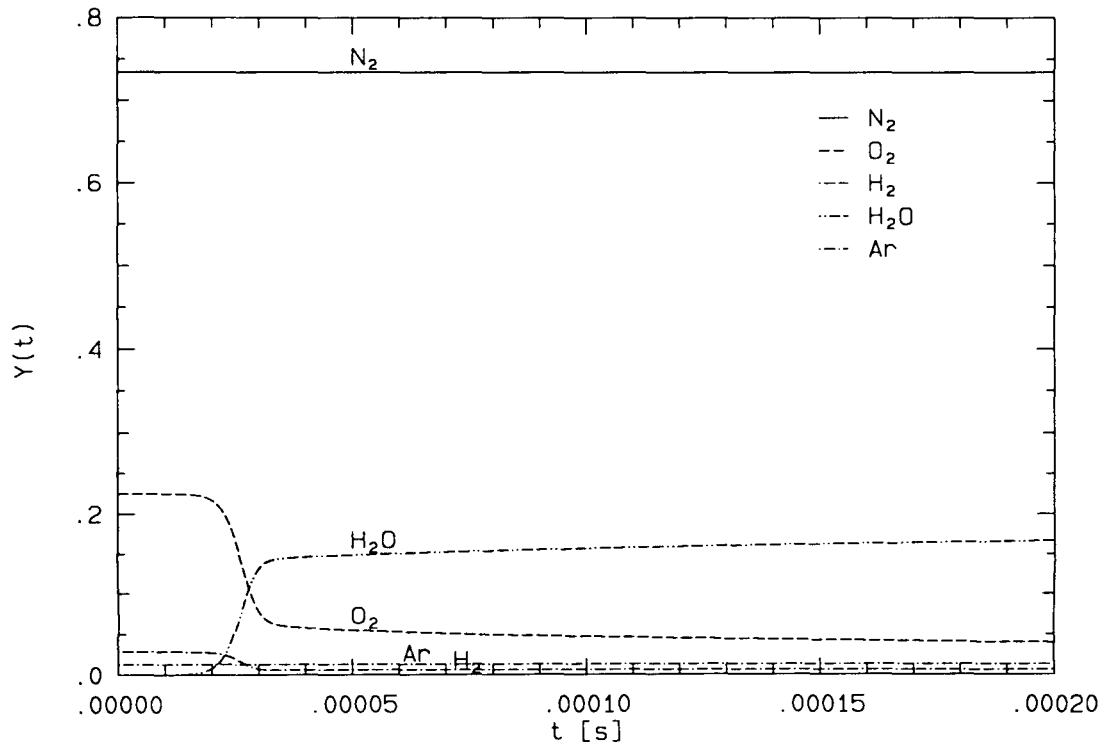


FIG. 4.2.1b Mass fraction of five species at initial start-up.

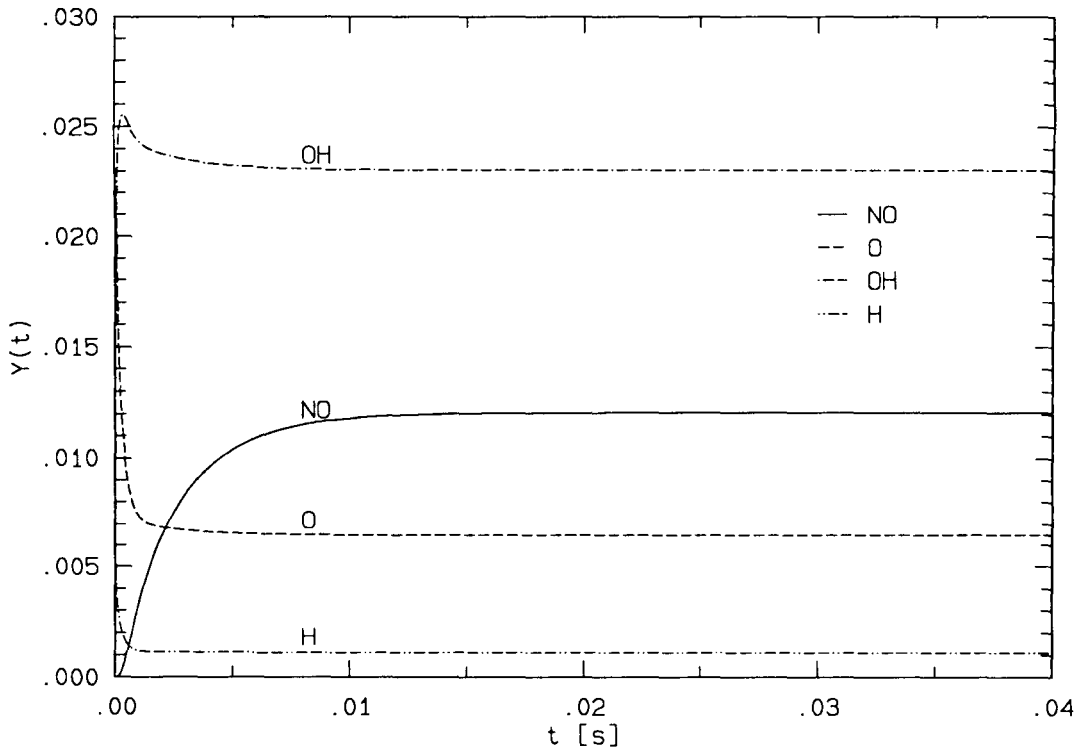


FIG. 4.2.2a Mass fraction of four radicals.

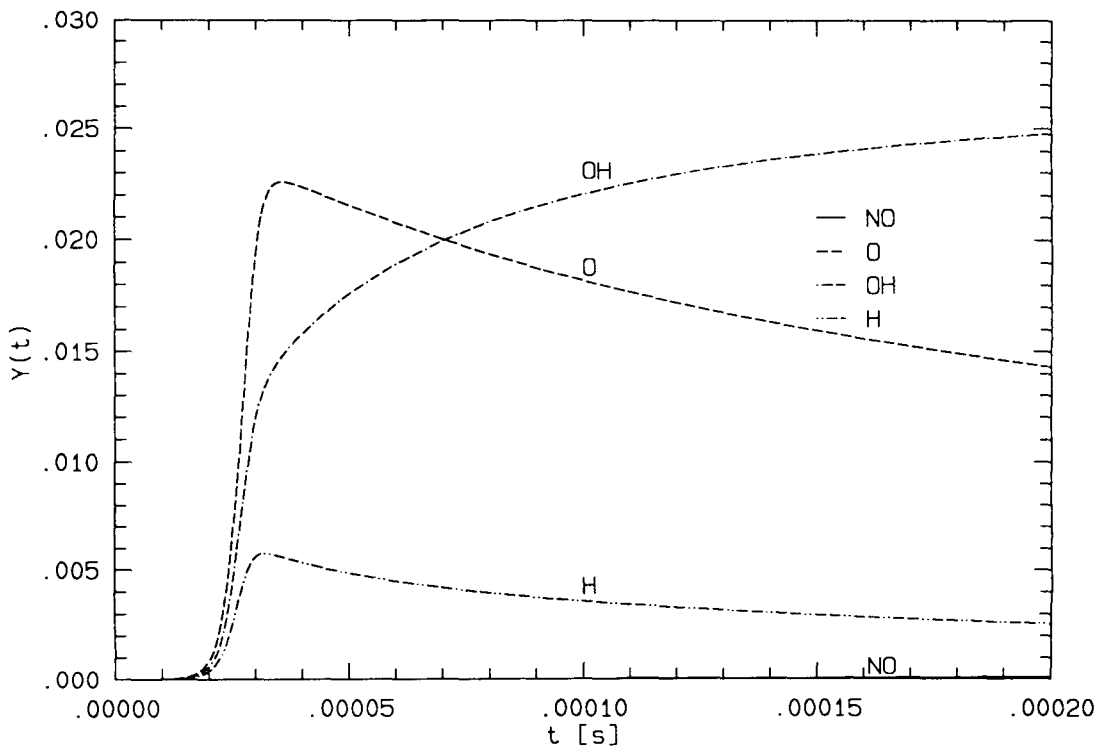


FIG. 4.2.2b Mass fraction of four radicals at initial start-up.

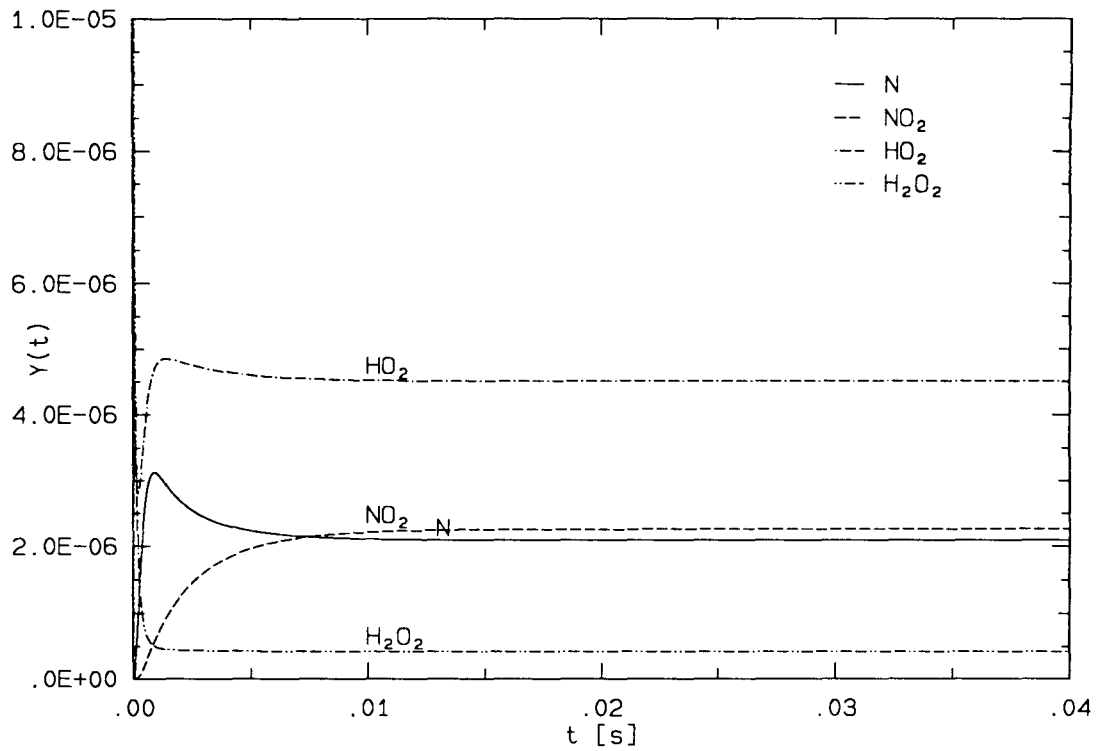


FIG. 4.2.3a Mass fraction of four trace radicals.

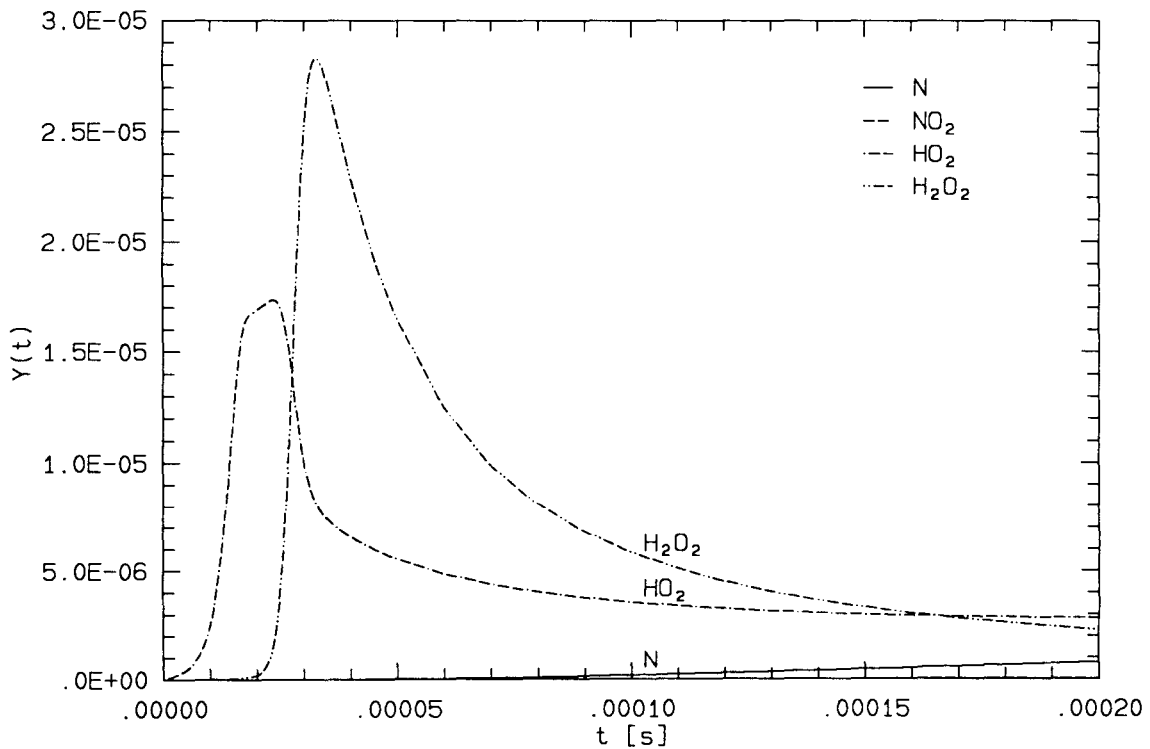


FIG. 4.2.3b Mass fraction of four trace radicals at initial start-up.

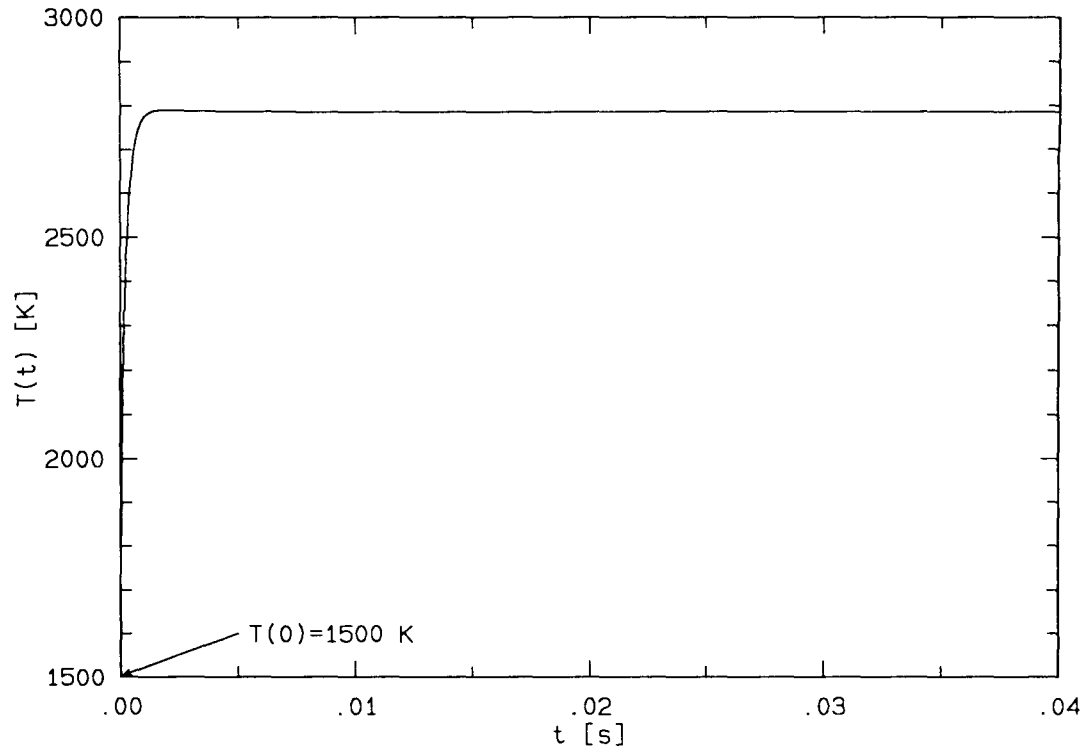


FIG. 4.2.4 Time history of temperature.

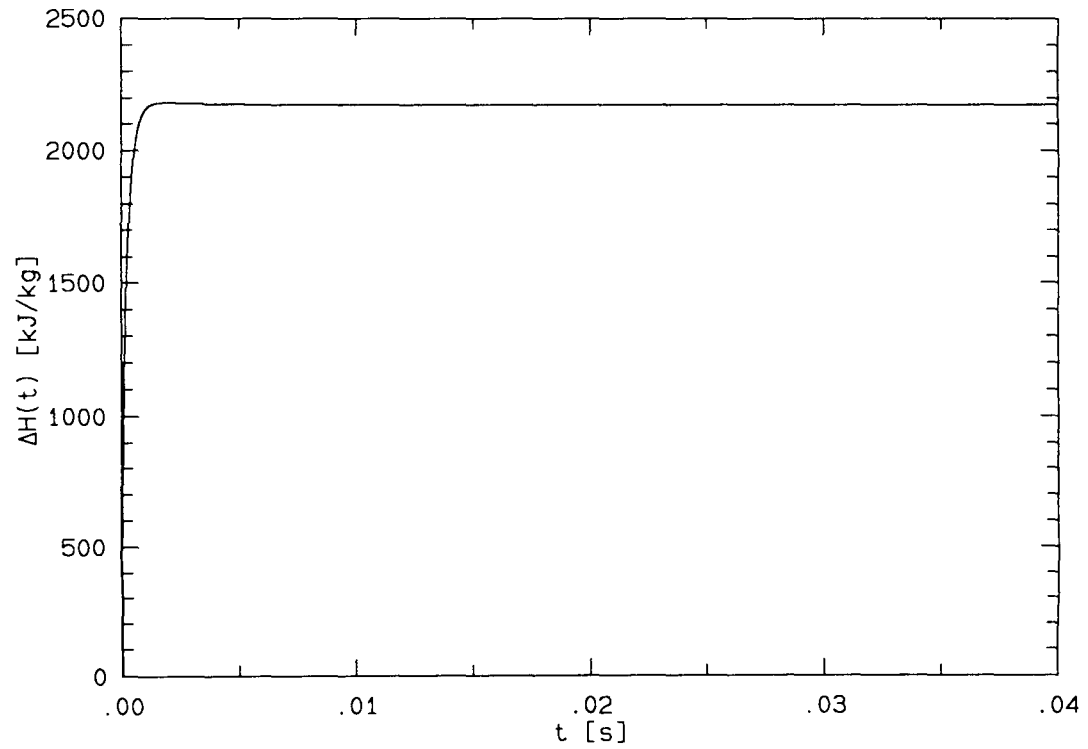


FIG. 4.2.5a Time history of heat release.

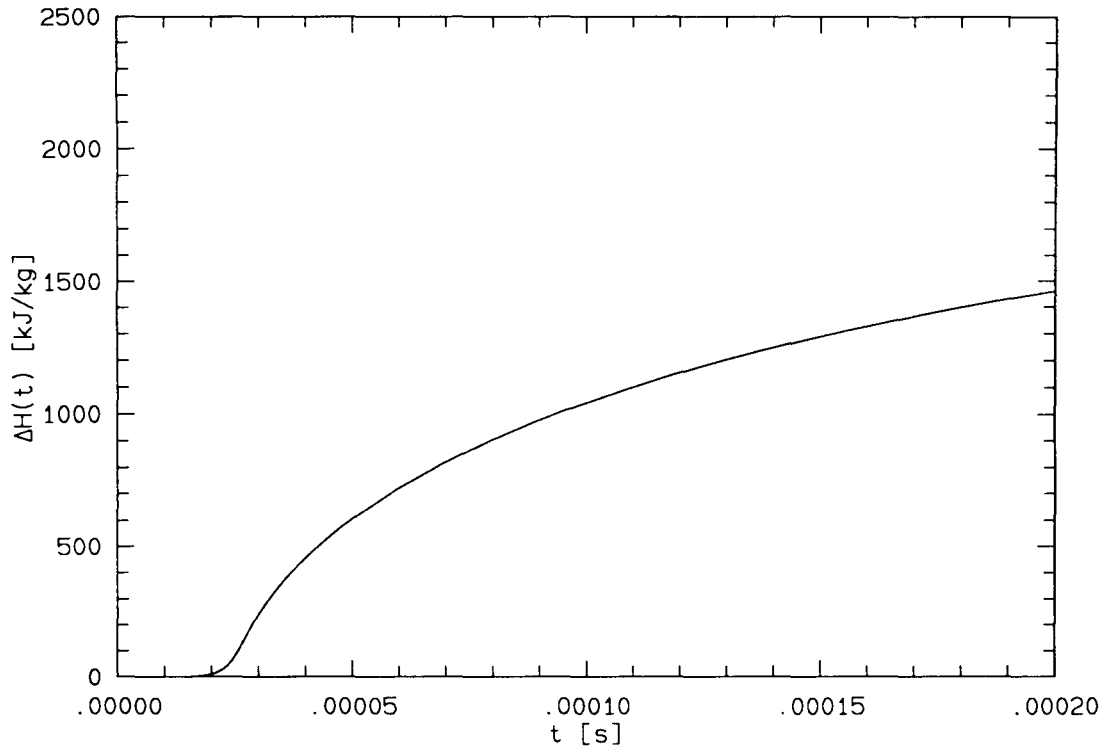


FIG. 4.2.5b Time history of heat release at initial start-up.

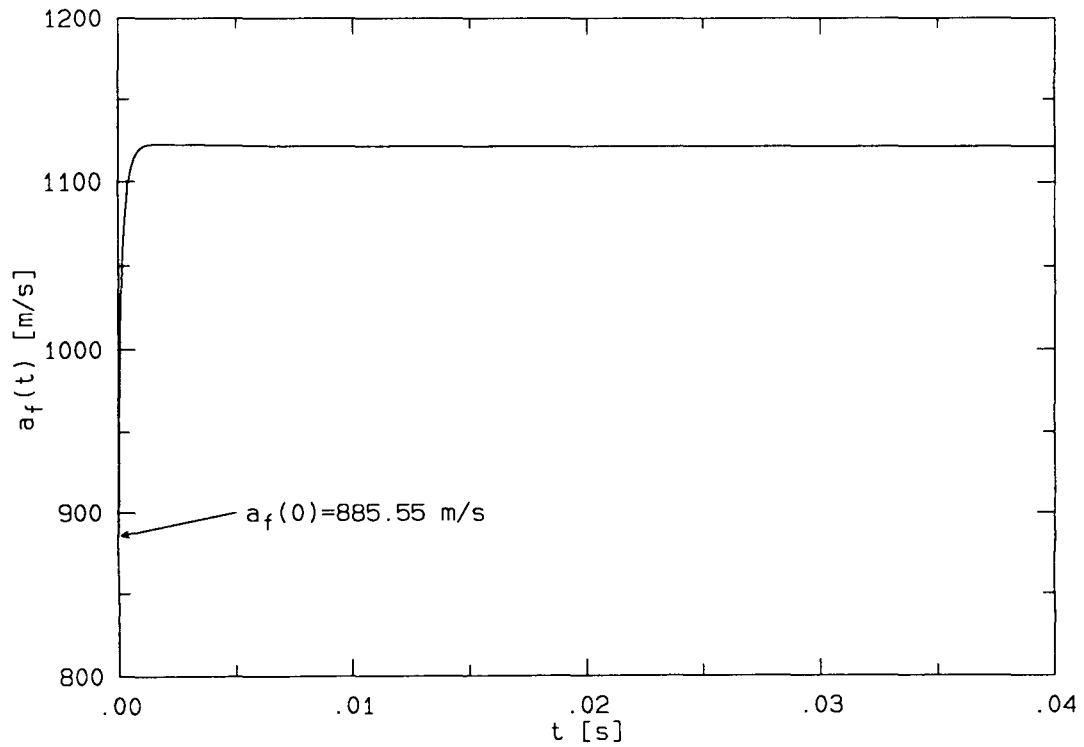


FIG. 4.2.6 Time history of frozen speed of sound.

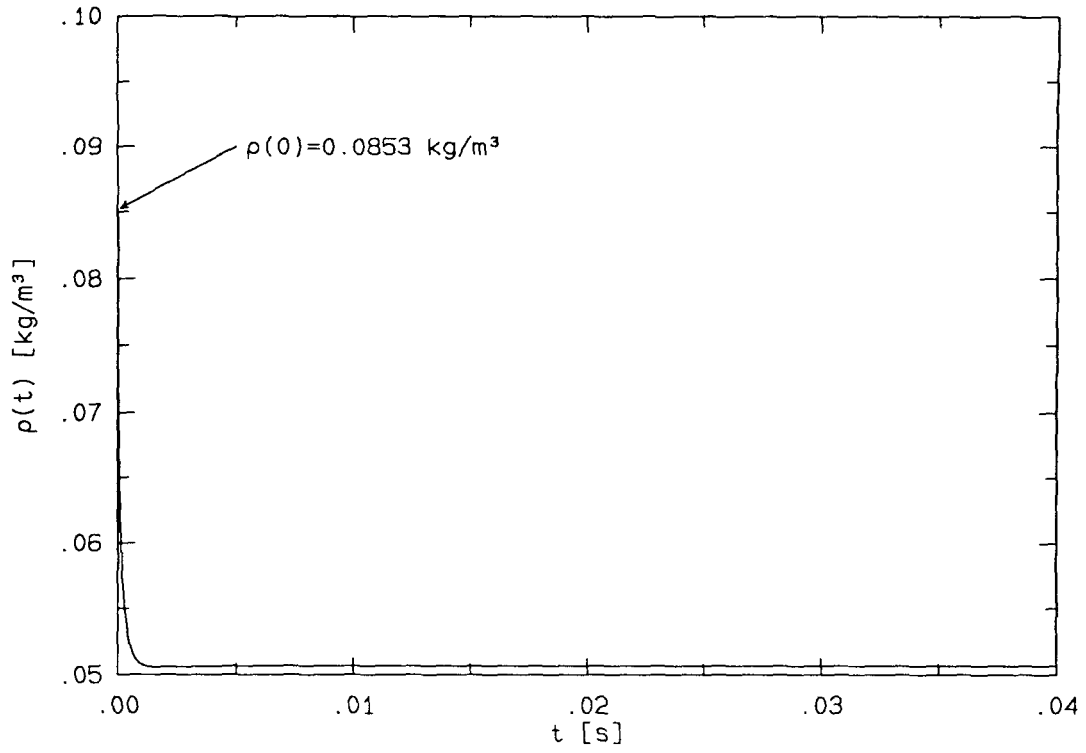


FIG. 4.2.7 Time history of density.

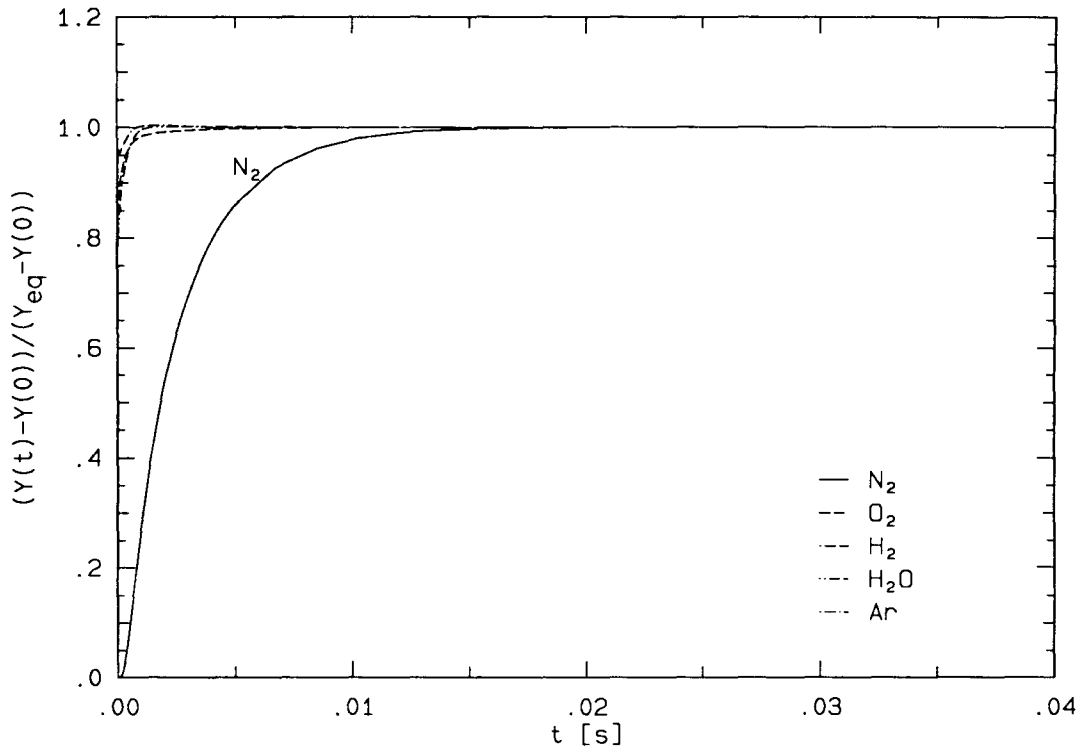


FIG. 4.2.8a Normalized mass fraction of five species.

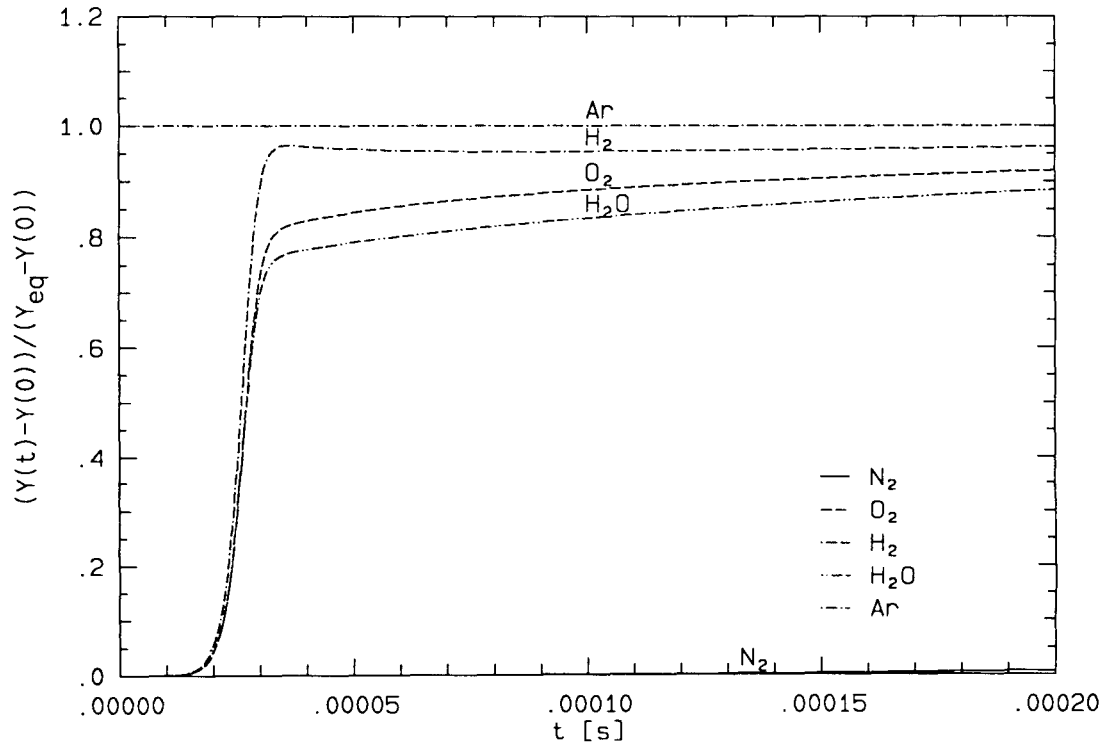


FIG. 4.2.8b Normalized mass fraction of five species at initial start-up.

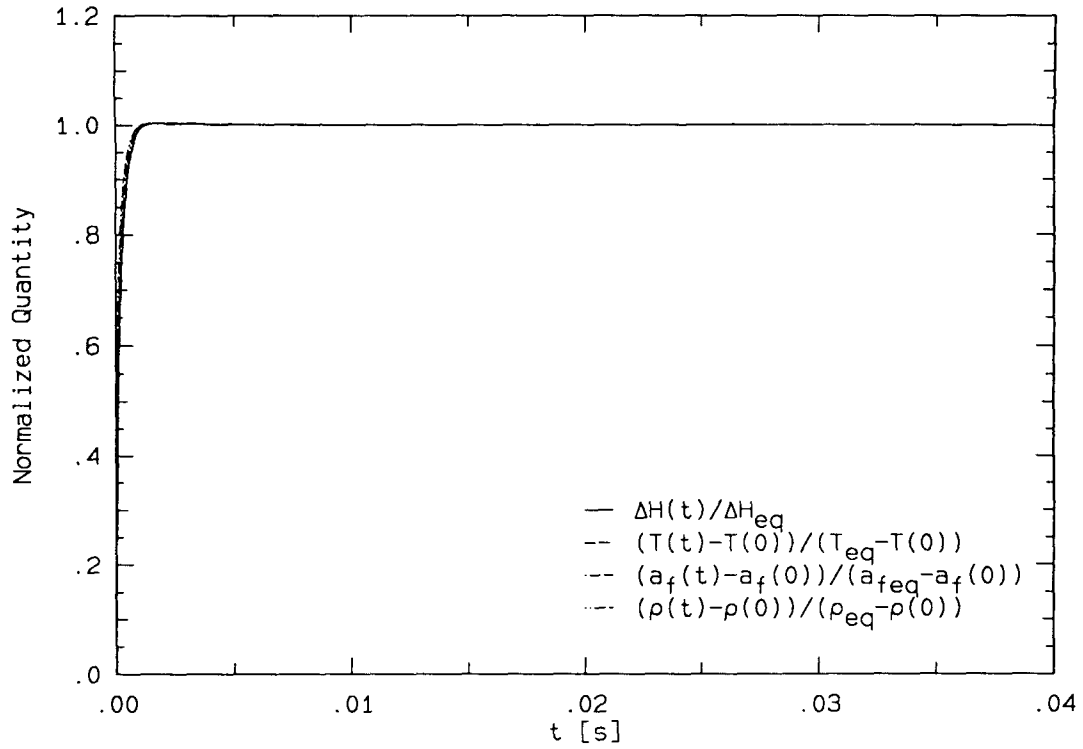


FIG. 4.2.9a Normalized heat release, temperature, sound speed and density.

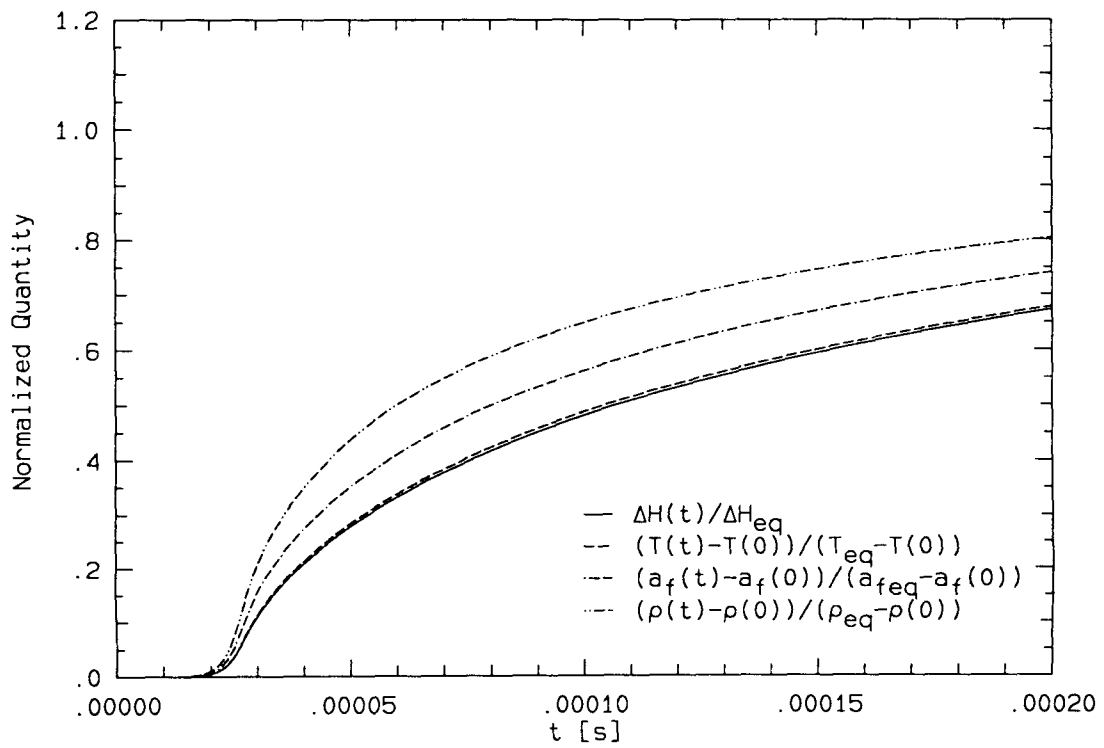


FIG. 4.2.9b \hat{T} , $\widehat{\Delta H}$, \hat{a}_f and $\hat{\rho}$ at initial start-up.

4.3 Variation of Equivalence Ratio

Hydrogen-air combustion is calculated at five equivalence ratios:

$$\phi = \begin{cases} 0.6 \\ 0.8 \\ 1.0 \\ 1.2 \\ 1.4 \end{cases}$$

The evolution of normalized chemical heat release is shown in figure 4.3.1a for a time of 0.04 second. The initial start-up region is expanded in figure 4.3.1b. Other gloss quantities such as temperature, density and the frozen speed of sound are found to behave similar to the heat release and hence are not shown. The quantities that carry their own characteristics are the species compositions. Significant difference in behavior is generally observed among the radicals, but the overall effects of equivalence ratio on composition can still be depicted by the heat release.

A feature characteristic of hydrogen-air combustion is observed in figure 4.3.1a: an overshoot following the fast-rise. In other words, the equilibrium value at unity is exceeded. The same behavior is also observed in the evolution of temperature. Explanation may be drawn from the fast initial formation and destruction of certain high energy radicals together with the slow formation of some other radicals towards equilibrium. Comprehensive arguments are postponed until section 4.5 since the same phenomenon is to be observed in the temperature and pressure calculations.

The changes introduced by the five different equivalence ratios over the time scale calculated are very small. All five cases exhibited a relatively short initial delay followed by an explosive rise and finally terminated through a decelerated approach to equilibrium. The fact that all five curves nearly approach the unity level at the upper time limit of figure 4.3.1a indicates the sufficiency of time considered. As small as the effect of equivalence ratio may appear, some distinct features are observed at a finer scale in figure 4.3.1b. The start-up behavior and fast-rise behavior are discussed next.

4.3.1 Start-up behavior

A clue as to why the stoichiometric fuel-air ratio ($\phi = 1.0$) is a good reference value is provided in table 4.3.1 where the first inflexion point, the slope at that point and the extrapolated start-up time are listed. A minimum start-up time is achieved at ϕ equals 1.0, meaning that the initial progress of combustion is optimized. An important conclusion for such an observation is that the initial progress is not directly related to the reactions of hydrogen (H_2) and oxygen (O_2). The argument can be drawn by examining the production equation the rate controlling reaction step which, by assumption, determines the progress during start-up. The chemical production rate in such a step is given by

$$\dot{\omega}_j = \nu_j'' k(T) R \quad j \in \text{products}, \quad (4.3.1)$$

where

$$R = \left[\prod_{k=1}^K \left(\frac{P}{R_u T} \right)^{\nu_k'} \right] \prod_{k=1}^K X_k^{\nu_k'}$$

The initial conditions for the five equivalence ratio cases are identical except for composition. Since the changes during the initial start-up are very small, the major difference in equation 4.3.1 between the five cases is introduced by the factor R or more precisely by the contribution of the composition of hydrogen and oxygen related species. At minimum start-up time, $\dot{\omega}_j$ must be maximum which implies that the contribution of hydrogen and oxygen related species is also maximum. It is not difficult to show that R is not a maximum at ϕ equals 1.0 if the related species are H_2 and O_2 .* Therefore, the chain initiating reactions in the first induction stage are more likely to involve radicals in hydrogen and oxygen. Nevertheless, both table 4.3.1 and figure 4.3.1b indicate that the start-up time is only slightly affected by equivalence ratio; in other words, the rates of the hydrogen related rate controlling reactions are weak functions of hydrogen concentration and hence can only involve low order kinetics in hydrogen.

Initial Stage	Equivalence Ratio ϕ				
	0.6	0.8	1.0	1.2	1.4
Inflexion at t [s]	3.25×10^{-5}	3.14×10^{-5}	3.11×10^{-5}	3.13×10^{-5}	3.17×10^{-5}
$\overline{\Delta H}$	5.23×10^{-2}	5.82×10^{-2}	6.49×10^{-2}	7.19×10^{-2}	7.86×10^{-2}
$\frac{d\overline{\Delta H}}{dt}$ [s^{-1}]	9.12×10^3	1.10×10^4	1.26×10^4	1.41×10^4	1.53×10^4
Start-up at t_s [s]	2.68×10^{-5}	2.61×10^{-5}	2.60×10^{-5}	2.62×10^{-5}	2.66×10^{-5}

TABLE 4.3.1 Inflexion point and extrapolated start-up time for five equivalence ratios.

* The ratio of C_{H_2} to C_{O_2} is 2 at ϕ equals 1.0.

4.3.2 Fast-rise behavior

The most noticeable effect of equivalence ratio is observed during the explosive rise. Figure 4.3.1b as well as figure 4.3.1a show that the heat release for higher equivalence ratios has steeper rise following the initial delay. A monotonic increase in slope with equivalence ratio at the inflexion point is indicated in table 4.3.1. This implies that the relative abundance of hydrogen is important for the explosive stage during combustion. More precisely, the fast chain branching reactions responsible for the rate of fast-rise must be hydrogen related. On the other hand, the slow ones are less likely to be hydrogen related. The time required to reach the inflexion point does not increase monotonically with equivalence ratio but instead has a minimum at ϕ equals 1.0 as in the start-up stage. The above findings are supported by two calculations at the more extreme ratios of 0.4 and 2.5. Comparing to the stoichiometric case, their results show that the rise is largely inhibited at the lower value while a limited steepening in the rise is observed at the higher value. Therefore, the chain branching is less violent at low hydrogen abundance while close to the stoichiometric amount is immediately consumed at higher abundance. Only slight increases in the start-up time and the time at inflexion are found in the two cases.

4.3.3 Conditions at chemical equilibrium

For the five equivalence ratios considered, 95% of the equilibrium heat release is reached within 2 milliseconds with lesser time required at the higher ratios. Since the combustor residence time is also estimated to be of milliseconds, examination of the equilibrium conditions in the five cases may provide useful measure of their individual combustion performance. The numerical results are listed in table 4.3.2.

According to the equilibrium conditions, more energy is released per unit mass as equivalence ratio increases. However, the trend suggests that a turning point may exist at a certain higher ϕ ; that is, a decrease in energy release would occur for equivalence ratio beyond that value. A similar increase in equilibrium temperature with equivalence ratio is observed up to ϕ equals 1.2 where a decrease begins. The equilibrium temperature calculated is equivalent to the adiabatic flame temperature for pre-mixed hydrogen and air. While many previous investigations have shown that the maximum flame temperature should occur at the stoichiometric fuel-air ratio ($\phi = 1$), the maximum is found to occur near ϕ equals 1.2 in this calculation. The discrepancy may be a result of the temperature dependent thermodynamic properties used since most of the other calculations assumed

constant average properties. As an example, the mass averaged specific heat at constant pressure (\bar{C}_p , *c.f.* equation 2.4.6) in this calculation ranges from 1.5 to 1.8 $J/(gK)$ over the five equivalence ratios at equilibrium.

Equilibrium Condition	Equivalence Ratio ϕ				
	0.6	0.8	1.0	1.2	1.4
Heat Release ΔH [J/g]	1666.31	1961.94	2172.68	2322.28	2428.89
Temperature T [K]	2605.74	2727.26	2786.62	2807.09	2803.85
Density ρ [kg/m^3]	0.06001	0.05454	0.05069	0.04779	0.04551
Sound Speed a [m/s]	1032.57	1081.43	1121.03	1154.37	1183.23
Composition Y_N	4.71×10^{-7}	1.30×10^{-6}	2.09×10^{-6}	2.49×10^{-6}	2.49×10^{-6}
Y_{N_2}	7.34×10^{-1}	7.31×10^{-1}	7.28×10^{-1}	7.26×10^{-1}	7.23×10^{-1}
Y_{NO}	1.69×10^{-2}	1.53×10^{-2}	1.21×10^{-2}	8.89×10^{-3}	6.33×10^{-3}
Y_{NO_2}	7.24×10^{-6}	4.25×10^{-6}	2.26×10^{-6}	1.14×10^{-6}	5.71×10^{-7}
Y_O	5.22×10^{-3}	6.81×10^{-3}	6.47×10^{-3}	5.17×10^{-3}	3.75×10^{-3}
Y_{O_2}	7.78×10^{-2}	4.39×10^{-2}	2.32×10^{-2}	1.20×10^{-2}	6.15×10^{-3}
Y_{OH}	1.58×10^{-2}	2.15×10^{-2}	2.30×10^{-2}	2.17×10^{-2}	1.89×10^{-2}
Y_H	2.25×10^{-4}	6.19×10^{-4}	1.12×10^{-3}	1.60×10^{-3}	1.98×10^{-3}
Y_{H_2}	8.44×10^{-4}	2.37×10^{-3}	4.80×10^{-3}	8.07×10^{-3}	1.20×10^{-2}
Y_{HO_2}	6.35×10^{-6}	6.03×10^{-6}	4.50×10^{-6}	2.94×10^{-6}	1.80×10^{-6}
Y_{H_2O}	1.36×10^{-1}	1.66×10^{-1}	1.88×10^{-1}	2.04×10^{-1}	2.15×10^{-1}
$Y_{H_2O_2}$	4.19×10^{-7}	4.75×10^{-7}	4.27×10^{-7}	3.36×10^{-7}	2.46×10^{-7}
Y_{Ar}	1.30×10^{-2}	1.29×10^{-2}	1.29×10^{-2}	1.28×10^{-2}	1.27×10^{-2}

TABLE 4.3.2 Equilibrium conditions for five equivalence ratios.

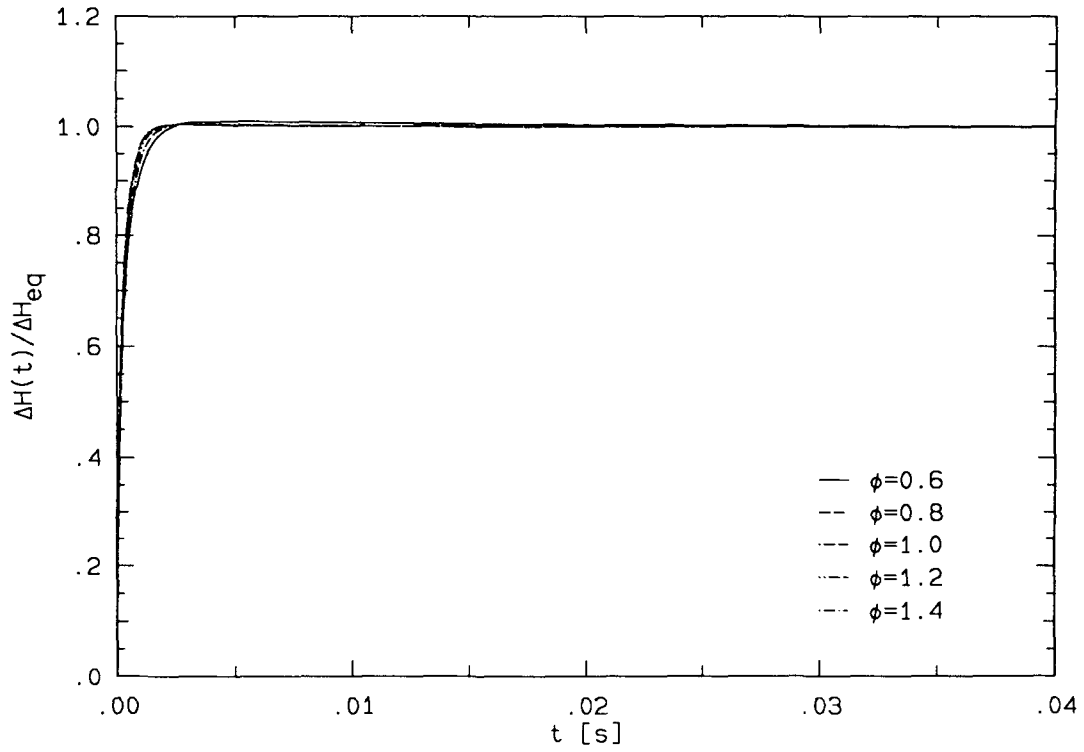


FIG. 4.3.1a Heat release for five equivalence ratios.

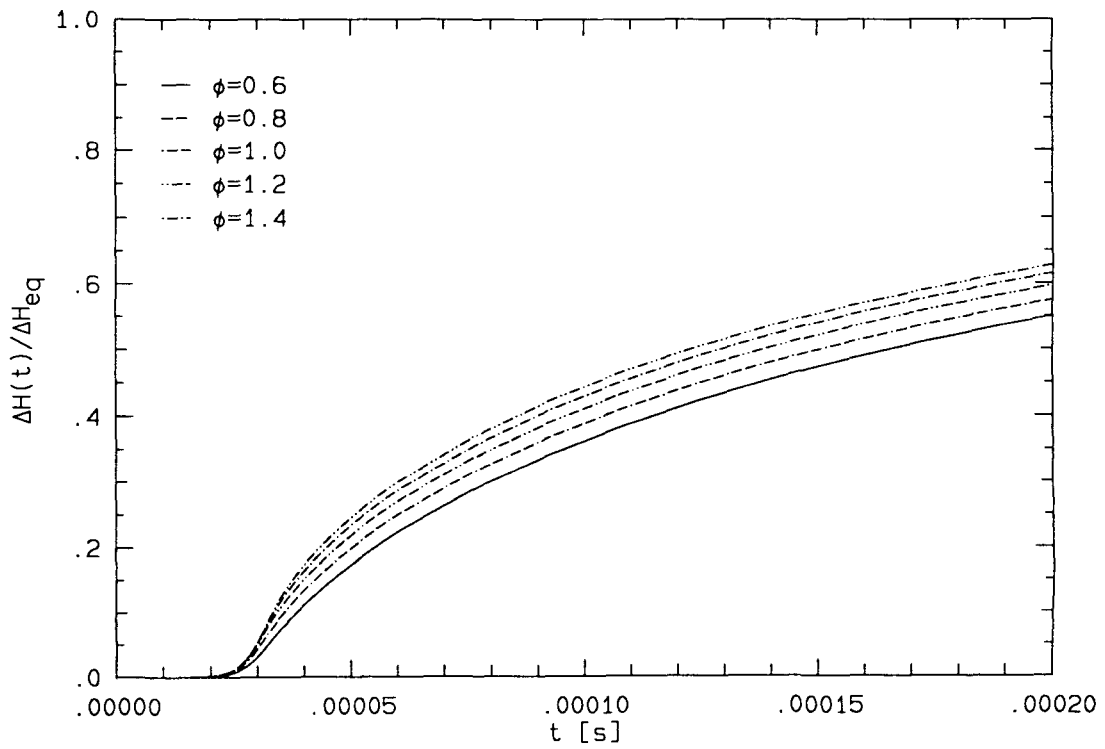


FIG. 4.3.1b Heat release at initial start-up.

4.4 Variation of Initial Temperature

The values of initial temperature first studied were 500, 1000, 1500, 2000 and 2500 *K*. The results for all except the first are shown because no noticeable change in the chemical system is observed over a period of 10 seconds which is two orders larger than the time scale at interest. For this reason, three other low end values* are explored to determine the low temperature combustion characteristics. The following results therefore include seven initial temperatures:

$$T_0 = \begin{cases} 850 K \\ 900 K \\ 950 K \end{cases} \quad \text{for the lower initial temperature range}$$

and

$$T_0 = \begin{cases} 1000 K \\ 1500 K \\ 2000 K \\ 2500 K \end{cases} \quad \text{for the higher initial temperature range}$$

A dramatic effect of initial temperature is demonstrated by the first case in figure 4.4.1a. The overall effect is shown in figure 4.4.1b. for the last six cases. Note that the time scales of the two plots are very different since the first case requires approximately 0.7 second to start while the others requires less than 0.005 second.

4.4.1 Start-up behavior

The first prominent effect shown in figure 4.4.1a and 4.4.1b is a monotonic increase in start-up time as initial temperature decreases. More importantly, the increase is very acute as the initial temperature drops below 900 *K*. The extrapolated start-up times for T_0 equals 900, 950, 1000 *K* and T_0 equals 1500, 2000, 2500 *K* are shown at fine scales in figure 4.4.2a and 4.4.2b respectively. The case of T_0 equals 850 *K* is shown separately in figure 4.4.1a at a cruder scale since the time involved is much bigger. In the figures, indicated by the '+' symbols are the inflexion points at which the start-up times are extrapolated. The lines of tangency and the extrapolated points are indicated by arrows. Values of their slopes and locations are provided in table 4.4.1a and 4.4.1b.

* These values were selected through trial and error. Any temperature below the lowest one would require excessive computational time and is rendered impractical.

Initial Stage	Initial Temperature T_0 [K]		
	850	900	950
Inflexion at t [s]	6.91×10^{-1}	2.14×10^{-3}	6.15×10^{-4}
$\Delta \bar{H}$	3.69×10^{-1}	2.64×10^{-1}	2.35×10^{-1}
$\frac{d\Delta \bar{H}}{dt}$ [s^{-1}]	2.38×10^3	9.17×10^3	1.02×10^4
Start-up at t_s [s]	6.91×10^{-1}	2.11×10^{-3}	5.91×10^{-4}

TABLE 4.4.1a Inflexion point and start-up time for lower initial temperatures.

Initial Stage	Initial Temperature T_0 [K]			
	1000	1500	2000	2500
Inflexion at t [s]	4.22×10^{-4}	3.11×10^{-5}	9.70×10^{-6}	4.68×10^{-6}
$\Delta \bar{H}$	2.15×10^{-1}	6.49×10^{-2}	3.37×10^{-2}	3.50×10^{-2}
$\frac{d\Delta \bar{H}}{dt}$ [s^{-1}]	1.13×10^4	1.26×10^4	1.60×10^4	2.76×10^4
Start-up at t_s [s]	4.03×10^{-4}	2.60×10^{-5}	7.59×10^{-6}	3.41×10^{-6}

TABLE 4.4.1b Inflexion point and start-up time for higher initial temperatures.

The correlation of start-up time with initial temperature is extracted based on the rate equation. It is argued that there exist certain *critical* conditions which are identical for all initial conditions. For example, it is probable that a reacting system must reach certain temperature or the compositions of some species must reach certain levels before the overall chemical progress rate can suddenly take-off. In either case, the start-up time indicates when these critical conditions are achieved. Integration of the rate equations over the duration of the start-up time should then produce the critical levels which are common to all initial temperatures.

The results of the correlation study should reflect the behavior of the rate controlling reactions since the time required for start-up is determined by the slowest reactions. The start-up stage is signified by a slow accumulation of radicals which initiate the explosive stage of chain branching. Upon termination, a sudden rise begins as represented by the heat release. The slow and small overall changes during the initial start-up suggest that the initial behavior may be approximated by integrating the rate equations in time with the temperature held at its initial value and the other slow varying parameters held at certain effective values. In terms of the governing equations 3.3.3 and 3.3.4, the start-up behavior is approximated for each initial temperature by:

$$\frac{dY_k}{dt} \approx \left(\frac{m_k}{\rho} \dot{\omega}_k \right)_{T_0, \bar{Y}} \quad \text{for } k = 1, K, \quad (4.4.1a)$$

and

$$\frac{dT}{dt} \approx \left(-\frac{1}{\bar{C}_p} \sum_{k=1}^K h_k \frac{dY_k}{dt} \right)_{T_0, \tilde{Y}} \quad (4.4.1b)$$

where a ‘ \sim ’ is used to represent the effective value. Although ρ , \bar{C}_p , h_k and $\dot{\omega}_k$ in the equations are all functions of temperature, the first three are much weaker functions compared to the fourth which is an exponential function of temperature according to the Arrhenius representation of rate coefficients. If there exist certain chain initiating reactions with slow but comparable rates such that chain branching is introduced as their products reach certain critical compositions, the dependence of start-up time on temperature should be reflected through $\dot{\omega}_k$ in equation 4.4.1a. As the production rate is concerned, the appropriate composition variables would include molar concentration and mole fraction. Let the combined effect of the dominating reactions be that of a single one, the above statements translated to:

$$(C_j)_{\text{critical}} \approx C_j(0) + \tilde{\nu}_j'' \tilde{A} T_0^{\tilde{\beta}} e^{\left(-\frac{\tilde{E}_a}{R_u T_0} \right)} \tilde{R} t_s \quad j \in \text{reactant} \quad (4.4.2a)$$

and

$$(X_j)_{\text{critical}} \approx X_j(0) + \frac{R_u T_0}{P} \tilde{\nu}_j'' \tilde{A} T_0^{\tilde{\beta}} e^{\left(-\frac{\tilde{E}_a}{R_u T_0} \right)} \tilde{R} t_s \quad j \in \text{reactant} \quad (4.4.2b)$$

for the two candidates. The temperature related components in $\dot{\omega}_j$ is written explicitly in both equations for correlation study. For the other terms, C_j and X_j represent the molar concentrations and the mole fractions respectively; $\tilde{\nu}_j''$ are the effective stoichiometric coefficient; T_0 is the initial temperature and \tilde{R} is the product of the effective reactant concentrations raised to the power of their stoichiometric coefficients. The destruction aspect in the reverse step has been ignored since it is assumed that only one of the steps can be dominant. In addition, the same overall reaction must remain to be the rate controlling one over a range of temperature in order for the previous equations to hold. The present analysis relies on the fact that the seven cases studied are within or partially included in such temperature range. The equation for a critical temperature has not been formulated. Its existence in the start-up stage is not likely since the temperatures are found to be very different at the start-up time for the seven cases. In short, the relevant functional relationships of the *critical* conditions with initial temperature and start-up time are

$$(C_j)_{\text{critical}} \approx C_j(0) + a_{1j} T_0^b e^{\left(-\frac{c}{T_0} \right)} t_s \quad (4.4.3a)$$

and

$$(X_j)_{\text{critical}} \approx X_j(0) + a_{2j} T_0^{b+1} \exp \left(-\frac{c}{T_0} \right) t_s \quad (4.4.3b)$$

such that a_{1j} , a_{2j} , b and c are constants. Either $(C_j)_{\text{critical}}$ or $(X_j)_{\text{critical}}$ is also constant by assumption. Examination of the species concentration and mole fraction at the start-up time shows that this is indeed possible. Despite the significantly different time scale in the seven cases, comparable concentrations and fractions are found at the start-up time for several species. Quantitative results are plotted in figures 4.4.3a and 4.4.3b for six initial temperatures. The plots are presented such that a line at unity would imply constant concentration or fraction at all six temperatures. The case of the lowest initial temperature is not included because its behavior is radically different. Analysis and special treatment of this behavior is considered in section 4.4.2 for the low temperature cases.

By comparing the concentrations and mole fractions at the start-up times, five species which may possibly satisfy equation 4.4.3a or 4.4.3b are selected out of a possible thirteen (*c.f.* table 3.6.3b). They are O, OH, H, HO₂ and H₂O. Four of them are considered the best candidates while HO₂ may or may not satisfy either equation. In other words, as the concentration and mole fraction for the other four species vary significantly less than one order of magnitude over the six initial temperatures, those of the fifth vary nearly one order of magnitude. The remaining species have variations of at least two orders of magnitudes. These variations are compared based on the dimensionless quantities \bar{C}_j and \bar{X}_j and the results are plotted in figures 4.4.3a and 4.4.3b respectively. Normalization is based on the conditions at $T_0 = 1500\text{ K}$:

$$\bar{C}_j \equiv \frac{C_j(t_s) - C_j(0)}{C_j(T_0 = 1500\text{ K}; t_s) - C_j(T_0 = 1500\text{ K}; 0)} \quad (4.4.4a)$$

and

$$\bar{X}_j \equiv \frac{X_j(t_s) - X_j(0)}{X_j(T_0 = 1500\text{ K}; t_s) - X_j(T_0 = 1500\text{ K}; 0)} \quad (4.4.4b)$$

The initial values may be omitted from the definitions since they are zero for the five selected species. The reference conditions are given in tables 4.4.1c and 4.4.1d. The conditions at the inflexion point are also shown in the tables.

	$C_{\text{O}} [M]$	$C_{\text{OH}} [M]$	$C_{\text{H}} [M]$	$C_{\text{HO}_2} [M]$	$C_{\text{H}_2\text{O}} [M]$
Start-up	1.3334×10^{-8}	8.5325×10^{-9}	8.8090×10^{-8}	3.6995×10^{-11}	1.0448×10^{-7}
Inflexion	5.6405×10^{-8}	3.3787×10^{-8}	3.0816×10^{-7}	2.8878×10^{-11}	3.8257×10^{-7}

TABLE 4.4.1c Concentrations at start-up time and inflexion point for $T_0 = 1500\text{ K}$.

	X_{O}	X_{OH}	X_{H}	X_{HO_2}	$X_{\text{H}_2\text{O}}$
Start-up	3.3241×10^{-3}	2.1271×10^{-3}	2.1961×10^{-2}	9.2227×10^{-6}	2.6046×10^{-2}
Inflexion	1.4640×10^{-2}	8.7695×10^{-3}	7.9984×10^{-2}	7.4953×10^{-6}	9.9296×10^{-2}

TABLE 4.4.1d Mole fractions at start-up time and inflexion point for $T_0 = 1500 \text{ K}$.

Comparison between figures 4.4.3a and 4.4.3b shows that the data for mole fraction are generally closer to unity and hence is a better candidate for correlation study. Although neither figures indicate that any of the concentrations or mole fractions are constant, calculation of the production rates of the selected species at the start-up time shows that an error of up to ± 0.5 in \bar{C} or \bar{X} may be introduced by the uncertainty in the extrapolation. Critical concentrations or mole fractions are also expected to exist at the inflexion point. For this reason, concentrations and mole fractions at the inflexion point are computed and plotted in figures 4.4.4a and 4.4.4b. Better agreement is obtained since the error in extrapolation is eliminated. The result for mole fraction is again superior to that of concentration. The choice of mole fraction will become more evident (*c.f.* section 4.5.1) as the variation of pressure is studied.

The proposed correlation in equation 4.4.3b is selected for further study. By assumption, $(X_j)_{\text{critical}}$ is a constant at all initial temperature for each j in the dominant reaction. The initial compositions are all identical for all the temperatures. Therefore, the quotient

$$\frac{(X_j)_{\text{critical}} - X_j(0)}{a_{2j}} \propto \frac{(X_j)_{\text{critical}} - X_j(0)}{\tilde{\nu}_j''}$$

is a constant if the five selected species belong to the same stoichiometric reaction and equation 4.4.3b becomes independent of j . A single parametric correlation is obtained after some rearrangement:

$$\log_e(t_s) \approx \log_e(p_0) + p_1 \log_e\left(\frac{1}{T_0}\right) + p_2 \frac{1}{T_0}, \quad (4.4.5)$$

where p_0 , p_1 and p_2 are constant parameters given by

$$p_0 \equiv \frac{(X_j)_{\text{critical}} - X_j(0)}{a_{2j}} = \frac{P}{R_u} \frac{(X_j)_{\text{critical}}}{\tilde{\nu}_j'' \tilde{A} \tilde{R}}$$

$$p_1 \equiv b = \tilde{\beta} + 1 \quad \text{and}$$

$$p_2 \equiv c = \frac{\tilde{E}_a}{R_u}.$$

The fact that $X_j(0)$ equal zero for all five radicals has been used in p_0 . Accordingly, p_1 is dimensionless whereas p_0 and p_2 have the units of $[K^{p_1}s]$ and $[K]$ respectively. Equation 4.4.5 is written loosely regardless of dimension for the purpose of parametric fit: to find the values of p_0 , p_1 and p_2 which best fit the $(T_0; t_s)$ data. It is important to notice that the parameters are derived for a single overall reaction pertaining to the essential species in a particular stage. The parameters should either reflect the behavior of the slowest *reaction step* or the combined behavior of several steps if their rates are comparable. Of most importance is the parameter p_2 since it is proportional to the activation energy and has exponential effect on reaction rate (see equation 4.4.2b). Hence, its value should result in an activation energy relevant to the slowest step or steps.** The other two parameters have lesser meaning since p_0 is a combination of several average quantities and p_1 , relating to the temperature exponent in the rate coefficient, is easily contaminated by the effect of faster reactions.

Correlation fits are performed via a FUNC[†] utility. The result shows an excellent fit for the data from T_0 equals 950 to 2500 K . Values of the fitted parameters are

$$\left\{ \begin{array}{l} p_0 = 1.91011 \times 10^{-9} \\ p_1 = -0.51521 \\ p_2 = 8672.97 \end{array} \right. \Rightarrow \left\{ \begin{array}{l} \tilde{\beta} = -1.51521 \\ \tilde{E}_a = 17224.5 \text{ cal/mol} \end{array} \right.$$

over five data sets with a standard deviation of 0.0269. Recall by comparing figures 4.4.3b and 4.4.4b that a better agreement in the mole fractions is achieved at the inflexion point; therefore, a better fit should be obtained here if the time at inflexion is used in the correlation instead of t_s . As expected, a deviation of 0.0210 is achieved with very similar parameter values:

$$\left\{ \begin{array}{l} p_0 = 4.42005 \times 10^{-10} \\ p_1 = -0.74651 \\ p_2 = 8590.04 \end{array} \right. \Rightarrow \left\{ \begin{array}{l} \tilde{\beta} = -1.74651 \\ \tilde{E}_a = 17059.8 \text{ cal/mol} \end{array} \right.$$

A plot of the fitted curves along with the data points is provided in figure 4.4.7 where the agreement is exemplified. A t^* is introduced in the plot for dimensional purpose. It has the value of one second.

** Reactions having comparable rates over a range of temperature must also have similar activation energies.

† Developed by Prof. P. Dimotakis of the California Institute of Technology, Pasadena, California.

Before analysing the implication of the results, their reliability and their sensitivity to the fit must be examined. If the fit is nearly perfect, small uncertainty in the parameters can be approximated by

$$\Delta p_i \approx \left| \frac{\partial p_i}{\partial t_s} \right|_{p_j, j \neq i} \Delta t_s + \left| \frac{\partial p_i}{\partial T_0} \right|_{p_j, j \neq i} \Delta T_0 \quad i = 0, 2 .$$

Since T_0 is an input quantity of known value, the second term on the right hand side of the equation can usually be discarded. The expressions for Δp_i are obtained by applying the partial derivatives to equation 4.4.5. For example, the uncertainty in the first parameter is

$$\frac{\Delta p_0}{p_0} \approx \frac{\Delta t_s}{t_s} + \left(p_1 + \frac{p_2}{T_0} \right) \frac{\Delta T_0}{T_0} .$$

Similar expressions can be written for the other two parameters. But regardless of their exact forms, the three uncertainties are related through

$$\frac{\Delta p_0}{|p_0|} = \frac{\Delta p_1}{|p_1|} (|p_1| \log_e(T_0)) = \frac{\Delta p_2}{|p_2|} \left(\frac{|p_2|}{T_0} \right)$$

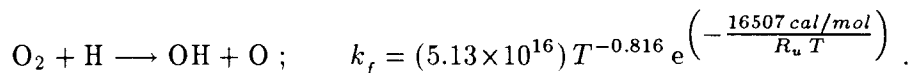
or

$$\left\{ \begin{array}{l} \frac{\Delta p_1}{|p_1|} = \left(\frac{1}{|p_1| \log_e(T_0)} \right) \frac{\Delta p_0}{|p_0|} \\ \frac{\Delta p_2}{|p_2|} = \left(\frac{T_0}{|p_2|} \right) \frac{\Delta p_0}{|p_0|} \end{array} \right. .$$

Dimensions are again ignored in the relations. The magnitude of p_0 is very small, usually less than $\mathcal{O}(10^{-5})$; p_1 is of $\mathcal{O}(1)$ and p_2 is of $\mathcal{O}(1)$ to $\mathcal{O}(10^4)$. The initial temperature is of $\mathcal{O}(10^3)$ for the cases considered. Therefore, according to the last expressions, the reliability of p_1 parameter is about the same as p_0 while that of p_2 can be much worse or better.

In the two sets of results obtained for the fits on start-up time and inflexion time, T_0 is about a tenth of p_2 ; hence, the uncertainty in p_2 is approximately 10% that of p_0 and p_1 . But the minimum deviation in either fit is not negligibly small and rather large uncertainties are expected in all three parameters. As an example, a deviation of 3% in the start-up time fit would allow variations in $\log_e(p_0)$, p_1 and p_2 of approximately ± 1 , ± 0.2 and ± 60 respectively which are not negligible percentages of the fitted values.

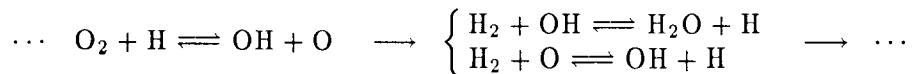
Having mentioned the reliability of the parameters, their implication can be examined. Despite that the two p_0 obtained for the start-up time and the inflexion point are quite different, the other parameters are similar. This implies that the rate controlling reactions in the initial stage continue to dominate in the chain branching stage. The values of $\tilde{\beta}$ and \tilde{E}_a together with the four species identified in figure 4.4.3b and 4.4.4b suggest that reaction 3 in table 3.6.3a is a probable candidate of rate controlling reaction:



Two other steps with similar activation energies are reactions 2b and 11b in table 3.4a.[‡] These possibilities are ruled out because their reactants only include species whose concentrations are zero initially and their temperature exponents have a positive sign.

4.4.2 Low temperature behavior

The previous parameters are deduced for T_0 equals 950 to 2500 K . A change in behavior at low temperature can be observed in figures 4.4.3a through 4.4.4b for the radical concentrations and is further exemplified in figure 4.4.7 by the departure of the data at $T_0 = 850$ and 900 K from the fitted curves. The most probable explanation of the discrepancy is that the rate controlling reactions that dominate at higher temperatures cease to remain dominant at these temperatures; thus, violating one of the essential assumptions required for the correlation. A hint is provided by the involvement of two additional reactions. Mikolatis^[10] has pointed out that reaction 3 is responsible for the generation of O, OH and H radicals which initiate the branched chain cycle in connection with reactions 2 and 4:



Although the activation energies of reaction 2 and 4 are approximately 1/4 and 1/2 that of reaction 3, their pre-exponent constants are at least six orders smaller. Therefore, the effect of reaction 3 is dominant at moderately high temperature as reflected by the fitted results in the range T_0 equals 950 to 2500 K . The rates of the three reactions become similar at a temperature of ~ 900 K , resulting in an exponential departure of behavior near that temperature.

To account for the low temperature behavior solely from the above explanation is not sufficient. The data in figure 4.4.7 indicate that the start-up time approaches infinity at low initial temperature faster than can be anticipated by the three reactions alone. Possibility of accumulated numerical error at the relatively larger time scale in the two cases has been checked and eliminated. Therefore, even slower reactions must become dominant, namely those that have very low activation energy and small temperature exponent such that they remain active at low temperature. In an attempt to find out what are the responsible reactions, the radical concentrations are examined at the start-up time for the 850 K case. Two radicals are found to have appreciable fractions when compared to

[‡] They correspond to the reverse steps of reactions 2 and 11 in table 3.6.3a respectively.

the higher temperature cases. Among the two is HO_2 which has been cited earlier for its possible role in the start-up regime. The other one is H_2O_2 which has shown little significance. In the scale of figure 4.4.3b, their dimensionless mole fractions based on the definition of equation 4.4.4b are

$$\begin{cases} \bar{X}_{\text{HO}_2}(T_0 = 850 \text{ K}) \simeq 5 & \text{and} \\ \bar{X}_{\text{H}_2\text{O}_2}(T_0 = 850 \text{ K}) \simeq 623 \end{cases}$$

while all other radicals have $\bar{X}(T_0 = 850 \text{ K})$ less than $\mathcal{O}(10^{-2})$.[‡] Despite this finding, a fit of equation 4.4.5 on the three lowest temperature data fails to yield any parameters* relevant to the reactions of HO_2 or H_2O_2 . Therefore, those two species are not the determining factors for the start-up time. The excessive build up of HO_2 and H_2O_2 merely means that the reactions responsible for their destruction are not very active at low temperature while the counter part of these reactions remain relatively active. Instead, a graduate transfer of dominance must be occurring near 900 K . It is for this reason that the correlation equation cannot be applied to determine the rate controlling reaction. The change in start-up time following the transition is again expected to satisfy the fit in equation 4.4.5 and the best fit should resemble the more or less linear portion in figure 4.4.7. Unfortunately, to determine the extent of the transition and to obtain enough low temperature data for parametric fit through numerical calculations would become excessively time consuming. Linearly extrapolated behavior would estimate a start-up time of 467 and 3×10^{31} seconds if the transition extends to T_0 equals 800 and 500 K respectively. Calculation of the first case shows that start-up is not yet encountered at 500 seconds, implying that the transition extends below 800 K ; the second case is not attempted.

Theoretically, the start-up time is finite unless the temperature goes to zero. Nevertheless, an exponentially fast increase in start-up time is observed even at 850 K . The trend suggests that the time may approach infinity at a non-zero temperature. It may be useful to extrapolate from the low temperature data what the limiting temperature is. In a combustion problem for aircraft engines, the time scale is the combustor residence time which is of $\mathcal{O}(\text{millisecond})$ in the SCRAMJET engine at interest. In this respect, the start-up time is nearly infinite for the 850 K case and is definitely infinite in the 800 K case. The addition of a fourth parameter in equation 4.4.5 may model the existence of a limiting temperature. The modified formula is

$$\log_e(t_s) \approx \log_e(p_0) + p_1 \log_e \left(\frac{1}{T_0 - T_m} \right) + p_2 \frac{1}{T_0 - T_m}, \quad (4.4.7)$$

[‡] \bar{C} behaves the same way except with larger $\bar{C}_{\text{HO}_2}(T_0 = 850 \text{ K})$ and $\bar{C}_{\text{H}_2\text{O}_2}(T_0 = 850 \text{ K})$.

* Exact solutions are obtained since there are only three parameters and three data points.

where T_m is introduced such that

$$\lim_{T_0 \downarrow T_m} t_s \rightarrow \infty .$$

For extrapolation purpose, four data points ($T_0 = 850, 900, 950, 1000 K$) are used to solve for the parameters exactly. The result is

$$\left\{ \begin{array}{l} T_m = 805.92 K \\ p_0 = 1.98265 \times 10^{-11} \\ p_1 = -2.56665 \\ p_2 = 641.693 \end{array} \right. .$$

Use of the inflexion point data in equation 4.4.6 leads to a remarkably close T_m of 806.08 K . Segments of the resulting curves are plotted in figure 4.4.7. The other three parameters, unfortunately, do not bear any meaning in this formulation.

4.4.3 Explosive rise behavior

Following the slow start-up, chain branching sets in. The result is an explosive combustion process signified by rapid heat release and temperature rise. Termination of the explosive stage is signified by the inflexion in heat release where chain breaking has just become dominant. Some effort is dedicated in this section to explore the behavior from the start-up to the inflexion.

In contrast with the effect of equivalence ratio, the rise following start-up occurs at a comparable rate for all initial temperatures. Evidences are shown pictorially in the magnified insert in figure 4.4.1b and quantitatively in table 4.4.1. According to the table, the slopes at the inflexion points change within 55% except for the highest and lowest temperature cases. The impact of low temperature on start-up behavior has been mentioned. Different chain branching characteristic is therefore expected during fast-rise. At the higher end, the expanded curve for T_0 equals 2500 K in figure 4.4.2b helps to explain the departure. The ‘bump’ which occurs at ~ 6 microsecond suggests that the kinetic in the initial stages is different from the other cases where no similar structure is observed. The departure of \overline{C}_{HO_2} at T_0 equals 2500 K from the trend of the other initial temperatures shown in figures 4.4.3a and 4.4.3b provides some indication of what might be involved. However, no attempt has been made to analyze the particular kinetic since no extended effect is noticeable. The data in figures 4.4.4a and 4.4.4b for the inflexion points** show that the unusual trend diminishes rapidly with time.

** Also see figure 4.4.5a and 4.4.5b which will be described later.

Recall from the results of figure 4.4.4b that the mole fractions of O, OH, H and H₂O are nearly constant at the inflexion point independent of initial temperature. Combining this with the results of figure 4.4.3b, the change in mole fractions from start-up to inflexion must also be constant. Then in the spirit of equations 4.4.5, the dominant kinetic in the explosive stage may also be extracted from parametric fit. The relevant time duration in this case is the rise time given by

$$t_r \equiv t_{\text{inflexion}} - t_s$$

and the relevant composition is

$$\Delta X_j \equiv X_j(t_{\text{inflexion}}) - X_j(t_s).$$

A dimensionless change in mole fraction $\overline{\Delta X}$ can be defined referring to the conditions at T_0 equals 1500 K:

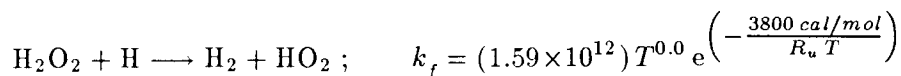
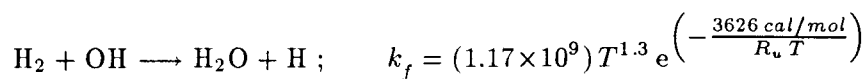
$$\overline{\Delta X}_j \equiv \frac{\Delta X_j}{\Delta X_j(T_0 = 1500 \text{ K})}.$$

This is similar to equation 4.4.4b, but the mole fractions at t_s are not zero and cannot be removed. $\overline{\Delta X}$ of four species at six initial temperatures are plotted in figure 4.4.5b. The lines are generally close to unity. Similar dimensionless change in concentrations are plotted in figure 4.4.5a for comparison. The lines in this case are not as close to unity. A previously selected radical, HO₂, is not included in the plots since its composition varies much wider over initial temperatures. On the other hand, H₂O₂ appears to be of rising importance in this stage. Their dimensionless changes in mole fraction are shown in figure 4.4.6.

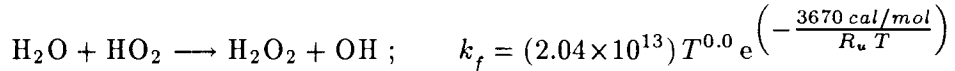
A parametric fit of rise time verse initial temperature over the range $T_0 = 950$ to 2500 K produces the following result:

$$\left\{ \begin{array}{l} p_0 = 2.23496 \times 10^{-1} \\ p_1 = 1.65088 \\ p_2 = 1976.16 \end{array} \right. \Rightarrow \left\{ \begin{array}{l} \tilde{\beta} = 0.65088 \\ \tilde{E}_a = 3924.65 \text{ cal/mol} \end{array} \right.$$

The deviation is 0.0243. According to $\tilde{\beta}$ and \tilde{E}_a , the dominant reactions include



and



which corresponds to reactions 2, 17 and the reverse step of reaction 19[†] in table 3.6.3a. The first reaction is in agreement with Mikolatis^[10]'s branched chain cycle of reactions 2, 3 and 4 in the fast-rise stage. The importance of the last two reactions is not exactly certain.

The low temperature data again do not fit into the above result. The presence of a transition as in the start-up period may best explain the departure. However, the possible role of HO₂ and H₂O₂ cannot be overlooked either. In the lowest temperature case, the change in mole fraction for all radicals is approximately one percent of that at $T_0 = 1500 \text{ K}$ except for the above two. Some indication is given in figure 4.4.6. For example, $\overline{\Delta X}$ for H₂O₂ is -9 for the lowest temperature case, implying a depletion. The previous analysis has shown that an excessive amount of H₂O₂ is created during the start-up stage at low temperature (*c.f.* section 4.4.2). This means that a large amount of H₂O₂ is rapidly destroyed during fast-rise which may in part contribute to the departure in behavior.

4.4.4 Conditions at chemical equilibrium

The asymptotic effect of initial temperature on the combustion process is given by the equilibrium conditions. Except for the 850 *K* case, the higher initial temperature cases ($T_0 = 900$ to 2500 *K*) reach 95% of the equilibrium heat release within 5 milliseconds. In other words, the equilibrium conditions are good approximations of the combustor exit conditions. The results are shown in tables 4.4.2a and 4.4.2b.

The heat release is by definition zero at the beginning of reaction. Therefore, the above values show that less available energy per unit mass is released as initial temperature increases. In the context of engine performance, it is then more favorable to have low combustor inlet temperature. This requirement is compromised by two factors: combustor pressure and residence time. Consider an ideal diffuser, a lower combustor inlet temperature would require less compression in the diffuser, resulting in lower pressure and higher flow speed at the diffuser exit which are both adverse consequences. The undesired effect of reduced pressure on combustor performance is discussed in the following section. The effect of increased flow speed is to reduce the combustor residence time whereas longer start-up time is required at lower inlet temperature. The second factor is not very important for

[†] Same as reaction 19b in table 3.4a.

vehicles with hypersonic inlet condition at the diffuser. In this case, the kinetic energy of the inlet flow is large enough such that a large change in temperature can be achieved by a small fractional change in flow speed.

The reason for reduced heat release at higher initial temperatures is the increased survivability of high energy radicals. In this respect, higher combustor inlet temperature may still be tolerated if the energy can be recovered through radical recombination in the downstream components. This aspect is discussed in chapter 4 where the chemical kinetic in a two-dimensional expansion nozzle is analyzed.

Equilibrium Condition	Initial Temperature T_0 [K]		
	850	900	950
Heat Release ΔH [J/g]	2794.90	2755.33	2714.25
Temperature T [K]	2586.22	2603.80	2620.96
Density ρ [kg/m ³]	0.05629	0.05579	0.05531
Sound Speed a [m/s]	1061.11	1065.94	1070.72
Composition Y_N	4.12×10^{-7}	4.79×10^{-7}	5.55×10^{-7}
Y_{N_2}	7.31×10^{-1}	7.30×10^{-1}	7.30×10^{-1}
Y_{NO}	7.10×10^{-3}	7.47×10^{-3}	7.85×10^{-3}
Y_{NO_2}	1.30×10^{-6}	1.37×10^{-6}	1.44×10^{-6}
Y_O	2.15×10^{-3}	2.38×10^{-3}	2.64×10^{-3}
Y_{O_2}	1.47×10^{-2}	1.53×10^{-2}	1.60×10^{-2}
Y_{OH}	1.27×10^{-2}	1.34×10^{-2}	1.42×10^{-2}
Y_H	4.02×10^{-4}	4.43×10^{-4}	4.86×10^{-4}
Y_{H_2}	2.94×10^{-3}	3.09×10^{-3}	3.23×10^{-3}
Y_{HO_2}	2.14×10^{-6}	2.31×10^{-6}	2.48×10^{-6}
Y_{H_2O}	2.17×10^{-1}	2.15×10^{-1}	2.12×10^{-1}
$Y_{H_2O_2}$	2.69×10^{-7}	2.83×10^{-7}	2.96×10^{-7}
Y_{Ar}	1.29×10^{-2}	1.29×10^{-2}	1.29×10^{-2}

TABLE 4.4.2a Equilibrium conditions for lower initial temperatures.

Equilibrium Condition	Initial Temperature T_0 [K]			
	1000	1500	2000	2500
Heat Release ΔH [J/g]	2671.65	2172.68	1571.46	901.84
Temperature T [K]	2637.72	2786.62	2908.96	3013.03
Density ρ [kg/m ³]	0.05484	0.05069	0.04724	0.04428
Sound Speed a [m/s]	1075.46	1121.03	1164.42	1206.64
Composition Y_N	6.39×10^{-7}	2.09×10^{-6}	5.08×10^{-6}	1.03×10^{-5}
Y_{N_2}	7.30×10^{-1}	7.28×10^{-1}	7.26×10^{-1}	7.25×10^{-1}
Y_{NO}	8.22×10^{-3}	1.21×10^{-2}	1.58×10^{-2}	1.93×10^{-2}
Y_{NO_2}	1.52×10^{-6}	2.26×10^{-6}	2.94×10^{-6}	3.51×10^{-6}
Y_O	2.90×10^{-3}	6.47×10^{-3}	1.17×10^{-2}	1.84×10^{-2}
Y_{O_2}	1.67×10^{-2}	2.32×10^{-2}	2.89×10^{-2}	3.35×10^{-2}
Y_{OH}	1.50×10^{-2}	2.30×10^{-2}	3.09×10^{-2}	3.78×10^{-2}
Y_H	5.32×10^{-4}	1.12×10^{-3}	1.94×10^{-3}	2.96×10^{-3}
Y_{H_2}	3.38×10^{-3}	4.80×10^{-3}	6.07×10^{-3}	7.12×10^{-3}
Y_{HO_2}	2.65×10^{-6}	4.50×10^{-6}	6.39×10^{-6}	8.05×10^{-6}
Y_{H_2O}	2.10×10^{-1}	1.88×10^{-1}	1.65×10^{-1}	1.43×10^{-1}
$Y_{H_2O_2}$	3.09×10^{-7}	4.27×10^{-7}	5.09×10^{-7}	5.52×10^{-7}
Y_{Ar}	1.29×10^{-2}	1.29×10^{-2}	1.29×10^{-2}	1.29×10^{-2}

TABLE 4.4.2b Equilibrium conditions for higher initial temperatures.

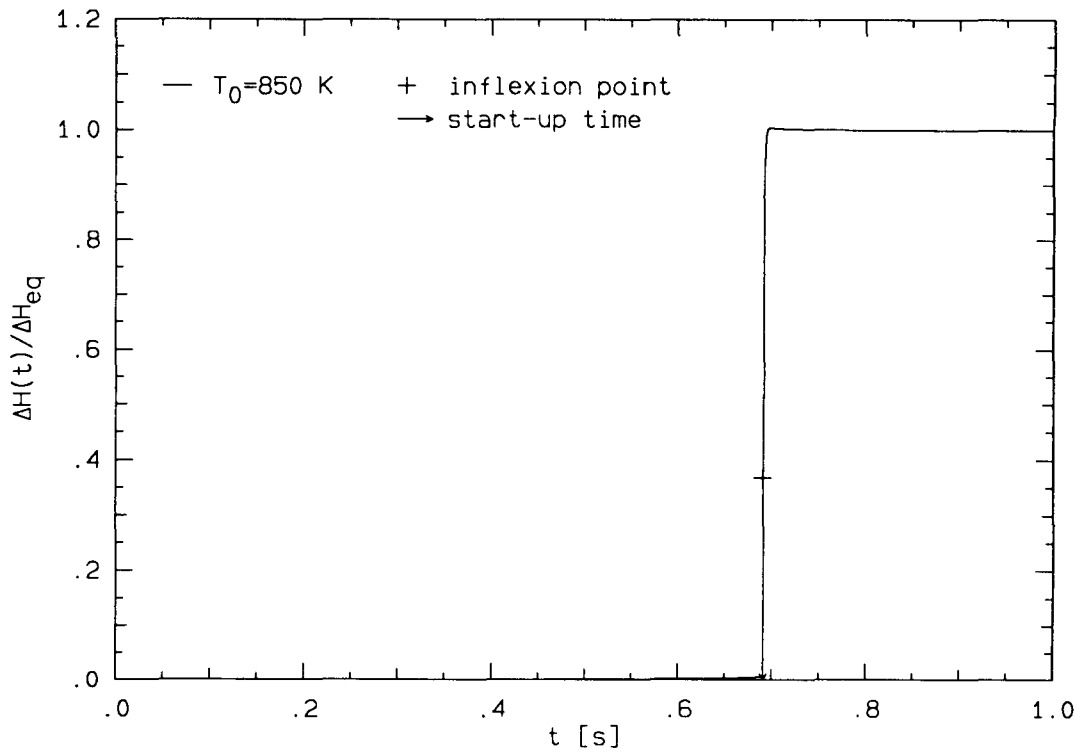


FIG. 4.4.1a Heat release for initial temperature equals 850 K.

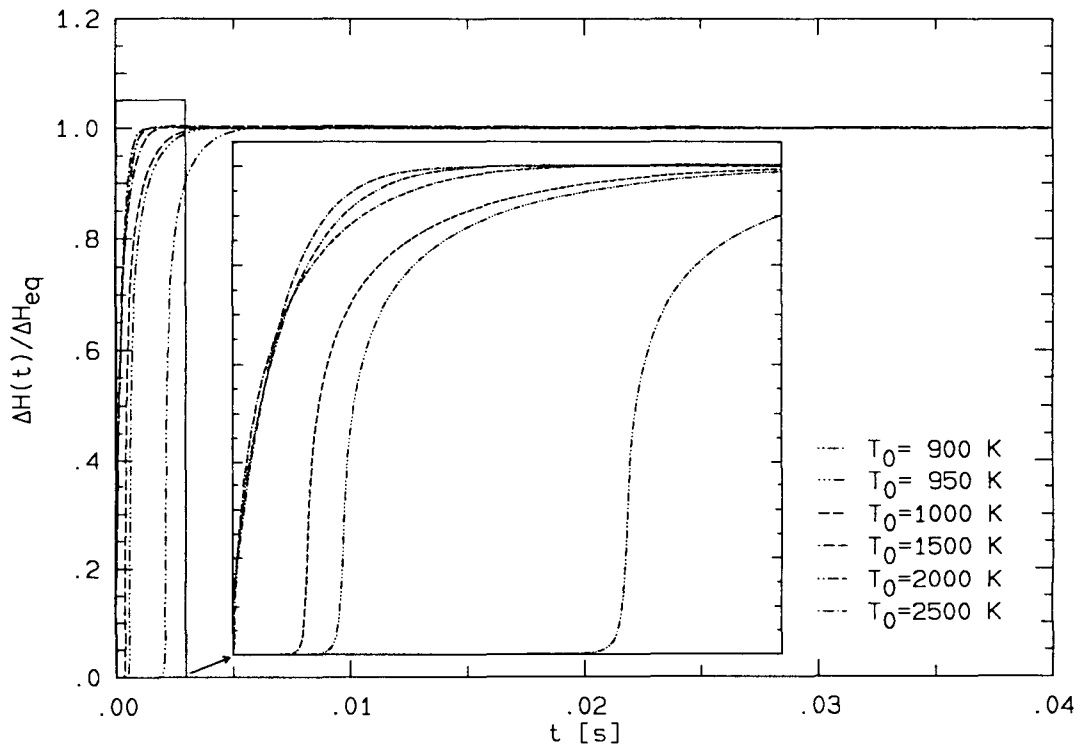


FIG. 4.4.1b Heat release for 6 initial temperatures.

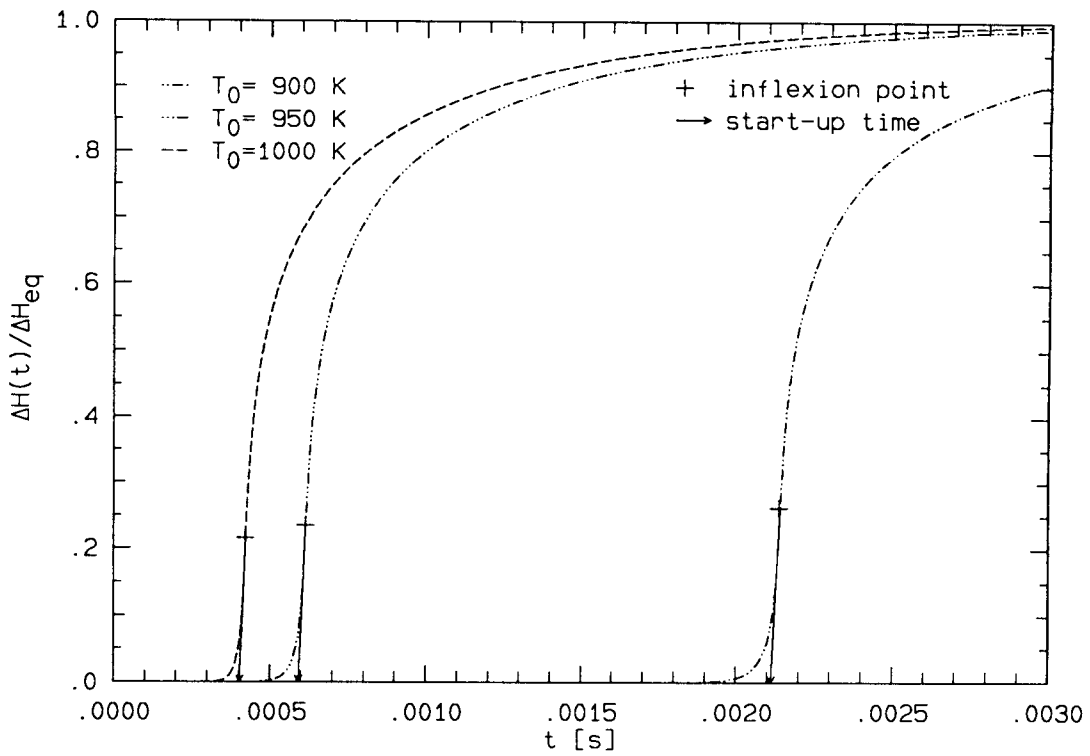


FIG. 4.4.2a Heat release at initial start-up for intermediate initial temperatures.

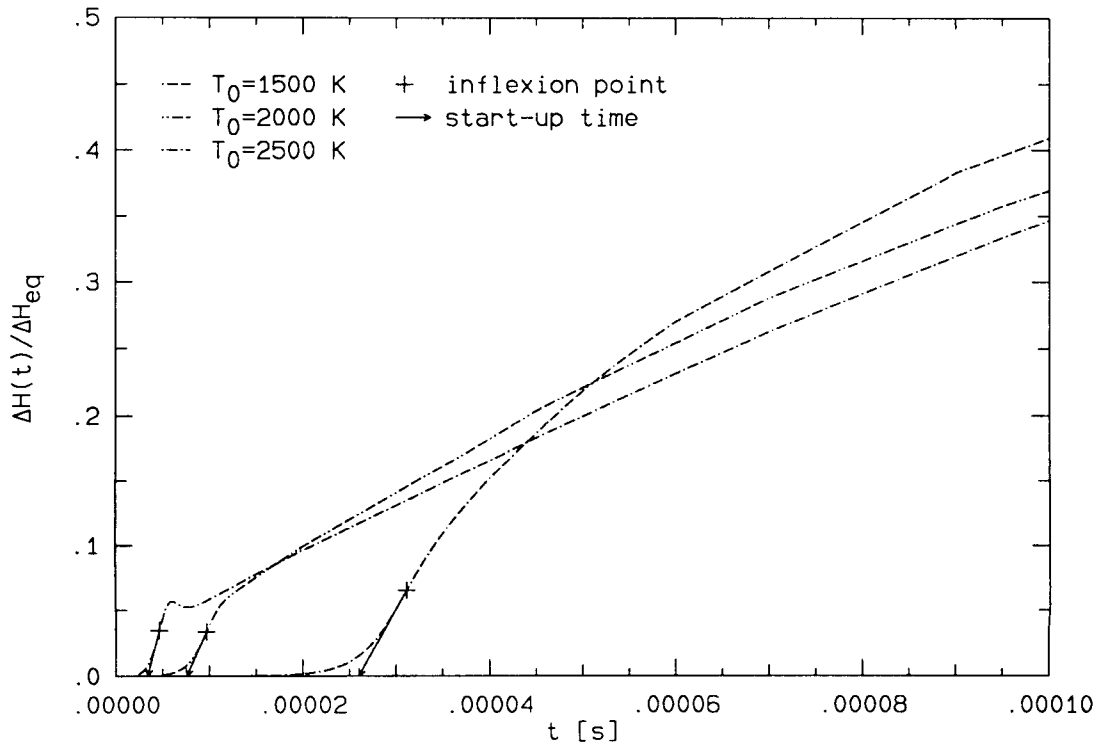


FIG. 4.4.2b Heat release at initial start-up for high initial temperatures.

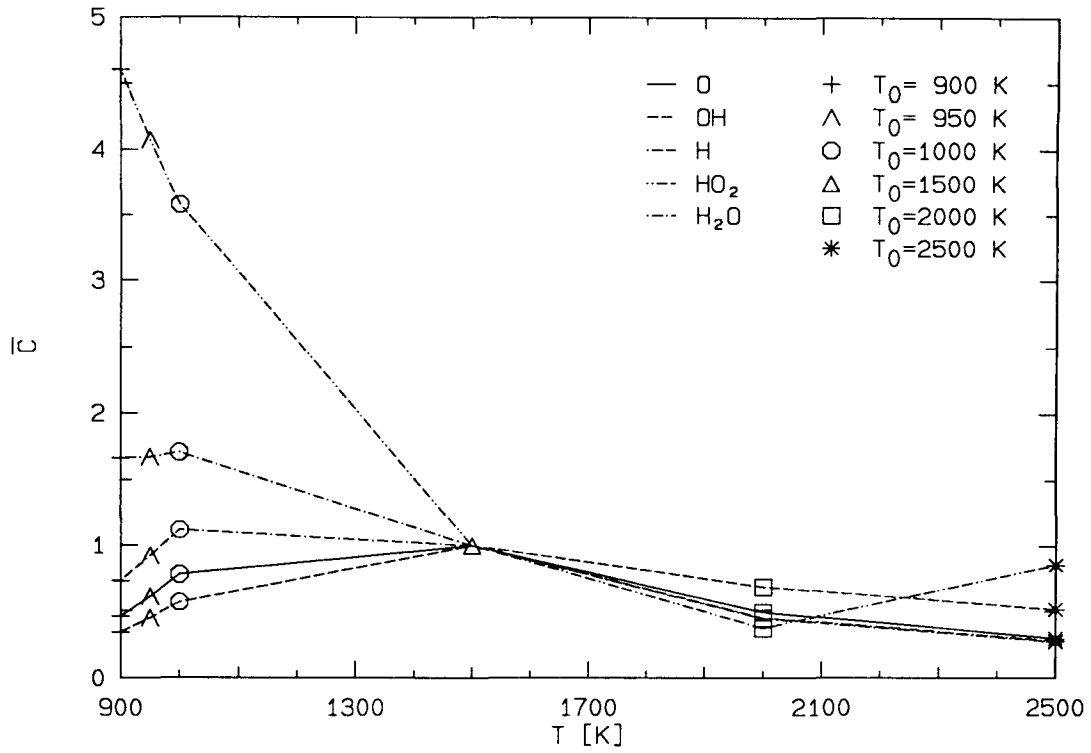


FIG. 4.4.3a Concentration for five species at start-up time for six initial temperatures.

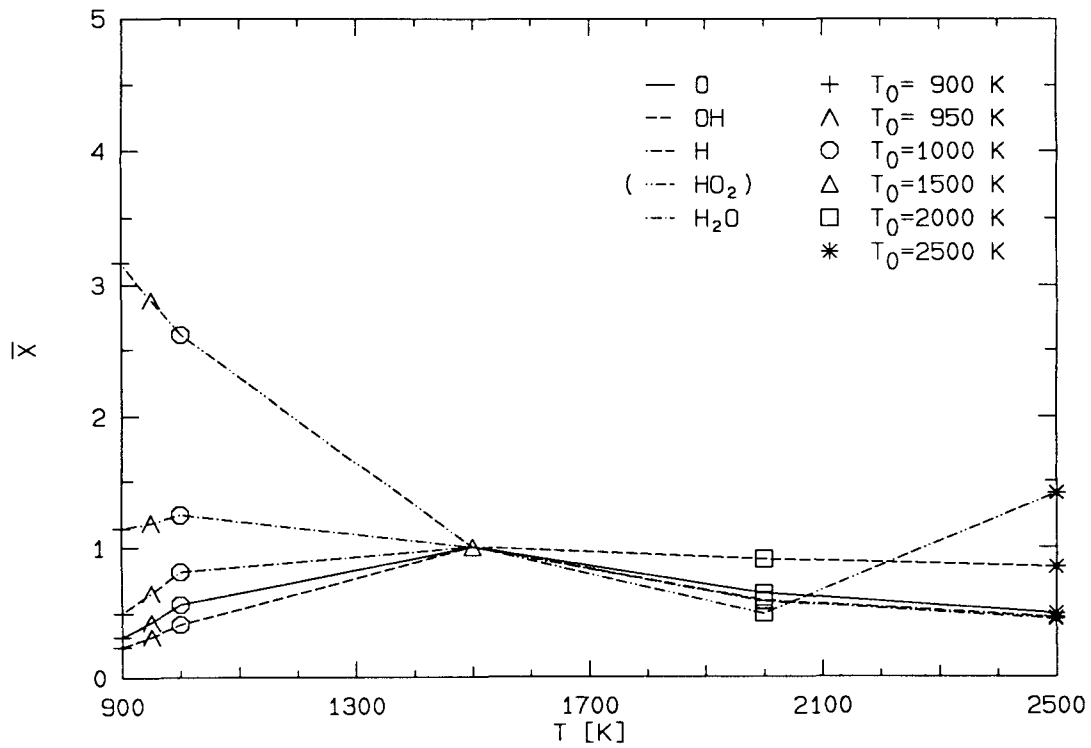


FIG. 4.4.3b Mole fraction for five species at start-up time for six initial temperatures.

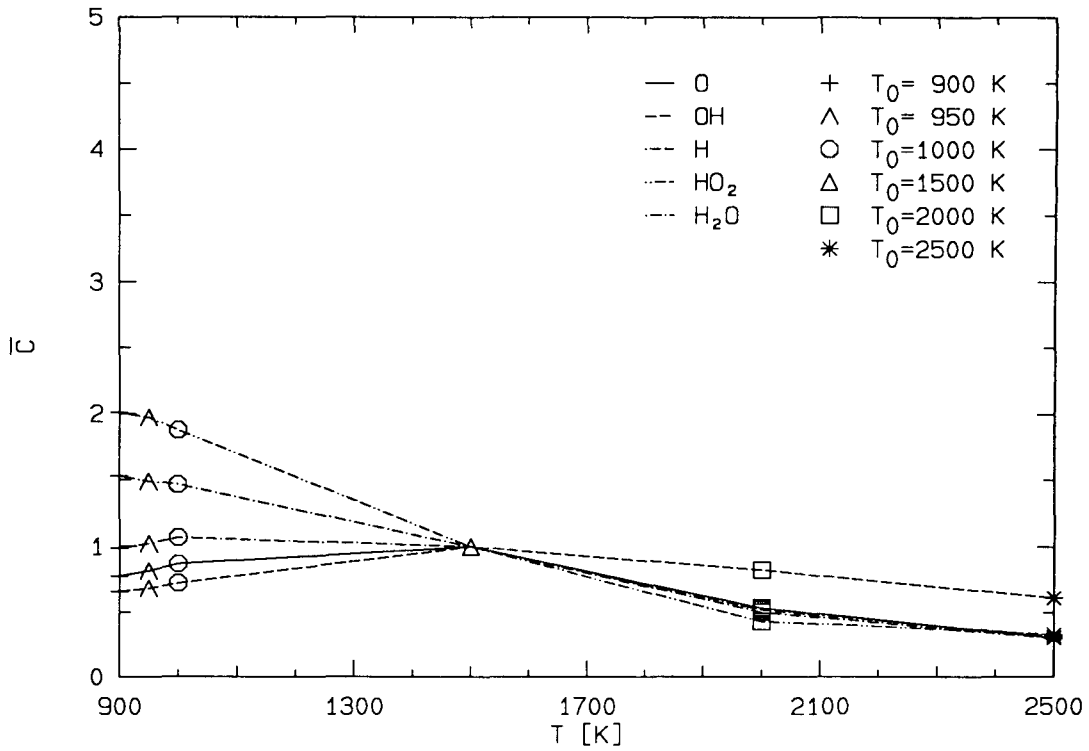


FIG. 4.4.4a Concentration for five species at inflexion for six initial temperatures.

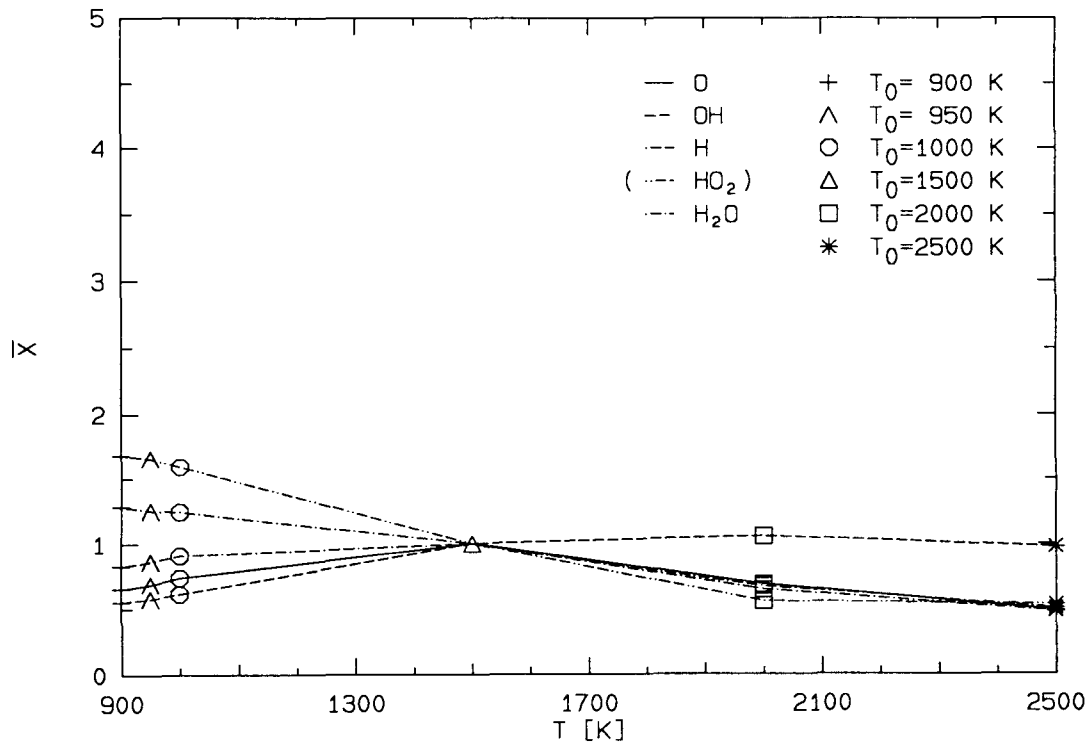


FIG. 4.4.4b Mole fraction for five species at inflexion for six initial temperatures.

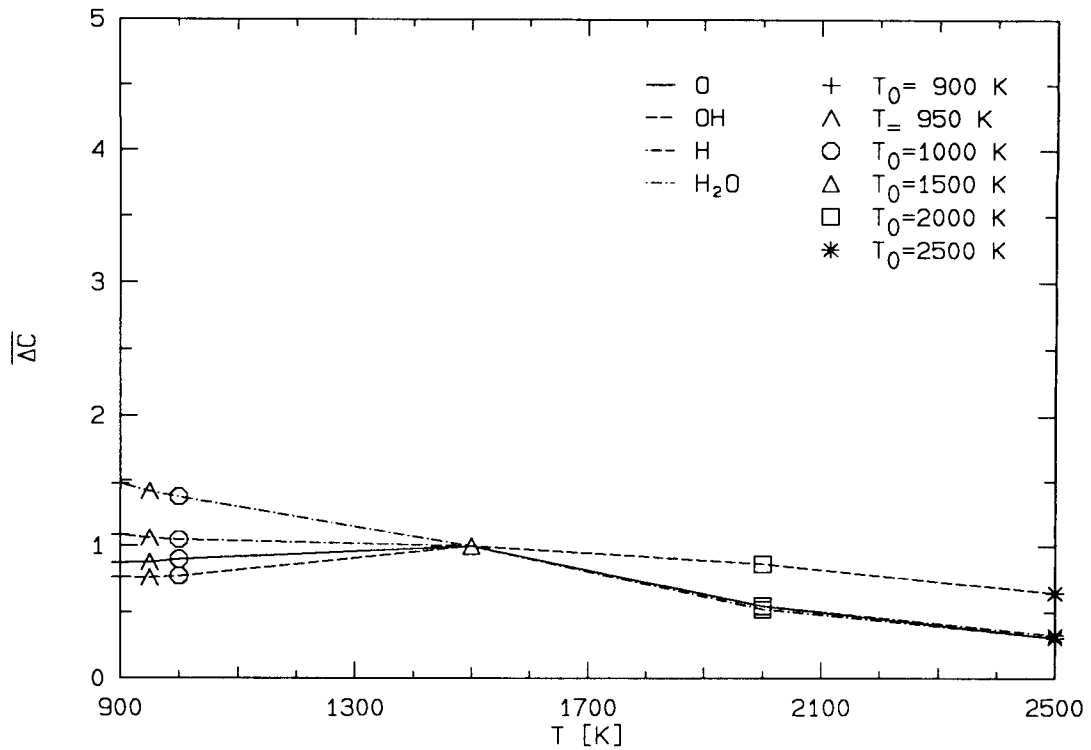


FIG. 4.4.5a Change in concentration for four species during fast-rise.

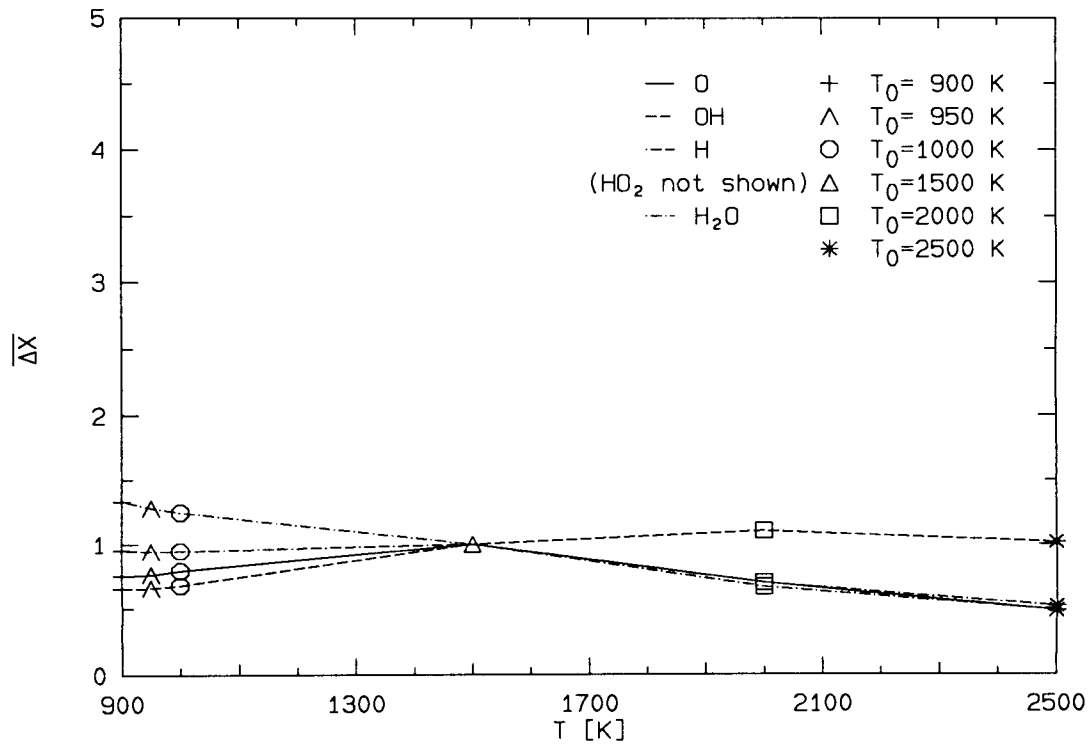


FIG. 4.4.5b Change in mole fraction for four species during fast-rise.

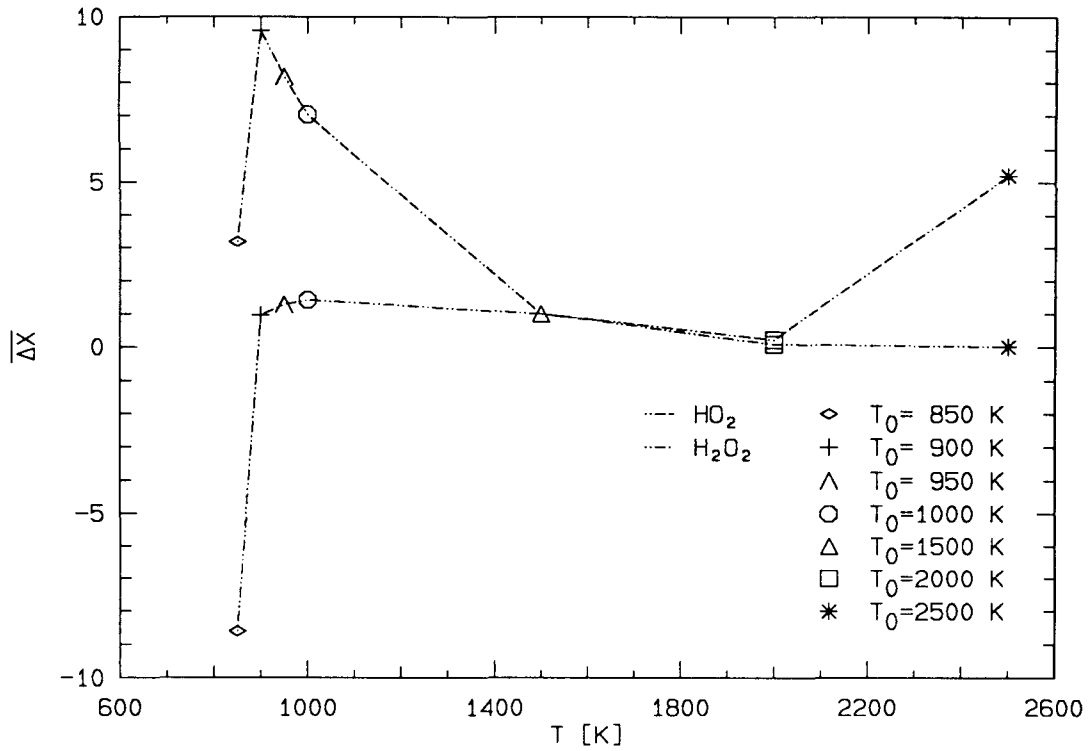


FIG. 4.4.6 Change in mole fraction for HO_2 and H_2O_2 during fast-rise.

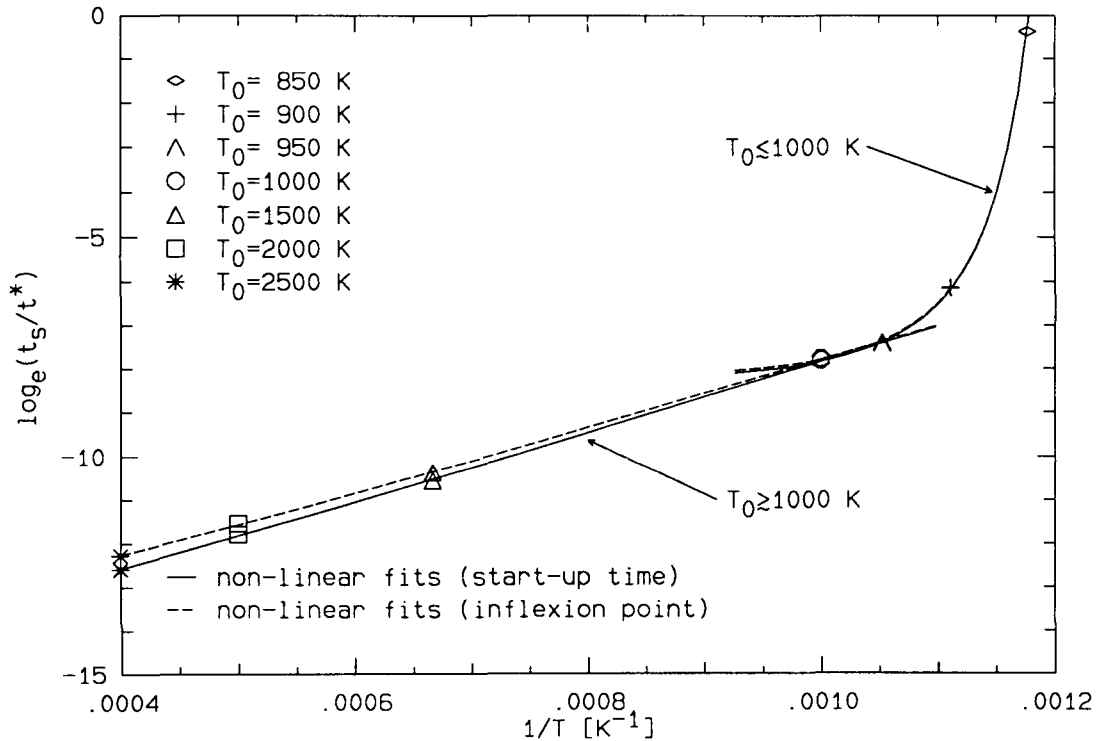


FIG. 4.4.7 Fits of start-up time and inflexion point with initial temperature.

4.5 Variation of Pressure

Five combustor pressures are chosen for this study:

$$P = \begin{cases} 0.1 \text{ atm} \\ 0.3 \text{ atm} \\ 0.5 \text{ atm} \\ 0.7 \text{ atm} \\ 1.0 \text{ atm} \end{cases}$$

The range chosen is not very large but is believed to be sufficient for combustor performance study. In short, the range represents one logarithmic decade. This is due to the nature of the rate equation.* Detailed reason will become clear as the results are presented.

As in the previous analyses, the heat release during combustion is examined for each pressure. The evolution of normalized heat release is plotted in figure 4.5.1a with a linear time scale and in figure 4.5.1b with a logarithmic time scale. A quantity t^* that equals 1 sec is used in the second plot for dimensional purpose. The similarity and spacing between the curves in the second plot suggest why those pressures are chosen.

The overshoot which was first observed in the equivalence ratio study is again obvious from the figures. An explanation can be drawn from the fast and slow formation and destruction of certain radicals when compared to the rate of heat release though H_2O formation. Examples of such radicals are OH and NO. The evolution of their normalized mass fractions is plotted in figure 4.5.2a while that of H_2O is shown in figure 4.5.2b. In this example, OH is considered the fast species and NO is considered the slow one since OH approaches equilibrium much faster than H_2O whereas NO approaches much slower. Note that the rise and fall in the normalized plots also indicate formation and destruction respectively since the initial mass fractions of those species are zero. The energy initially produced through the formation of H_2O is locked up in the fast formation of OH. As the formation of H_2O continues, the rapid destruction of such radicals results in an excessive heat release. The excess heat is to be absorbed eventually by the slow forming radical NO which results in a 'bump' during the time when excess heat is present. In general, any species falling in the fast category has the same function as OH and similarly for the slow ones.

* It involves the product of concentrations which are proportional to pressure.

4.5.1 Start-up behavior

The initial behavior is depicted in figure 4.5.3 at a refined scale. The inflexion point and start-up time for each pressure are indicated by the symbols '+' and '✓' respectively. A general increase in start-up time is observed as pressure decreases. The uniformity in the changes among the curves suggests that certain pressure scaling may be possible. To test this hypothesis, the correlation of start-up time with pressure is studied. In table 4.5.1, the start-up time together with the inflexion point at which extrapolation is performed are listed.

Initial Stage	Pressure P [atm]				
	0.1	0.3	0.5	0.7	1.0
Inflexion at t [s]	1.49×10^{-4}	5.10×10^{-5}	3.11×10^{-5}	2.24×10^{-5}	1.58×10^{-5}
$\Delta \bar{H}$	4.09×10^{-2}	5.23×10^{-2}	6.49×10^{-2}	7.64×10^{-2}	9.11×10^{-2}
$\frac{d\Delta \bar{H}}{dt}$ [s^{-1}]	1.68×10^3	6.23×10^3	1.26×10^4	2.07×10^4	3.56×10^4
Start-up at t_s [s]	1.25×10^{-4}	4.26×10^{-5}	2.60×10^{-5}	1.88×10^{-5}	1.33×10^{-5}

TABLE 4.5.1 Inflexion point and extrapolated start-up time for five pressures.

The existence of distinct start-up and inflexion points in the five pressure cases indicates the existence of certain critical mole fractions and the assumptions similar to that in the initial temperature correlation studies can again be made. However, temperature becomes a slow varying quantity which implies that the rate coefficient of the overall rate determining step is nearly constant. Equation 4.4.1a now reads

$$\frac{dY_k}{dt} \approx \left(\frac{m_k \dot{\omega}_k}{\rho} \right)_{P, \tilde{Y}} \quad \text{for } k = 1, K, \quad (4.5.1)$$

where pressure is now a parameter. In $\dot{\omega}_k$, constant effective values of the rate coefficients can be used, but the product of reactant concentrations can not since concentration is a function of pressure. The factor \tilde{R} in equation 4.4.2a or 4.4.2b is no longer constant and must therefore be written in term of pressure. Consider the initial conditions, the temperature and fractional compositions including mole fractions are held unchanged at each pressure. Also note that

$$C_k = \frac{P}{R_u T} X_k.$$

Then the initial concentration is only a function of pressure. In a particular reaction, the effective product of reactant concentrations is given by

$$\tilde{R} \approx \left(\prod_{k=1}^K \tilde{X}_k^{\nu'_k} \right) \prod_{k=1}^K \left(\frac{P}{R_u T} \right)^{\nu'_k} \quad (4.5.2a)$$

where \tilde{X}_k approximately equal their initial values and ν'_k are the reactant stoichiometric coefficients. It may be simply written as

$$\tilde{R} \approx \tilde{r} P^n, \quad (4.5.2b)$$

where \tilde{r} and n are constants. Assume that the combined effects of the rate controlling reactions can be represented by a single step,** the equation corresponding to 4.4.2b is

$$(X_j)_{\text{critical}} \approx X_j(0) + \frac{R_u T_0}{P} \tilde{\nu}_j'' \tilde{k} \tilde{r} P^{\tilde{n}} t_s \quad j \in \text{rate controlling species}. \quad (4.5.3)$$

In equations 4.5.2a and 4.5.2b, n is an integer constant. It is not necessarily so in the last equation according to the single step approximation. A *tilde* is used to signify the difference. A simple expression is obtained by combining the constants:

$$(X_j)_{\text{critical}} \approx X_j(0) + a_j \left(\frac{P}{P_a} \right)^{\tilde{n}-1} t_s. \quad (4.5.4)$$

A constant P_a equals one atmospheric pressure has been added since [atm] is used as the unit for P . Finally, a single correlation can be obtained by noting that the quotient of $((X_j)_{\text{critical}} - X_j(0))$ and ν_j'' is a constant independent of j . The formula is linear in logarithmic scale; that is,

$$\log_{10}(t_s) \approx \log_{10}(p_0) - p_1 \log_{10} \left(\frac{P}{P_a} \right), \quad (4.5.5)$$

where p_0 and p_1 are constant parameters given by

$$p_0 \equiv \frac{(X_j)_{\text{critical}} - X_j(0)}{a_j} = \frac{1}{R_u \tilde{T}} \frac{(X_j)_{\text{critical}} - X_j(0)}{\tilde{\nu}_j'' \tilde{k} \tilde{r} P_a^{\tilde{n}-1}},$$

$$p_1 \equiv \tilde{n} - 1.$$

The first parameter, p_0 , has the dimension of time. Its value, however, is not important. The second parameter, p_1 , is related to the pressure scaling suggested in figure 4.5.1b. It also indicates the nature of kinetic in the overall dominant reaction. The integer n in equations 4.5.2a and 4.5.2b represents the order of kinetic in a reaction. For example, n equals 1 implies a first order kinetic or a dissociation reaction (*c.f.* section 1.3.2.). In this way, \tilde{n} or $(p_1 + 1)$ represents the effective order of kinetics.

** This is not a reversible step.

In the above derivation, two requirements are assumed to hold: the single overall step is *significantly* slower than all other reactions over a range of pressure and this step remains the slowest over the same pressure range. The second requirement is essentially identical to one of the assumptions in the temperature correlation study. The first requirement is needed since a change in pressure by one order of magnitude may result in a change in a rate of two or three orders of magnitude in each reaction; the rate controlling effect of a two-body reaction may well be taken over by a three-body one by lowering the pressure or vice versa if their rates are close. How *significantly* slower the overall step must be depends on the range of pressure at interest. If these requirements are satisfied (along with the previously stated assumptions) in all or several of the five pressures considered, meaningful parameters could be deduced from the data.

Linear least square fit is performed on the $(\log_{10}(t_s), \log_{10}(\frac{P}{P_a}))$ data sets in the five pressure cases. Values of the resulting parameters are:

$$\begin{cases} p_0 = 1.32416 \times 10^{-5} \\ p_1 = 0.97438 \end{cases} \quad \Rightarrow \quad \tilde{n} = 1.97438 .$$

A deviation of 0.00105 is achieved in the fit, reflecting high linearity. Even better fit is obtained if the time at the inflexion point is used in place of t_s . The deviation in this case is 0.000629 with a p_1 remarkably close to the previous one.

$$\begin{cases} p_0 = 1.58325 \times 10^{-5} \\ p_1 = 0.97447 \end{cases} \quad \Rightarrow \quad \tilde{n} = 1.97447 .$$

The fitted curves together with the data points are shown at $\log_{10} - \log_{10}$ scale in figure 4.5.4. A value of t^* equals one second and P_a equals one atmospheric pressure are used as normalizing factors.

In either fit, the value of p_1 implies $\tilde{n} \sim 2$; that is, the kinetic is predominantly second order and two-body. This is in agreement with the result of the initial temperature study where reaction 3, a two-body reaction, in table 3.6.3a was found to dominate the start-up regime. Since \tilde{n} is slightly less than one, dissociation reactions must also be important. It has been claimed that the initial build-up of O radicals is partly due to the dissociation of O_2 . Of least significance in the start-up regime are the three-body reactions.

At this point, the use of a critical mole fraction rather than a critical concentration has become evident. If the latter were used, a factor of pressure would disappear from equation 4.5.4 such that p_1 is equivalent to \tilde{n} . Since p_1 is less than one, the above result would imply the existence of zero order kinetic which is not true.

Also of importance is the uniformity in behavior over the pressure range considered. Unlike the previous study where low temperature cases must be treated separately, no departure in behavior is observed in the pressure range of 0.1 to 1.0 *atm*. As a result, the effects of chamber pressure on combustor performance has become more straightforward since the selected range is believed to bracket the operating level for the engine at interest.

4.5.2 Fast-rise behavior

Variations of equivalence ratio and initial temperature have shown little effects on the fast-rise behavior following start-up. More observable effects are noticed in this study. The violent explosive behavior of the fast-rise stage is found to lessen at lower pressure. Nevertheless, a distinct fast-rise can be observed in all five cases. Linearity in the behavior with pressure can again be checked by studying the duration of the fast-rise which is defined from the start-up time to the inflexion point. The correlation of the rise time with pressure is examined according to equation 4.5.5. The result shows that \tilde{n} is also ~ 2 . The fitted parameters are

$$\begin{cases} p_0 = 2.59090 \times 10^{-6} \\ p_1 = 0.97493 \end{cases} \implies \tilde{n} = 1.97493 ,$$

with a deviation of 0.00342. Comparing to the initial stage, the second parameter indicates that the kinetics involved are only slightly altered, but the effective composition and temperature must be quite different according to the change in p_0 . This is not surprising since the rates of change in composition and temperature during the rise are much larger.

4.5.3 Scaling with pressure: Mole fraction

Referring to equation 4.5.5, the remarkable linearity exemplified by the fits on the five pressure data in both the start-up and fast-rise periods implies that p_1 and \tilde{n} are indeed constant at least up to the inflexion point. When applied to equation 4.5.4, this result suggests that a time scale given by

$$\tilde{t}(\tilde{n}, P; t) \sim \left(\frac{P}{P_a} \right)^{\tilde{n}-1} t$$

may be introduced such that the mole fractions for the rate controlling species evolve similarly for all pressure. Of course, the scaling in the start-up period and the fast-rise period need not be the same. The appropriate expressions are

$$\tilde{t}_I(\tilde{n}_I, P; t) \equiv \left(\frac{P}{P_a}\right)^{\tilde{n}_I-1} (t - t_{I0}) \quad \text{for } t_{I0} \leq t \leq t_{II0} \quad (4.5.6a)$$

and

$$\tilde{t}_{II}(\tilde{n}_{II}, P; t) \equiv \tilde{t}_I(\tilde{n}_I, P; t_{II0}) + \left(\frac{P}{P_a}\right)^{\tilde{n}_{II}-1} (t - t_{II0}) \quad \text{for } t_{II0} \leq t \leq t_{III0} \quad (4.5.6b)$$

in the first two periods respectively. The roman-numerals in the subscripts ‘I’, ‘II’, ‘III’ and so on are used to denote the corresponding stages. The quantity t_{I0} is the initial time which is zero for this calculation; t_{II0} is the start-up time and t_{III0} is the time at the inflexion point. The values of these times depend on the pressure. If a scaling also exists for the time greater than t_{III0} , the appropriate expression would be

$$\tilde{t}_{III}(\tilde{n}_{III}, P; t) \equiv \tilde{t}_{II}(\tilde{n}_{II}, P; t_{III0}) + \left(\frac{P}{P_a}\right)^{\tilde{n}_{III}-1} (t - t_{III0}) \quad \text{for } t_{III0} \leq t \leq \infty. \quad (4.5.6c)$$

In order to be similar, the functional relationships

$$f_{Ij}(\tilde{t}_I) = X_j(P; t) - X_j(P; t_{I0}) \quad j \in \text{rate controlling species} \quad (4.5.7a)$$

and

$$f_{IIj}(\tilde{t}_{II}) = X_j(P; t) - X_j(P; t_{II0}) \quad j \in \text{rate controlling species} \quad (4.5.7b)$$

must be identical in each period for all P . The nominal values for \tilde{n}_I and \tilde{n}_{II} are 1.97438 and 1.97493 in the two periods respectively according to the fitted results.

An example incorporating the scaling of equations 4.5.6a and 4.5.6b is demonstrated in figure 4.5.5 for the mole fraction of OH at five different pressures. The OH radical is chosen for the demonstration because it was found to be of importance in the first two stages in the temperature study. Although the values for \tilde{n} are slightly less than 2.0 according to the fitted results, a value of 2 has been used in both scaling equations since the kinetics involving OH can only be two- or three-body. Also recall that the fitted parameters were found based on the time at start-up and the time at inflexion measured from the heat release curve. Therefore, the parameters reflect integrated behavior rather than that of a single species. Nevertheless, the difference is small and the use of the times defined by the heat release produces very good collapse in the curves. In addition, the start-up time and inflexion point corresponding to the mole fraction of OH are not far from those of the heat

release according to the figure: the inflexion points and the extrapolated start-up times of the collapsed mole fraction curves generally fall within the shaded regions which bound the inflexion points and start-up times for the heat release at \tilde{n}_I equals \tilde{n}_{II} equals one. If the fitted values for \tilde{n} had been used, the shaded regions would collapse to two vertical lines while the curves would not collapse as well. It must be emphasized that the similarity between the five curves during the two initial stages is excellent whether the chosen or fitted \tilde{n} is used. In either case, the value of $\tilde{t}_I(\tilde{n}_I, P; t_{I10})$ and $\tilde{t}_{II}(\tilde{n}_{II}, P; t_{II0})$ are nearly independent of pressure. They are approximately 1.2827×10^{-5} and 1.5209×10^{-5} scaled seconds respectively.

The application of equation 4.5.6c is not expected to be as well. The overall kinetics following the second period generally do not remain constant. The dominant role of the supposedly small set of rate controlling reactions effective prior to the inflexion point must have either transferred to another set of reactions or slowly faded away as the chemical processes approach equilibrium; at this point, the forward and reverse steps of all reactions have comparable rates and are equally important. Therefore, the evolution of mole fraction towards chemical equilibrium is not expected to obey any single scaling as the assumption of irreversible rate controlling steps breaks down. It is possible that periods with

$$\tilde{n}_{III} = \text{constant} \quad \text{for } t_{III0} \leq t \leq t_{IV0} ,$$

$$\tilde{n}_{IV} = \text{constant} \quad \text{for } t_{IV0} \leq t \leq t_{V0} ,$$

...

and so on can be found following the inflexion; however, a continuously changing scale such that

$$\tilde{n} = \tilde{n}(t) \neq \text{constant} \quad \text{for } t \rightarrow \infty$$

is more likely as the chemical process eventually changes from one dominated by a small group of reactions to one governed by all reaction steps. In addition, the equilibrium mole fraction for each species is not the same at different pressures.

Two of the features just discussed can also be demonstrated via the previous example. Figure 4.5.5 shows that the behavior towards equilibrium obviously does not follow that in the first two stages. Empirical scaling with a constant \tilde{n}_{III} was attempted with partial success. To be precise, a value of \tilde{n}_{III} equals 3 causes part of the curves following the inflexion points to collapse but no value \tilde{n}_{IV} succeeds as the mole fractions of OH approach their equilibrium values. The results are shown in figures 4.5.6a 4.5.6b. Note that the scaled time in both figures is composed of three types of scaling according to equations 4.5.6a to 4.5.6c. The inflexion point for the heat release curve is used as t_{III0} . From figure 4.5.6b, similarity is very good up till the turning point at which the mole fraction of OH

begins to decrease asymptotically towards equilibrium. This indicates the existence of a third period with scaling valid from the inflexion point to the turning point. That is, there exists a function

$$f_{\text{III OH}}(\tilde{t}_{\text{III}}) = X_{\text{OH}}(P; t) - X_{\text{OH}}(P; t_{\text{III0}}) \quad \text{for } t_{\text{III0}} \leq t \leq t_{\text{IV0}}, \quad (4.5.7c)$$

where t_{IV0} is the time at the turning point. In reality, the chemical kinetic cannot switch from a majority of order 2 to a majority of order 3 instantaneously. The transition from \tilde{n}_{II} equals 2 to \tilde{n}_{III} equals 3 is signified by a small departure between the curves in a region immediately following the inflexion point (*c.f.* figure 4.5.6a). The existence of a third period for the mole fraction of OH can be anticipated by observing the distinct turning point before equilibrium is approached. This is depicted in figure 4.5.2a through the normalized mass fraction of OH. The key is that the mole fractions at the five pressures are the same at the turning points, implying the possible application of equation 4.5.4 and hence a third scaling. The collapsed turning point is shown in figure 4.5.6b near \tilde{t} equals 0.00012.

The idea of a transition following the inflexion point may not be too convincing since the small region of departure shown in figure 4.5.6a appears to have certain structure. The curves seems to be over scaled by having too large a \tilde{n} ($\tilde{n}_{\text{III}} = 3$) in the region. A better result might be obtained if the value of \tilde{n}_{II} ($\tilde{n}_{\text{II}} = 2$) were used up to the end of that region. This leads to the conclusion that the inflexion point might not be a good representation of the end of the second or fast-rise period. Although chain branching is just overcome by chain breaking at the inflexion, its effect is very likely to sustain further beyond. An alternate definition of the end of the second period would be the time at which the tangent at the inflexion point intersects with the tangent at the following turning point.[†] Unfortunately, the result obtained according to this definition is worst mainly because the mole fraction at the newly defined time is not the same over the five pressures. The existence of yet another period between the second and third is not likely since the insertion of a different scaling between the two would mean that a new \tilde{n}_{III} must be chosen and it is contradictory that two different \tilde{n}_{III} can scale the curves equally well. Therefore, the inflexion point will continue to be used as the termination of fast-rise and the notion of a transition following the inflexion is adopted.

Failure of scaling on mole fraction beyond the turning point is in part due to the difference in its equilibrium level at different pressures. Even though a constant \tilde{n}_{IV} is not expected, it may be worthwhile to find a scaling that can approximate the overall behavior

[†] The asymptote at equilibrium should be used if no turning point exists following the inflexion.

of OH towards equilibrium. For this purpose, the mole fractions must be normalized by their equilibrium values such that all compositions approach unity as time goes to infinity. The form of \tilde{t} is same as before; but the previous similarity equations must be modified to

$$f_{\text{IVOH}}(\tilde{t}_{\text{IV}}) = \frac{X_{\text{OH}}(P; t) - X_{\text{OH}}(P; t_{\text{IV}0})}{X_{\text{OH}}(P; \infty) - X_{\text{OH}}(P; t_{\text{IV}0})} \quad \text{for } t \geq t_{\text{IV}0} . \quad (4.5.7d)$$

This is applied and a \tilde{n}_{IV} of approximately 2.65 is found. The result is plotted in figure 4.5.7. The ordinate in this figure is not compatible with the previous ones since it has been normalized. Also note that the decreasing trend in mole fraction towards equilibrium has become an increasing trend towards unity.

4.5.4 Scaling with pressure: Heat release and Temperature

The scaling of OH in the last example has little application to the combustion problem. Of better use is the scaling for overall quantities such as the chemical heat release. If a scaling can be found, it is possible to predict the heat release at any time for any pressure. Therefore, the heat release is used as an example in this section.

The most important difference between the heat release and the composition of a species (*e.g.*, the mole fraction of OH used in section 4.5.3) is that the former represents the combined behavior of all species while the latter pertains to individual behavior only. As a result, distinct periods of integral order of kinetics may not be possible. The scaling is expected to behave like the last period in the OH case where only average kinetics can be found. However, the heat release does evolve similar the rate controlling kinetics prior to the inflexion point. The proximity of start-up time and inflexion point between the OH mole fraction and the heat release is a demonstration. Unfortunately, neither the absolute nor the normalized heat release has the same value at those points over the five pressures. The variations are approximately 3% for the absolute values and 2% for the normalized. For this reason, the normalized heat release is used in the scaling so that the initial similarity is good and that all curves approach unity at equilibrium.

The scaling is divided into three regions: from the starting point to start-up, from start-up to inflexion point and from inflexion point to equilibrium. The scaled times in the three regions are defined by equations 4.5.6a to 4.5.6c. Instead of using the values of fitted parameters found separately in the start-up and fast-rise regions for \tilde{n} (*c.f.* sections 4.5.1 and 4.5.2), a value of 1.97447 is used for both \tilde{n}_{I} and \tilde{n}_{II} . This was found in section 4.5.1 to be of better fit from the starting point to inflexion point. Accordingly, $\tilde{t}_1(\tilde{n}_1, P; t_{10})$ and

$\tilde{t}_{\text{II}}(\tilde{n}_{\text{II}}, P; t_{\text{III0}})$ are approximately 1.3271×10^{-5} and 1.5840×10^{-5} scaled seconds respectively. \tilde{n}_{III} is found empirically and has a value of approximately 2.75. This value is chosen such that the best collapse of the curves occurs near $\widehat{\Delta H}$ equals 0.9. The result is plotted in figure 4.5.8.

As an application of this scaling, the above results can be used to determine, for example, how much time is required to reach 95% of the equilibrium heat release at a combustor pressure of 0.4 atm. This can be accomplished by rearranging equation 4.5.6c:

$$t = t_{\text{III0}} + (\tilde{t}_{\text{III}}(\tilde{n}_{\text{III}}, P; t) - \tilde{t}_{\text{II}}(\tilde{n}_{\text{II}}, P; t_{\text{III0}})) \left(\frac{P}{P_a} \right)^{-(\tilde{n}_{\text{III}}-1)} \quad \text{for } t_{\text{III0}} \leq t \leq \infty. \quad (4.5.8)$$

Furthermore, since \tilde{n}_I and \tilde{n}_{II} are the same, equation 4.5.6b reduces to

$$\tilde{t}_{\text{II}}(\tilde{n}_{\text{II}}, P; t) \equiv \left(\frac{P}{P_a} \right)^{\tilde{n}_{\text{II}}-1} (t - t_{\text{I0}}) \quad \text{for } t_{\text{I0}} \leq t \leq t_{\text{III0}},$$

where t_{I0} is the starting point and is zero and \tilde{n}_{II} is equal to 1.97447. Therefore,

$$\begin{aligned} \tilde{t}_{\text{II}}(\tilde{n}_{\text{II}}, P; t_{\text{III0}}) &\simeq 1.5209 \times 10^{-5} \text{ s} = \text{constant in } P \\ \implies t_{\text{III0}}(P \text{ at } 0.4 \text{ atm}) &= 3.7143 \times 10^{-5}. \end{aligned}$$

From figure 4.5.8, the 95% point occurs at

$$\tilde{t}_{\text{III}} \simeq 3.00 \times 10^{-4} \text{ s}.$$

Substitute these results into equation 4.5.8 and use

$$\tilde{n}_{\text{III}} \simeq 2.75$$

the real time required is

$$t \simeq 1.45 \times 10^{-3} \text{ s}.$$

The scaling of normalized temperature is the same as that of heat release. In fact, the resulting plot shown in figure 4.5.9 exactly resembles figure 4.5.8. The change in the overall thermodynamic properties of the system during the reaction must therefore be small.

4.5.5 Conditions at chemical equilibrium

For completeness, the equilibrium conditions for the five pressure cases are shown in table 4.5.2.

Equilibrium Condition	Combustor Pressure P [atm]				
	0.1	0.3	0.5	0.7	1.0
Heat Release ΔH [J/g]	1927.01	2094.20	2172.68	2224.38	2279.06
Temperature T [K]	2644.25	2741.25	2786.62	2816.46	2848.01
Density ρ [kg/m ³]	0.01056	0.03080	0.05069	0.07038	0.09970
Sound Speed a [m/s]	1100.87	1114.72	1121.03	1125.13	1129.41
Composition Y_N	1.54×10^{-6}	1.92×10^{-6}	2.09×10^{-6}	2.20×10^{-6}	2.31×10^{-6}
Y_{N_2}	7.29×10^{-1}	7.28×10^{-1}	7.28×10^{-1}	7.28×10^{-1}	7.28×10^{-1}
Y_{NO}	1.07×10^{-2}	1.17×10^{-2}	1.21×10^{-2}	1.23×10^{-2}	1.25×10^{-2}
Y_{NO_2}	1.12×10^{-6}	1.82×10^{-6}	2.26×10^{-6}	2.60×10^{-6}	3.02×10^{-6}
Y_O	8.79×10^{-3}	7.19×10^{-3}	6.47×10^{-3}	6.01×10^{-3}	5.54×10^{-3}
Y_{O_2}	2.79×10^{-2}	2.47×10^{-2}	2.32×10^{-2}	2.23×10^{-2}	2.12×10^{-2}
Y_{OH}	2.42×10^{-2}	2.35×10^{-2}	2.30×10^{-2}	2.27×10^{-2}	2.22×10^{-2}
Y_H	1.55×10^{-3}	1.25×10^{-3}	1.12×10^{-3}	1.04×10^{-3}	9.56×10^{-4}
Y_{H_2}	5.23×10^{-3}	4.95×10^{-3}	4.80×10^{-3}	4.69×10^{-3}	4.58×10^{-3}
Y_{HO_2}	2.42×10^{-6}	3.72×10^{-6}	4.50×10^{-6}	5.09×10^{-6}	5.77×10^{-6}
Y_{H_2O}	1.80×10^{-1}	1.85×10^{-1}	1.88×10^{-1}	1.90×10^{-1}	1.92×10^{-1}
$Y_{H_2O_2}$	1.52×10^{-7}	3.09×10^{-7}	4.27×10^{-7}	5.27×10^{-7}	6.57×10^{-7}
Y_{Ar}	1.29×10^{-2}	1.29×10^{-2}	1.29×10^{-2}	1.29×10^{-2}	1.29×10^{-2}

TABLE 4.5.2 Equilibrium conditions for five combustor pressures.

Although only three scaling examples were examined, other quantities are also expected to scale the same way. The results generally indicate that the time required to reach a certain percentage of the equilibrium is proportional to $\frac{P}{P_a}$ raised to the power -2.0 to -1.5 ; that is, the time increases exponentially as pressure decreases. Therefore, caution must be taken when considering the equilibrium values since some of the level might never be reached in an aircraft engine if the pressure is too low.

Some overall effects of pressure can be extracted from the table. First of all, energy release tends to favor higher pressure. This is because the formation of several abundant radicals is inhibited as pressure increases. These include O, OH and H. The exception is NO which increases with pressure. On the other hand, the increase in equilibrium heat

release or temperature is not very large over a ten fold increase in pressure. Of noticeable change is the density which is not surprising according to the gas law.

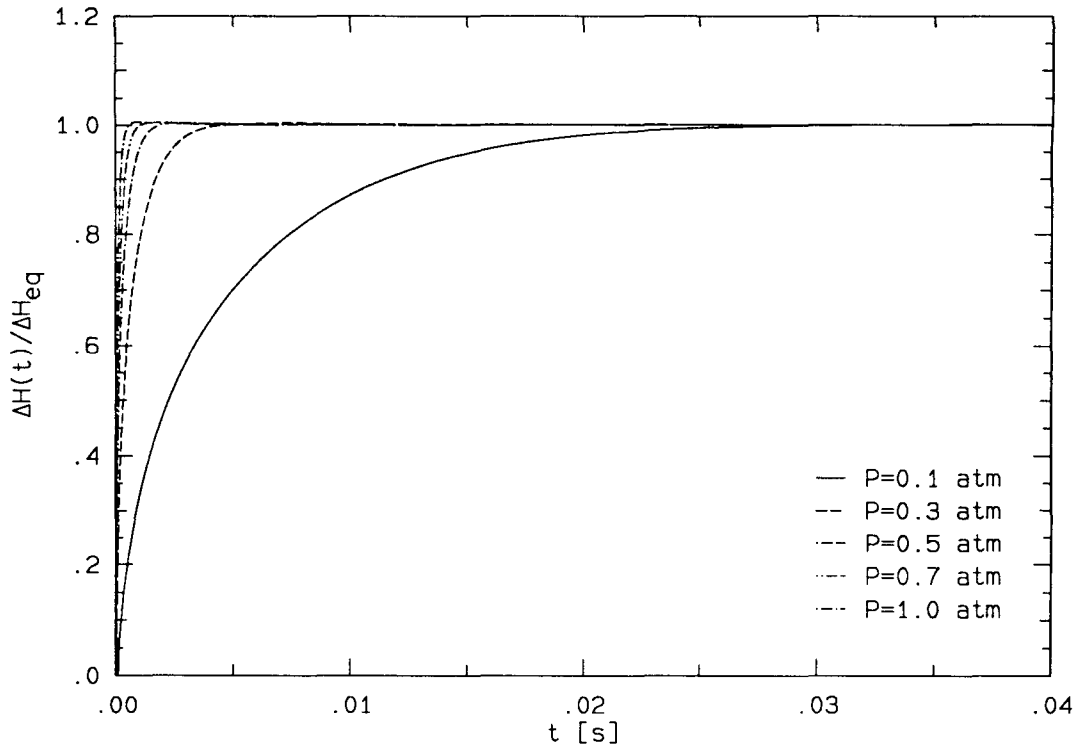


FIG. 4.5.1a Heat release for five combustor pressures.

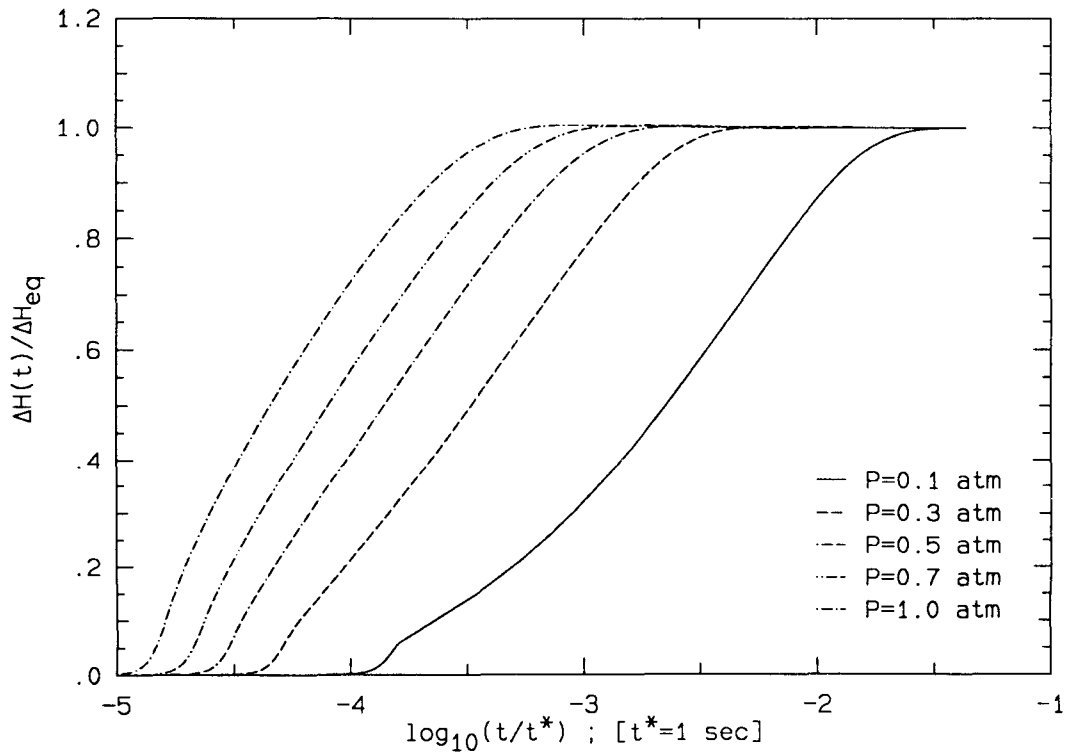


FIG. 4.5.1b Heat release at logarithmic time scale.

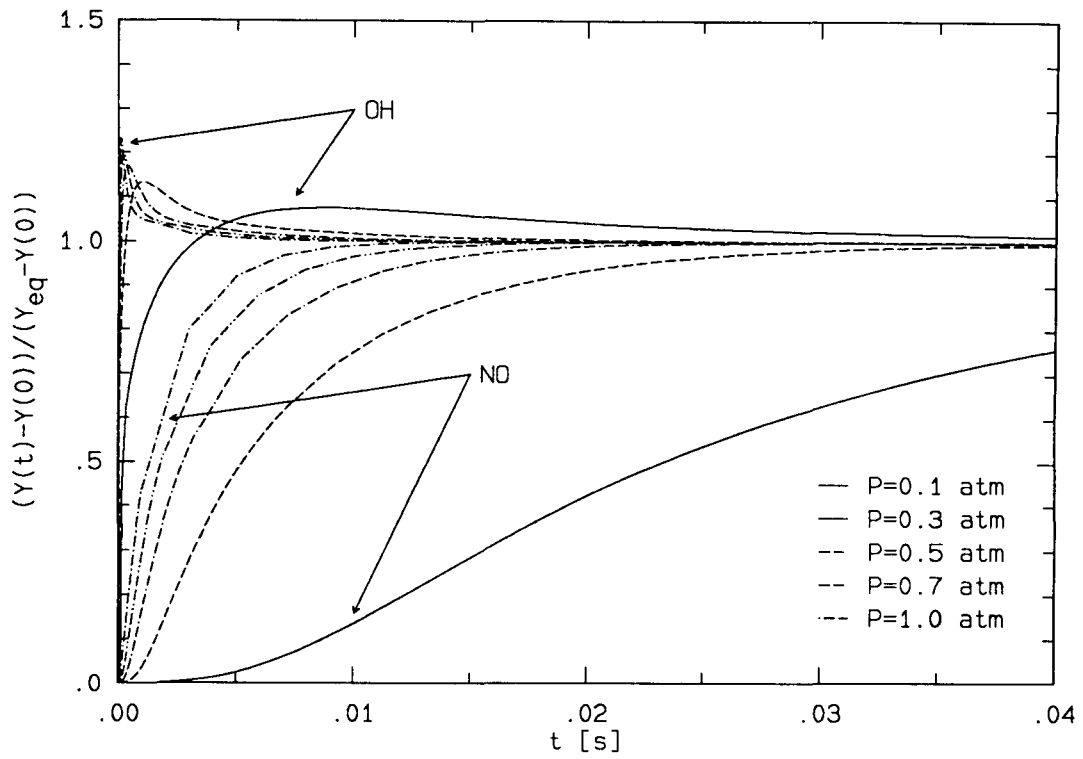
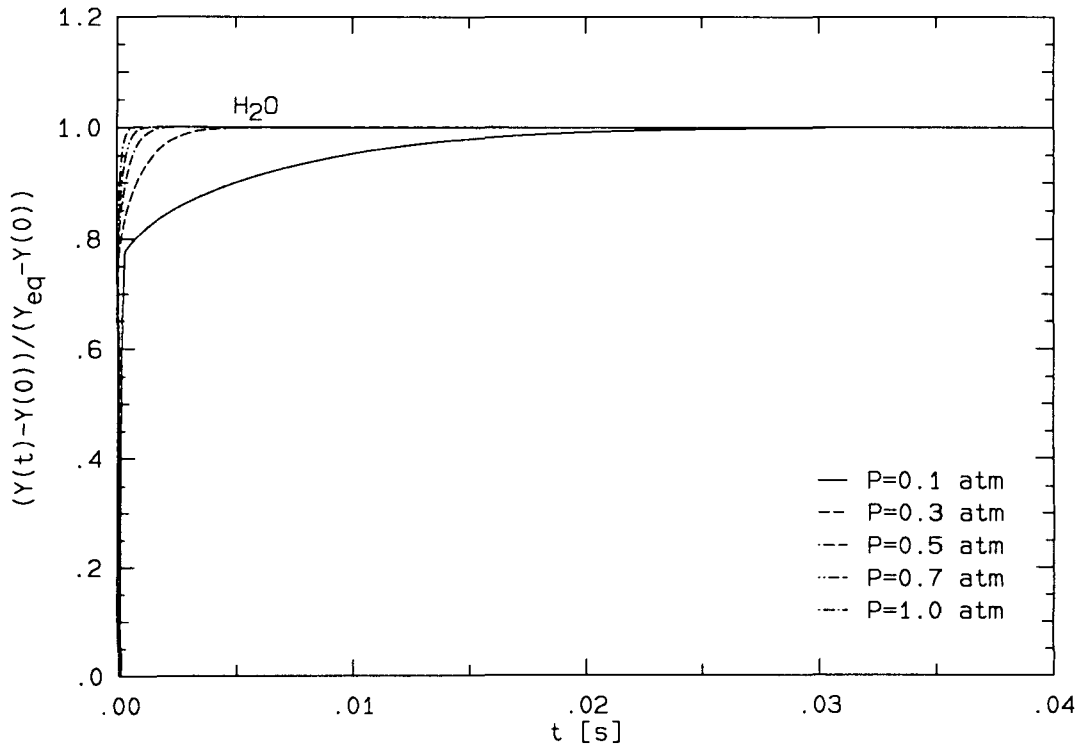


FIG. 4.5.2a Mass fraction of NO and OH.

FIG. 4.5.2b Mass fraction of H₂O.

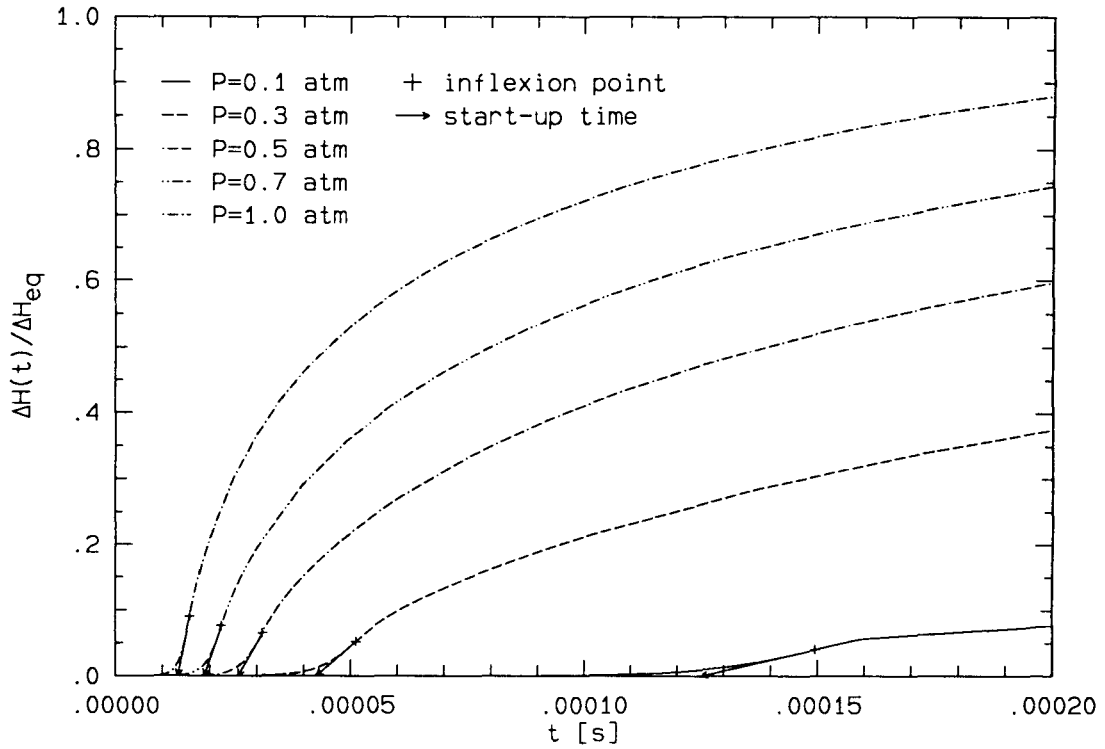


FIG. 4.5.3 Heat release at initial start-up.

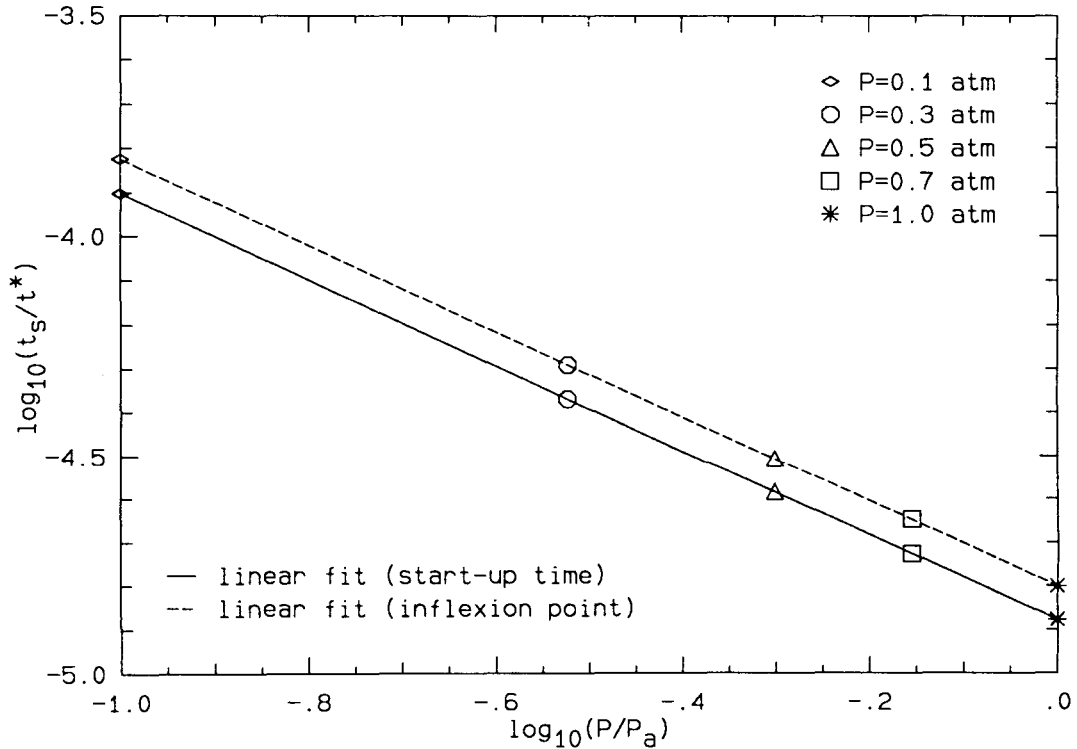


FIG. 4.5.4 Fits of start-up time and inflexion point with combustor pressure.

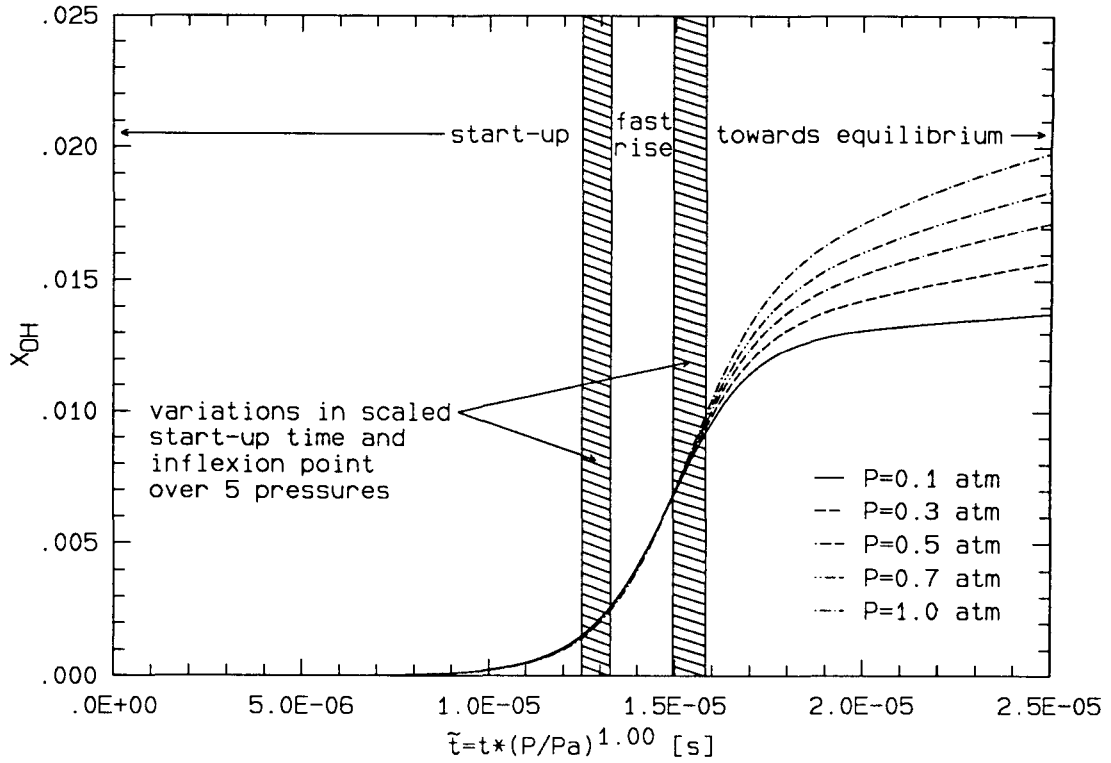


FIG. 4.5.5 Mole fraction of OH versus scaled time of first two periods.

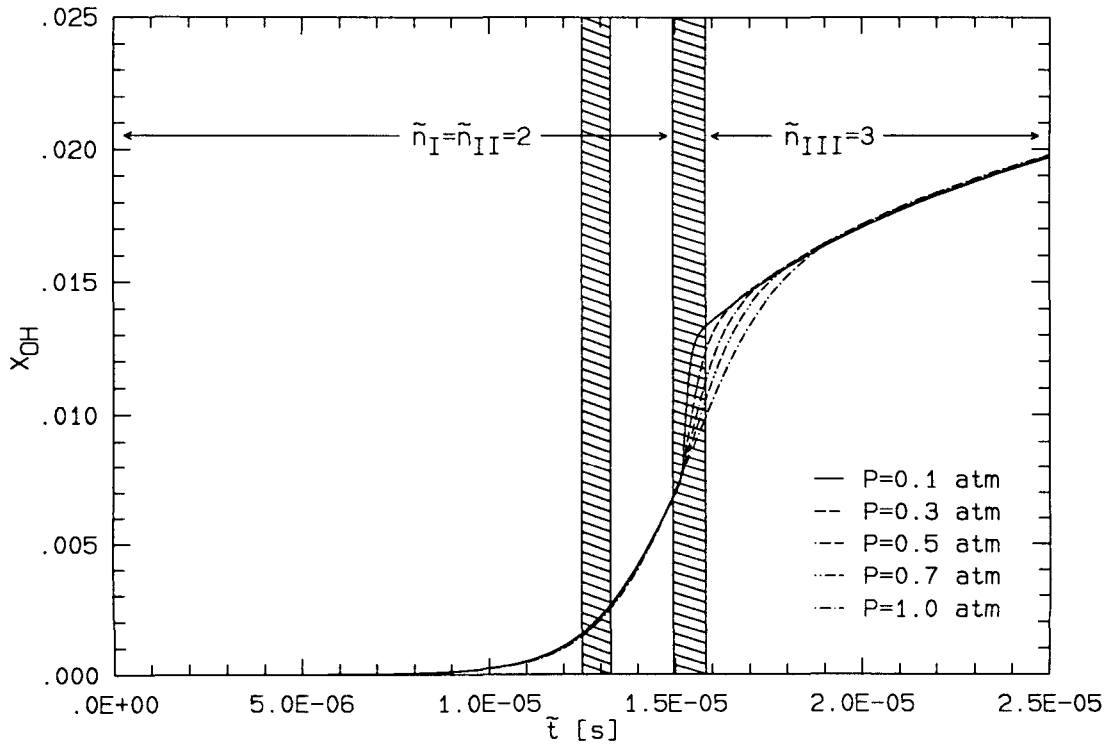


FIG. 4.5.6a Transition in scaling on OH mole fraction from second to third period.

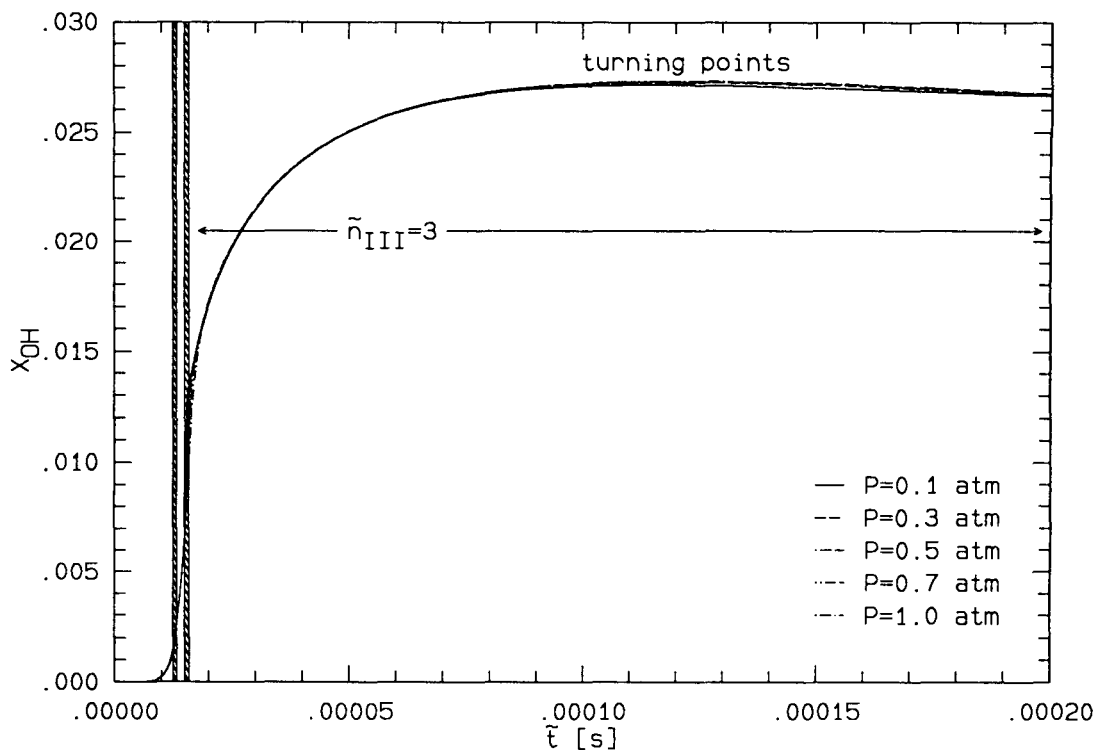


FIG. 4.5.6b Mole fraction of OH versus scaled times of three periods.

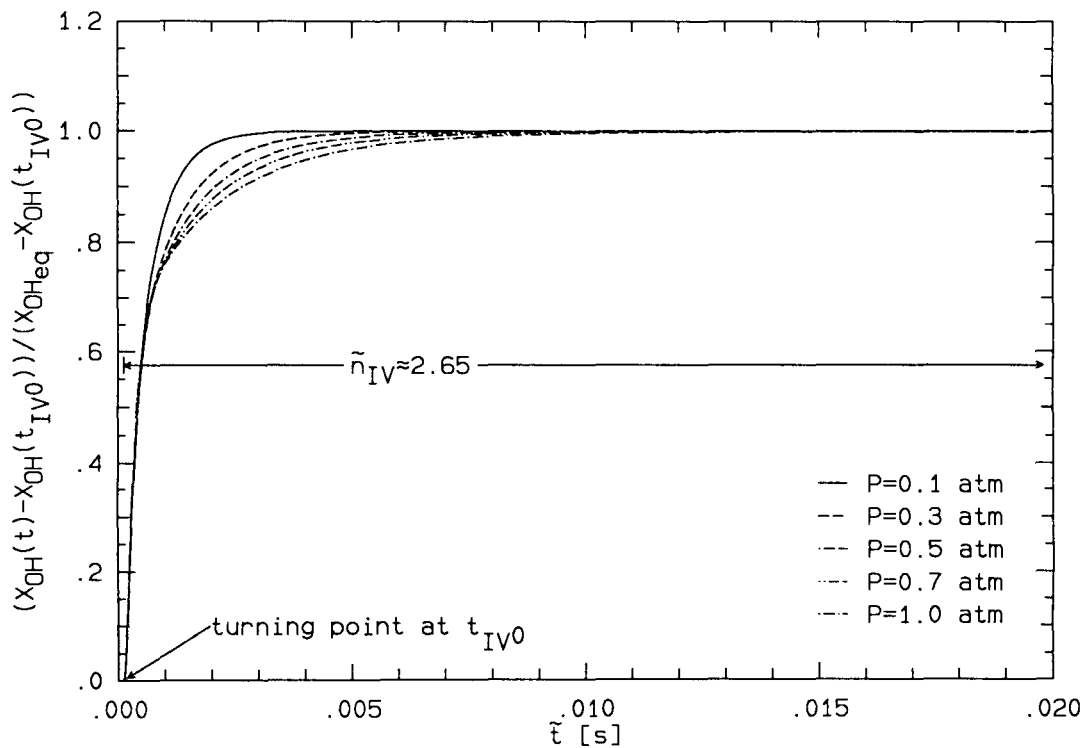


FIG. 4.5.7 Normalized mole fraction of OH versus scaled time towards equilibrium.

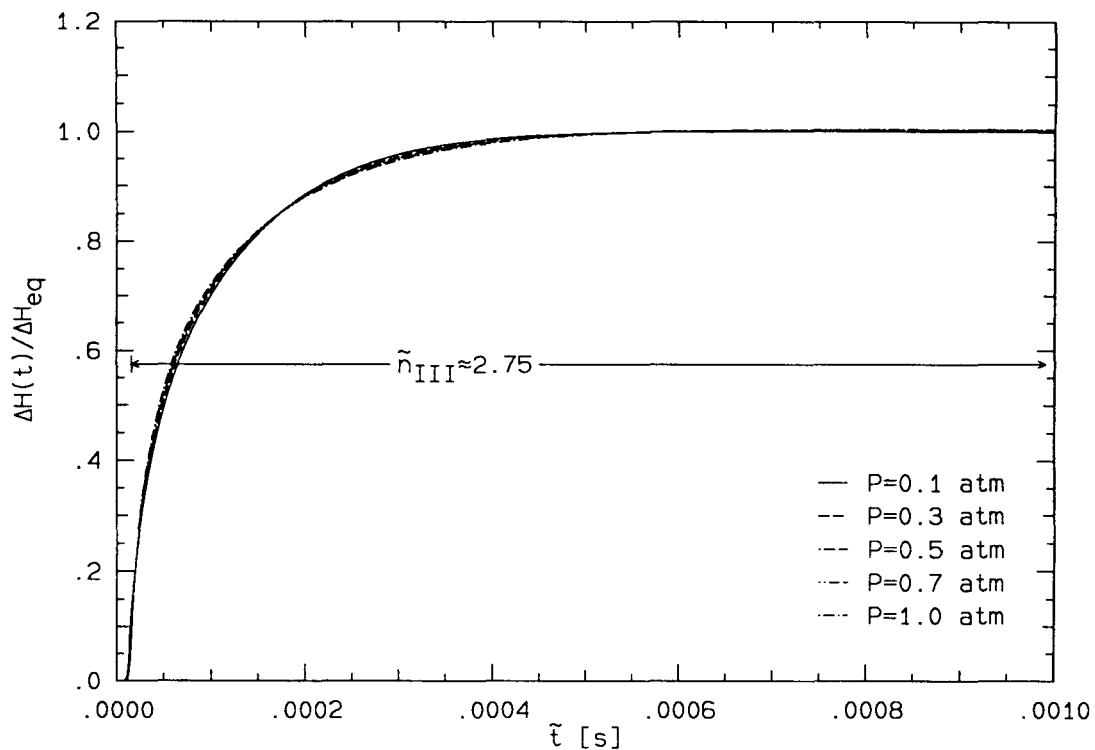


FIG. 4.5.8 Heat release verses scaled time.

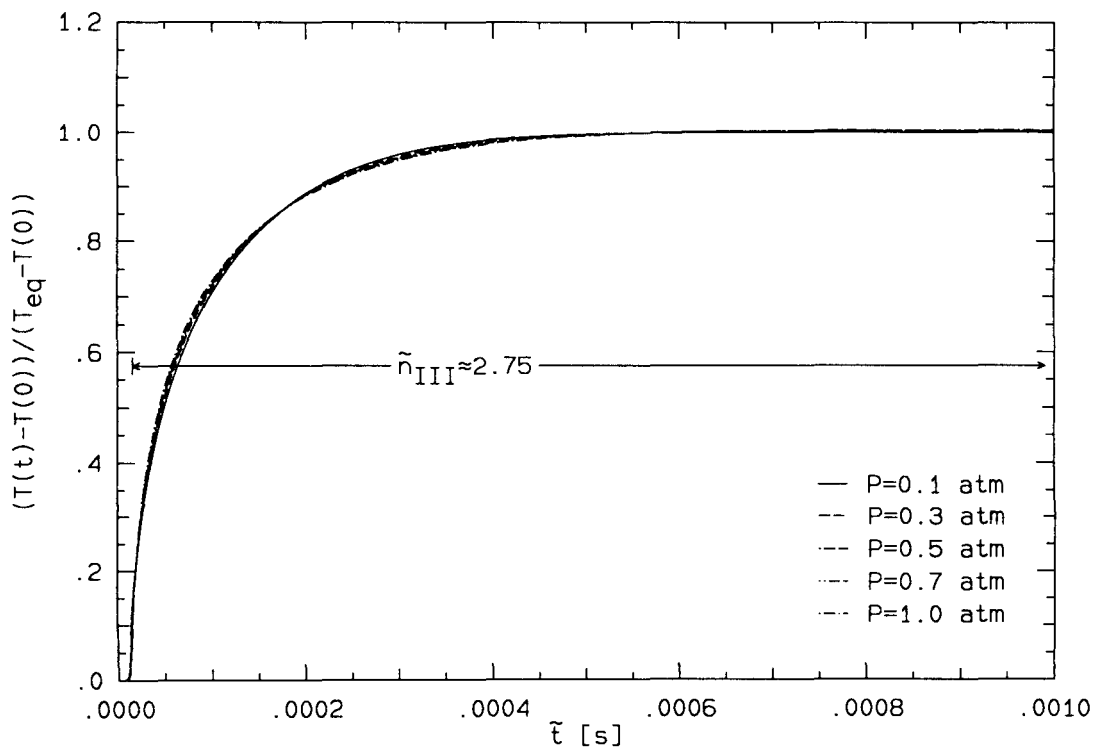


FIG. 4.5.9 Temperature verses scaled time.

4.6 Discussion

The effects of equivalence ratio, initial or combustor inlet temperature and combustor pressure have been studied about the reference conditions. The results are quantified based on the evolution of the chemical heat release: the time required to reach the fast-rise, the rate of rise, the time required to reach a fixed percentage of the equilibrium level and the total amount of heat release at equilibrium. For the equivalence ratio, progress of combustion is found to be the fastest near a ratio of 1.2. Any higher or lower values would result in slower reactions. On the other hand, the total heat release per unit mass of fuel initially added is higher at lower equivalence ratios.

The effect of initial temperature is found to be the strongest, especially on the time required to reach the fast-rise. At temperatures above approximately 1000 K , the chemistry evolves as if only a small group of reactions is present initially; that is, the rate of progress increases according to the temperature dependence of the rate coefficients of those reactions. At temperatures below approximately 900 K , this is no longer true and the progress rate decreases much faster than can be predicted by the temperature dependence of any one group of reaction. In other words, the entire set of reaction steps is important and the choice of the reaction set is crucial at low temperature. The rate of rise, however, is only slightly affected by the initial temperature.

The major effect of different combustor pressures is to alter the span of the start-up stage, the fast-rise stage and the eventual approach towards equilibrium. These durations are found to be proportional to the pressure raised to certain powers. In addition, the evolution due to different pressure can be made similar by transforming the time coordinate in each stage according to the corresponding power.

Although the cases studied in this chapter include wide ranges of equivalence ratio, initial temperature and combustor pressure, one quantity is found to remain nearly unaltered in all the cases. The explosion time, or the duration of fast-rise, defined by the time from the initial start-up to the inflexion point on the chemical heat release is found to be of $\mathcal{O}(10^{-5})\text{ sec}$ regardless of equivalence ratio, initial temperature and combustor pressure. This may be deduced from the results in tables 4.3.1, 4.4.1a and b, and 4.5.1. The implication is that the most important factor hindering the hydrogen-air combustion is the start-up time.

When applied to the performance of an aircraft engine, some of the results suggest that the combustion of hydrogen and air may be seriously inhibited under certain conditions.

These include a combustor inlet temperature of less than $\sim 900\text{ K}$ or a combustor pressure of less than $\sim 0.3\text{ atm}$ at which no appreciable chemical change can occur within a combustor residence time of $\mathcal{O}(10^{-3})\text{ sec}$. The same adverse effect can be caused by equivalence ratios very much greater than one or close to zero. But these ratios are rarely encountered unless the fuel and the air are very poorly mixed. The situations involving low temperature and low pressure, however, may occur more often. For example, insufficient compression at the diffuser and low flight Mach number can result in one or both of the situations. Among the two, low inlet temperature must be avoided since the effect is more drastic. For this reason, methods for improving the combustor performance at low temperature are investigated in the following chapter.

CHAPTER 5

Finite-Rate Chemical Reaction in a Combustor

Part III: Special Combustor Conditions

5.1 Introduction

There are several possible methods for improving combustion rate at low initial temperature. Two parameters which have been fixed in the previous calculations include the initial composition and the combustor pressure profile. The former was assumed to contain pure hydrogen (H_2) and air (N_2 , O_2 , etc.) while the latter was assumed to be constant. The combustor end conditions may not be very sensitive to these assumptions for any inlet temperature over 900 K ; but this may not be true at lower temperatures. The effects obtained by altering these parameters are analyzed in this chapter. Of particular interest is the case of inlet temperature equals 850 K studied previously. Higher temperature cases are also considered to allow comparison.

The importance of initial composition is suggested in sections 4.4 and 4.5. Variation of initial temperature shows that the combustion of hydrogen and air is suddenly accelerated when certain radicals have reached some critical mole fractions. Variation of combustor pressure support the same conclusion. The example of pressure scaling of mole fraction indicates that certain radicals can have the same mole fraction at start-up independent of the combustor pressure. Therefore, the introduction of some radicals in the initial mixture may reduce the start-up delay.

On the other hand, instead of using a constant combustor pressure, a time varying pressure may be imposed. Fluctuating pressure may be introduced in a combustor through non-uniform fuel-air mixing or small disturbance in the flow. In fact, pressure fluctuation is forced in the combustor flow according to a particular combustor design. It has been proposed that fuel-air mixing in the NASP engine be furnished by a series of oblique shocks* at the combustor inlet. Such a design has been studied experimentally and computationally by researchers**. The effect of fluctuating pressure may alter the behavior of a chemical

* Dr. Marble , JPC, Caltech.

** For example, see Waitz^[15] and Yang^[17].

reaction by changing the temperature and the reactant collision frequency. The result of this analysis, however, should not be viewed as the behavior of a one-dimensional combustor but instead the behavior of hydrogen-air reaction under fluctuating pressure. It is clear from equation 3.3.1 that the one-dimensional flow assumption is no longer valid when the pressure is not a constant.

5.2 Hydrogen Radical in Initial Composition

The study of the effect of initial temperature on the start-up time in section 4.4 suggests the possible role of some radicals in initiating the explosive reaction during fast-rise. The data shown in figure 4.4.3b indicate that some radicals has nearly the same mole fraction at the start-up point over a range of initial temperatures. These radicals include O, OH, H and possibly HO₂. In the parametric study of chapter 4, their compositions are zero initially and they are slowly accumulated during the start-up stage. Therefore, a reduction in the start-up time may be achieved by introducing sufficient amount of those radicals into the initial mixture. This has been tested with the four radicals; H is found to produce the most significant effect.

The amount of H added initially is taken as a multiple of the mole fraction of H found at the start-up time of the case:

$$\left\{ \begin{array}{l} \phi = 1.0 \\ P = 0.5 \text{ atm} . \\ T_0 = 850 \text{ K} \end{array} \right.$$

In that case, the initial mole fraction of H is zero, but at the start-up point,

$$\left\{ \begin{array}{l} X_{0H}(t_{s0}) \simeq 5.2343 \times 10^{-2} , \quad \text{where} \\ t_{s0} = 0.693613 \text{ s} . \end{array} \right.$$

A subscript '0' is used to indicate the reference values. In this way, the mole fraction of H to be added initially is

$$X_H(t = 0) = R_H X_{0H}(t_{s0}) ,$$

where R_H is the multiplicative factor. Calculations are conducted for fourteen values of R_H in the range:

$$1.35 \times 10^{-6} \leq R_H \leq 4.04 \times 10^{-1} .$$

In the calculations, the initial amount of H_2 is adjusted so that H_2 and H together constitute an equivalence ratio of 1.0. The start-up time in each case is measured (*c.f.* section 4.1) and normalized by the reference value t_{s0} . The result is plotted in figure 5.2.1a verse R_H . As a large reduction in the start-up time is achieved, the ratio t_s/t_{s0} is plotted in a logarithmic scale.

Figure 5.2.1a shows that the reduction begins at very low value of R_H . To see this, part of the figure is expanded and plotted in figure 5.2.1b. It shows that a noticeable reduction begins when the initial amount of H is approximately 3×10^{-4} times $X_{0H}(t_{s0})$ and a 1000 times reduction in t_s has already been achieved when $X_H(t=0)$ is approximately 5.5×10^{-4} times $X_{0H}(t_{s0})$. However, any subsequent increase in $X_H(t=0)$ only improves the start-up time by a small percentage.

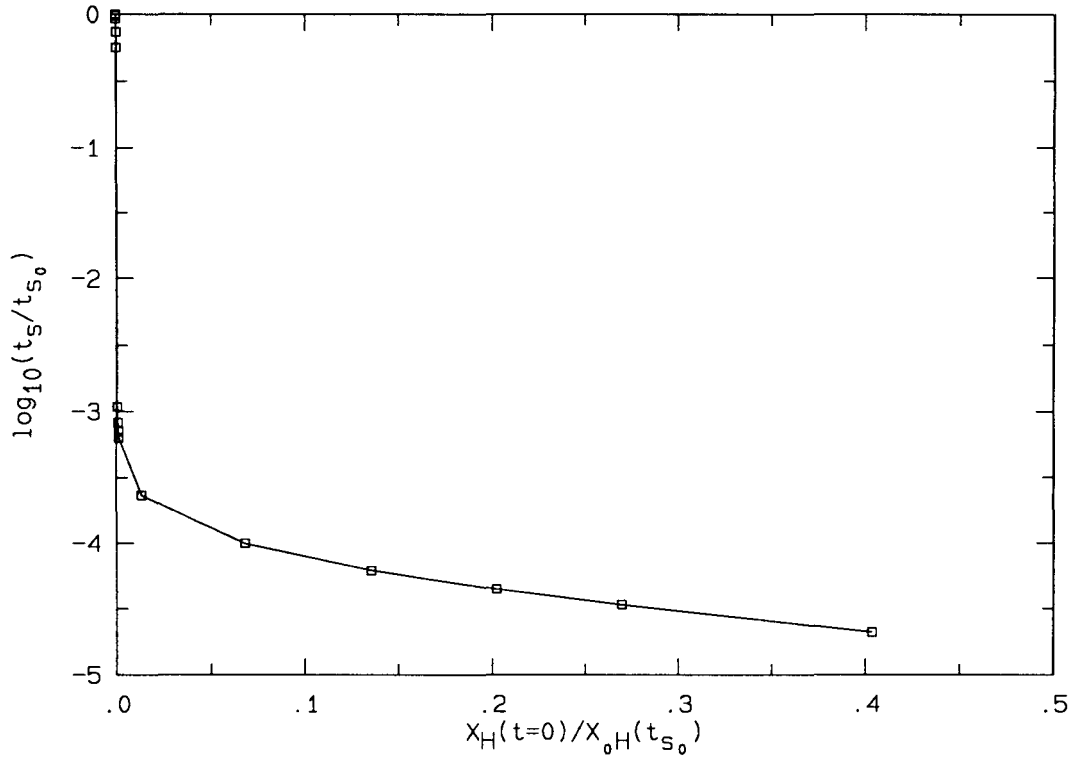


FIG. 5.2.1a Reduction in start-up time from the addition of $X_H(t=0)$.

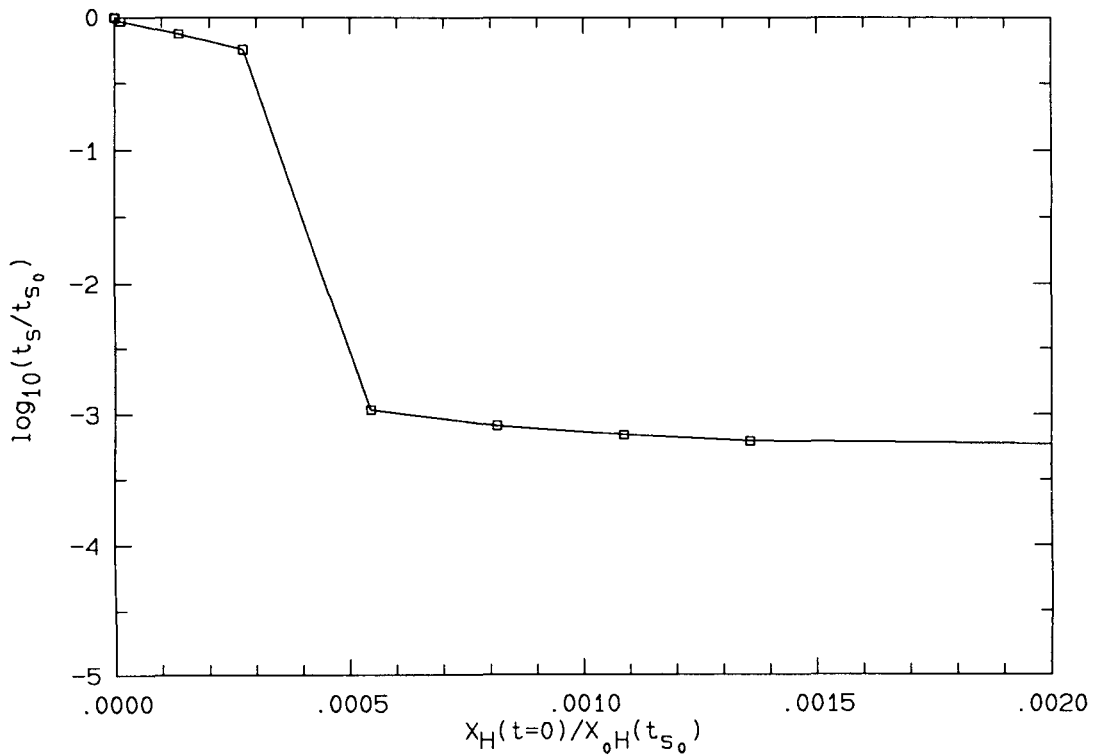


FIG. 5.2.1b Reduction in start-up time for very small amount of $X_H(t=0)$.

5.3 Fluctuating Pressure Boundary Condition

The governing equations derived in chapter 2 for a static homogeneous medium can be applied in this case. They have been summarized in section 2.4. Unlike the one-dimensional combustor calculation where pressure is constant, a fluctuating pressure would have a non-zero contribution to the energy conservation in equation 2.4.2. Again assume that the system is closed and there is no external heat addition. The governing equations are:

$$\frac{dY_k}{dt} = \frac{m_k}{\rho} \dot{\omega}_k \quad \text{for } k = 1, K, \quad (5.3.1)$$

$$\sum_{k=1}^K h_k \frac{dY_k}{dt} + \bar{C}_p \frac{dT}{dt} - \frac{1}{\rho} \frac{dP}{dt} = 0, \quad (5.3.2)$$

and for a mixture of perfect gas,

$$P = \rho \frac{R_u}{\bar{m}} T. \quad (5.3.3)$$

The chemical production rate $\dot{\omega}_k$ is given by equation 2.4.4. Other quantities such as \bar{m} and \bar{C}_p are also defined in chapter 2. The fluctuating pressure is to be represented by a sinusoidal function of the form:

$$P(t) = P_{\text{avg}} + P_{\text{amp}} \sin(2\pi f t), \quad (5.3.4)$$

where P_{avg} is the average pressure and P_{amp} is the amplitude of fluctuation. The frequency of fluctuation is given by f in Hz .

The amplitude of fluctuation is found to be of much lesser effect than the frequency. Therefore, only the results of the frequency study are to be shown. The pressure function in equation 5.3.4 is imposed in five cases of initial temperatures from $850 K$ to $1500 K$. The equivalence ratio is fixed at 1.0 while P_{avg} and P_{amp} are fixed at $0.5 atm$ and $0.1 atm$ respectively. A positive amplitude is used so that the function begins with a rising cycle at t equals zero. The frequency relevant in each case is of $\mathcal{O}(1/t_{s0})$ where t_{s0} is the start-up time when either P_{amp} or f is zero. A number of frequencies are used for each initial temperature, resulting in the plot of figure 5.3.1. The x -axis is the dimensionless quantity $f t_{s0}$. This represents the number of cycles that can be fitted into the duration of the *original* start-up time, t_{s0} . The y -axis represents the fractional reduction in the start-up time given by t_s/t_{s0} . It is plotted in a logarithmic scale.

The result shows that a large reduction is only achieved in the two low initial temperature cases ($850 K$ and $900 K$). The number of cycles that may be fitted in the original t_{s0} is of $\mathcal{O}(10)$ while there is a factor of ~ 30 in the reduction. For the three higher temperature cases, the maximum improvement always occurs near $f t_{s0}$ equals 0.5. The reduction factor, however, is only ~ 3 .

In addition to the start-up time, the response of a chemical species to fluctuating pressure is also studied. In view of the previous finding, the response of radicals are of particular interest. The case of an initial temperature of 850 K and frequency of 10 Hz is to be discussed. The pressure profile is plotted in figure 5.3.2 versus a normalized time defined by ft (*i.e.* the number of cycles). Only one cycle is shown because the start-up has been found to occur within half a cycle.[†] The evolution of Y_{H} , Y_{H_2} , Y_{OH} and $Y_{\text{H}_2\text{O}}$ are shown respectively in figures 5.3.3, 5.3.4, 5.3.5 and 5.3.6 over the same time scale. The initial fractions of the radicals are very small and the relationship between their generation and pressure fluctuation cannot be detected. This is not surprising since the previous section has shown that the generation of a small amount of H ($X_{\text{H}} \sim 3 \times 10^{-5}$) is sufficient to reduce the start-up time by a large factor. The relationship is much clearer following the fast-rise or in the second half of the pressure cycle. The species response to the fluctuation by relaxing toward the appropriate equilibrium. The interesting behavior is that the composition of H, OH, H_2 falls during pressure drop while the amount of H_2O increase. The opposite happens when the pressure rises in the last quarter of the cycle. This result suggests that more H_2O , and hence chemical energy, may be extracted from a near equilibrium hydrogen-air mixture by lowering the pressure. A similar situation is found when the combustor product is passed into an expanding nozzle. This is to be studied in chapters 7 and 8 following the formulation of a two-dimensional reacting nozzle model.

[†] Approximately 7 cycles can be fitted in the original start-up time t_{s0} .

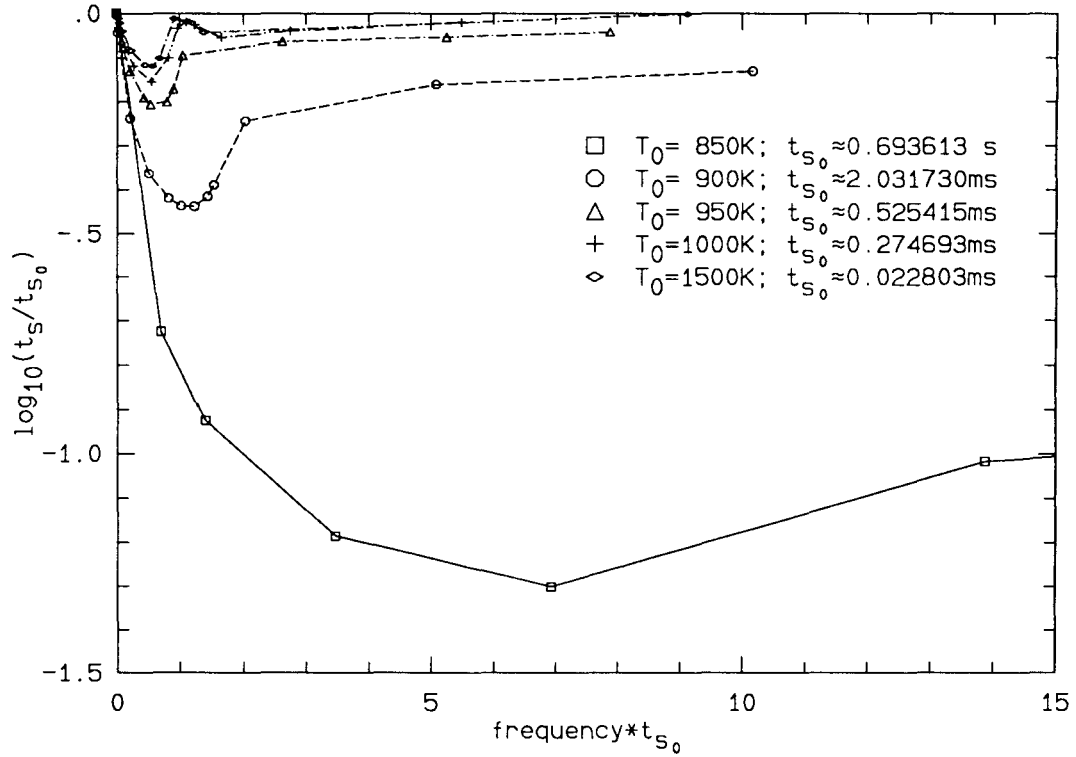


FIG. 5.3.1 Reduction in start-up time from fluctuating pressure for 5 initial temperatures.

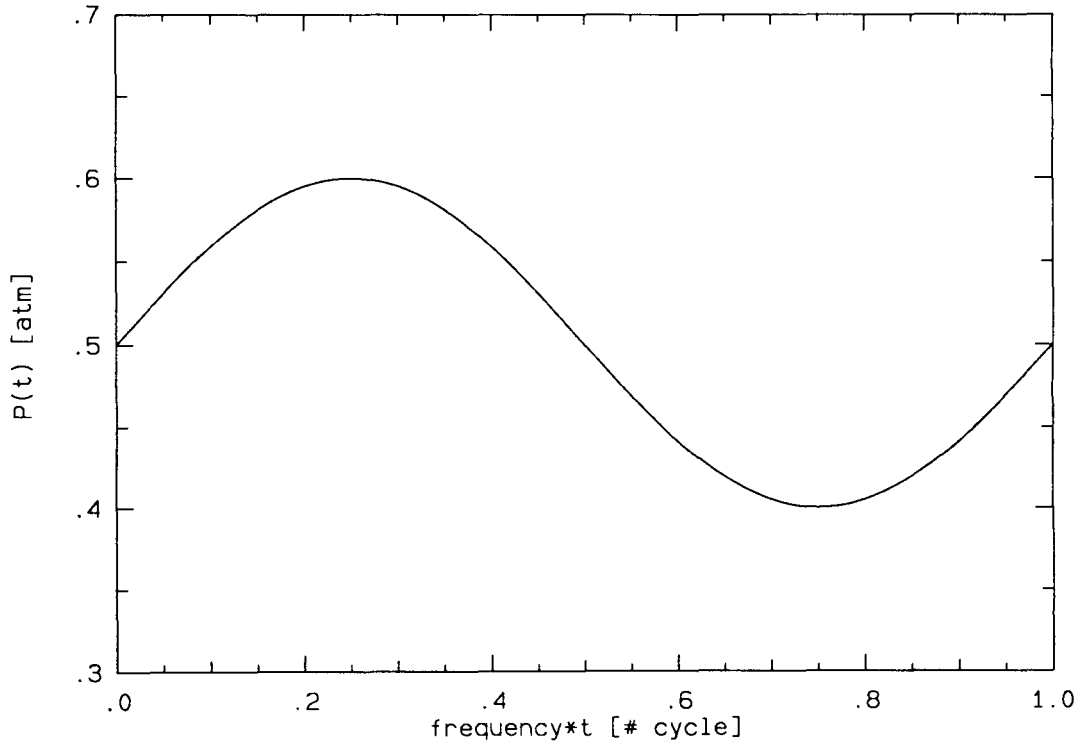


FIG. 5.3.2 Fluctuating pressure profile for a frequency of 10 Hz.

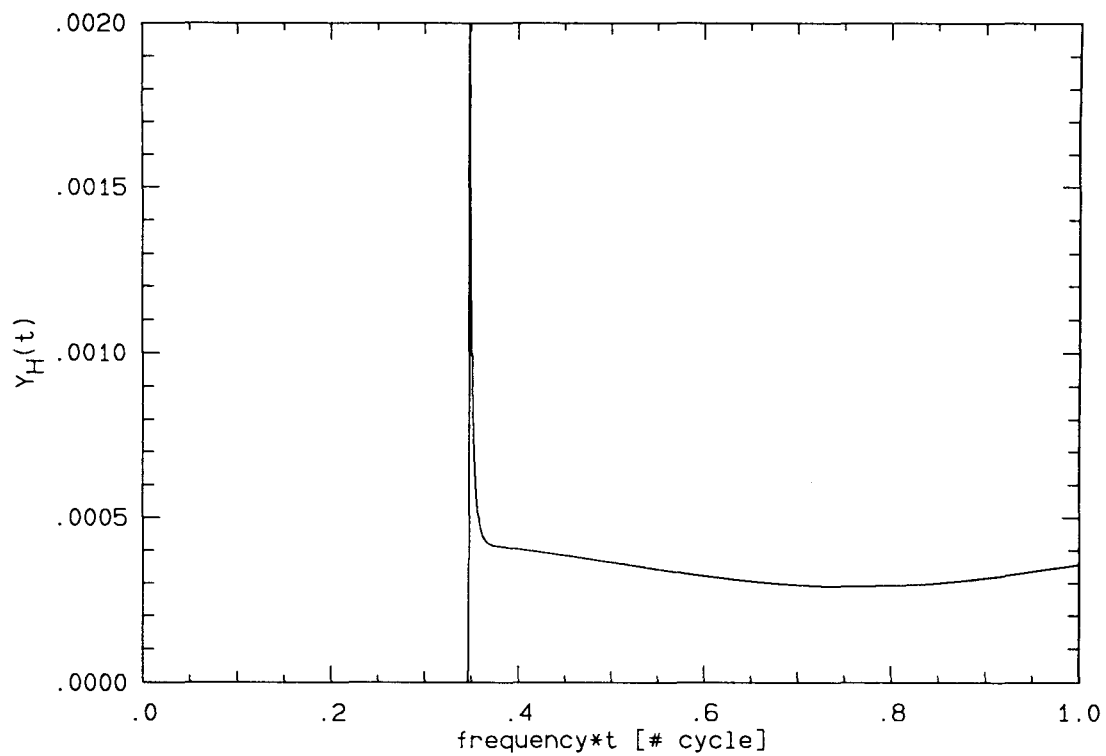
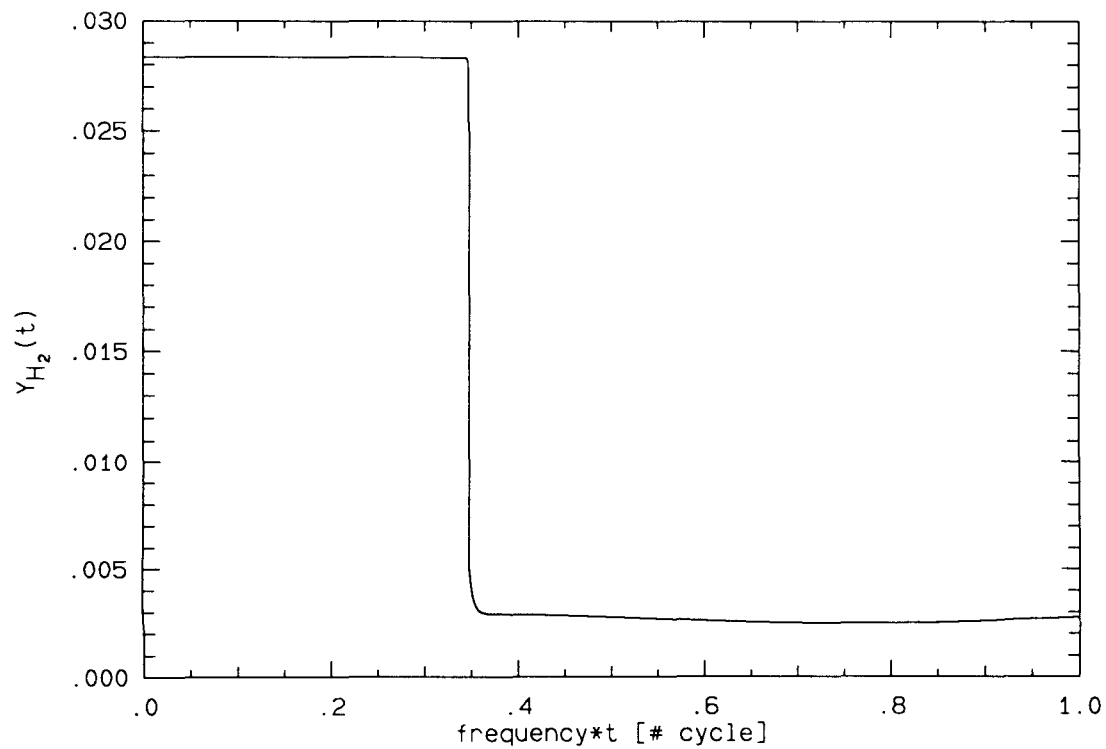


FIG. 5.3.3 Mass fraction of H in one pressure cycle.

FIG. 5.3.4 Mass fraction of H_2 in one pressure cycle.

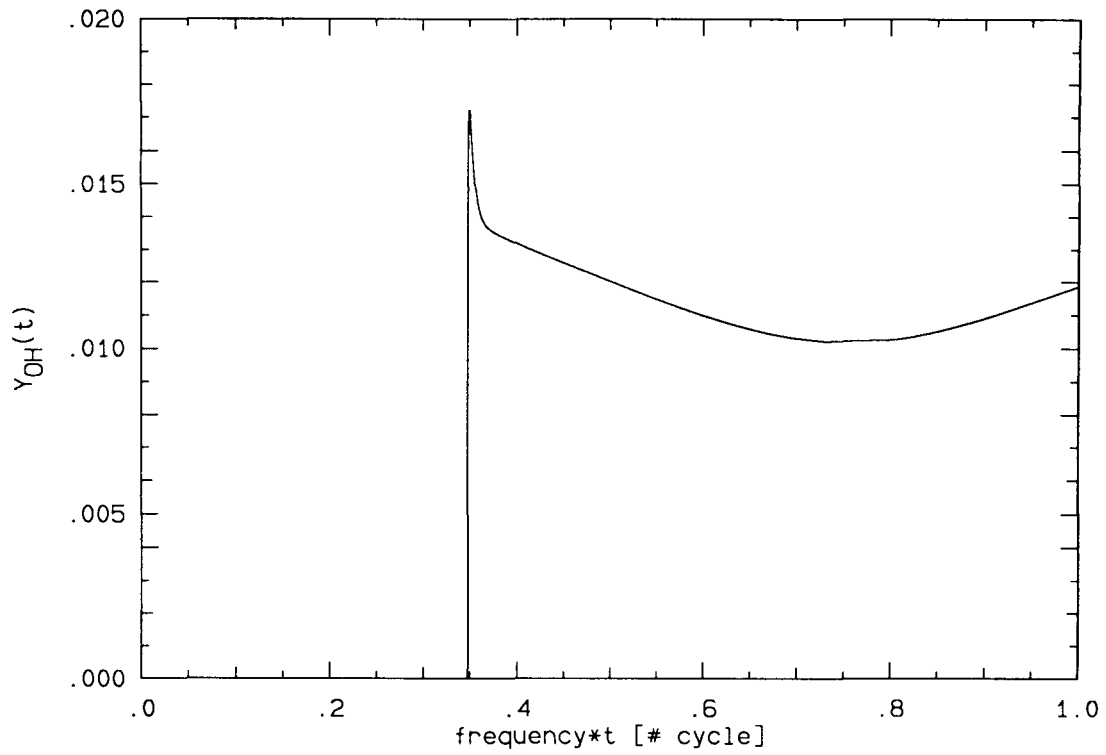
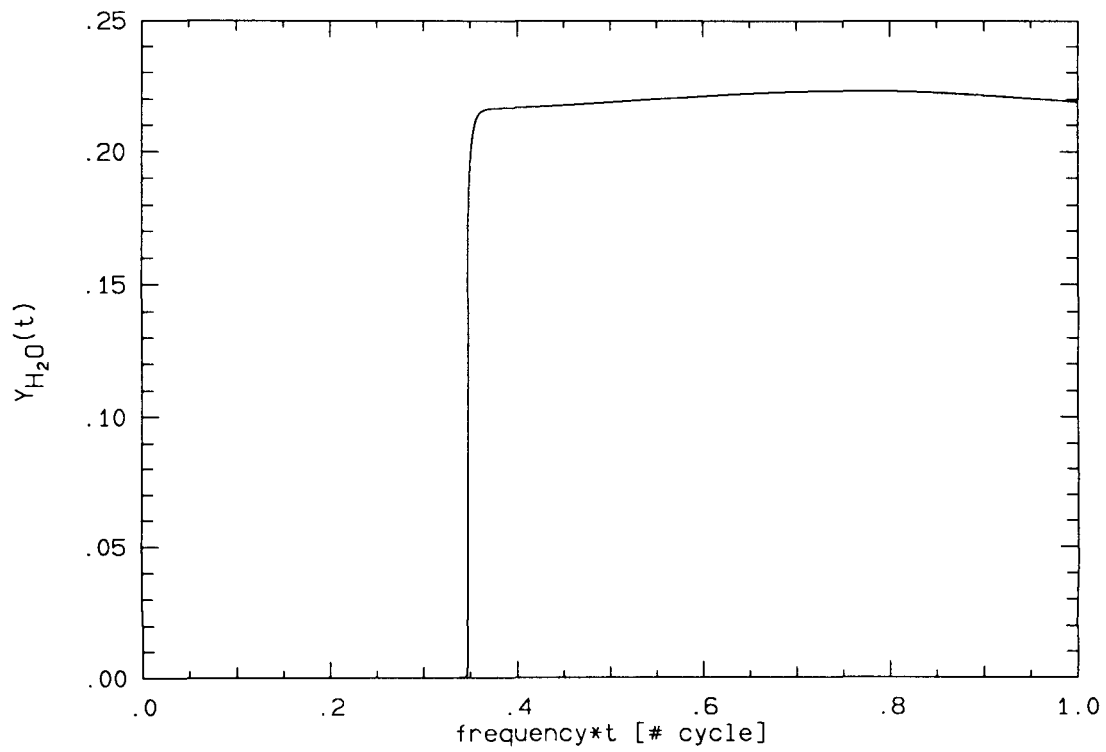
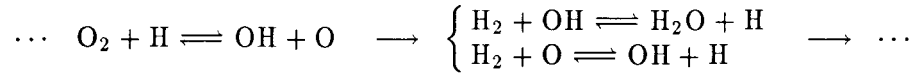


FIG. 5.3.5 Mass fraction of OH in one pressure cycle.

FIG. 5.3.6 Mass fraction of H₂O in one pressure cycle.

5.4 Explanation

To understand the exact kinetics underlying the observed responses would involve analyses similar to those presented in chapter 4. Nevertheless, some simple explanations can be suggested without going into much depth. The role of H in the branched chain cycle



has been noted in section 4.4.2. For every H radical consumed in the chain reaction, two are produced. Therefore, a small amount of H may be sufficient to start the chain. For the fluctuating pressure, if the rise in pressure is timed such that an increase in temperature and an increase in concentration of a certain rate determining species are nearly synchronized, that chemical process is enhanced. It is also true that a chemical process can be enhanced by suppressing some of the competing processes which produce a temperature drop and a reduction in their reactant concentrations.

CHAPTER 6

Reacting Flow in a Two-Dimensional Expansion Nozzle

Part I: Formulation

6.1 Background

In order to design an efficient propulsion system for the hypersonic NASP, major components of the system are being studied by separate research groups. The three-component propulsion system described in chapter 3 is usually adopted as most of the design requirements are not yet well specified. A crude diffuser model has been described in Appendix II. A one-dimensional combustor model has been studied and analyzed extensively in chapter 3 to 5. Focus of this chapter is on the last component, the afterbody expansion nozzle. Emphasis is again on the chemical processes, their response under expansion and their effect on the expanding flow. The key feature to be analyzed is the phenomenon of *freezing*.

Although the behavior of hydrogen-air combustion under various conditions has been analyzed thoroughly, direct application of those results to the reacting nozzle flow problem is limited and a separate analysis must be conducted. The previous calculations were one-dimensional and at constant pressure. Fluctuating pressures as sinusoidal functions of time were briefly studied with some interesting results. But in either case, pressure was treated as a parameter — a forcing function or boundary condition which was independent of the chemical reactions. The transport problem was decoupled from the reacting system and was not considered in those calculations. These conditions certainly are not valid in the nozzle since the nature of the flow as well as the pressure distribution have direct bearing on the performance of the engine. The relationship and the *coupled* effect between the chemical processes and the other physical parameters are crucial in this context.

To model the nozzle problem requires at least a two-dimensional environment. Since the emphasis of this study is on the chemistry rather than on the flow, a two-dimensional nozzle is sufficient. Besides, it is more difficult to analyze the interaction in a three-dimensional environment due to the higher complicity in the flow. The boundary conditions describe the constraints on the dependent variables along the nozzle walls. A common practice in an *analysis problem* is to replace the boundary conditions on pressure by the geometry of

the walls. In this case, the boundary conditions become *static*. The case where a boundary constraint on pressure is specified constitutes a *design problem*; it is useful in determining optimal nozzle geometry. Although the two problems are governed by the same equation set, to solve the problems require very different formulations. It is sufficient in this preliminary analysis to use the static boundary conditions; in other words, geometry of the nozzle will be specified in each calculation.

Some physical constraints and conditions must be known in order to complete the nozzle model. First of all, there are constraints on species diffusion, thermo-conduction, viscous stress, gravity force, heat addition, and so on which must be set appropriately. Then there are inlet conditions, boundary conditions and, possibly, exit conditions. Most of the constraints can be set according to the NASP flight condition and some commonplace assumptions. Other conditions can be closely estimated or approximated. For example, the inlet conditions can be estimated from the previous combustor calculations, rigid heat insulating nozzle walls can be assumed*, and the necessity of exit conditions can be eliminated by imposing a strictly supersonic and shock-free flow. A more complete set of assumptions together with their foundations are described in the following section.

6.2 Model

Some of the essential features in the nozzle model have just been outlined. These include a two-dimensional environment and a nozzle of known geometry; the chemistry and the expanding nature of the flow are also to be represented accurately. The assumptions that follow are constructed based on these requirements and some knowledge about the vehicle. Also taken into account is the computational efficiency which is often compromised by the accuracy of the model.

A major assumption incorporated in the current model is that the flow be steady. In other words, the inlet conditions as well as the boundary conditions are constant in time. The quantities of interest in the steady problem become the spatial distributions of all the dependent variables. The unsteady problem is of course a more accurate representation of the flow in a real nozzle. Unsteadiness and disturbances in the components upstream of the nozzle is extremely common. For example, nonuniform fuel-air mixing in the combustor may result in a pressure wave and fluctuating chemical composition propagating into the nozzle.

* The nozzle wall is essentially the outer limit of a boundary layer where heat conduction is negligible, *c.f.* section 6.2.

Turbulence is another major concern. The flow field due to such time dependent conditions may produce very different nozzle performances compared to the steady calculation. But the difficulty in formulating an unsteady problem is far greater especially in numerical sense due to the involvement of possible shock and flow instability.

Other simplifications are made based on a cruising flight condition for the vehicle. According to a free stream Mach number range of 15 to 25 at a moderate flight altitude, the speed at the nozzle inlet would still be of the order 10^3 m/s. The kinematic viscosity of a hydrogen-air combustion product is of the order 10^{-4} m²/s.** The Reynold's number would then be of the order 10^7 based on a nozzle height of approximately one meter. The effect of viscosity can therefore be ignored since the inertial force is much bigger than the viscid force. This is a good approximation in the main body of the flow, but the effect of boundary layer at the nozzle wall is lost. In a general problem, the full solution is obtained by matching the inviscid solution with the appropriate boundary layer solution at the boundary layer edge. The flow calculated in the present model therefore constitutes only part of the solution — that of flow bounded by the edges of the boundary layers along the nozzle walls. The actual wall geometry corresponding to each calculation can be estimated using the boundary layer thickness deduced from the inviscid solution at the matching line.

The assumption of an inviscid flow also implies that species diffusion and heat conduction can be neglected in the main body of the flow. This is because the effects of diffusion and thermal conduction are of the same order as viscosity provided that the flow is not highly ionized. The mobility of free electron in an ionized gas is much larger than ordinary atomic or molecular species; consequently, diffusion and conduction must be included even though viscosity can be ignored. The hydrogen-air system in the nozzle is not expected to encounter much ionic interactions and hence they are not included in this calculation.

The pictorial description of the current nozzle closely resembles that of figure 2.2.1b. It is reproduced in figure 6.2.1 with some minor changes. While the evolution of a particle along its path is not affected by the particles evolving along neighbouring paths in a one-dimensional problem, they are inter-dependent in the two-dimensional nozzle. But steadiness allows each variable to be specified by the spatial coordinates only and the particle paths to be replaced by the streamlines.

The basic assumptions made in the nozzle model are summarized as follows:

** Although the coefficient of viscosity increases with temperature, the kinematic viscosity decreases. The stated value was estimated for ~ 1000 K.

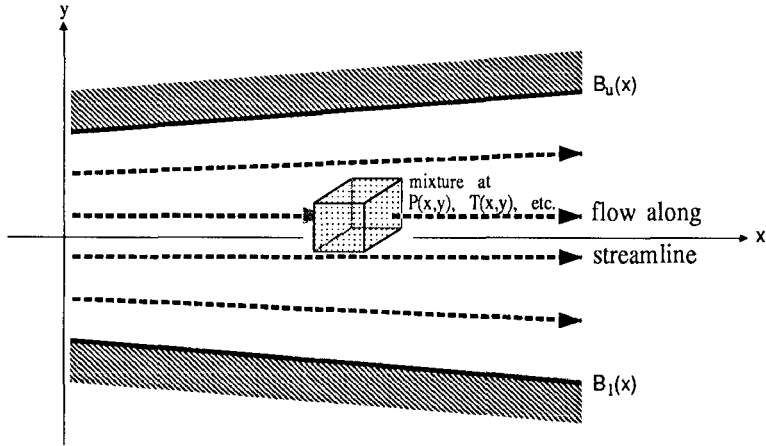


FIG. 6.2.1 Two-dimensional nozzle model

- i. Flow is steady,
- ii. Diffusive and conductive time scales are large compared to that of convection.
- iii. Viscosity can be ignored.
- iv. Body force is negligible.
- v. State equation is that for a mixture of *perfect* gas.
- vi. Geometry of nozzle wall is known.
- vii. Nozzle wall is rigid and non-porous.

The first five items are directly related to the governing equations while the last two are constraints on the boundary conditions. The resulting expressions and conditions after their application are described shortly.

6.3 Multi-Component Flow Problem

The equations are best written in terms of the x - y Cartesian coordinates.[†] The x -coordinate is used for the longitudinal streamwise direction while the y -coordinate is used for the lateral cross-stream direction. Since the problem is steady, all dependent variables are inherently functions of x and y only. Vectors are often used in the derivation. When individual components are involved, they are indicated by the subscript x or y . Other indices usually denote the different chemical species. The partial derivatives will be written explicitly to prevent confusion.

[†] As a two-dimensional system is considered, extension to a three-dimensional system is very simple in the rectangular coordinates.

Recall that there are three types of equation governing the evolution of a static system (*c.f.* section 3.3). They are the rate equation, the state equation and the energy equation. The conservation of mass is implicit through the use of fractional composition and need not be considered independently. In the reacting nozzle *flow* problem, the flux must be considered and mass conservation is not implicit even with the use of fractional composition. Momentum conservation must also be considered to comply with the law of motion. A detailed account of these equations is given by Kuo^[9]; but with the assumptions made in this model, the reduced equations are very similar to those of a single-component system. Their derivation is therefore not included. An exception is the rate equation which describes the evolution of the individual chemical species. A brief discussion is given in the following section for this purpose.

6.3.1 Rate equation

The molar production rate of a species due to chemical reactions was derived in section 2.3.2 for a static system. The same result remains valid in the dynamical case because the chemical production rate is a point function of temperature, pressure and composition and is not altered by the dynamical state. The result according to section 2.3.2. is:

$$\dot{\omega}_k = \sum_{i=1}^I (\nu''_{ki} - \nu'_{ki}) \left(\sum_{j=1}^K \alpha_{ji} C_j \right) \left[k_{ji} \prod_{j=1}^K C_j^{\nu'_{ji}} - k_{ri} \prod_{j=1}^K C_j^{\nu''_{ji}} \right] \quad \text{for } k = 1, K, \quad (6.3.1.1)$$

where $\dot{\omega}_k^\ddagger$ is the molar production rate of the k^{th} species per unit time. A total of K species and I reactions are assumed in the expression. Taking into account the flux of each species, the conservation of a species implies that

$$\frac{\partial}{\partial x} (\rho Y_k u_x) + \frac{\partial}{\partial y} (\rho Y_k u_y) = m_k \dot{\omega}_k \quad \text{for } k = 1, K. \quad (6.3.1.2)$$

These are the *continuity* equations for a multi-component system. *Mass fraction* is chosen to represent species composition as mass conservation is concerned. While the diffusion velocity has been neglected, all species translate with the same velocity \mathbf{u} .

The former expression can also be viewed as the governing equation for the individual mass fraction. But a more explicit expression in Y_k can be obtained by noting that

$$\sum_{k=1}^K m_k \dot{\omega}_k \equiv 0 \quad \text{for all } (x, y)$$

‡ See section 2.3 for explanations on the symbols in equation 6.3.1.1.

since no net mass shall be created nor destroyed due to chemical reactions. Summing equation 6.3.1.2 over k and making use of the last condition results in the more transparent continuity equation of a mixture:

$$\frac{\partial}{\partial x}(\rho u_x) + \frac{\partial}{\partial y}(\rho u_y) = 0 .$$

Multiplying this equation by Y_k and subtracting from equation 6.3.1.2 give the desired rate equation in terms of Y_k :

$$\rho \left(u_x \frac{\partial Y_k}{\partial x} + u_y \frac{\partial Y_k}{\partial y} \right) = m_k \dot{\omega}_k \quad \text{for } k = 1, K . \quad (6.3.1.3)$$

6.3.2 State equation

Besides the species composition which must be considered individually, other dependent variables in the problem are average quantities. These include the state variables pressure, temperature and density. Their relationship is given by

$$P = \rho \frac{R_u}{\bar{m}} T , \quad (6.3.2)$$

which is the state equation for a mixture of perfect gas. The average molar mass, \bar{m} , is a function of the composition, namely,

$$\bar{m} = \frac{1}{\sum_{k=1}^K \frac{Y_k}{m_k}} .$$

6.3.3 Continuity equation

The continuity equation describes the conservation requirement on the mass density. It was obtained when the rate equation for Y_k was derived. The result is restated here:

$$\frac{\partial}{\partial x}(\rho u_x) + \frac{\partial}{\partial y}(\rho u_y) = 0 . \quad (6.3.3)$$

6.3.4 Momentum equations

Without any viscous stresses or body forces, the momentum equation only involves the balance between momentum flux and pressure gradient:

$$\rho \left(u_x \frac{\partial u_x}{\partial x} + u_y \frac{\partial u_x}{\partial y} \right) = -\frac{\partial P}{\partial x} \quad (6.3.4a)$$

and

$$\rho \left(u_x \frac{\partial u_y}{\partial x} + u_y \frac{\partial u_y}{\partial y} \right) = -\frac{\partial P}{\partial y} \quad (6.3.4b)$$

in the x and y directions respectively. Note that these equations are again transparent to the multi-component aspect of the problem.

6.3.5 Energy equation

The conservation of energy must take into account the existence of chemical reaction. This is accomplished by taking

$$h_k(T) = \int_{T_r}^T C_{pk}(T) dT + \Delta h_{f,k}^r$$

such that the chemical energy or the heat of formation $\Delta h_{f,k}^r$ is included in the enthalpy. This definition also conforms with the enthalpy tabulated in most thermodynamic data bases which include the JANAF tables. Let

$$\bar{h} = \sum_{k=1}^K h_k Y_k$$

be the specific enthalpy for the mixture, then the energy equation in terms of \bar{h} is

$$\rho \left(u_x \frac{\partial \bar{h}}{\partial x} + u_y \frac{\partial \bar{h}}{\partial y} \right) = u_x \frac{\partial P}{\partial x} + u_y \frac{\partial P}{\partial y} . \quad (6.3.5)$$

Equations 6.3.1.3, 6.3.2, 6.3.3, 6.3.4a, 6.3.4b and 6.3.5 comprise the governing set. These are $K + 5$ equations for the variable set

$$(Y_k, P, T, \rho, u_x, u_y)$$

which also contains $K + 5$ entries. Although more variables appear in the equations, some of them are interrelated. For example, the concentration C_j can be written in terms of Y_k and two state variables, the rate coefficients $k_{f,k}$ and $k_{r,k}$ are known functions of temperature, the average enthalpy \bar{h} depends on the composition and $h_k(T)$ which are also known functions[‡], . . . , and so on. Description of the problem is therefore complete.

[‡] They are fitted functions according to known thermodynamic data.

The remaining concern is on the boundary conditions. Since the nozzle problem is studied as a component of a supersonic RAMJET engine, it is reasonable to assume that the flow be *supersonic* throughout the domain at interest. If the possibility of shock is eliminated, the governing differential equations remain *hyperbolic* and *no* condition downstream of the nozzle (*e.g.* , at the exit) needs to be specified. This is because there are only three sets of supersonic characteristics* for this particular problem: the streamlines and Mach waves in two directions. Information is carried by the streamlines from upstream; therefore, the first boundary input can be specified by providing the values of the dependent variables at the inlet of the nozzle. Disturbance introduced by a fixed wall geometry (*analysis* problem) or pressure condition on a wall (*design* problem) is carried by a Mach wave into the flow. In other words, two additional boundary constraints are necessary to provide the information required by the two Mach waves. The last two items in the model assumptions constitute an analysis problem. The rigid and non-porous wall conditions require that flow be tangential to the wall; that is, the wall boundary is equivalent to a streamline or simply

$$\frac{u_y}{u_x} = \frac{dB}{dx} \quad (6.3.6)$$

along

$$y = B(x)$$

on each of the two walls where $B(x)$ is a *continuous* function describing the geometry of a solid wall. Since the diffusion terms and heat conduction terms have been neglected in the equations, they do not produce any extra boundary constraints.

6.4 Coordinate Transformation — the Von Mises transformation

In the governing set previously described, five of the equations, namely equations 6.3.1.3 and 6.3.3 through 6.3.5, are partial differential equations with respect to the independent variables x and y ; the remaining state equation is an algebraic relation only. A closer look at the former five equations reveals that the *substantial derivative* always appears on the left hand side:

$$u_x \frac{\partial}{\partial x} + u_y \frac{\partial}{\partial y} .$$

* See Vincenti^[14], section 14.

Even the boundary condition in equation 6.3.6 can be manipulated to this form. Therefore, the left hand side of the equations may be largely simplified if one of the coordinates is chosen to lie along the streamline. Such a transformation was introduced by Von Mises to transform the spatial coordinates into streamwise and streamfunction coordinates. Let the new coordinates be $\xi(x, y)$ and $\psi(x, y)$ respectively. The streamfunction ψ for a compressible fluid is defined by

$$\frac{\partial \psi}{\partial x} = -\frac{\rho}{\rho_0} u_y \quad (6.4.1a)$$

and

$$\frac{\partial \psi}{\partial y} = \frac{\rho}{\rho_0} u_x \quad (6.4.1b)$$

such that any line of constant ψ is tangential to the velocity vector. By construction, the continuity equation (6.3.3) is satisfied identically for any continuous function $\psi(x, y)$. With the appropriate boundary conditions on the streamfunction, say at a certain x -location, $\psi(x, y)$ is uniquely defined. The normalization constant ρ_0 is determined according to those conditions. Choice of the streamwise coordinate is not as critical. It is convenient to let

$$d\xi = dx \quad (6.4.2)$$

so that a constant ξ corresponds to a constant x . This is useful since a boundary input is the nozzle inlet conditions which are often specified at a constant x location.

While x and ξ are identical except by an additional constant, the transformation is invertible if y is a single value function in ψ . That is, the streamlines cannot turn backwards or the flow must be *unidirectional*. In this way,

$$(x, y) \longleftrightarrow (\xi, \psi)$$

and the partial derivatives with respect to x and y can be written in terms of ξ and ψ :

$$\begin{aligned} \frac{\partial}{\partial x} &= \frac{\partial \xi}{\partial x} \frac{\partial}{\partial \xi} + \frac{\partial \psi}{\partial x} \frac{\partial}{\partial \psi} \\ \frac{\partial}{\partial y} &= \frac{\partial \xi}{\partial y} \frac{\partial}{\partial \xi} + \frac{\partial \psi}{\partial y} \frac{\partial}{\partial \psi} \end{aligned} .$$

Using expressions 6.4.1a and 6.4.1b and noting that

$$\frac{\partial \xi}{\partial x} = 1 \quad \text{and} \quad \frac{\partial \xi}{\partial y} = 0 ,$$

the x - y derivatives are now given by

$$\begin{aligned} \frac{\partial}{\partial x} &= \frac{\partial}{\partial \xi} - \frac{\rho}{\rho_0} u_y \frac{\partial}{\partial \psi} \\ \frac{\partial}{\partial y} &= \frac{\rho}{\rho_0} u_x \frac{\partial}{\partial \psi} \end{aligned} \quad (6.4.3)$$

As intended, the substantial derivative is simplified to

$$u_x \frac{\partial}{\partial x} + u_y \frac{\partial}{\partial y} = u_x \frac{\partial}{\partial \xi} .$$

Transformation of the partial differential equations are now straight forward. These include the rate, continuity, momentum and energy equations. First consider the momentum equations in the new coordinates:

$$\frac{\partial u_x}{\partial \xi} = -\frac{1}{\rho u_x} \frac{\partial P}{\partial \xi} + \frac{1}{\rho_0} \frac{u_y}{u_x} \frac{\partial P}{\partial \psi} \quad (6.4.4a)$$

$$\frac{\partial u_y}{\partial \xi} = -\frac{1}{\rho_0} \frac{\partial P}{\partial \psi} \quad (6.4.4b)$$

which are obtained by applying equation 6.4.3 directly. Recall that the wall streamlines must be tangential to nozzle boundaries (*c.f.* equation 6.3.6) according to the fixed geometry assumption. The quantity under constraint is the ratio $\frac{u_y}{u_x}$ (or the flow angle) rather than the Cartesian velocity components. It is then more convenient to write the velocity vector in terms of its norm and direction. Let

$$\left\{ \begin{array}{l} q = |\mathbf{u}| = \sqrt{u_x^2 + u_y^2} \\ \tan \theta = \frac{u_y}{u_x}, \quad -\frac{\pi}{2} < \theta < \frac{\pi}{2} \end{array} \right.$$

such that

$$\left\{ \begin{array}{l} u_x = q \cos \theta \\ u_y = q \sin \theta . \end{array} \right.$$

Multiply equation 6.4.4b by u_y and add to 6.4.4a give

$$\frac{\partial q}{\partial \xi} = -\frac{1}{\rho q} \frac{\partial P}{\partial \xi} . \quad (6.4.5a)$$

Differentiating the expression for $\tan \theta$ with respect to ξ produces

$$\begin{aligned} \frac{1}{\cos^2 \theta} \frac{\partial \theta}{\partial \xi} &= \frac{\partial}{\partial \xi} \left(\frac{u_y}{u_x} \right) \\ &= \frac{1}{u_x} \left(\frac{\partial u_y}{\partial \xi} - \frac{u_y}{u_x} \frac{\partial u_x}{\partial \xi} \right) . \end{aligned}$$

The derivatives in the last parentheses can be eliminated using expressions 6.4.4a and 6.4.4b. The desired differential equation for θ is obtained after some simplification:

$$\frac{\partial \theta}{\partial \xi} = \frac{\tan \theta}{\rho q^2} \frac{\partial P}{\partial \xi} - \frac{1}{\rho_0 q \cos \theta} \frac{\partial P}{\partial \psi} . \quad (6.4.5b)$$

The rate equation is transformed in a similar manner:

$$\begin{aligned} \rho q \cos \theta \frac{\partial Y_k}{\partial \xi} &= m_k \dot{\omega}_k \\ \Rightarrow \frac{\partial Y_k}{\partial \xi} &= \frac{m_k \dot{\omega}_k}{\rho q \cos \theta} \quad \text{for } k = 1, K \end{aligned} \quad (6.4.6)$$

where $\dot{\omega}_k$ is given by equation 6.3.1.1. Direct transformation of the energy equation gives rise to an expression for the specific enthalpy \bar{h} :

$$\begin{aligned} \rho q \cos \theta \frac{\partial \bar{h}}{\partial \xi} &= q \cos \theta \frac{\partial P}{\partial \xi} \\ \Rightarrow \frac{\partial \bar{h}}{\partial \xi} &= \frac{1}{\rho} \frac{\partial P}{\partial \xi}. \end{aligned}$$

But \bar{h} is given by

$$\left\{ \begin{array}{l} \bar{h} = \sum_{k=1}^K h_k Y_k \quad \text{and} \\ h_k(T) = \int_{T_r}^T C_{pk}(T) dT + \Delta h_{fk}^r; \end{array} \right.$$

therefore,

$$\begin{aligned} \frac{\partial \bar{h}}{\partial \xi} &= \sum_{k=1}^K Y_k \frac{\partial h_k}{\partial \xi} + \sum_{k=1}^K h_k \frac{\partial Y_k}{\partial \xi} \\ &= \sum_{k=1}^K Y_k \frac{dh_k}{dT} \frac{\partial T}{\partial \xi} + \sum_{k=1}^K h_k \frac{\partial Y_k}{\partial \xi} \\ &= \sum_{k=1}^K Y_k C_{pk} \frac{\partial T}{\partial \xi} + \sum_{k=1}^K h_k \frac{\partial Y_k}{\partial \xi} \end{aligned}$$

and the energy equation becomes

$$\bar{C}_p \frac{\partial T}{\partial \xi} + \sum_{k=1}^K h_k \frac{\partial Y_k}{\partial \xi} = \frac{1}{\rho} \frac{\partial P}{\partial \xi}$$

where

$$\bar{C}_p \equiv \sum_{k=1}^K Y_k C_{pk}.$$

Substitution of the rate equation (6.4.6) gives

$$\frac{\partial T}{\partial \xi} = \frac{1}{\rho \bar{C}_p} \left(\frac{\partial P}{\partial \xi} - \frac{1}{q \cos \theta} \sum_{k=1}^K h_k m_k \dot{\omega}_k \right). \quad (6.4.7)$$

Finally, the continuity equation is considered. It results in an expression involving the derivative of ρ :

$$\frac{\partial}{\partial \xi}(\rho q \cos \theta) - \frac{\rho}{\rho_0} q \sin \theta \frac{\partial}{\partial \psi}(\rho q \cos \theta) + \frac{\rho}{\rho_0} q \cos \theta \frac{\partial}{\partial \psi}(\rho q \sin \theta) = 0 .$$

Breaking down the last two terms and simplifying give:

$$\begin{aligned} & \frac{\partial}{\partial \xi}(\rho q \cos \theta) + \frac{\rho}{\rho_0} \rho q^2 \frac{\partial \theta}{\partial \psi} = 0 \\ \Rightarrow & \frac{1}{\rho} \frac{\partial \rho}{\partial \xi} + \frac{1}{q} \frac{\partial q}{\partial \xi} - \tan \theta \frac{\partial \theta}{\partial \xi} + \frac{\rho}{\rho_0} \frac{q}{\cos \theta} \frac{\partial \theta}{\partial \psi} = 0 . \end{aligned} \quad (6.4.8)$$

Previously mentioned are $K + 4$ partial differential equations, namely equations 6.4.5a, 6.4.5b, 6.4.6, 6.4.7 and 6.4.8, involving the derivatives of $K + 5$ variables. The additional condition comes from the state equation which is algebraic. Since the derivative in density appears only in the continuity equations, it can be eliminated using the state relation without much augmentation to the differential equation. For a mixture of perfect gas, the state relation may be written as

$$\rho = P \frac{\bar{m}}{R_u T} \quad ; \quad \bar{m} = \frac{1}{\sum_{k=1}^K \frac{Y_k}{m_k}} .$$

Logarithmic differentiation with respect to ξ immediately produce:

$$\begin{aligned} \frac{1}{\rho} \frac{\partial \rho}{\partial \xi} &= \frac{1}{P} \frac{\partial P}{\partial \xi} + \frac{1}{\bar{m}} \frac{\partial \bar{m}}{\partial \xi} - \frac{1}{T} \frac{\partial T}{\partial \xi} \\ &= \frac{1}{P} \frac{\partial P}{\partial \xi} + \frac{1}{\bar{m}} \left(-\bar{m}^2 \sum_{k=1}^K \frac{1}{m_k} \frac{\partial Y_k}{\partial \xi} \right) - \frac{1}{T} \frac{\partial T}{\partial \xi} \\ &= \frac{1}{P} \frac{\partial P}{\partial \xi} - \frac{\bar{m}}{\rho q \cos \theta} \sum_{k=1}^K \dot{\omega}_k - \frac{1}{T} \frac{\partial T}{\partial \xi} . \end{aligned}$$

The continuity equation after combining with the last result becomes

$$\frac{1}{P} \frac{\partial P}{\partial \xi} - \frac{\bar{m}}{\rho q \cos \theta} \sum_{k=1}^K \dot{\omega}_k - \frac{1}{T} \frac{\partial T}{\partial \xi} + \frac{1}{q} \frac{\partial q}{\partial \xi} - \tan \theta \frac{\partial \theta}{\partial \xi} + \frac{\rho}{\rho_0} \frac{q}{\cos \theta} \frac{\partial \theta}{\partial \psi} = 0 . \quad (6.4.9)$$

As the derivative in ρ has been eliminated, there are only $K + 4$ dependent variables, (Y_k, P, T, q, θ) , governed by the $K + 4$ coupled differential equations. Density is considered according to the state relation as a function of the dependent variables (*c.f.* equation 6.3.2).

The independent variables in the transformed plane are ξ and ψ . To obtain the coordinates in the physical plane requires the inverse transformation. By exact differentials,

$$d\xi = \frac{\partial \xi}{\partial x} dx + \frac{\partial \xi}{\partial y} dy \quad \text{and}$$

$$d\psi = \frac{\partial \psi}{\partial x} dx + \frac{\partial \psi}{\partial y} dy ,$$

or simply

$$d\xi = dx$$

$$\text{and} \quad d\psi = -\frac{\rho}{\rho_0} q \sin \theta dx + \frac{\rho}{\rho_0} q \cos \theta dy \quad (6.4.10)$$

according to equations 6.4.1a, 6.4.1b and 6.4.2. As a result, the desired inversions are

$$dx = d\xi$$

$$\text{and} \quad dy = \tan \theta d\xi + \frac{\rho_0}{\rho} \frac{1}{q \cos \theta} d\psi .$$

Integrating the equation pair over appropriate limits produces the desired physical coordinates. The first inverse equation simply means that

$$x(\xi) - x_0 = \xi - \xi_0 , \quad (6.4.11a)$$

where x_0 and ξ_0 correspond to a reference location (usually at the nozzle inlet) in the two coordinates. The second inverse can be approached in two ways: along constant ψ or at constant ξ ; the corresponding relations are

$$\left\{ \begin{array}{l} \frac{\partial y}{\partial \xi} = \tan \theta \quad \Rightarrow \quad y(\xi, \psi) - y(\xi_0, \psi) = \int_{\xi_0}^{\xi} \tan \theta d\xi \quad \text{or} \\ \frac{\partial y}{\partial \psi} = \frac{\rho_0}{\rho} \frac{1}{q \cos \theta} \quad \Rightarrow \quad y(\xi, \psi) - y(\xi, \psi_l) = \int_{\psi_l}^{\psi} \frac{\rho_0}{\rho} \frac{1}{q \cos \theta} d\psi . \end{array} \right. \quad (6.4.11b)$$

The constants ψ_l and ψ_u are defined at the *lower* and *upper* nozzle walls respectively by

$$\left\{ \begin{array}{l} \psi_l = \psi(x, y_l(x)) \\ \psi_u = \psi(x, y_u(x)) \end{array} \right. \quad \text{and} \quad (6.4.12)$$

since the transformation guarantees that the streamfunction has constant value at a wall. Their geometries are specified as boundary inputs by

$$\left\{ \begin{array}{l} y_l = B_l(x) \\ y_u = B_u(x) \end{array} \right. \quad \text{and} \quad (6.4.13)$$

at the two walls.

Finally, the equivalence of the wall boundary condition in equation 6.3.6 is written in the transformed plane as

$$\left\{ \begin{array}{l} \tan(\theta(\xi, \psi_l)) = \frac{dB_l}{d\xi} \\ \tan(\theta(\xi, \psi_u)) = \frac{dB_u}{d\xi} \end{array} \right. \quad \text{and} \quad (6.4.14)$$

6.5 Transformed Governing Equations

The governing set at question includes K rate equations, one continuity equation, two momentum equations (2-D) and one energy equation involving the partial derivatives of Y_k , P , T , q and θ . There is also an algebraic relation for ρ . The equations listed in their respective order are:

the **rate equations**:

$$\frac{\partial Y_k}{\partial \xi} = \frac{m_k \dot{\omega}_k}{\rho q \cos \theta} \quad \text{for } k = 1, K \quad (6.5.1)$$

where

$$\dot{\omega}_k = \sum_{i=1}^I (\nu''_{ki} - \nu'_{ki}) \left(\sum_{j=1}^K \alpha_{ji} C_j \right) \left[k_{fi} \prod_{j=1}^K C_j^{\nu'_{ji}} - k_{ri} \prod_{j=1}^K C_j^{\nu''_{ji}} \right] \quad \text{for } k = 1, K,$$

the modified **continuity equation**:

$$\frac{1}{P} \frac{\partial P}{\partial \xi} - \frac{\bar{m}}{\rho q \cos \theta} \sum_{k=1}^K \dot{\omega}_k - \frac{1}{T} \frac{\partial T}{\partial \xi} + \frac{1}{q} \frac{\partial q}{\partial \xi} - \tan \theta \frac{\partial \theta}{\partial \xi} + \frac{\rho}{\rho_0} \frac{q}{\cos \theta} \frac{\partial \theta}{\partial \psi} = 0, \quad (6.5.2)$$

the **momentum equations**:

$$\frac{\partial q}{\partial \xi} = -\frac{1}{\rho q} \frac{\partial P}{\partial \xi} \quad (6.5.3a)$$

and

$$\frac{\partial \theta}{\partial \xi} = \frac{\tan \theta}{\rho q^2} \frac{\partial P}{\partial \xi} - \frac{1}{\rho_0 q \cos \theta} \frac{\partial P}{\partial \psi}, \quad (6.5.3b)$$

the **energy equation**:

$$\frac{\partial T}{\partial \xi} = \frac{1}{\rho \bar{C}_p} \left(\frac{\partial P}{\partial \xi} - \frac{1}{q \cos \theta} \sum_{k=1}^K h_k m_k \dot{\omega}_k \right), \quad (6.5.4)$$

plus the **state equation**:

$$\rho = P \frac{\bar{m}}{R_u T}, \quad \bar{m} = \frac{1}{\sum_{k=1}^K \frac{Y_k}{m_k}}. \quad (6.5.5)$$

Although not one of the governing equations, the formulae for inverse transformation are necessary so that the results can be presented in the physical plane. The inverse relation for x is trivial according to equation 6.4.11a. For y , the first alternative in equation 6.4.11b has been chosen:

$$\frac{\partial y}{\partial \xi} = \tan \theta . \quad (6.5.6)$$

Further manipulation of the equations is necessary to aid numerical implementation and to simplify treatment of boundary conditions. The first task is to write the equation set in the form

$$\frac{\partial \mathbf{Z}}{\partial \xi} = \mathbf{F} \left(\mathbf{Z}, \frac{\partial \mathbf{Z}}{\partial \psi} \right) \quad (6.5.7)$$

where the variable set is represented by

$$\mathbf{Z} \equiv [Y_k, P, T, q, \theta]^T \quad (6.5.8)$$

and \mathbf{F} is a vector function. In this way, the equations can be solved as *ordinary* differential equations along lines of constant ψ 's if the function \mathbf{F} is known and can be evaluated numerically for any given \mathbf{Z} and boundary conditions. It is not difficult to obtain the exact functional form of \mathbf{F} since the ξ -derivatives in the governing set are first order and linear. A representative result is provided by $\partial P / \partial \xi$ because of its role in all except the rate equation. The following result is obtained after some algebraic manipulations:

$$\begin{aligned} \frac{\partial P}{\partial \xi} = & \left\{ \frac{q \cos \theta}{1 - q^2 \cos^2 \theta \left(\frac{\rho}{P} - \frac{1}{\bar{C}_p T} \right)} \right\} \left(-\bar{m} \sum_{k=1}^K \dot{\omega}_k + \frac{1}{\bar{C}_p T} \sum_{k=1}^K h_k m_k \dot{\omega}_k \right. \\ & \left. + \frac{\rho}{\rho_0} \tan \theta \frac{\partial P}{\partial \psi} + \frac{\rho}{\rho_0} \rho q^2 \frac{\partial \theta}{\partial \psi} \right) . \end{aligned} \quad (6.5.9)$$

It is then a matter of substitution to express $\frac{\partial T}{\partial \xi}$, $\frac{\partial q}{\partial \xi}$ and $\frac{\partial \theta}{\partial \xi}$ in terms of \mathbf{Z} and $\frac{\partial \mathbf{Z}}{\partial \psi}$. The results are listed in appendix IV.

6.5.1 Singular conditions

An immediate consequence of the transformation is that the derivatives with respect to ξ are singular when the flow is perpendicular to the streamwise (or ξ) direction. They are exemplified by the presence of the term $\cos \theta$ in several denominators. The *unidirectional flow* requirement in the transformation together with this singularity then assert that

$$|\theta| \not\geq \frac{\pi}{2}.$$

Due to the importance of the value of θ , directions of the coordinate axes must be carefully selected since the angle is measured from the x -axis. But this problem is sometimes inevitable as the x - y axes are chosen such that the available nozzle inlet conditions are at a constant x or ξ -location whenever possible.

Also noticeable is another singularity similar to that presented in all *transonic* problems. It occurs when the denominator in the braces of equation 6.5.9 goes to zero; that is, when

$$1 - q^2 \cos^2 \theta \left(\frac{\rho}{P} - \frac{1}{\bar{C}_p T} \right) = 0.$$

The importance of the *frozen speed of sound* in a reacting flow is marked by this condition. This can be shown after some manipulations:

$$\begin{aligned} 1 &= q^2 \cos^2 \theta \left(\frac{\rho}{P} - \frac{1}{\bar{C}_p T} \right) \\ &= q^2 \cos^2 \theta \left(\frac{\bar{m}}{R_u T} - \frac{1}{\bar{C}_p T} \right) \\ &= q^2 \cos^2 \theta \left(\frac{\bar{m}}{\bar{C}_p R_u T} \right) \left(\bar{C}_p - \frac{R_u}{\bar{m}} \right) \\ &= \frac{q^2 \cos^2 \theta}{\frac{\bar{C}_p R_u}{\bar{C}_v \bar{m}} T} \end{aligned}$$

where the state equation has been used in the second step and the relation

$$\frac{R_u}{\bar{m}} = \bar{C}_p - \bar{C}_v$$

has been used in the third. The denominator in the last step is related to the frozen speed of sound a_f (*c.f.* appendix II) by

$$\begin{aligned} a_f^2 &\equiv \left(\frac{\partial P}{\partial \rho} \right)_{S, Y_k} \\ &= \frac{\bar{C}_p R_u}{\bar{C}_v \bar{m}} T. \end{aligned}$$

Therefore, the singular condition is equivalent to

$$\frac{q \cos \theta}{a_f} = 1$$

or

$$M_{\xi f} = 1$$

where $M_{\xi f}$ is the frozen Mach number in the ξ -direction.

6.6 Numerical Implementation

The method most suitable for the current setup is *finite-differencing* in the ξ - ψ plane. Such an approach is a direct consequence of the *Von Mises* transformation. In many circumstances, the nozzle inlet conditions are specified at a constant ξ -location or can be approximated to be so by a combination of analytic calculation and numerical interpolation. The nozzle walls are also represented by constant ψ 's by construction. As a result, the boundary in the ξ - ψ plane is rectangular and the use of finite-differencing is obvious.

To confer with some physical aspects of the problem, the approach adopted is to start with the nozzle inlet conditions and march downstream in the ξ -direction following lines of constant ψ (steady streamlines or particle paths).** This is preferable since chemical reactions naturally evolve along particle paths and it is more convenient to increment their changes in the ξ -direction. But for the same reason, some variables can acquire very high ξ -gradient and the differential equation set is inherently *stiff* when integrated in the ξ -direction. The approach is also favored by the requirement that the nozzle walls be at constant ψ 's (ψ_l and ψ_u). Stiffness is of lesser importance in the ψ -direction but equal emphasis lies on the treatment of the two-point wall boundary condition.

In order to achieve optimal accuracy and efficiency when incrementing the ξ -coordinate, a numerical subroutine library, LSODE^[4], is employed. It is especially designed for solving systems of *linear stiff ordinary differential equations*; a short description of which is given in appendix VI. In the form of equation 6.5.7, the set is *quasi*-linear and is ordinary along constant ψ . Application of the solver routines is therefore straightforward provided that the equation can be evaluated at any ξ -location. Detailed formulation is described shortly. Although finite-differencing is implicit in the solver and the ξ variable is incremented step-wise in actuality, its discreteness is irrelevant in the following formulation and, hence, will not be represented as such for clarity.

** An alternative approach is to follow the supersonic characteristics. A different formulation is however required; more details are given by Vincenti^[14].

Explicit finite-differencing must be applied in the ψ -coordinate so as to evaluate equation 6.5.7 for any given $\mathbf{Z}(\xi)$ and wall geometries. There is a difficulty associated with the grid spacing in the ψ -direction. The effect of some wall geometries is to impose very high ψ -gradients near the boundary. The use of uniformly fine grid throughout the ψ -domain is inefficient and expensive computationally. Instead of resorting to adaptive ψ -grid, uniform spacing is adopted; but the differencing schemes in approximating the ψ -derivatives are designed carefully so as to allow reasonable accuracy for all geometries with moderate resolution. Some analytic results are incorporated in the process.

In the ξ - ψ plane, ξ is treated as a continuous coordinate; the other coordinate is discretized and denoted by ψ_j . Uniform grid then implies that

$$\psi_j = \psi_l + (j - 1)\Delta\psi, \quad j = 1, N, \quad (6.6.1)$$

where $\Delta\psi$ is the spacing. Both the lower and upper limits in the ψ -domain are fixed, namely between ψ_l and ψ_u . Therefore, $\Delta\psi$ is a function of N :

$$\Delta\psi = \frac{\psi_u - \psi_l}{N - 1},$$

where N is the number of streamlines including the two walls. It is also a measure of the resolution in the problem. The differential equation sets relevant are the discretized versions of 6.5.7:

$$\left. \frac{\partial \mathbf{Z}}{\partial \xi} \right|_{\psi_j} = \mathbf{F} \left(\mathbf{Z}_j, \frac{\partial P_j}{\partial \psi}, \frac{\partial \theta_j}{\partial \psi} \right), \quad j = 1, N \quad (6.6.2)$$

for the N variable sets

$$\mathbf{Z}_j \equiv [Y_{k,j}, P_j, T_j, q_j, \theta_j]^T = \mathbf{Z}(\xi, \psi_j). \quad (6.6.3)$$

The exact functional form of \mathbf{F} is obtained by applying equation 6.5.9 to the governing equations. The result is listed in appendix IV. It is then clear that the ψ -derivatives involved are only those of P and θ .

Since \mathbf{Z}_j is presumably known at every ξ -step, the only concern in evaluating 6.6.2 is to find the ψ -derivatives of P and θ at N points. Centered differencing scheme is desired because interior derivatives are involved and no derivative discontinuity[†] is expected in either variable. A three-point scheme is also preferred so as to minimize the difficulty at the boundaries. To satisfy these requirements and at the same time achieve high accuracy, the *Padé*'s 4th order implicit scheme is adopted. For a variable of known values $f(\psi_j; \dots)$, the interior derivatives are given by:

$$f'_{j-1} + 4f'_j + f'_{j+1} = \frac{3}{\Delta\psi} (f_{j+1} - f_{j-1}) + \mathcal{O}(\Delta\psi^4), \quad j = 2, N - 1, \quad (6.6.4)$$

[†] Derivative discontinuities may arise from an expansion fan due to a sharp turn; in this situation, a one-sided scheme is desirable at the discontinuity.

where

$$f'_j \equiv \left. \frac{\partial f}{\partial \psi} \right|_{\psi_j}.$$

Note that these equations are equivalent to those of a *cubic spline* fit through f_1 to f_N . As there are only $N - 2$ equations, *two* additional conditions are necessary to determine the N derivatives for each variable. Therefore, *four* additional conditions are needed for the variables P and θ .

Two of the conditions can be extracted as a result of the constraints at the walls. The geometry conditions in equation 6.4.14 is equivalently stated as

$$\left\{ \begin{array}{l} \theta(\xi, \psi_l) \equiv \theta_l = \tan^{-1} \left(\frac{dB_l}{d\xi} \right) \\ \theta(\xi, \psi_u) \equiv \theta_u = \tan^{-1} \left(\frac{dB_u}{d\xi} \right) \end{array} \right. , \quad -\frac{\pi}{2} < \theta < \frac{\pi}{2}$$

for the angles at the lower and upper walls respectively. Consequently, the derivatives of θ with respect to ξ are also known functions. Direct differentiation of the former equation gives

$$\left\{ \begin{array}{l} \frac{d\theta_l}{d\xi} = \frac{\frac{d^2 B_l}{d\xi^2}}{1 + \left(\frac{dB_l}{d\xi} \right)^2} = \cos^2 \theta_l \frac{d^2 B_l}{d\xi^2} \\ \frac{d\theta_u}{d\xi} = \frac{\frac{d^2 B_u}{d\xi^2}}{1 + \left(\frac{dB_u}{d\xi} \right)^2} = \cos^2 \theta_u \frac{d^2 B_u}{d\xi^2} \end{array} \right. \quad \text{and} \quad (6.6.5)$$

But the partial derivative of θ with respect to ξ must satisfy the differential equation

$$\frac{\partial \theta}{\partial \xi} = \text{Function} \left(Y_k, P, T, q, \theta, \frac{\partial P}{\partial \psi}, \frac{\partial \theta}{\partial \psi} \right)$$

for which the exact expression is given in appendix IV. When this equation is evaluated at the boundaries, the left hand side is equivalent to that in equation 6.6.5 and two conditions can be drawn relating the ψ -derivatives of P and θ at the walls. In short, the conditions take the forms

$$a_l P'_l + b_l \theta'_l = c_l \quad (6.6.6a)$$

and

$$a_u P'_u + b_u \theta'_u = c_u \quad (6.6.6b)$$

at the lower and upper walls respectively. The coefficients a_l, b_l, \dots, b_u and c_u are functions of $Z(\xi, \psi_l)$ and $Z(\xi, \psi_u)$; their algebraic forms can be inferred according to equations IV.7a and IV.7b of appendix IV. A *prime* notation has been used to represent $\partial/\partial\psi$ since the present concern is in determining the ψ -derivative. Also note that the subscripts 'l' and 'u' are equivalent to the indices '1' and 'N' in the discretized plane. In an analytic calculation, the two conditions are redundant since the boundary constraint is sufficiently prescribed by equation 6.4.14; but they are very useful for the scheme described in equation 6.6.4 since it does not provide sufficient conditions for the evaluation of P'_j and θ'_j even though P_j and θ_j are known. To complete the *Padé's* scheme requires two more conditions. A simple and efficient way of imposing those conditions is through numerical differencing. The method is described as follows.

6.7 Determination of P'_j and θ'_j – The Interpolation/ Extrapolation Method

Equations 6.6.6a and 6.6.6b have the advantage of being *exact*. Unfortunately, no other exact conditions can be drawn from the governing equations (*c.f.* Appendix IV)[‡]. To supply the remaining conditions necessary in the determination of P'_j and θ'_j , an inexpensive means is to approximate two of those derivatives directly using differencing schemes. However, they must be approximated with an error of $\mathcal{O}(\Delta\psi^4)$ or higher so as to preserve the accuracy of the *Padé's* 4th order scheme. These methods are rarely used for general purposes since they involve at least five neighbouring points. But they can be derived without difficulty using Taylor's expansion. Suppose that g is a function of ψ and

$$g_{n-3} \equiv g(\psi_n - 3\Delta\psi) \quad \dots \quad g_{n+1} \equiv g(\psi_n + \Delta\psi) \quad \dots \quad \text{and} \quad g_{n+4} \equiv g(\psi_n + 4\Delta\psi).$$

Each of these quantities can be expanded about ψ_n as a power series of $\Delta\psi$. Depending on the number of points involved, linear combinations of the series then provide several representations of the first derivative g'_n . Four possibilities are considered best for the current purpose. Two of them are centered schemes:

$$g'_n = \frac{1}{12\Delta\psi} (g_{n-2} - 8g_{n-1} + 8g_{n+1} - g_{n+2}) + \mathcal{O}(\Delta\psi^4) \quad (6.7.1a)$$

$$g'_n = \frac{1}{60\Delta\psi} (-g_{n-3} + 9g_{n-2} - 45g_{n-1} + 45g_{n+1} - 9g_{n+2} + g_{n+3}) + \mathcal{O}(\Delta\psi^6) \quad (6.7.1b)$$

[‡] Any further manipulation such as cross differentiation of the governing equations only introduces new ψ -derivatives which would require more conditions for their evaluations as far as the *Padé's* scheme is concerned.

while the others are slightly one-sided:

$$g'_n = \frac{1}{12\Delta\psi} (-3g_{n-1} - 10g_n + 18g_{n+1} - 6g_{n+2} + g_{n+3}) + \mathcal{O}(\Delta\psi^4) \quad (6.7.1c)$$

$$g'_n = \frac{1}{60\Delta\psi} (2g_{n-2} - 24g_{n-1} - 35g_n + 80g_{n+1} - 30g_{n+2} + 8g_{n+3} - g_{n+4}) + \mathcal{O}(\Delta\psi^6) . \quad (6.7.1d)$$

In these schemes, n must be at least two or larger when higher accuracy is desired.

There are some limitations as to which two derivatives should be approximated among P'_j 's and θ'_j 's. The possibility of calculating any derivative *at* the walls has been eliminated; otherwise, purely one-sided differencing schemes must be employed and their approximations are often poor. There only remain two choices:

- (1) calculate one derivative for P and one for θ at $n \sim N/2$;
- (2) calculate two derivatives for the same variable (either P or θ) at n and $N - n + 1$.

Since there is no physical reason why the derivatives should be approximated for one variable and not the other, the first choice is naturally preferred. The error due to numerical approximation is then evenly distributed over P'_j and θ'_j . But there are circumstances when this choice fails. Depending on the values of the coefficients a_l , a_u , b_l and b_u in relations 6.6.6a and 6.6.6b, the derivatives approximated for P and θ may contradict with the relations.[‡] The second choice, on the other hand, can apply under those circumstances. Its disadvantage being that the error in the ψ -derivatives may compound and become considerably large when two numerical approximations are imposed on the same variable. For this reason, it appears that the two methods should be used in combination — the second one is applied only when the first one fails. Unfortunately, the results from using the two methods to calculate the $2N$ derivatives, P'_j 's and θ'_j 's, differ enough that switching from one formulation to another at times may cause mathematical problems. Considering also the difficulty in implementation when logical tests must be imposed at every step to determine which method is appropriate*, the first method is abandoned entirely. The second method, despite the possibility of a compounded error, can apply at all times in a supersonic problem if the two derivatives are approximated for θ . According to test results, the error from using the second method alone is slightly larger than that from using the two in combination; but the gain in computational efficiency is significant. In the case of acute wall geometry, all the mentioned methods performed poorly.

[‡] In general, this happens when the coefficient matrix $\begin{pmatrix} a_l & b_l \\ a_u & b_u \end{pmatrix}$ is singular.

* This is a significant draw-back as far as programing in supercomputers is concerned.

Having decided which two derivatives to approximate, the equations necessary for solving P'_j and θ'_j are completed. Rewriting the *Padé's* scheme for P'_j and θ'_j , relations 6.6.6a and 6.6.6b, and imposing two ψ -derivatives of θ with a differencing scheme, $2N$ equations for the $2N$ derivatives of P and θ are obtained which can be solved completely. The set is subdivided into four groups for clarity:

$$\left. \begin{aligned} P'_1 + 4P'_2 + P'_3 &= \frac{3}{\Delta\psi}(P_3 - P_1) \\ P'_2 + 4P'_3 + P'_4 &= \frac{3}{\Delta\psi}(P_4 - P_2) \\ &\vdots \\ P'_{N-2} + 4P'_{N-1} + P'_N &= \frac{3}{\Delta\psi}(P_N - P_{N-2}) \end{aligned} \right\} \begin{array}{l} (N-2) P'_j \text{ equations} \\ \text{from } \textit{Padé's} \text{ scheme,} \\ (6.7.2) \end{array}$$

$$\left. \begin{aligned} \theta'_1 + 4\theta'_2 + \theta'_3 &= \frac{3}{\Delta\psi}(\theta_3 - \theta_1) \\ \theta'_2 + 4\theta'_3 + \theta'_4 &= \frac{3}{\Delta\psi}(\theta_4 - \theta_2) \\ &\vdots \\ \theta'_{N-2} + 4\theta'_{N-1} + \theta'_N &= \frac{3}{\Delta\psi}(\theta_N - \theta_{N-2}) \end{aligned} \right\} \begin{array}{l} (N-2) \theta'_j \text{ equations} \\ \text{from } \textit{Padé's} \text{ scheme,} \\ (6.7.3) \end{array}$$

$$\left. \begin{aligned} \theta'_n &= \frac{1}{12\Delta\psi}(\theta_{n-2} - 8\theta_{n-1} + 8\theta_{n+1} - \theta_{n+2}) \\ \theta'_{N-n+1} &= \frac{1}{12\Delta\psi}(\theta_{N-n-1} - 8\theta_{N-n} + 8\theta_{N-n+2} - \theta_{N-n+3}) \end{aligned} \right\} \begin{array}{l} 2 \text{ derivatives} \\ \text{from differencing,} \\ (6.7.4) \end{array}$$

and

$$\left. \begin{aligned} a_l P'_1 + b_l \theta'_1 &= c_l \\ a_u P'_N + b_u \theta'_N &= c_u \end{aligned} \right\} \begin{array}{l} 2 \text{ analytic relations} \\ \text{from wall boundaries.} \\ (6.7.5) \end{array}$$

As a demonstration, the two derivatives for θ are approximated using 6.7.1a in the last group. This requires that n be greater than or equal to 3. Any of the other three schemes can be used alternatively but different restrictions must be imposed on n .

Based on this setup, the $2N$ equations are not entirely coupled. They can be separated into four groups and solved independently. In terms of the *cubic spline* interpretation of the *Padé's* scheme, each group can be solved via an *interpolation* or *extrapolation*. The procedures are outlined in three steps as follows:

1. Calculate the derivatives θ'_{n+1} to θ'_{N-n} . This calculation is equivalent to a cubic spline *interpolation* through θ_n to θ_{N-n+1} since θ'_n and θ'_{N-n+1} are known explicitly. For this reason, this segment can be solved independently. There are $N - 2n$ equations which can be expressed in short as

$$\mathbf{A} \begin{pmatrix} \theta'_{n+1} \\ \vdots \\ \vdots \\ \vdots \\ \theta'_{N-n} \end{pmatrix} = \mathbf{B} \begin{pmatrix} \theta_{n+1} \\ \vdots \\ \vdots \\ \vdots \\ \theta_{N-n} \end{pmatrix} + \begin{pmatrix} -\frac{3}{\Delta\psi}\theta_n - \theta'_n \\ \vdots \\ 0 \\ \vdots \\ \frac{3}{\Delta\psi}\theta_{N-n+1} - \theta'_{N-n+1} \end{pmatrix} \quad (6.7.6)$$

where \mathbf{A} and \mathbf{B} are constant $(N - 2n) \times (N - 2n)$ coefficient matrices given by

$$\mathbf{A} = \begin{pmatrix} 4 & 1 & \dots & \dots & 0 \\ 1 & 4 & 1 & & \vdots \\ 0 & & \ddots & & 0 \\ \vdots & & 1 & 4 & 1 \\ 0 & \dots & \dots & 1 & 4 \end{pmatrix} \quad \text{and} \quad \mathbf{B} = \frac{3}{\Delta\psi} \begin{pmatrix} 0 & 1 & \dots & \dots & 0 \\ -1 & 0 & 1 & & \vdots \\ 0 & & \ddots & & 0 \\ \vdots & & -1 & 0 & 1 \\ 0 & \dots & \dots & -1 & 0 \end{pmatrix}.$$

These matrices are tri-diagonal since their elements are derived from the *Padé's* scheme. In addition, \mathbf{A} has *diagonal dominance* and is non-singular; many standard methods are available in solving equation 6.7.6. Note that even though \mathbf{A} is constant and its inverse needs only be computed once, it is more economical to solve the algebraic equations directly through approximately $2(N - 2n)$ forward- and backward-substitution operations.**

2. Calculate the derivatives θ'_{n-1} to θ'_1 and θ'_{N-n+2} to θ'_N . This is accomplished by substituting the values of θ'_n , θ'_{n+1} , θ'_{N-n} and θ'_{N-n+1} from the first segment into two set of *Padé* equations. Only forward-substitution is necessary when the equations are arranged in the following manner:

$$\begin{aligned} \theta'_{n-1} + 4\theta'_n + \theta'_{n+1} &= \frac{3}{\Delta\psi}(\theta_{n+1} - \theta_{n-1}) \\ \theta'_{n-2} + 4\theta'_{n-1} + \theta'_n &= \frac{3}{\Delta\psi}(\theta_n - \theta_{n-2}) \\ &\vdots \\ \theta'_1 + 4\theta'_2 + \theta'_3 &= \frac{3}{\Delta\psi}(\theta_3 - \theta_1) \end{aligned} \quad (6.7.7a)$$

** See, for example, Ralston and Rabinowitz^[11] for details.

and

$$\begin{aligned}
\theta'_{N-n} + 4\theta'_{N-n+1} + \theta'_{N-n+2} &= \frac{3}{\Delta\psi}(\theta_{N-n+2} - \theta_{N-n}) \\
\theta'_{N-n+1} + 4\theta'_{N-n+2} + \theta'_{N-n+3} &= \frac{3}{\Delta\psi}(\theta_{N-n+3} - \theta_{N-n+1}) \\
&\vdots \\
\theta'_{N-2} + 4\theta'_{N-1} + \theta'_N &= \frac{3}{\Delta\psi}(\theta_N - \theta_{N-2}).
\end{aligned} \tag{6.7.7b}$$

At this point, the second reason why θ'_n and θ'_{N-n+1} are approximated rather than those for P can be explained. The present selection leads to the single most important consequence that θ'_1 and θ'_N are determined in the calculation just described. These quantities can then be applied to equation 6.7.5 to obtain P'_1 and P'_N provided that a_l and a_u are nonzero. But according to equations IV.7a and IV.7b of appendix IV,

$$a_l \sim a_u \propto \frac{M_f^2 - 1}{M_f^2} \quad \text{where} \quad M_f \equiv \frac{q}{a_f}$$

is the frozen Mach number. The two coefficients must therefore be nonzero since the flow is strictly supersonic by assumption. Consider the other alternative in which P'_n and P'_{N-n+1} were approximated. The determination of θ'_1 and θ'_N from equation 6.7.5 would then require that b_l and b_u be nonzero which is not always true since

$$b_l \sim b_u \propto \tan \theta$$

and either coefficient becomes zero whenever θ does. A half-nozzle with a flat wall at zero inclination would have been unmanageable with this method.

In these two segments, the calculations constitute the *extrapolation* aspect of the method. For example, the set of equations in 6.7.7a is equivalent to a cubic spline fit through θ_1 to θ_n with the first and second derivatives specified at the n^{th} location.

3. Calculate the derivatives P'_2 to P'_{N-1} . With P'_1 and P'_N known, this segment again calls for an *interpolation* and can be solved exactly like the first one. The governing matrix equation has the form

$$\mathbf{A} \begin{pmatrix} P'_2 \\ \vdots \\ \vdots \\ \vdots \\ P'_{N-1} \end{pmatrix} = \mathbf{B} \begin{pmatrix} P_2 \\ \vdots \\ \vdots \\ \vdots \\ P_{N-1} \end{pmatrix} + \begin{pmatrix} -\frac{3}{\Delta\psi} P_1 - P'_1 \\ \vdots \\ 0 \\ \vdots \\ \frac{3}{\Delta\psi} P_N - P'_N \end{pmatrix}. \tag{6.7.8}$$

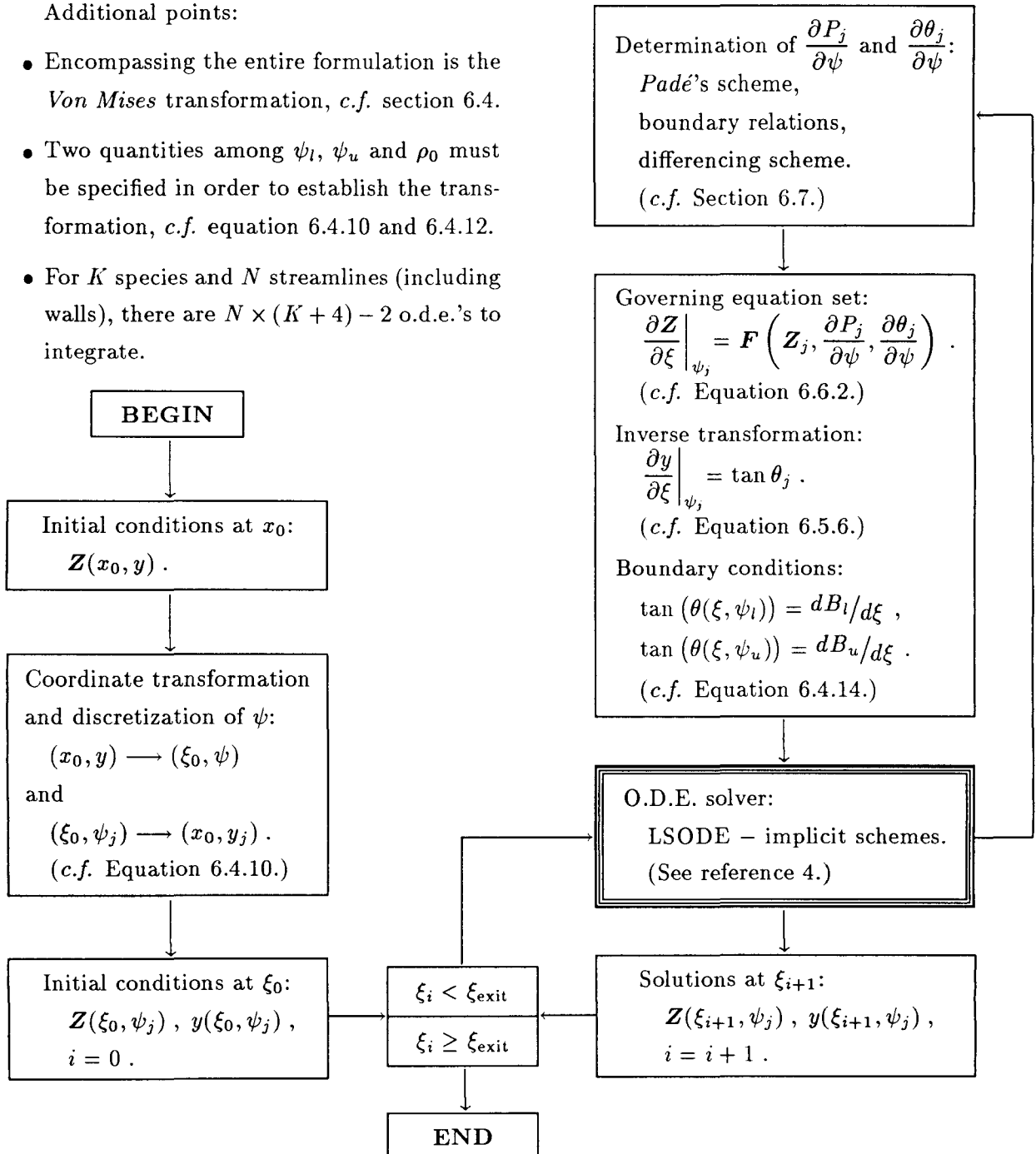
The matrices \mathbf{A} and \mathbf{B} are as before except that their dimensions are now $(N-2) \times (N-2)$.

6.8 Summary of implementation procedures

A number of elements has been developed in this chapter in order to construct a computational model for the supersonic nozzle (analysis) problem. A complete list of procedures for solving such a model involves many lengthy equations. Nevertheless, it can be presented in a concise block format.

Additional points:

- Encompassing the entire formulation is the *Von Mises* transformation, *c.f.* section 6.4.
- Two quantities among ψ_l , ψ_u and ρ_0 must be specified in order to establish the transformation, *c.f.* equation 6.4.10 and 6.4.12.
- For K species and N streamlines (including walls), there are $N \times (K + 4) - 2$ o.d.e.'s to integrate.



The scheme outlined is implemented into a FORTRAN program. In section 7.3, capability of the program is demonstrated through some sample calculations. At the same time, its limitation is also demonstrated through a case with acute wall geometry. Special treatment is subsequently developed to handle such difficulties. Final version of the nozzle program and some informative results are fully described in Chapter 7.

CHAPTER 7

Reacting Flow in a Two-Dimensional Expansion Nozzle

Part II: Numerical Results

7.1 Introduction

The nozzle problem is designed for one important purpose — to investigate the phenomenon of *freezing* in a hydrogen-air combustion product. The aim is to determine if any of the species would become chemically inactive during expansion and, if so, how sensitive are the freezing processes of those species to the rate of expansion and the nature of the inlet flow. This problem is directly related to the feasibility of the proposed SCRAMJET engine for the NASP. As the nozzle is the final stage of the engine, freezing of some high energy radicals would inhibit the conversion of stored chemical energy into propulsion power. Ideally, a maximum amount of chemical energy is extracted when the chemistry is at equilibrium.

Of special interest is the effect of wall curvature. It has been known that freezing tends to occur under a high rate of expansion. Therefore, a gentle wall curvature is preferred during expansion. But this has the undesirable effect that the resulting nozzle may become impractically long since the flow must preferably expand to the ambient pressure at the exit. A perfect gas analysis (no chemical reactions) has estimated a length of $\mathcal{O}(10^1)$ meters to achieve ideal expansion in the NASP nozzle. The length problem becomes particularly acute since the physical dimension of the NASP has also limited the nozzle length to within $\mathcal{O}(10^1)$ meters. Therefore, the desirable expansion rate must be at least as sharp as the perfect gas design. It is then necessary to determine the trade off between sharp curvature and freezing in this context.

At this stage of development, most of the design parameters for the NASP propulsion system are not yet well specified. Assumptions have to be imposed in constructing the two-dimensional nozzle model; they were described in the previous chapter. Remaining to be described are the two inputs for the nozzle *analysis* problem — the inlet conditions and the wall geometry. They are directly responsible for the behaviors of the flow field as well as the chemical processes in the nozzle. Therefore, it is essential that they be

deduced from the best knowledge of the NASP. While the information leading to the inlet conditions has been considered in the combustor calculations in Chapters 3 and 4, there are several possibilities for the wall geometry according to different designs. Some maintain solid boundaries on both walls while some incorporate a free streamline as a boundary. Because of their importance, lengthier discussions on the two inputs are given in separate sections.

7.2 System Description

The variable set \mathbf{Z} has already been chosen in chapter 6. The species and reaction sets for the hydrogen-air system has also been selected in chapter 3* for the combustor calculation. There remains only the inlet conditions and wall geometry to be described. In addition, some essential dimensions in the nozzle are also to be discussed.

7.2.1 Inlet conditions

The quantities at question are the element of \mathbf{Z} given in

$$\mathbf{Z}(x_0, y) = [Y_k(x_0, y), P(x_0, y), T(x_0, y), q(x_0, y), \theta(x_0, y)]^T ,$$

where x_0 denotes the inlet location. The former one-dimensional diffuser (*c.f.* Appendix II) and combustor (*c.f.* Chapter 3) calculations may supply very good estimates on their average magnitudes. The problem, however, is not in finding the relative magnitudes but in presenting their y -distributions.

The simplest case is one of uniform distributions. That is to assume constant profiles for all except $\theta(x_0, y)$. This is applicable when the difference between the initial angles at the two walls, $|\theta_u(x_0) - \theta_l(x_0)|$, is small enough such that θ can be assumed to vary *linearly* with y . This approximation is not as crude as it seems because the walls at the combustor exit are expected to be nearly parallel**. In this way, the former one-dimensional calculations can be used.

* See also appendix III.

** As near equilibrium chemistry is desired at the combustor exit, a 1-D constant pressure combustor model would imply that $dArea/dx$ is also nearly zero.

In the other cases, the distributions can only be estimated *qualitatively*. For instance, shock enhanced mixing in the combustor would induce a spatially fluctuating temperature profile at the nozzle inlet; but neither the amplitude nor the peak-to-peak separation is well known. Nevertheless, if $T(x_0, y)$ and $q(x_0, y)$ are known, the remaining distributions can again be approximated using the one-dimensional calculations. The principle is to approximate the inlet flow by a finite number of one-dimensional streamtubes, each constituting a diffuser-combustor calculation. The mean flow angle in each tube is deduced from its area change.

7.2.2 Wall geometry

The functions

$$y = B_l(x) \quad \text{and} \\ y = B_u(x)$$

which appeared repeatedly in the formulation, are the desired descriptions of the lower and upper wall geometries. They are arbitrary in general except for two basic restrictions arising from the formulation. Firstly, the geometries must be sufficiently smooth such that $d^2 B/d^2 x$'s ($\sim d\theta_{\text{walls}}/dx$) are finite. These derivatives are vital in the calculation through their roles in equations IV.7a and IV.7b (see also section 6.6.1). Secondly, the nozzle must be purely divergent since the formulation is not designed to handle any strong shock.

A specific nozzle design is to be considered. It has been proposed that the lower side of the nozzle be open to the ambient near the exit of the combustor. Consequently, the natural boundary of that wall becomes the free streamline between the free-stream oblique shock and the expanding nozzle flow. This type of design is beyond the capability of the present formulation since the geometry of the free streamline, and hence the geometry of the nozzle, is not known *before* the calculation. [†] But an approximate case can be studied. Provided that the oblique shock is sufficiently strong, curvature of the matching streamline would remain small for some extent and an inclined *flat* wall can be assumed. The angle of inclination can be estimated from a shock-expansion fan matching calculation. This type of geometry is informative for studying both the behavior of the reacting flow and the performance of the numerical scheme. It is therefore adopted for the nozzle analyses.

[†] Matching between free-stream and expanding flow must be performed *during* calculation.

Consider the mentioned design and recall that a major parameter in the study is the wall curvature, a simple and effective representation of the wall geometry is one that is composed of three segments — an inlet segment of zero curvature and angle θ_{in} , a turning segment of maximum curvature $1/R_t$ (or minimum radius of curvature R_t), and an exit segment of zero curvature and angle θ_{ex} . Smoothness of the nozzle requires that dB/dx and $d\theta/dx$ be continuous along all three segments and at the two matching points. The first and third segments are linear functions. To simplify matters, a 4th order polynomial is used for the turning segment. The coefficients of the polynomial and the matching point with the exit segment are defined by six conditions:

$$\left\{ \begin{array}{l} B(x_1) = y_1 , \\ \frac{dB}{dx} \Big|_{x_1} = \tan \theta_{\text{in}} , \quad \frac{d^2B}{dx^2} \Big|_{x_1} = 0 , \\ \frac{dB}{dx} \Big|_{x_2} = \tan \theta_{\text{ex}} , \quad \frac{d^2B}{dx^2} \Big|_{x_2} = 0 \quad \text{and} \\ \max \left| \frac{d^2B}{dx^2} \right| = \frac{1}{R_t} . \end{array} \right.$$

The resulting polynomial has the form

$$y(x) = c_0 + c_1(x - x_1) + c_3(x - x_1)^3 + c_4(x - x_1)^4 \quad (7.2.2.1)$$

with coefficients

$$\begin{aligned} c_0 &= y_1 , \\ c_1 &= \tan \theta_{\text{in}} , \\ c_3 &= \frac{4}{9} \frac{1}{(\tan \theta_{\text{ex}} - \tan \theta_{\text{in}}) R_t^2} \quad \text{and} \\ c_4 &= -\frac{4}{27} \frac{1}{|\tan \theta_{\text{ex}} - \tan \theta_{\text{in}}| (\tan \theta_{\text{ex}} - \tan \theta_{\text{in}}) R_t^3} . \end{aligned} \quad (7.2.2.2)$$

In addition, the matching location at the end of the polynomial, x_2 , and the location of maximum curvature, x_t , are given by

$$\begin{aligned} x_2 &= x_1 + \frac{3}{2} |\tan \theta_{\text{ex}} - \tan \theta_{\text{in}}| R_t \quad \text{and} \\ x_t &= \frac{x_1 + x_2}{2} \\ &= x_1 + \frac{3}{4} |\tan \theta_{\text{ex}} - \tan \theta_{\text{in}}| R_t . \end{aligned} \quad (7.2.2.3)$$

Having setup the basic formulae, complete descriptions of the nozzle geometries can be given. The mathematical forms of the upper and lower wall geometries are assumed to be identical. It is only necessary to consider one description. Introducing the wall height, h_{in} , at the inlet location, x_0 , the wall geometry is

$$\left\{ \begin{array}{l} B_1(x) = h_{\text{in}} + \tan \theta_{\text{in}}(x - x_0) \quad \text{for } x_0 \leq x \leq x_1, \\ B_2(x) = B_1(x_1) + \tan \theta_{\text{in}}(x - x_1) + c_3(x - x_1)^3 + c_4(x - x_1)^4 \quad \text{for } x_1 \leq x \leq x_2, \\ B_3(x) = B_2(x_2) + \tan \theta_{\text{exl}}(x - x_2) \quad \text{for } x \geq x_2 \end{array} \right. \quad (7.2.2.4)$$

with the coefficients c_3 and c_4 given by the expressions in 7.2.2.2. Note that each geometry is identified by five parameters — h_{in} , θ_{in} , θ_{ex} , x_1 and R_t — in which the orientation of a wall is determined by the signs of θ_{in} and θ_{ex} . Although there is no restriction on the two angles in the formulae, they must be selected to yield a divergent nozzle. The location of maximum curvature and the extension of the turning segment can also be varied according to equation 7.2.2.3.

Sample geometries have been calculated for the case of θ_{in} equals zero, θ_{ex} equals 30° , x_1 equals zero and five R_t 's. $B(x)$ is shown in figures 7.2.2a while $d\theta/dx$ (*c.f.* equation 6.6.5) is shown in figure 7.2.2b. In addition to showing the rate of turn, figure 7.2.2b also indicates that this type of geometry is only continuous up to $d\theta/dx$ ($\sim d^2B/d^2x$).

It is convenient to use a symmetric nozzle or a half-nozzle for the purpose of analysis. The phenomenon of *freezing* and the effect of wall curvature can be studied under either circumstances. However, to simulate the actual NASP nozzle problem generally requires a *non-symmetric* configuration. In the solid wall design, it is desirable for the *lower* wall to have a minimal degree of divergence since it is expected to be exposed to the free-stream. Due to the lack of detailed knowledge about the NASP nozzle design, this type of configuration is not considered in the present study.

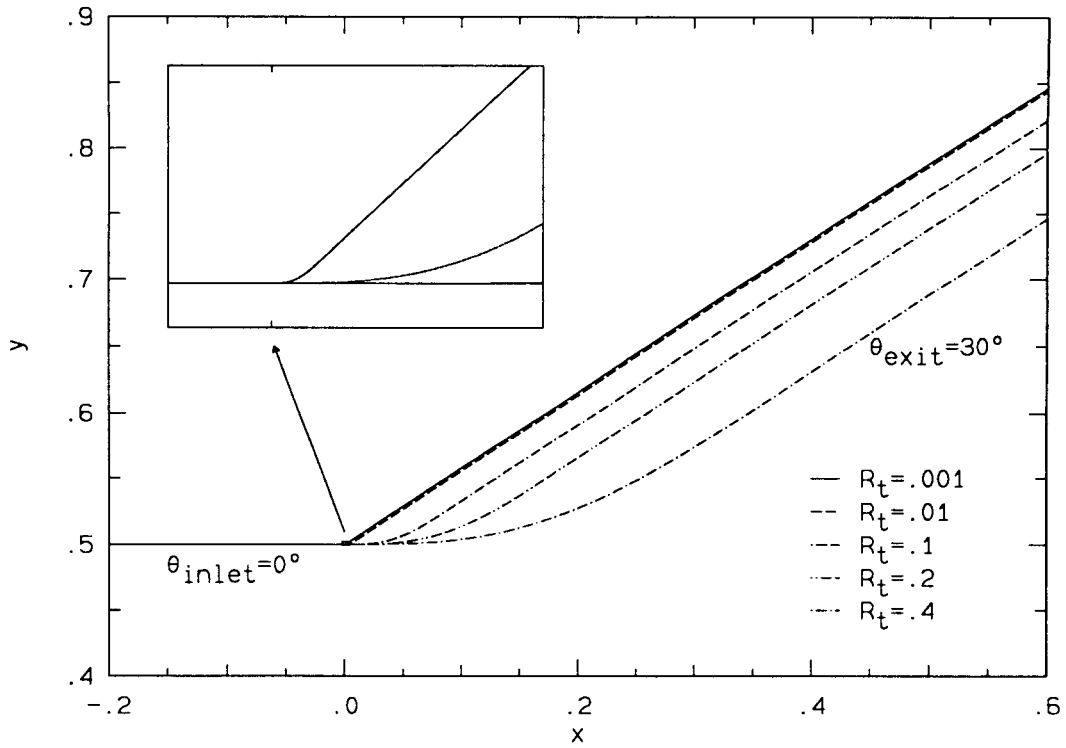


FIG. 7.2.2a Turn geometry for five radius of curvatures.

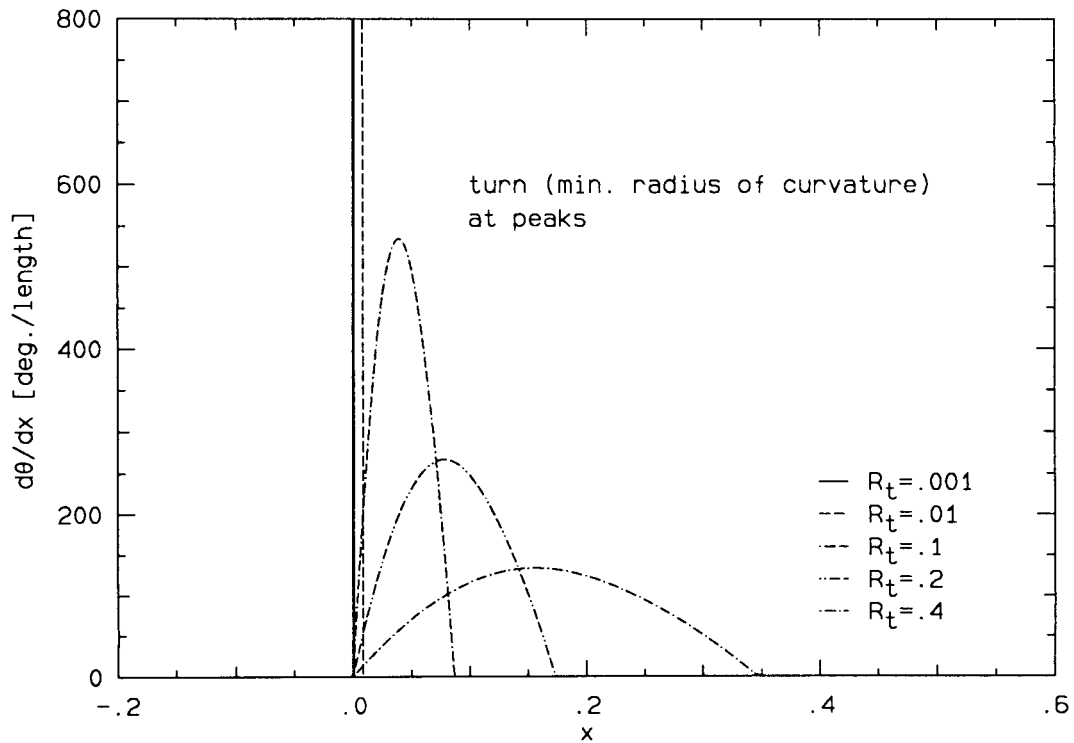


FIG. 7.2.2b Rate of turn for five radius of curvatures.

7.2.3 Nozzle dimensions

Not yet described are the two nozzle dimensions — the inlet height in the y -coordinate and the overall length in the x -coordinate. The inlet height is necessary in order to prescribe the wall geometries (*c.f.* equations 7.2.2.4). The length determines the domain of calculation since the problem is solved by marching in the x -direction (or ξ - equivalently). Upper limits on the dimensions may be estimated from the overall vehicle dimensions and its thrust requirement. This leads to an approximate nozzle size of:

$$\text{Nozzle Inlet Height} \lesssim 2 m$$

$$\text{Nozzle Overall Length} \lesssim 10 m$$

But nozzles of smaller scales can be used for analysis purpose.

A nozzle of smaller scale is sufficient for analysis purpose. However, in the context of finite-rate reactions, its dimensions must be large enough to allow (numerically) detectable chemical changes. Especially important is the relevant scale of the wall curvature. A chemical time can be defined as the duration over which significant chemical changes may occur. Let the minimum chemical time be denoted by τ_c , the corresponding length scale in the x -direction is approximately

$$L_x = q\tau_c \cos(|\theta|) .$$

The effect of chemical reaction in the y -direction is carried by the Mach waves characteristics as of any disturbance in a supersonic flow. Therefore,

$$L_y = q\tau_c \sin(|\theta| + \mu_f) .$$

The frozen Mach angle, μ_f , is to be introduced in chapter 8 where the supersonic characteristics in a reacting flow is discussed. Note that the scales depend on local variables and therefore are local scales. These length scales establish the lower limits for which finite-rate chemistry becomes important.

A lower limit of the time scale can be deduced empirically from the results of chapter 4. In the hydrogen-air system at interest, the smallest chemical time occurs during the branch-chain explosion of the stage of rapid energy release[‡]. The duration of explosion is of $\mathcal{O}(10^{-5})$ sec typically for the ranges of fuel-air ratio(0.6–1.4), initial temperature (850 K–2500 K) and pressure (0.1 atm–1.0 atm) considered. It is assumed that the explosion is mostly the result of one-way reactions so that the measured time reflects either the forward

[‡] An account on the subject is given in the last section of chapter 4.

or the reverse reaction rate rather than the combined production rate. Taking 10% of the explosion time as τ_c [‡] and a flow speed of $\mathcal{O}(10^3) m/s$, the minimum length scale in the flow direction would be:

$$\begin{cases} \tau_c \sim \mathcal{O}(10^{-6}) s \\ q \sim \mathcal{O}(10^3) m/s \\ \theta \sim 0 \end{cases} \implies L_x \sim \mathcal{O}(10^{-3}) m .$$

In other words, finite-rate chemistry may be significant even in a *millimeter* scale in the flow direction. It must be emphasized that L_x is a *lower* estimate; that is, chemical reactions in the nozzle system considered require at least L_x to achieve noticeable changes.

7.3 Setup of Preliminary Calculations

Some trial calculations have shown that a wide range of inlet conditions can be handled with the current formulation provided that $P(x_0, y)$ and $\theta(x_0, y)$ are sufficiently smooth distributions in y (and ψ). Applicability of the scheme, however, are very sensitive to the nozzle geometry. The capability and limitations of the computational nozzle model are demonstrated in four calculations: one with a step-like Mach number distribution at the inlet and three with different wall turn curvatures. The pressure, total enthalpy and species composition are uniformly distributed at the nozzle inlet and are identical in all three cases. Symmetric nozzles are used in the non-uniform inlet conditions case and two others. Walls with different turn curvature is used in the fourth case. Nevertheless, all cases have the same inlet height, the same exit angles and the same number of discretized streamlines.

The diffuser formulae of appendix II and combustor code of chapter 3 are used to arrive at the nozzle inlet conditions for the three cases. Specifically, the reference conditions listed in table 3.5 are used as inputs to the diffuser and the combustor. They are summarized as follows:

1. Ambient condition or diffuser inlet:
standard atmospheric pressure and temperature and composition; $M_\infty = 15$.
2. Diffuser exit or combustor inlet:
composition of air at equilibrium ; $\eta_{\text{eff}} = 0.985$; $M = 5$; $P = 1 \text{ atm}$; $\phi = 1.2$.
3. Combustor exit or nozzle inlet:
finite-rate chemistry and composition at 95% ΔH_{eq} ; $P = 1 \text{ atm}$.

[‡] This definition is equivalent to $\tau_c \simeq \Delta H_{eq} / \Delta \dot{H} \times 0.1$; *c.f.* chapter 4.

The point where the chemical heat release, ΔH , in the combustor reaches 95% of its equilibrium is taken as the nozzle inlet. This corresponds to a combustor length of 1.24 m. The *exit angle* is also chosen for a physical reason. A type of nozzle design discussed in section 7.2.2 is to have the combustor exit flow expand directly into the ambient stream. The nozzle wall is then equivalent to the dividing streamline between the oblique shock on the free-stream side and the expansion wave on the nozzle side. The conditions listed above or in table 3.5 lead to a specific flight condition. A two-dimensional steady shock-expansion fan matching calculation indicates that the dividing streamline has an initial angle of 19.604° relative to the free-stream.

The conditions just described lead to a set of nozzle inputs which are to be used in all calculations in this chapter as well as some in the next chapter. These inputs are collectively called **group 1** for the convenience of future reference. They are listed in table 7.3.1. Accordingly, the inputs to the four cases can be described in the much simplified format shown in table 7.3.2.

	Group1
Pressure P [atm]	1.0
Temperature T [K]	2757.5
Mach Number M	3.8008
Composition Y_{H}	0.0146×10^{-1}
Y_{H_2}	0.0761×10^{-1}
$Y_{\text{H}_2\text{O}}$	2.1026×10^{-1}
Y_{N}	0.0000×10^{-1}
Y_{N_2}	7.2908×10^{-1}
Y_{NO}	0.0144×10^{-1}
Y_{O}	0.0475×10^{-1}
Y_{O_2}	0.1207×10^{-1}
Y_{OH}	0.2053×10^{-1}
Y_{Ar}	0.1280×10^{-1}
Inlet Angle θ_{in} [deg]	0.0
Exit Angle θ_{ex} [deg]	19.604

TABLE 7.3.1 **Group 1** nozzle input parameters: inlet conditions and wall angles.

	Case 1	Case 2	Case 3	Case 4
Pressure	group 1			
Temperature	step-like*	group 1		
Mach Number	step-like*	group 1		
Composition	group 1			
Chemical Reaction State	<i>frozen</i>	<i>finite-rate</i>	<i>frozen</i>	<i>frozen</i>
Lower Wall: turn radius R_t [m]	1.00	0.80	0.10	0.20
turn begins x_1 [m]	0.00	0.00	0.00	0.00
turn at x_t [m]	0.267	0.213	0.0267	0.0534
turn ends x_2 [m]	0.534	0.427	0.0534	0.107
Upper Wall: turn radius R_t [m]	1.00	0.80	0.10	0.40
turn begins x_1 [m]	0.00	0.00	0.00	0.00
turn at x_t [m]	0.267	0.213	0.0267	0.107
turn ends x_2 [m]	0.534	0.427	0.0534	0.214
Inlet Height [m]	0.2			
No. of Streamlines N	41			

* See section 7.4

TABLE 7.3.2 Input parameters for 4 Cases.

7.4 Case 1: Inlet Mach number of a step-like hyperbolic tangent profile

There are two main reason for selecting this case. In the numerical point of view, a step-like Mach number distribution at the inlet is to introduce non-uniformities that may result in numerical problems. That is, the aim is to test the applicability of the code. In the analytic point of view, a step-like Mach may be used to simulate two layers of flow at different speeds and, that is, to create a rough approximation of a boundary layer and an outer flow. For this reason, a constant total enthalpy condition is imposed:

$$h_t = \frac{1}{2}q^2(x_0, y) + \sum_{k=1}^K h_k Y_k \Big|_{x_0, y} = \text{constant} .$$

The temperature distribution is then a result of the Mach number distribution.

The step-like Mach number to be used is defined by a hyperbolic tangent function. Suppose that the upper layer approaches Mach number M_U and the the lower layer approaches M_L , the distribution of Mach number at the inlet is

$$M_f(x_0, y) = \left(\frac{M_U + M_L}{2} \right) + \left(\frac{M_U - M_L}{2} \right) \tanh \left(\frac{y - y_{\text{step}}}{\delta y_{\text{step}}} \right) .$$

The condition is written in the x - y plane since the inlet condition is usually prescribed in the physical coordinates. The parameters y_{step} and δy_{step} are the center and width of the step respectively. The numbers used in this example are,

$$M_U = 3.8008$$

$$M_L = 2.2000$$

$$y_{\text{step}} = \text{nozzle inlet half-height,} \quad \text{and}$$

$$\delta y_{\text{step}} = \frac{\text{inlet width}}{N - 1} \times 3.$$

The step-width is chosen to span approximately three discrete streamlines. Furthermore, the value of h_t is taken to be

$$h_t = h_t(\text{at } M_f = M_U, T = 2757.5 \text{ K}).$$

This requirement limits the lowest value of M_L that can be used in the calculation. At the value of 2.2, the temperature in the low Mach number side is already 4900 K since the flow has extremely high enthalpy. Recall that the thermodynamic database is only available up to 5000 K . At the sonic point, the flow is estimated to have a temperature of 7000 K !

Although the Mach numbers are not drastically different, the streamline pattern of figure 7.4.1 clearly shows the two-layer nature of the flow. The streamline spacing is not uniform in the x - y since the inlet mass flux is not uniform. The density and speed are higher on the high Mach number side (upper-half) so that there are more streamlines. The feature of interest in the figure is the relative expansion ratios in the two streams. Both streams expand but the high Mach number side expands more.

The pressure along streamlines are shown in two plots: figure 7.4.2 for the lower wall up to streamline #18 and figure 7.4.3 for #19 up to the upper wall. Streamline #19 is approximately the point where the step-like inlet profile $M_f(x_0, y)$ begins to fall. The center of the step is between streamlines #13 and #14.

The distributions of P , T , M_f and q across the nozzle are plotted in figures 7.4.4, 7.4.5, 7.4.6 and 7.4.7 respectively at nine x -locations of 0.1 m interval. The pressure is uniform initially but subsequently altered by the wall turns as well as the disturbances from the step which are indicated by the inflexion in the curves. Step-like nature is found in the other plots. The width of the step increases in the streamwise direction but not to a large extent.

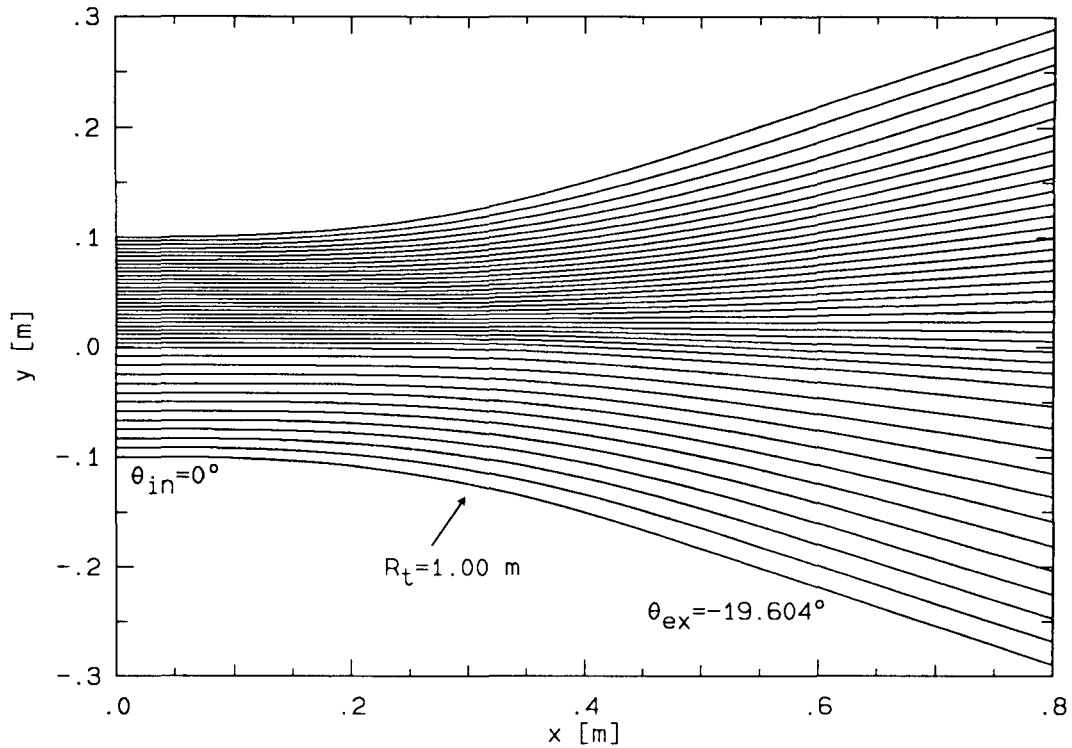


FIG. 7.4.1 Streamline pattern for a R_t of 1.00 m and a *step-like* inlet M_f .

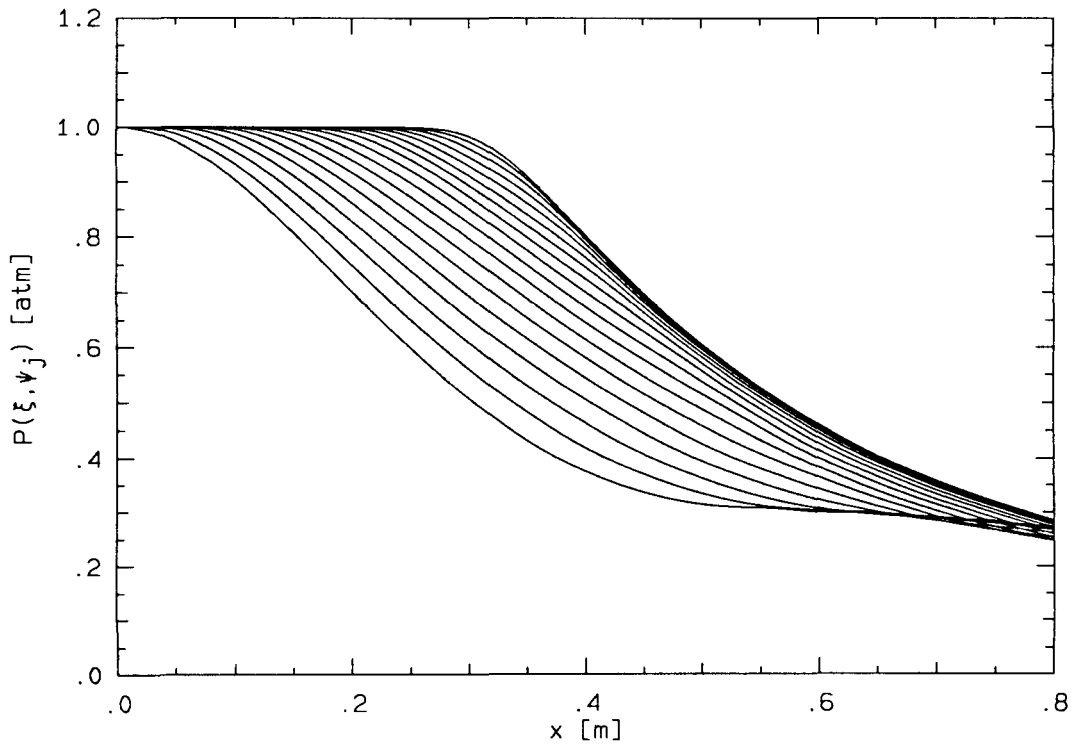


FIG. 7.4.2 Pressure along ψ_j , $j = 1, 18$ (bottom to top).

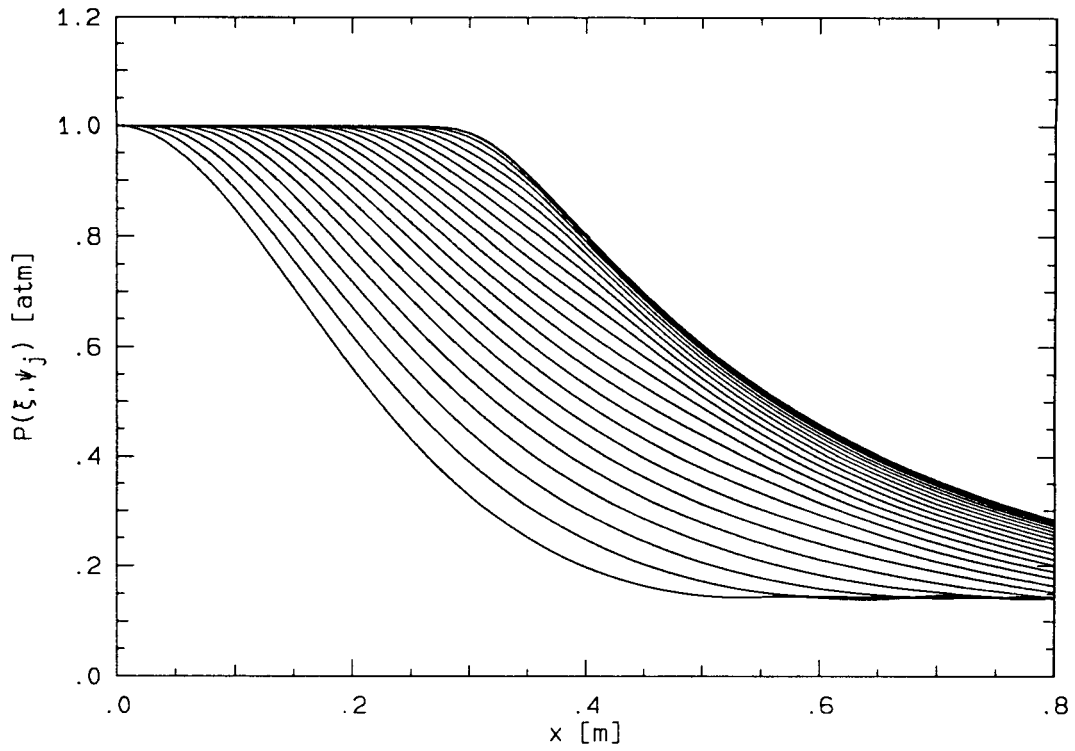


FIG. 7.4.3 Pressure along ψ_j , $j = 19, 41$ (top to bottom).

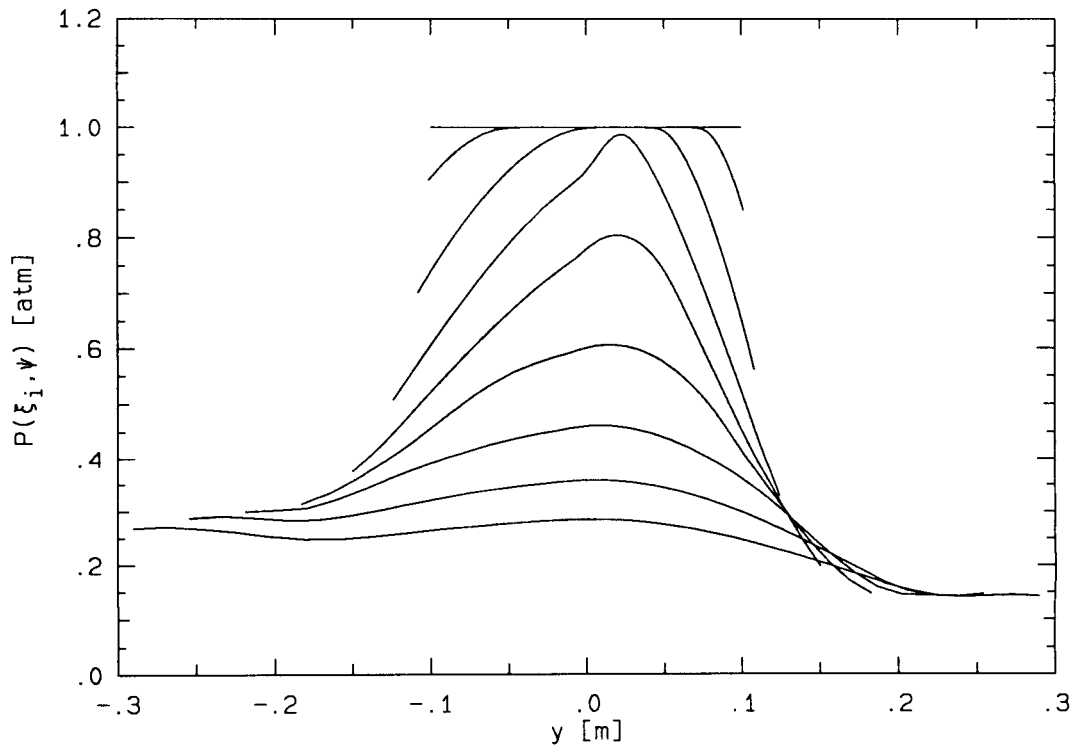


FIG. 7.4.4 Pressure across nozzle at $x_i = 0., .1, .2, \dots, .8$ m(top to bottom).

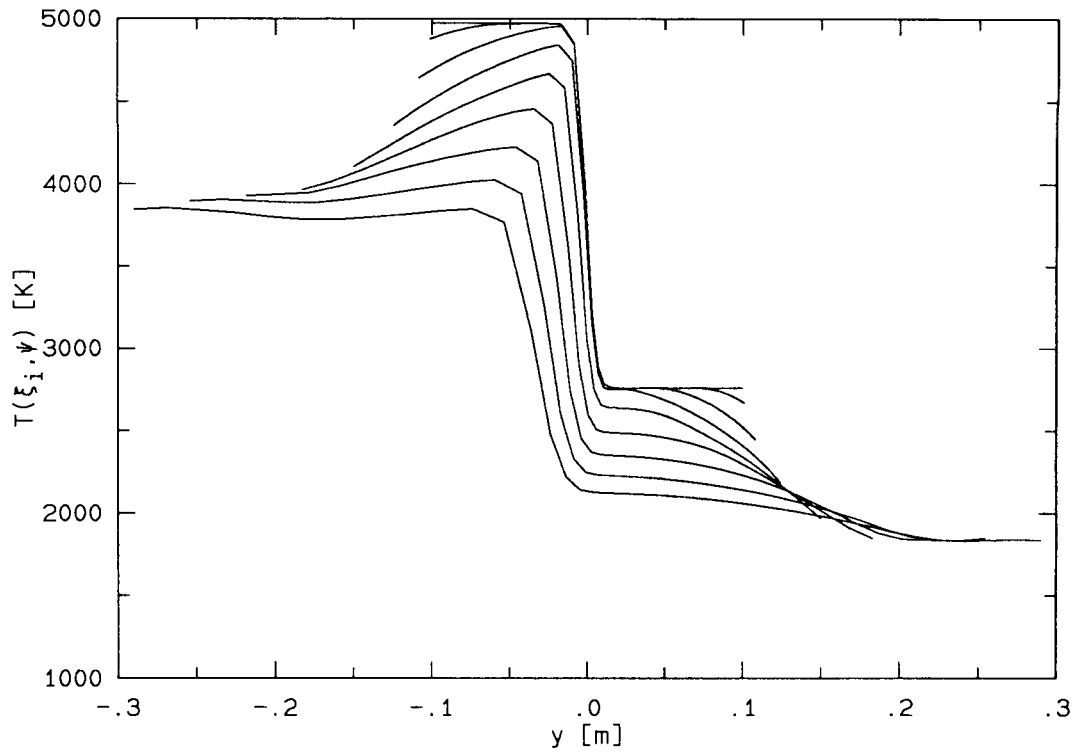


FIG. 7.4.5 Temperature across nozzle at $x_i = 0., .1, .2, \dots, .8 m$ (top to bottom).

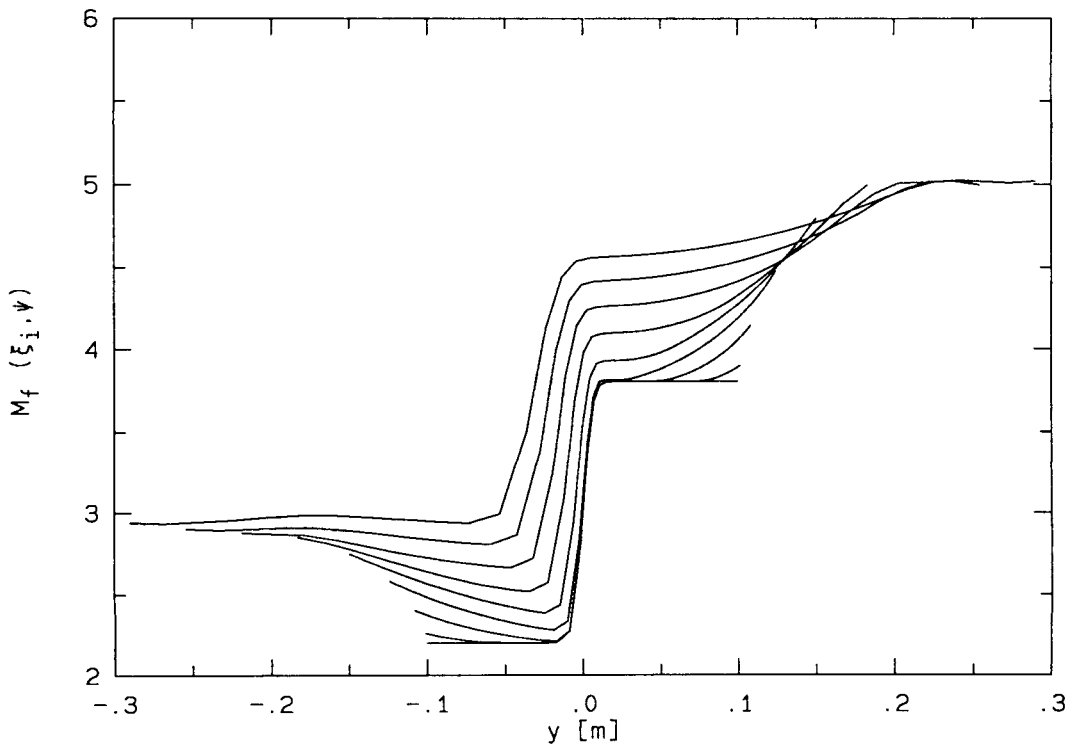


FIG. 7.4.6 Frozen Mach number across nozzle at $x_i = 0., .1, .2, \dots, .8 m$ (bottom to top).

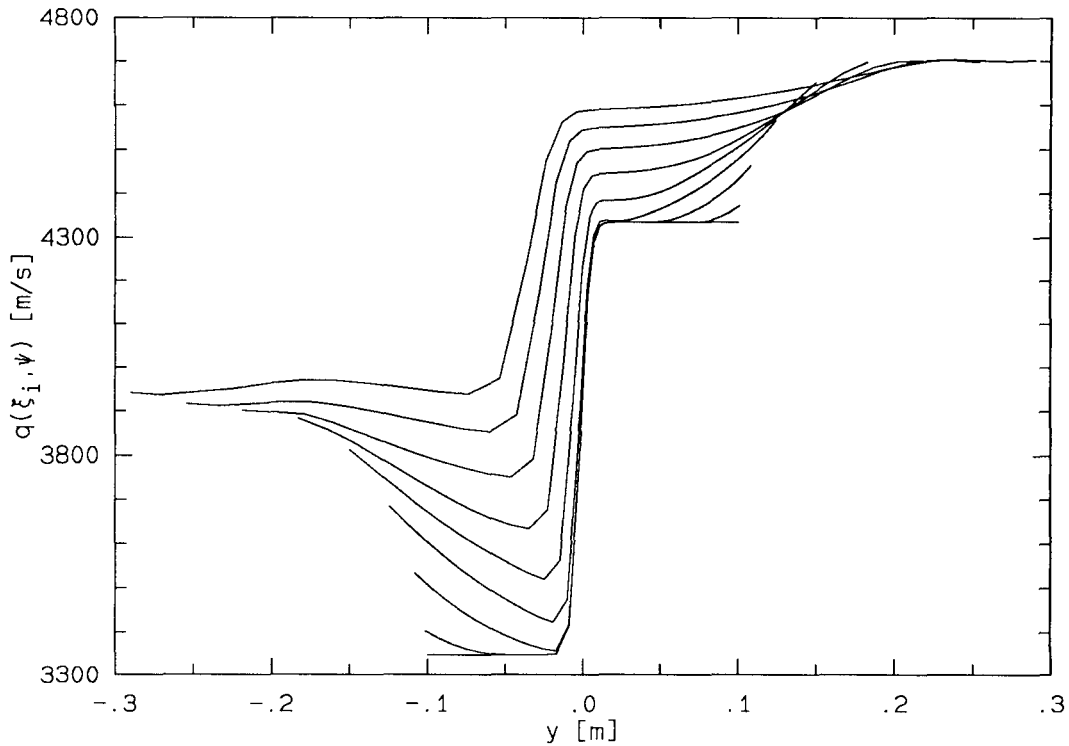


FIG. 7.4.7 Temperature across nozzle at $x_i = 0, .1, .2, \dots, .8 m$ (bottom to top).

7.5 Case 2: Uniform inlet conditions and a R_t of $0.8 m$ (i.e. $800 L_x$)

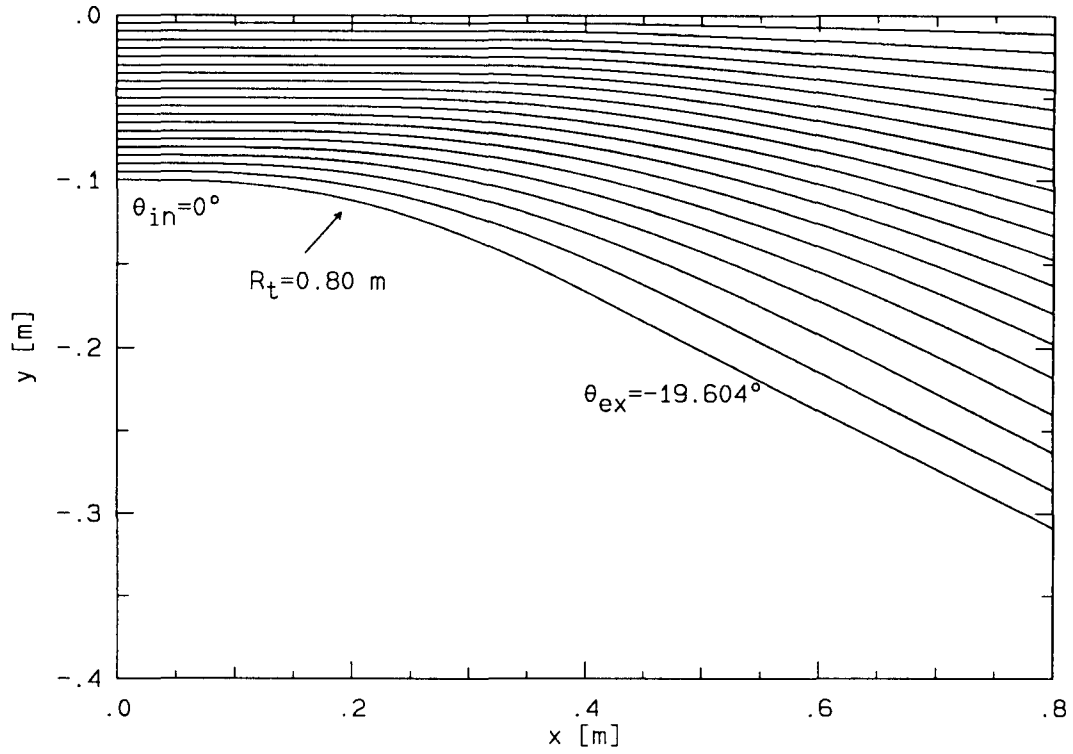
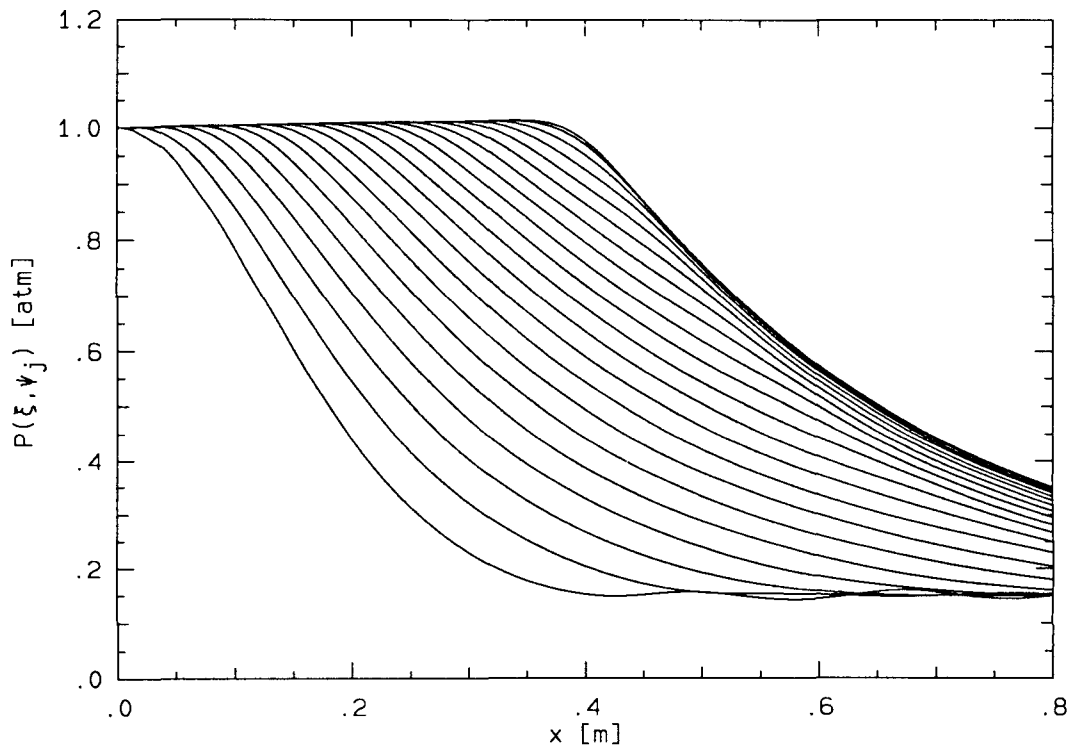
This example is constructed to simulate the effect of finite-rate chemistry on the flow variables in a *smooth* nozzle. The radius of curvature at the turn is large compared to the lower estimate of the reaction length L_x (c.f. section 7.2.3). Relatively speaking, most of the fast reactions should have time to exercise their effects before the effects of nozzle expansion set in. Consequently, flow variables are affected by the chemical reactions more so than the reverse. In terms of the nozzle height, R_t is 8 times the inlet half-width.

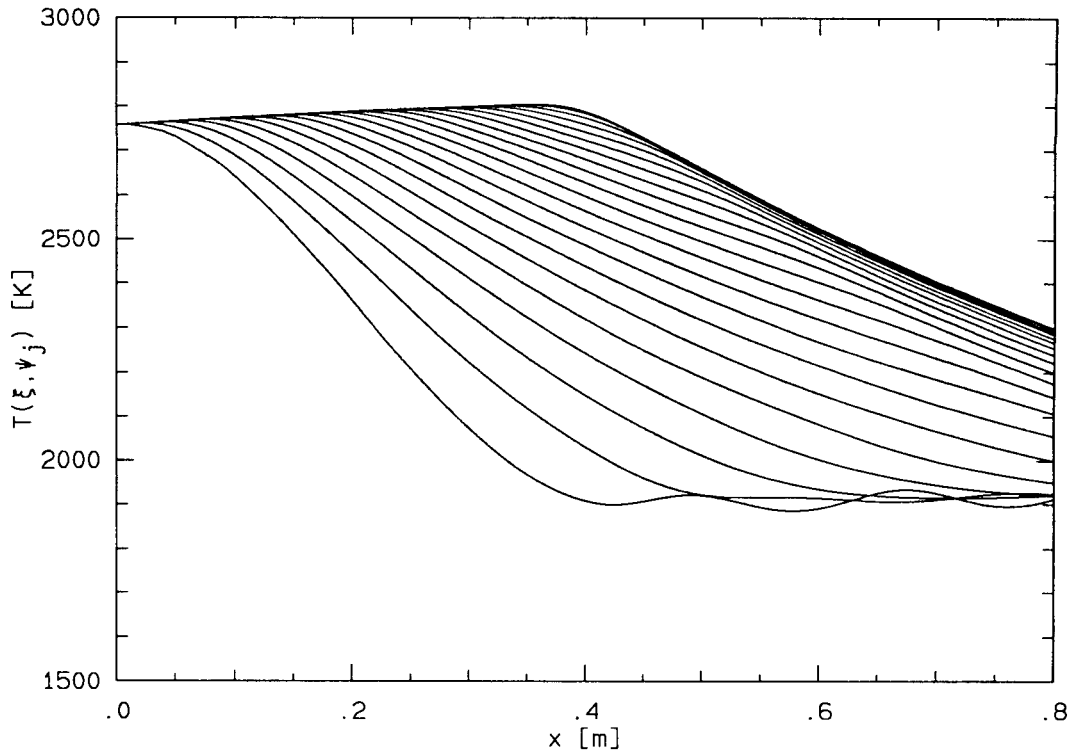
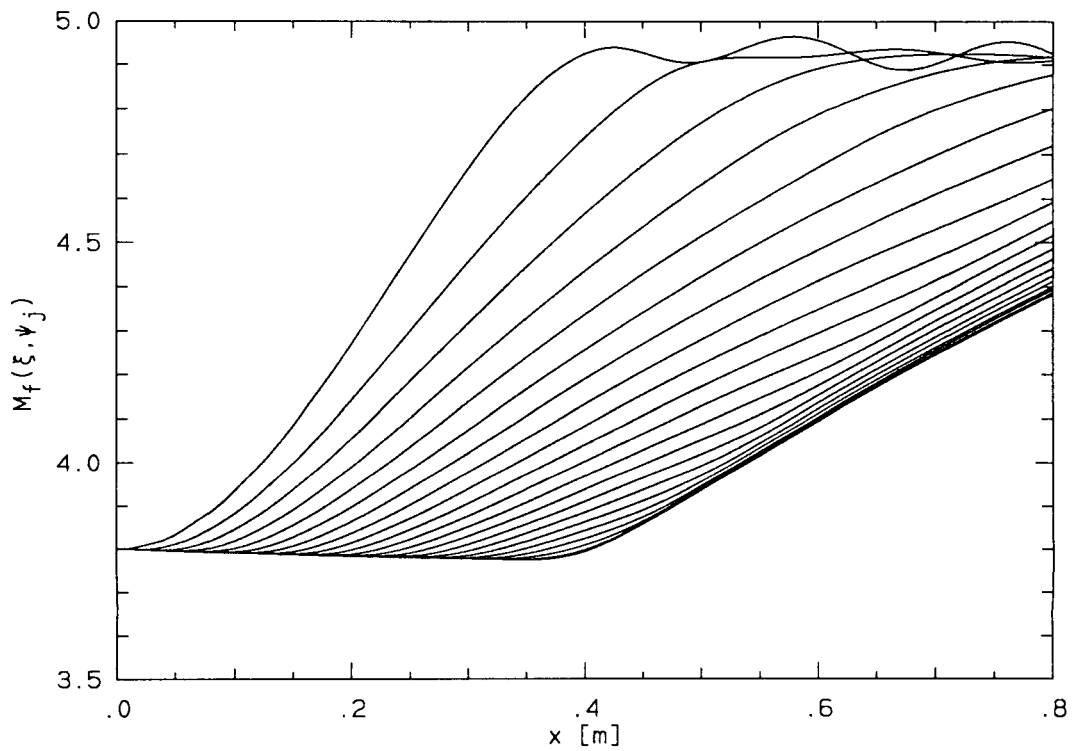
Since the inlet conditions are uniform, the results are presented along the discrete streamlines only. The streamline pattern along the wall up to the dividing streamline (nozzle is symmetric) is shown in figure 7.5.1. The pressure, temperature and Mach number distributions along those streamlines are shown in figure 7.5.2, 7.5.3 and 7.5.4 respectively.

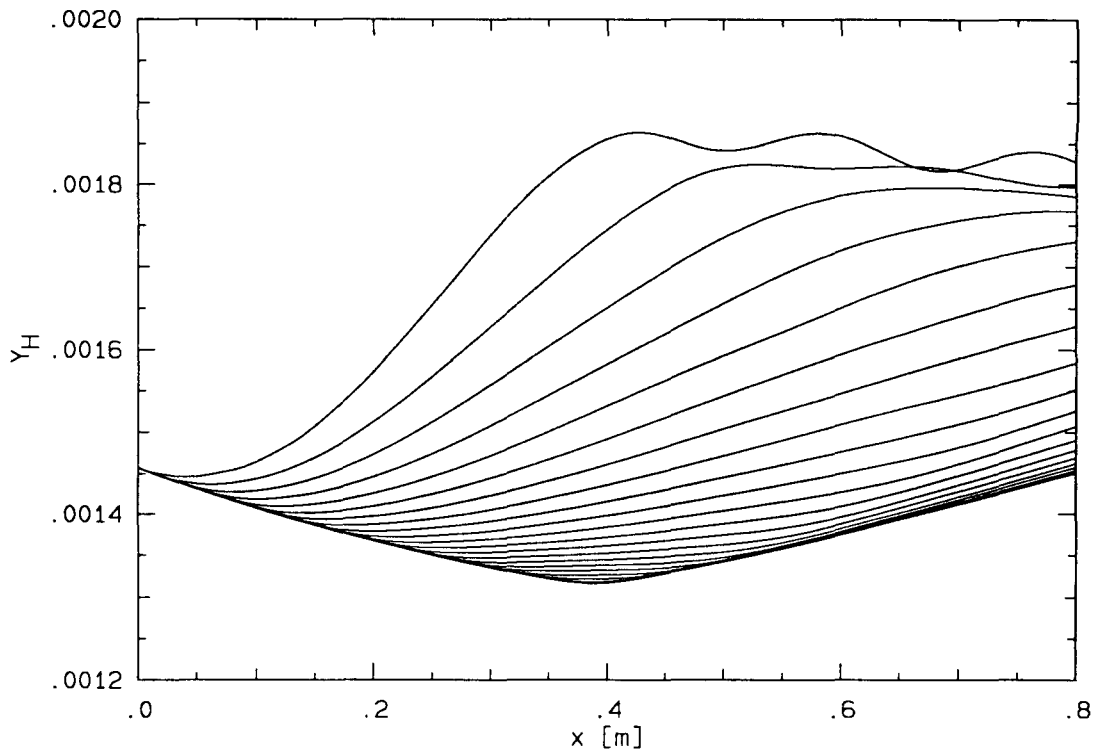
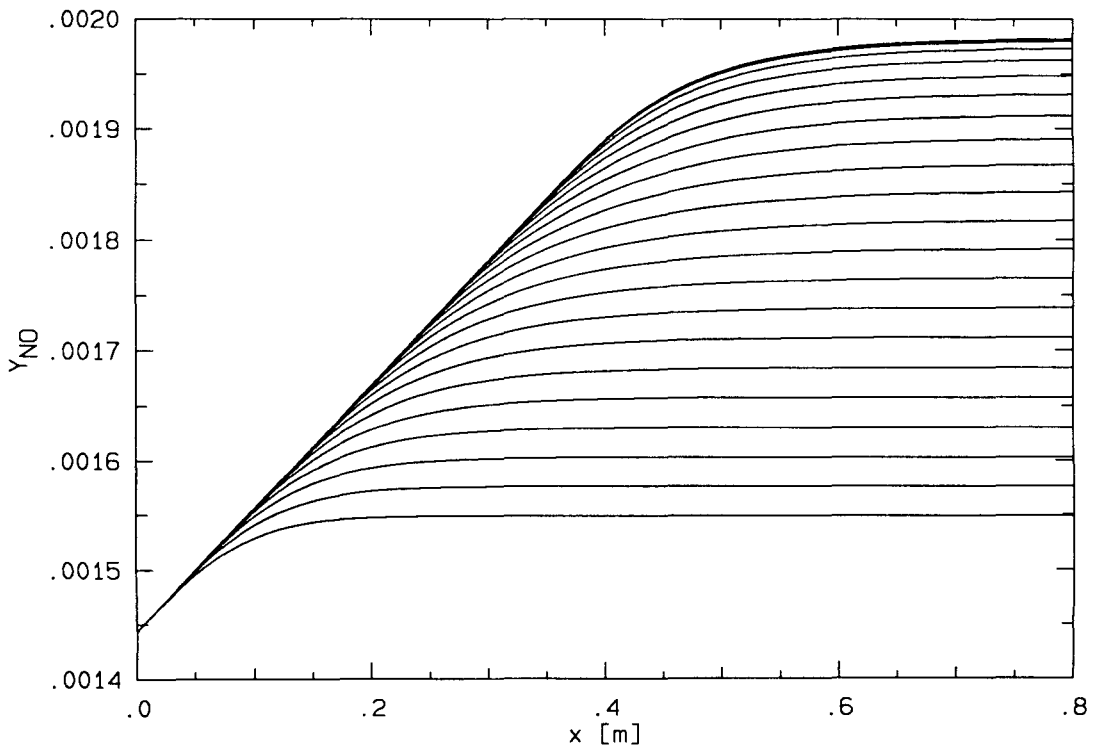
The overall effect of finite-rate reaction is best observed along the dividing streamline (#21). Slight increases in pressure and temperature are found which can only be explained by the presence of chemical reaction; otherwise, all variables should remain constant until the first disturbance from the wall has arrived. Recall that the inlet mixture is only at 95% of the combustor ΔH_{eq} . The behavior along the wall streamline cannot be described clearly due to numerical error. The only observable behavior is an increasing trend in temperature following the turn; thus indicating the effect of chemical reaction even when the pressure and temperature have dropped to approximately 0.14 atm and 1900 K . It has been found in chapter 4 that a hydrogen-air mixture can be very reactive at low pressure as long as sufficient active radicals are present; furthermore, a temperature of 1900 K is considered to be in the high range.

Mass fraction of the radical H is shown in figure 7.5.5. This species is of interest because it is essential for the formation of H_2O . Consider first along the dividing streamline or the lowest curve in the plot. Y_{H} drops initially, indicating its consumption, and then rises as the disturbance from the wall turn causes the pressure to drop. Along the wall streamline or the upper most curve, the increase in H follows shortly after the wall begins to turn. The important point is that the formation of H appears to be favored by an expansion. It can also be deduced that its formation is very sensitive to pressure changes since the pressure fluctuation (numerical error) along the wall is translated into a fluctuation in Y_{H} . It achieves a local maximum at the same point where P achieves a local minimum. It is unlikely that H is very sensitive to temperature since the T is at a local minimum at that point and the formation of radicals is rarely favored by a temperature drop.

A rather different behavior is presented by the radical NO. It is not considered an important species in the hydrogen-air combustion process, but some of the combustion energy can indeed be trapped in this radical. Its mass fraction is plotted in figure 7.5.6. Recall from chapter 4 that the chemical time scale for the NO_x reactions is much longer than that for H_2 -air combustion. Therefore, even though the nozzle inlet composition has been taken as the 95% ΔH_{eq} point of the combustor, the reaction in NO is far from equilibrium. The activity along the dividing streamline (the top curve in the figure) is explained by this fact. A feature observed in the figure is the phenomenon of *freezing*. Along the wall streamline, Y_{NO} becomes constant long before the turn has completed. Details regarding other species are discussed in latter sections after another scheme for handling the boundary error has been derived.

FIG. 7.5.1 Streamline pattern for a R_t of 0.80 m.FIG. 7.5.2 Pressure along ψ_j , $j = 1, 21$ (bottom to top).

FIG. 7.5.3 Temperature along ψ_j , $j = 1, 21$ (bottom to top).FIG. 7.5.4 Frozen Mach number along ψ_j , $j = 1, 21$ (top to bottom).

FIG. 7.5.5 Mass fraction of H along ψ_j , $j = 1, 21$ (top to bottom).FIG. 7.5.6 Mass fraction of NO along ψ_j , $j = 1, 21$ (bottom to top).

7.6 Case 3: Uniform inlet conditions and a R_t of $0.1 m$

This turn curvature is selected in an attempt to study the performance of the scheme when the turn curvature is of the same order as the inlet height while the number of discrete streamlines is of order 10. A frozen condition has been imposed on the chemistry. Since the results do present some numerical problems, no detail analysis is performed on the data. Shown in figure 7.6.1 are the pressure distribution along streamlines in the lower half nozzle. Numerical error is not obvious from the streamline pattern and is not shown. However, the pressure plot reveals that the pressure fluctuation along the wall is very large – much larger than in the case with R_t equals $0.8 m$ or $800 L_x$. This fluctuation is not confined to the wall but also displayed along the interior streamlines. A closer look at the numerical problem is given in section 7.8.

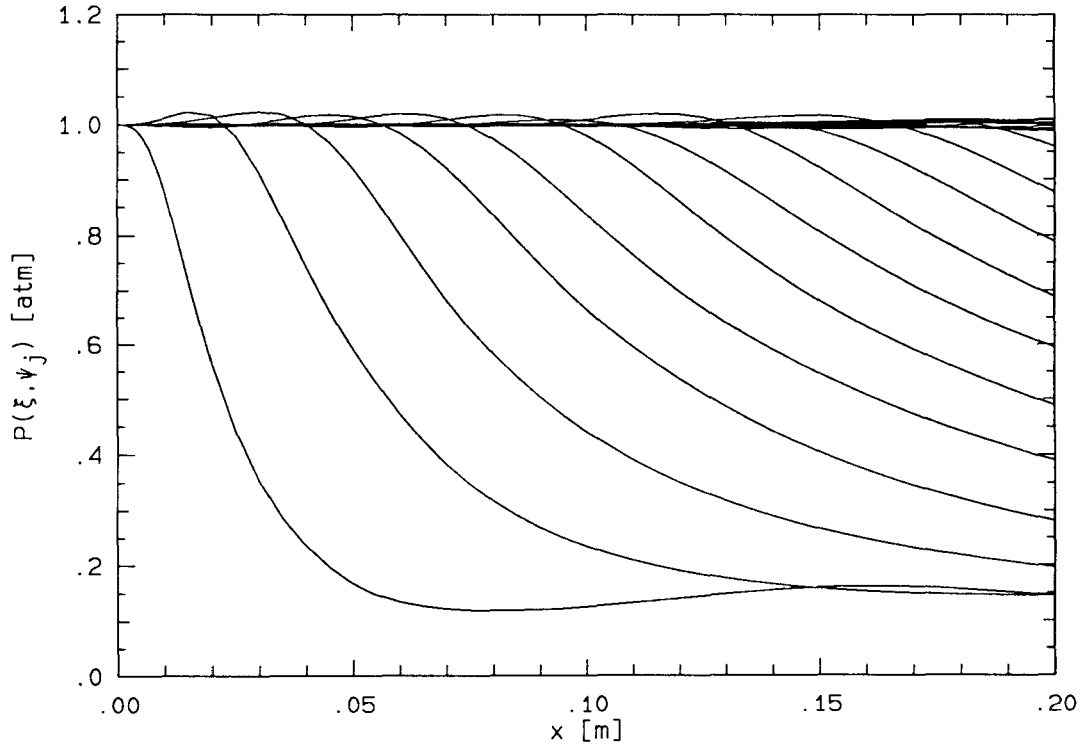


FIG. 7.6.2 Pressure along ψ_j for $R_t = 0.10 m$, $j = 1, 21$ (bottom to top).

7.7 Case 4: Uniform inlet conditions and R_t 's of 0.2 m and 0.4 m

It is sometimes likely that a scheme can handle symmetric geometry very well but fail in the other category. This calculation is constructed to answer this question. The turn radius is 0.20 m on the lower wall and 0.40 m on the upper wall. No unusual error due to non-symmetric geometry is observed in the results. The streamline pattern is shown in figure 7.7.1. Pressure along streamlines in the lower-half and upper-half nozzle are plotted separately in figures 7.7.2 and 7.7.3. Pressure fluctuations are still observed along the walls as in the previous cases.

Although the wall turns have different curvatures, they begin at the same x -location; and since the inlet condition is uniform, the disturbances from the two walls should arrive at the center streamline at the same point. Figure 7.7.4 shows that this requirement is satisfied. Pressure across the nozzle at five evenly spaced locations are plotted in the figure. On the last contour ($x = 0.4$ m), the disturbances from the walls meets exactly at the center ($y = 0$).

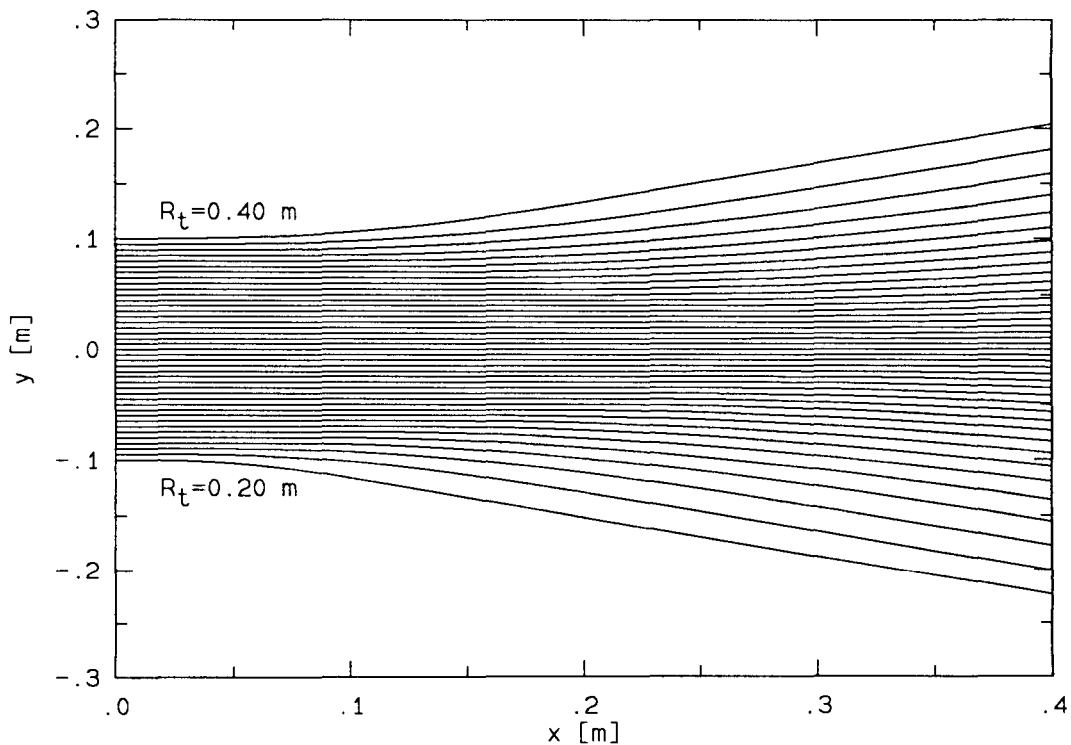
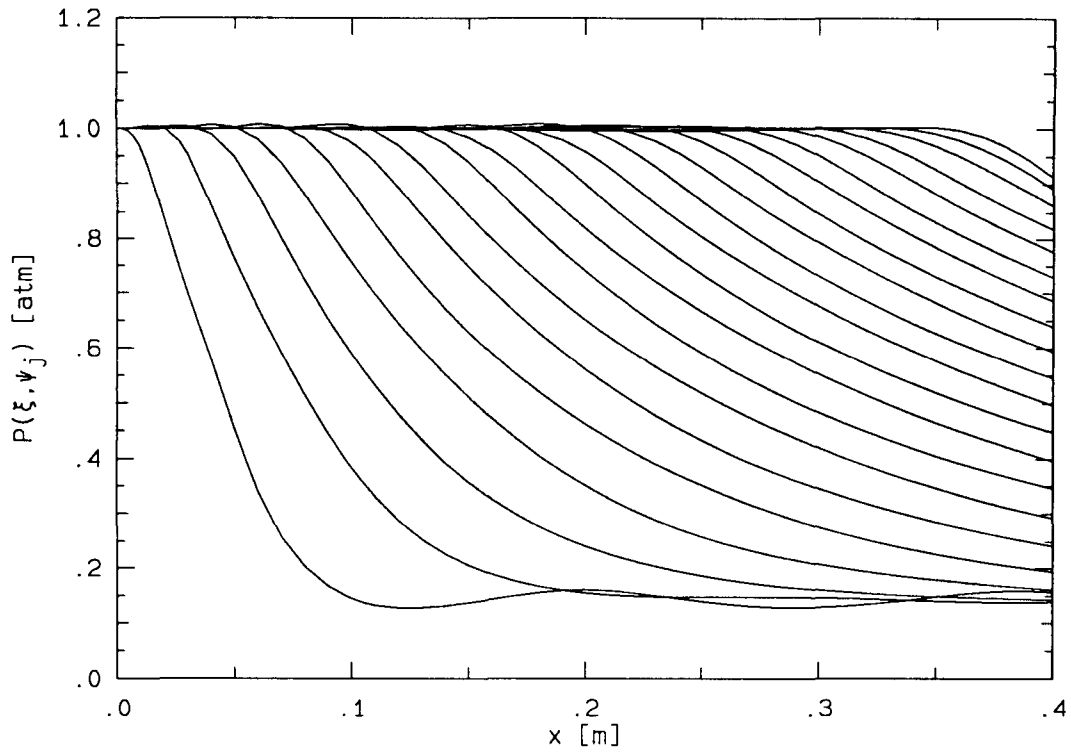
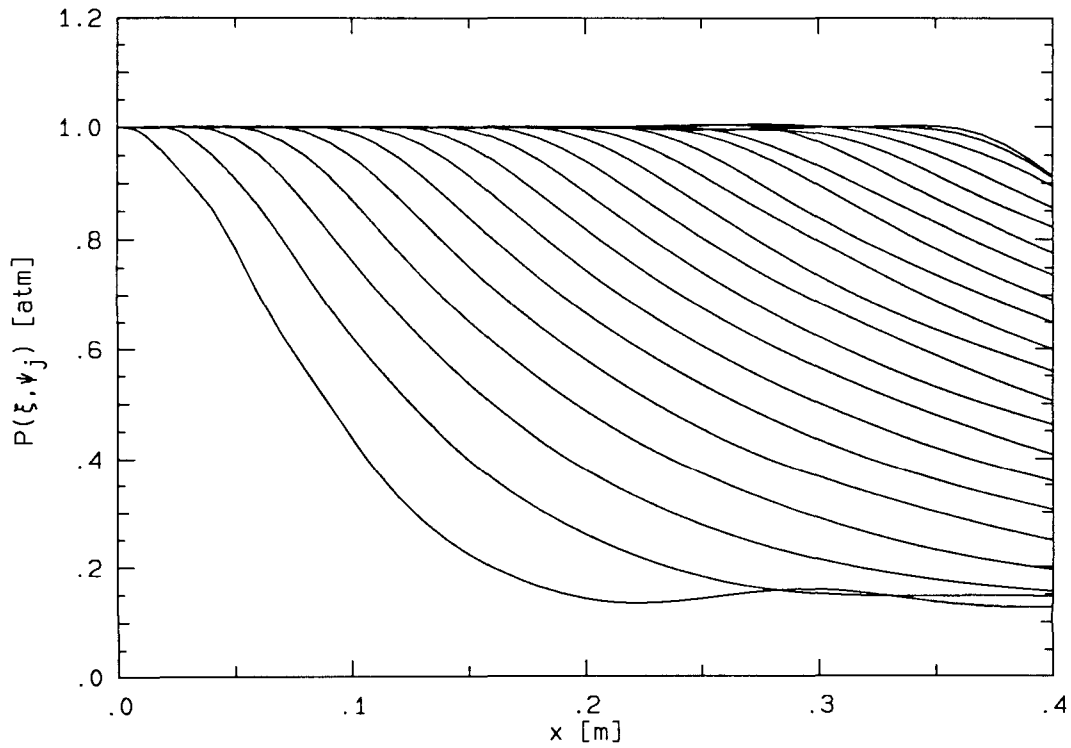


FIG. 7.7.1 Streamline pattern for a R_t of 0.80 m.

FIG. 7.7.2 Pressure along ψ_j , $j = 1, 21$ (bottom to top).FIG. 7.7.3 Pressure along ψ_j , $j = 21, 41$ (bottom to top).

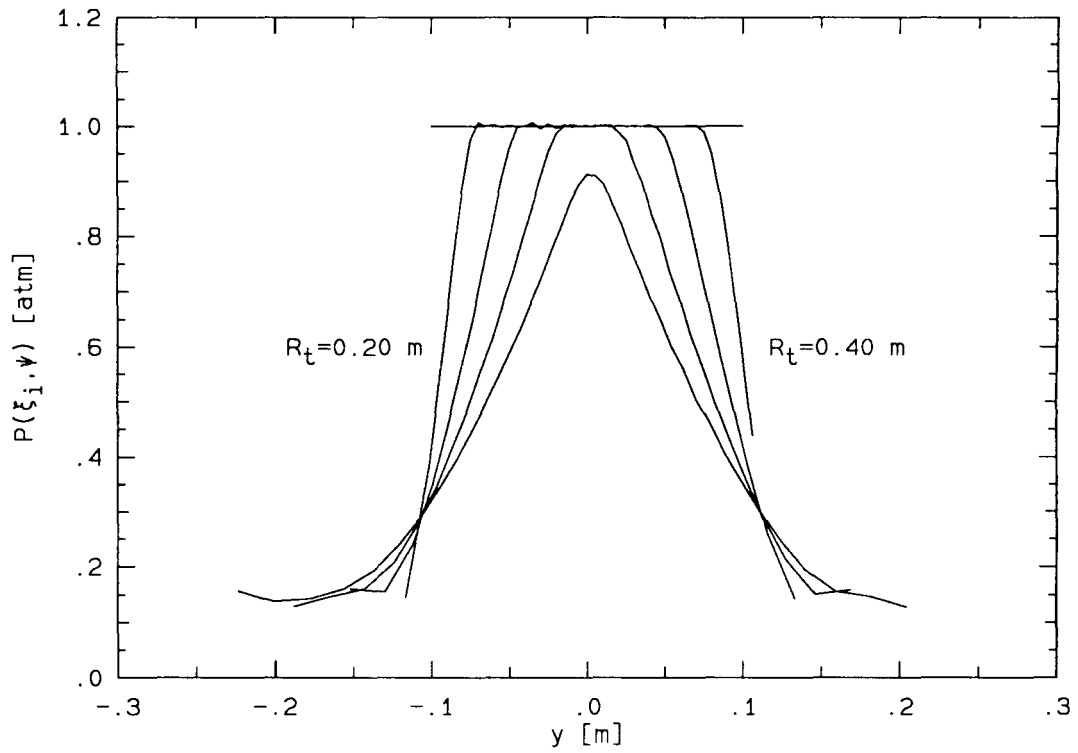


FIG. 7.7.4 Pressure across nozzle at $x_i = 0., .1, .2, .3, \& .4$ m (top to bottom).

7.8 Evaluation of the Numerical Scheme

Indicated by the examples in the previous sections is a degradation of accuracy in the numerical results with the sharpness of wall turn. Over the domains of calculation in those examples, the flow behavior along the walls in those examples should follow that of a simple wave. For cases 1 and 3 where *frozen* chemistry is imposed, the pressure, temperature, flow speed and so on along a wall streamline must be constant *downstream* of a turns*. The *finite-rate* chemistry in case 2 is not expected to alter this behavior very much. The computed results, however, indicate oscillatory distributions of those quantities along the wall streamlines as well as along the neighboring streamlines. Fluctuations along the wall streamlines are found to be most significant. The streamlines are also oscillatory in space except for those along the walls which are forced to concur with the nozzle geometries. In the examples, the amplitude of oscillation acquires a maximum in the first cycle following a turn and continues to attenuate in the streamwise direction. However, the maximum amplitude is found to increase rapidly with wall curvature.

7.8.1 Comments on the interpolation/extrapolation approach

Although there are many variables at concern, the error in the numerical solution is a result of the inability to predict $\partial P/\partial \xi|_{\psi_j}$ accurately along the N discretized streamlines ψ_j which in turn is due to the poor approximations of the ψ -derivatives P'_j and θ'_j ** . The oscillatory behavior described in earlier results indicate that P'_j and θ'_j must also be fluctuating with j . The interpolation/extrapolation method used to determine the $2N$ ψ -derivatives is described in section 6.7. The essential equations are restated here to aid the explanation:

$$\left. \begin{aligned} P'_1 + 4P'_2 + P'_3 &= \frac{3}{\Delta\psi}(P_3 - P_1) \\ P'_2 + 4P'_3 + P'_4 &= \frac{3}{\Delta\psi}(P_4 - P_2) \\ &\vdots \\ P'_{N-2} + 4P'_{N-1} + P'_N &= \frac{3}{\Delta\psi}(P_N - P_{N-2}) \end{aligned} \right\} \begin{array}{l} (N-2) P'_j \text{ equations} \\ \text{from Padé's scheme,} \end{array}$$

* That is, for $x_{\text{exit}} \leq x \leq x_2$ on each wall where x_2 is defined in section 7.2.2.

** $P'_j \equiv \frac{\partial P}{\partial \psi} \Big|_{\psi_j, \xi}$ and $\theta'_j \equiv \frac{\partial \theta}{\partial \psi} \Big|_{\psi_j, \xi}$ are derivatives along discretized streamlines ψ_j , $j = 1, N$.

$$\begin{array}{l}
 \theta'_1 + 4\theta'_2 + \theta'_3 = \frac{3}{\Delta\psi}(\theta_3 - \theta_1) \\
 \theta'_2 + 4\theta'_3 + \theta'_4 = \frac{3}{\Delta\psi}(\theta_4 - \theta_2) \\
 \vdots \\
 \theta'_{N-2} + 4\theta'_{N-1} + \theta'_N = \frac{3}{\Delta\psi}(\theta_N - \theta_{N-2})
 \end{array}
 \left. \vphantom{\begin{array}{l} \theta'_1 + 4\theta'_2 + \theta'_3 = \frac{3}{\Delta\psi}(\theta_3 - \theta_1) \\ \theta'_2 + 4\theta'_3 + \theta'_4 = \frac{3}{\Delta\psi}(\theta_4 - \theta_2) \\ \vdots \\ \theta'_{N-2} + 4\theta'_{N-1} + \theta'_N = \frac{3}{\Delta\psi}(\theta_N - \theta_{N-2}) \end{array}} \right\} \begin{array}{l} (N-2) \theta'_j \text{ equations} \\ \text{from Padé's scheme,} \end{array}$$

$$\begin{array}{l}
 \theta'_n = \frac{1}{12\Delta\psi}(\theta_{n-2} - 8\theta_{n-1} + 8\theta_{n+1} - \theta_{n+2}) \\
 \theta'_{N-n+1} = \frac{1}{12\Delta\psi}(\theta_{N-n-1} - 8\theta_{N-n} + 8\theta_{N-n+2} - \theta_{N-n+3})
 \end{array}
 \left. \vphantom{\begin{array}{l} \theta'_n = \frac{1}{12\Delta\psi}(\theta_{n-2} - 8\theta_{n-1} + 8\theta_{n+1} - \theta_{n+2}) \\ \theta'_{N-n+1} = \frac{1}{12\Delta\psi}(\theta_{N-n-1} - 8\theta_{N-n} + 8\theta_{N-n+2} - \theta_{N-n+3}) \end{array}} \right\} \begin{array}{l} 2 \text{ derivatives} \\ \text{from differencing,} \end{array}$$

and

$$\begin{array}{l}
 a_l P'_1 + b_l \theta'_1 = c_l \\
 a_u P'_N + b_u \theta'_N = c_u
 \end{array}
 \left. \vphantom{\begin{array}{l} a_l P'_1 + b_l \theta'_1 = c_l \\ a_u P'_N + b_u \theta'_N = c_u \end{array}} \right\} \begin{array}{l} 2 \text{ analytic relations} \\ \text{from wall boundaries.} \end{array}$$

This constitutes a set of $2N - 2$ difference equations in combination with two analytic expressions relating P' and θ' at the walls. The fluctuation of P'_j and θ'_j with j is a result of the $2N - 4$ implicit *Padé* equations which simulate exactly the *cubic spline* conditions. The errors introduced by the two difference equations for θ'_n and θ'_{N-n+1} are carried to all θ'_j for j equals 1 to N through the implicit scheme. Errors are then transferred to P' at the boundaries through the analytic expressions and eventually to all P'_j through the implicit scheme. The results are simply two wavy spline fits for $P(\psi)$ and $\theta(\psi)$.

It must be emphasized again that even though the error originates from the two explicit difference equations imposed for θ'_n and θ'_{N-n+1} , it is the two analytic conditions imposed at the boundaries that transfers the error to P'_j . The resulting error may either be amplified or reduced depending on the magnitudes of the coefficients a , b and c in the conditions. The dependence of c on the wall curvature (*c.f.* equations IV.7a and b) is directly responsible for the dependence of the error on turn curvature.

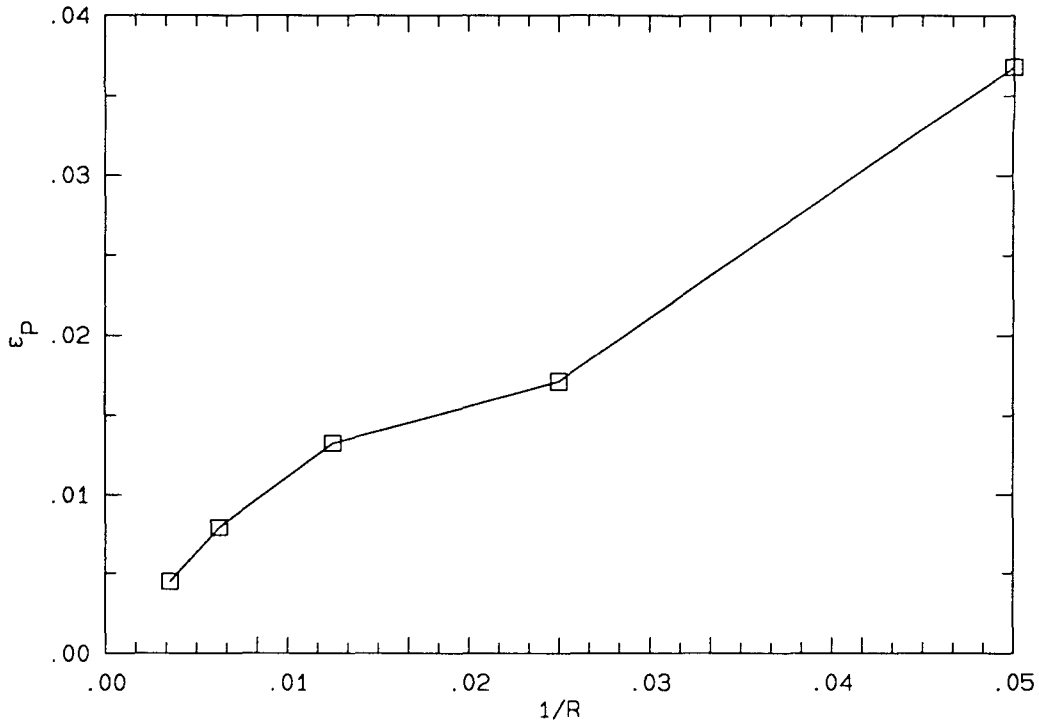


FIG. 7.8.2.1 Numerical error for five resolutions.

7.8.2 Limitation

This problem inherent with the numerical scheme has imposed a severe limitation to the range of nozzle geometries that can be analyzed. The error is driven by the lack of cross-stream resolution relative to the turn radius. However, to increase the resolution in a reacting flow calculation is expensive. The relationship between numerical error and resolution for the present scheme is estimated from the calculations in sections 7.4 to 7.7.

Numerical error is measured in terms of the wall pressure since it is the origin of the problem. In the four examples considered, simple wave conditions are satisfied along the walls. Therefore, the error may be quantified by

$$\epsilon_P \equiv \left(\frac{\max |P - P_{\text{simple wave}}|}{P_{\text{inlet}}} \right)_{\text{wall}} . \quad (7.8.2.1)$$

The simple wave solution is considered in chapter 8. The resolution is measured as the ratio of the wall turn radius to the streamline separation at the inlet. That is,

$$\bar{R} \equiv \frac{R_t}{(\Delta y)_{\text{inlet}}} . \quad (7.8.2.2)$$

The inlet streamline separation is uniform in all the examples except for the one in section 7.4. In that case, $(\Delta y)_{\text{inlet}}$ is the one nearest to the wall where ϵ_P is measured. The variation of ϵ_P with $1/\bar{R}$ is plotted in figure 7.8.2.1. Although the error approaches zero linearly as $1/\bar{R}$ does, it also grows exponentially with $1/\bar{R}$.

CHAPTER 8

Reacting Flow in a Two-Dimensional Expansion Nozzle**Part III: Characteristic Boundary Condition****8.1 Introduction**

To improve the accuracy of the numerical solution, the treatment of the boundary condition, namely the geometry, is to be modified. The former method employs a rather indirect approach (*c.f.* section 6.7). The boundary conditions are imposed on P'_1 , P'_N , θ'_1 and θ'_N which are then used to evaluate $\partial P/\partial \xi|_{\text{walls}}$ and subsequently other ξ -derivatives along the walls. The aim of the new approach is to relate the boundary conditions and $\partial P/\partial \xi|_{\text{walls}}$ or P directly. Since the nozzle is assumed to operate in the supersonic regime only, the desired connection is best provided by the supersonic characteristics.

Supersonic characteristics are known to be extremely useful for handling tough geometries. The characteristic equations and their application are very simple for a calorically perfect and non-reacting gas. In the current situation, a calorically imperfect and reacting gas is desired. The governing equations are also quite simple but their application is significantly more difficult. Therefore, the characteristic treatment is only applied to handle the boundary conditions while the formulation derived in chapter 6 remains in effect for the interior.

8.2 Characteristics Solution at Wall Boundaries — Simple Wave Solution

Before attempting the general solution, a specific case is considered — one of a *simple wave*. It presents the simplest solution obtainable from the supersonic characteristic formulation. The simple wave solution is valid in a nozzle with uniform inlet conditions up to the point where the first disturbance from one family of characteristic meets that from the other family. In the examples shown in sections 7.4, 7.6 and 7.7, the simple wave solution is indeed the valid solution. For cases with finite-rate chemistry, such as the one in section 7.5, the simple wave assumption is not satisfied. But it is nevertheless a good approximation if the disturbance from finite-rate chemistry is small compared to the effect of expansion.

Vincenti^[14] (1965) has derived a set of supersonic characteristic equations for a reacting flow. These equations can be manipulated based on the simple wave assumption to produce an expression relating $\partial P/\partial \xi$ and $\partial \theta/\partial \xi$ along a wall. Since $d\theta_{\text{wall}}/d\xi$ is known from the geometry, the desired quantity, $\partial P/\partial \xi|_{\text{wall}}$, is also known. The procedure is straight forward and the results are:

$$\sqrt{M_f^2 - 1} \frac{\partial P}{\partial \xi} = +\rho q^2 \frac{d\theta_l}{d\xi} - \frac{a_f}{\bar{C}_p T} \frac{1}{\cos(\theta_l - \mu_f)} \sum_{k=1}^K h_k m_k \dot{\omega}_k \quad \text{and} \quad (8.2.1a)$$

$$\sqrt{M_f^2 - 1} \frac{\partial P}{\partial \xi} = -\rho q^2 \frac{d\theta_u}{d\xi} - \frac{a_f}{\bar{C}_p T} \frac{1}{\cos(\theta_u + \mu_f)} \sum_{k=1}^K h_k m_k \dot{\omega}_k \quad (8.2.1b)$$

along the *lower* and *upper* walls respectively. The equations are different since different families of characteristics have been used. $d\theta_l/d\xi$ and θ_u are boundary conditions given by the wall geometries. The variables introduced by the characteristic method are M_f , a_f and μ_f . The significance of the frozen Mach number M_f is cited in section 6.5.1. It is defined as

$$M_f = \frac{q}{a_f} ,$$

where

$$a_f^2 \equiv \left(\frac{\partial P}{\partial \rho} \right)_{S, Y_k} = \frac{\bar{C}_p R_u}{\bar{C}_v \bar{m}} T .$$

An alternative expression for a_f can be found in appendix I. The above form is chosen such that a_f can be evaluated by knowing the temperature and composition only*. The frozen Mach angle, μ_f , depends only on M_f as in

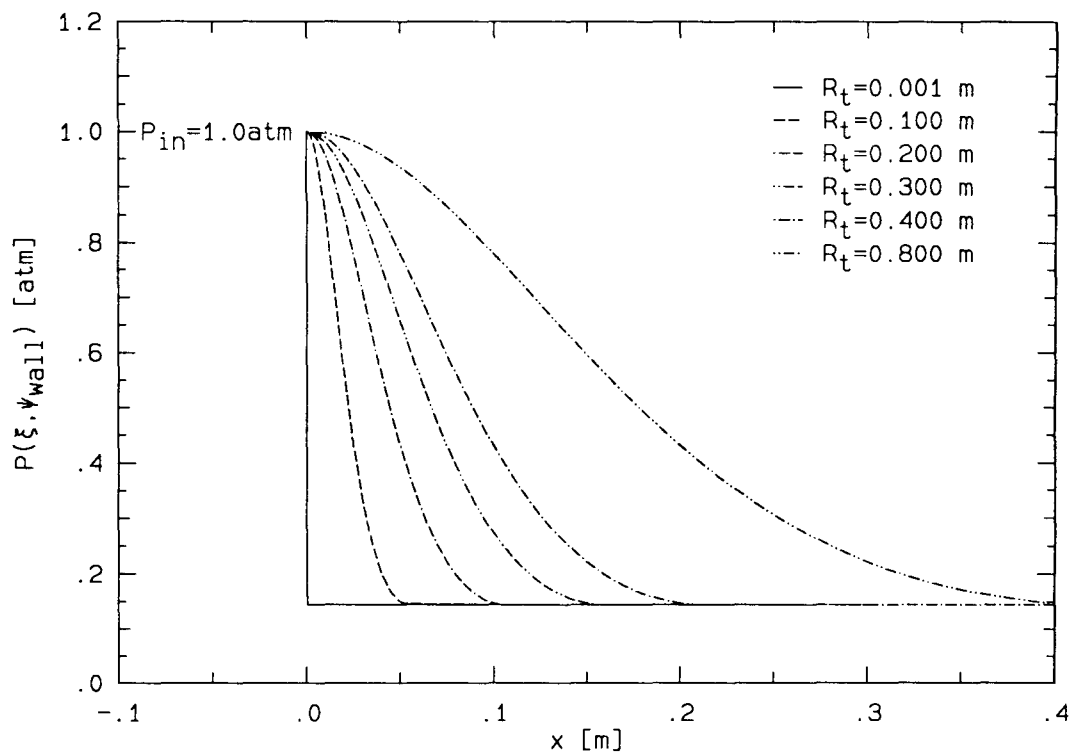
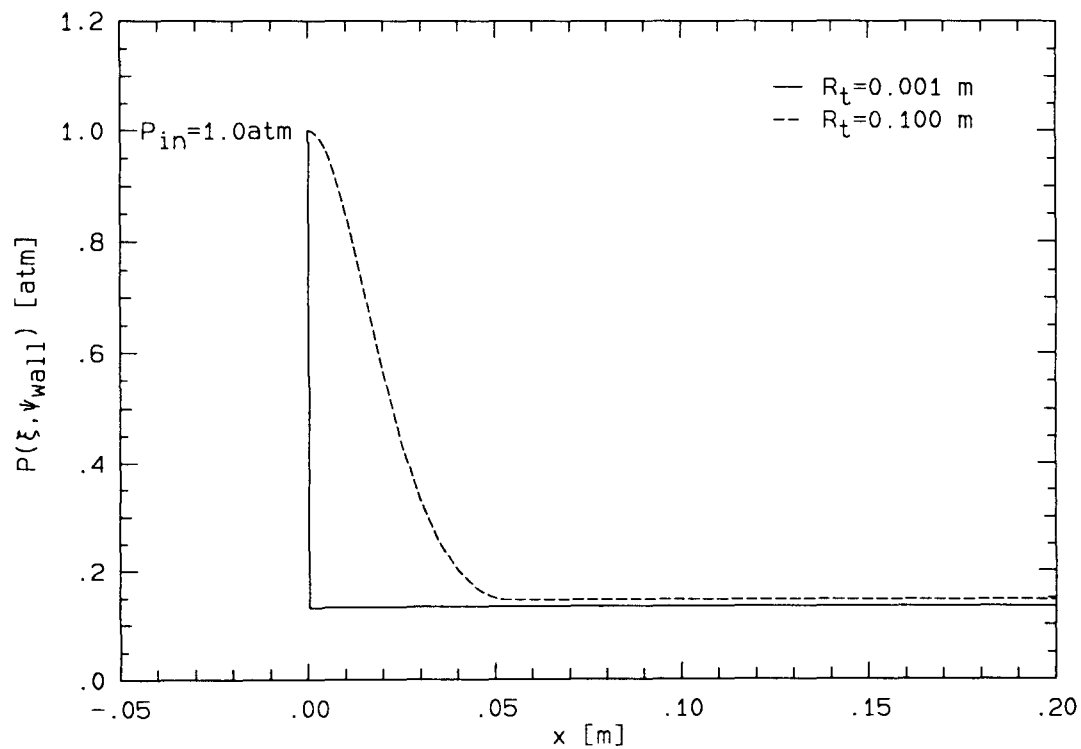
$$\tan \mu_f = \frac{1}{\sqrt{M_f^2 - 1}} \quad \text{or}$$

$$\sin \mu_f = \frac{1}{M_f} .$$

With the knowledge of $\partial P/\partial \xi|_{\text{walls}}$, the other ξ -derivatives along the walls are readily obtained (*c.f.* section 6.5). There is then no need to find P'_1 , P'_N , θ'_1 or θ'_N and the *Padé's* scheme can be replaced by center differencing to obtain the interior ψ -derivatives. Alternatively, the *Padé's* scheme can be preserved, but the four boundary derivatives must first be evaluated. This can be accomplished using equations 6.5.3b and 6.7.5 (or equations IV.2 and IV.5). It turns out a combination of the methods performs the best: center differencing for θ'_j and *Padé's* scheme for P'_j .

* Recall that $\bar{C}_p = \sum_{k=1}^K C_{pk}(T)Y_k$, $\bar{C}_v = \bar{C}_p - \frac{R_u}{\bar{m}}$ and $\bar{m} = \sum_{k=1}^K m_k Y_k$.

The numerical results of the simple wave solution are extremely good. Using the **group 1** input conditions of table 7.3.1, six frozen cases of wall turn radii 0.800, 0.400, 0.300, 0.200, 0.100 and 0.001 meters are computed. The pressure along the wall is plotted in figure 8.2.1. No oscillation is observed for any of the curvatures in the figure. In fact, the distributions of P , T and q are smooth along all streamlines. The smoothness is maintained even when the turn radius is in the *millimeter* scale. As the chemistry is frozen in these calculations, the introduction of finite-rate reactions with a simple wave approximation does not affect the stability of the approximate solution. The cases of R_t equals 0.100 and 0.001 with finite-rate chemistry are repeated. The wall pressure is plotted in figure 8.2.2.

FIG. 8.2.1 Wall pressure with 6 turn curvatures (*frozen* chemistry).FIG. 8.2.2 Wall pressure with 2 turn curvatures (*finite-rate* chemistry).

8.3 Characteristics Solution at Wall Boundaries — General Approach

A more general scheme can be derived based on the fundamental principles of supersonic characteristics. Without the simple wave assumption, analytic expressions for $\partial P/\partial \xi|_{\text{walls}}$ are no longer available. Numerical approximations must be used to implement the basic characteristic equations. The first task is to accurately translate the governing differential equations into a set of difference equations for P_{walls} , T_{walls} , q_{walls} and $Y_{k \text{ walls}}$. The final burden is to solve those nonlinear algebraic equations effectively.

In this formulation, the values of all the dependent variables are known at the boundaries. The differential equations $\partial P/\partial \xi, \dots$ and $\partial Y_k/\partial \xi$ derived in chapter 6 need only be integrated along the interior streamlines ψ_j for j equals 2 to $N - 1$. The P'_j and θ_j derivatives necessary for the evaluation of the ξ -derivatives are obtained with the same methods discussed in the simple wave solution — either through center differencing or the *Padé's* scheme. In case of the *Padé's* scheme, the values of $\partial P/\partial \xi|_{\text{walls}}$ can be approximated by numerical differencing.

There are three sets of characteristics in supersonic reacting flow. One of them, the streamline, has already been considered at length in chapter 6. The other two, the *frozen* Mach waves, are to provide the necessary information for the new boundary treatment. Derivation of the characteristic equations with chemical reactions is similar to the one without. The result obtained by Vincenti^[14] is adopted for the present purpose. Identifying the two Mach wave families by C_+ and C_- , their paths are described by

$$C_{\pm} : \frac{dy}{dx} = \tan(\theta \pm \mu_f). \quad (8.3.1)$$

The differential relations along C_{\pm} are

$$\sqrt{M_f^2 - 1} dP \pm \rho q^2 d\theta + \frac{a_f}{C_p T} \sum_{k=1}^K h_k m_k \dot{\omega}_k d\eta_{\pm} = 0 \quad (8.3.2)$$

respectively. $d\eta_{\pm}$ are the differential path lengths along the characteristics. The other quantities, M_f , a_f and μ_f , have been introduced in section 8.2. The arrangement of the three characteristics can be found in many references (*e.g.*, see Vincenti^[14]).

The equation of a Mach wave approaching a wall must be used in combination with the equations along a wall to solve for the dependent variables P_{wall} , T_{wall} , q_{wall} and $Y_{k \text{ wall}}$. The differential equations along the streamline characteristic are derived in chapter 6. They are evaluated at the walls to become:

$$\left. \frac{\partial T}{\partial \xi} \right|_{\xi, \psi_{\eta}} = \frac{1}{\rho C_p} \left(\frac{\partial P}{\partial \xi} - \frac{1}{q \cos \theta} \sum_{k=1}^K h_k m_k \dot{\omega}_k \right) \Big|_{\xi, \psi_{\eta}},$$

$$\left. \frac{\partial Y_k}{\partial \xi} \right|_{\xi, \psi_u} = \left. \frac{m_k \dot{\omega}_k}{\rho q \cos \theta} \right|_{\xi, \psi_u} \quad \text{for } k = 1, K \quad \text{and}$$

$$\frac{1}{2} q^2(\xi, \psi_u) + \sum_{k=1}^K h_k Y_k \Big|_{\xi, \psi_u} = \frac{1}{2} q^2(\xi_0, \psi_u) + \sum_{k=1}^K h_k Y_k \Big|_{\xi_0, \psi_u} . \quad (8.3.3)$$

The other wall equation is the boundary condition:

$$\theta_u \equiv \theta(\xi, \psi_u) = \tan^{-1} \left(\frac{dB_u}{d\xi} \right) . \quad (8.3.4)$$

The subscripts 'u' and 'l' are again used to identify the upper and lower wall respectively. Equation 8.3.3, although not yet introduced in chapter 6, is an exact replacement of the q -equation derived from energy conservation. Having shown the governing set, the first task is to put the differential equations along with 8.3.2 into algebraic (*i.e.*, difference) forms. The equations for the mass fractions Y_k present the stiff derivatives in the set and must be treated with care. An O.D.E. solver is employed to handle them such that $Y_k(\xi, \psi_u)$ can be assumed known quantities in the following formulation.

As Y_k are treated separately, there are only the temperature equation and the Mach wave characteristic equation to be considered. To impose difference approximations, all the dependent variables are assumed to be known at a location ξ_i for any ψ bounded by the walls. The goal is to find P , T and q at the points (ξ, ψ_{ul}) for any ξ is downstream of ξ_i . In the equations, ρ is rewritten in terms of P , T and $\bar{m}(Y_k)$. Logarithmic derivatives in P and T are then obtained in the temperature equation and its difference form is

$$\begin{aligned} \log T(\xi, \psi_u) - \log T(\xi_i, \psi_u) &= \frac{1}{2} \left\{ \left. \frac{R_u}{\bar{C}_p \bar{m}} \right|_{\xi, \psi_u} + \left. \frac{R_u}{\bar{C}_p \bar{m}} \right|_{\xi_i, \psi_u} \right\} \left(\log P(\xi, \psi_u) - \log P(\xi_i, \psi_u) \right) \\ &- \frac{1}{2} \left\{ \left. \frac{R_u}{\bar{m} \bar{C}_p P q} \sum_{k=1}^K h_k m_k \dot{\omega}_k \right|_{\xi, \psi_u} + \right. \\ &\quad \left. \left. \frac{R_u}{\bar{m} \bar{C}_p P q} \sum_{k=1}^K h_k m_k \dot{\omega}_k \right|_{\xi_i, \psi_u} \right\} \frac{\Delta \xi}{\frac{1}{2} (\cos \theta_u(\xi) + \cos \theta_u(\xi_i))} \end{aligned}$$

or

$$\begin{aligned}
T(\xi, \psi_y) = T(\xi_i, \psi_y) \exp & \left[\frac{1}{2} \left\{ \frac{R_u}{\bar{C}_p \bar{m}} \Big|_{\xi, \psi_y} + \frac{R_u}{\bar{C}_p \bar{m}} \Big|_{\xi_i, \psi_y} \right\} \log \frac{P(\xi, \psi_y)}{P(\xi_i, \psi_y)} \right. \\
& - \frac{1}{2} \left\{ \frac{R_u}{\bar{m} \bar{C}_p P q} \sum_{k=1}^K h_k m_k \dot{\omega}_k \Big|_{\xi, \psi_y} + \right. \\
& \left. \left. \frac{R_u}{\bar{m} \bar{C}_p P q} \sum_{k=1}^K h_k m_k \dot{\omega}_k \Big|_{\xi_i, \psi_y} \right\} \frac{\Delta \xi}{\frac{1}{2} (\cos \theta_y(\xi) + \cos \theta_y(\xi_i))} \right]
\end{aligned} \quad (8.3.5)$$

where $\Delta \xi$ is simply $\xi - \xi_i$. The C_{\pm} Mach wave equations are translated into

$$\begin{aligned}
P(\xi, \psi_y) - P(\xi_i, \psi_{\pm}) = & \\
\mp \frac{1}{2} \left\{ \frac{\bar{m} q^2}{R_u T \sqrt{M_f^2 - 1}} \Big|_{\xi, \psi_y} P(\xi, \psi_y) + \frac{\rho q^2}{\sqrt{M_f^2 - 1}} \Big|_{\xi_i, \psi_{\pm}} \right\} & (\theta_y(\xi) - \theta(\xi_i, \psi_{\pm})) \\
- \frac{1}{2} \left\{ \frac{a_f}{\bar{C}_p T \sqrt{M_f^2 - 1}} \sum_{k=1}^K h_k m_k \dot{\omega}_k \Big|_{\xi, \psi_y} + \right. & \\
\left. \frac{a_f}{\bar{C}_p T \sqrt{M_f^2 - 1}} \sum_{k=1}^K h_k m_k \dot{\omega}_k \Big|_{\xi_i, \psi_{\pm}} \right\} \Delta \eta_{\pm} . &
\end{aligned} \quad (8.3.6)$$

The differential elements have been replaced by two-point differences while their coefficients by two-point averages. These formulae are not unique. The above are chosen to allow straightforward computer implementation, fast convergence during iteration and moderately accurate solution. The coordinates (ξ_i, ψ_{\pm}) that appeared in equation 8.3.6 are the origins of the Mach waves which intersect the walls at (ξ, ψ_y) ; $\Delta \eta_{\pm}$ are the path lengths along those characteristics. The subscripts in the equations are arranged such that the upper wall is grouped with the C_+ family and the lower wall with the C_- .

It is clear that the origins of the Mach waves need not fall on any of the discrete streamlines. The values of ψ_{\pm} are back-traced from (ξ, ψ_y) and, therefore, depend on the paths of C_{\pm} . A geometric profile must be assumed for the characteristics. The first approximations are straight lines passing through (ξ, ψ_y) with slopes $\tan(\theta_y(\xi) \pm \mu_f(\xi, \psi_y))$ (c.f. equation 8.3.1). A better approximation which corresponds to the scheme in equations 8.3.5 and 8.3.6 is that of a *parabola*. This can be done by also imposing that the slopes

of the characteristics passing through (ξ_i, ψ_{\pm}) be $\tan(\theta \pm \mu_f)|_{\xi_i, \psi_{\pm}}$. The parabola profile leads to an implicit condition for each of ψ_{\pm} :

$$y(\xi_i, \psi_{\pm}) + \frac{\Delta\xi}{2} \tan\left(\theta(\xi_i, \psi_{\pm}) \pm \mu_f(\xi_i, \psi_{\pm})\right) = B_y(\xi) - \frac{\Delta\xi}{2} \tan\left(\theta_y(\xi) \pm \mu_f(\xi, \psi_y)\right). \quad (8.3.7)$$

The path lengths $\Delta\eta_{\pm}$ for this profile can be expressed as:

$$\Delta\eta_{\pm} = \frac{1}{2} \left\{ \zeta \sqrt{1 + \zeta^2} + \log\left(\zeta + \sqrt{1 + \zeta^2}\right) \right\} \Big|_{\zeta_{\pm}}^{\zeta_y} \frac{\Delta\xi}{\zeta_y + \zeta_{\pm}}, \quad (8.3.8)$$

where

$$\zeta_y \equiv \tan\left(\theta_y(\xi) \pm \mu_f(\xi, \psi_y)\right)$$

$$\zeta_{\pm} \equiv \tan\left(\theta(\xi_i, \psi_{\pm}) \pm \mu_f(\xi_i, \psi_{\pm})\right)$$

In the formulae presented so far, the variables are assumed to be known at (ξ_i, ψ_{\pm}) for any ψ_{\pm} . Clearly, interpolation must be used since the variables are only calculated along discrete streamlines ψ_j . A series of tests has shown that only *linear* interpolation is applicable to most cases. Any higher order method leads to unstable solutions at (ξ, ψ_y) . There is a difference between interpolating with respect to ψ and to y (*c.f.* equation 6.4.11b) but the former has been found to work better. Thus, for any variable f in the formulae, its value at ψ_{\pm} is given by

$$f(\psi_{\pm}) = f(\psi_m) + \frac{\psi_{\pm} - \psi_m}{\Delta\psi} \left(f(\psi_{m+1}) - f(\psi_m) \right) \quad \text{for } \psi_m \leq \psi_{\pm} < \psi_{m+1}. \quad (8.3.9)$$

The equation set for the boundary treatment is now complete. It can only be solved iteratively since the equations are coupled non-linearly. In other words, an initial guess of the solution must be made. The required accuracy of the guess necessary for convergence depends strongly on the state of chemical reaction which enters the equations through the terms containing $\sum_{k=1}^K h_k m_k \dot{\omega}_k$. The effect of these terms can be limited by using sufficiently small $\Delta\xi$. In this case, convergence is not difficult. A Newton-Raphson type iteration scheme is chosen for the following calculations.

The interior can be handled as in the simple wave case. In other words, $\partial P / \partial \xi|_{\text{walls}}$ must be approximated to calculate P'_j and θ'_j for j equals 2 to $N-1$. A backward differencing step can accomplish this without involving any extra evaluation along the boundaries:

$$\frac{\partial P}{\partial \xi} \Big|_{\xi, \psi_y} \approx \frac{P(\xi, \psi_y) - P(\xi_i, \psi_y)}{\Delta\xi}.$$

8.4 Accuracy of General Characteristic Treatment

A series of calculations is conducted to test the performance of the characteristic boundary treatment. The six cases considered in the simple wave formulations are repeated. Again, they use the **group 1** inputs of table 7.3.1 with six different wall turn curvatures. The error in the wall pressure, ϵ_P , is plotted against the reciprocal of the resolution, $1/R$ where ϵ_P and $1/R$ are defined in equations 7.8.2.1 and 7.8.2.2 respectively. The wall turn radii considered are 0.800, 0.400, 0.300, 0.200, 0.100 and 0.001 meters and their results are shown in figure 8.4.1. Note that the errors do not appear to grow exponentially towards the far end of the plot (low resolution side).

To show the effectiveness of the characteristic treatment, these errors are plotted in figure 8.4.2 together with those obtained for the previous interpolation and extrapolation method. The data point at R_t equals 0.001 m is excluded for the purpose of comparison. The error in the new method is in most cases smaller than that in the old one. Furthermore, this error also approaches zero linearly when $1/R$ goes to zero. The improvement is not drastic, but not shown in the figure is the fact that the characteristic treatment does not introduce any oscillatory distribution along the wall. This will become clear from the calculations to be presented.

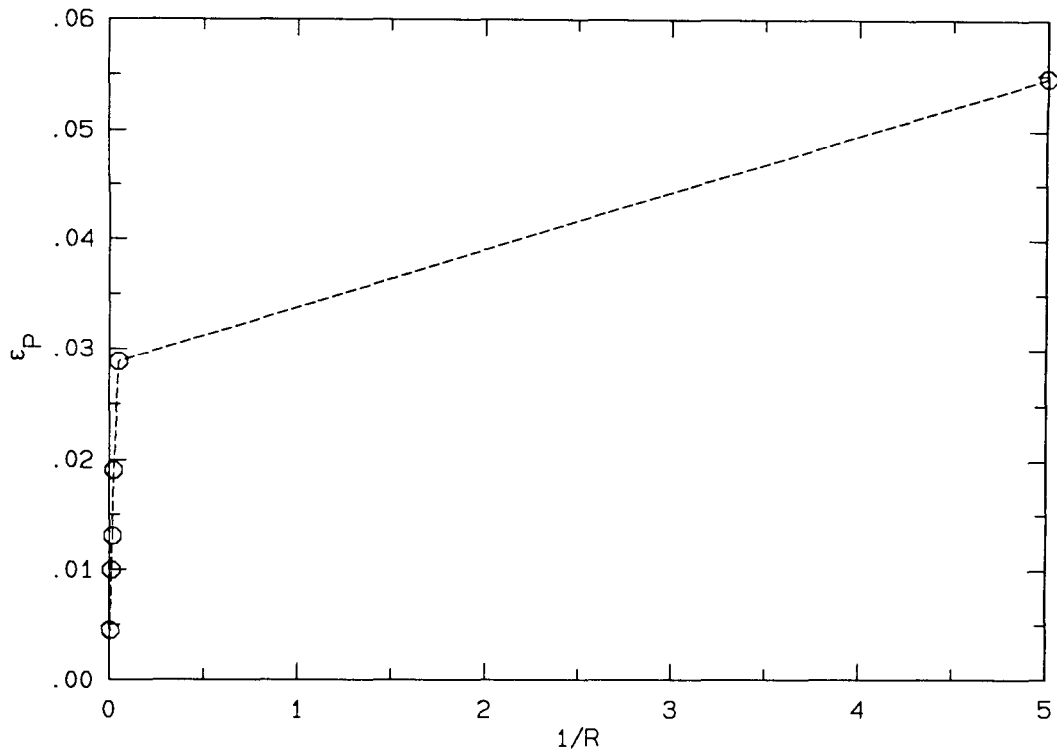


FIG. 8.4.1 Numerical error with characteristic treatment for 6 resolutions.

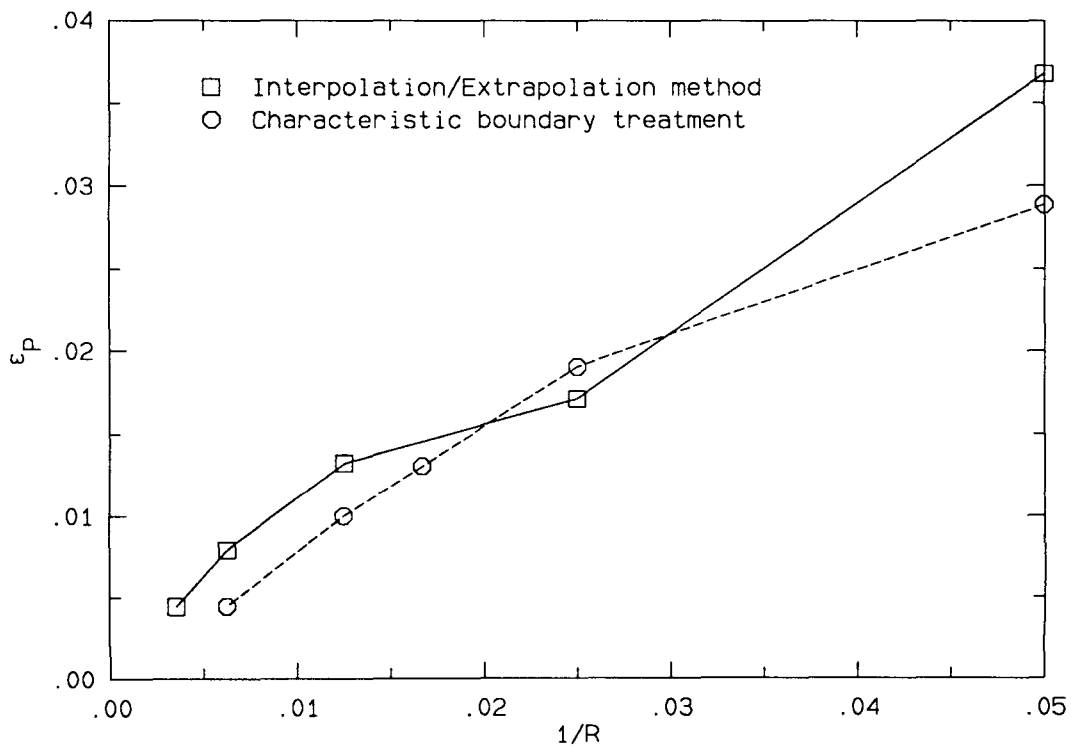


FIG. 8.4.2 Comparison of numerical errors from two boundary treatments.

8.5 Finite-rate Chemistry Calculations

So far, emphasis has been on the numerical scheme more so than on the flow behavior within the nozzle. It is the purpose of the following calculations to explore some of the interesting features in a reacting nozzle flow qualitatively. The general characteristic boundary treatment will be used to study finite-rate chemistry.

To be considered are five cases which may be categorized into two sets: one with an inlet pressure of 1.0 atm and the other of 0.1 atm . The input parameters for the first set is identical to those prescribed in **group 1** (*c.f.* table 7.3.1). It includes three cases of different turn curvatures. The second set has input parameters derived much the same way as **group 1** — that is, based on a diffuser-combustor calculation. These input parameters are entitled **group 2**.

There are two differences in the conditions leading to **group 1** and to **group 2**. One is the diffuser exit or combustor pressure; the other is the combustor exit location which is taken as the nozzle inlet. Nevertheless, the complete set of conditions of **group 2** are:

1. Ambient condition or diffuser inlet:
standard atmospheric pressure and temperature and composition; $M_\infty = 15$.
2. Diffuser exit or combustor inlet:
composition of air at equilibrium ; $\eta_{\text{eff}} = 0.985$; $M = 5$; $P = 0.1 \text{ atm}$; $\phi = 1.2$.
3. Combustor exit or nozzle inlet:
finite-rate chemistry over a length of 5 m in the combustor ; $P = 0.1 \text{ atm}$.

A length rather than a percentage of equilibrium heat release is specified for the combustor exit because the chemical processes under this combustor pressure is so slow that 61 m is needed to reach 95% of ΔH_{eq} . At the 5 m point, only 37% of ΔH_{eq} has been produced. Assuming that the combustor exit flow is to expand into the free-stream, a shock-expansion fan matching calculation can be used to estimate the initial angle of the dividing streamline relative to the free-stream. This angle is used as the nozzle exit angle. With these conditions, the **group 2** input parameters are computed and the results are listed in table 8.5.1. Finally, the inputs to the five cases to be studied are stated in table 8.5.2.

In the cases to be presented, the turn radius is also expressed in terms of a chemical length scale L_x . It is presented to provide a crude *order-of-magnitude* comparison between the expansion rate and the reaction time. Recall from section 7.2.3 where L_x was defined that the length is only a *lower* estimate. For a more precise scale, detailed calculations must be used to take into account all the conditions (P , T , Y_k , *etc.*) in each case.

	Group2
Pressure P [atm]	0.1
Temperature T [K]	1879.9
Mach Number M	4.4306
Composition Y_H	0.0556×10^{-1}
Y_{H_2}	0.0802×10^{-1}
Y_{H_2O}	1.7162×10^{-1}
Y_N	0.0000×10^{-1}
Y_{N_2}	7.2938×10^{-1}
Y_{NO}	0.0080×10^{-1}
Y_O	0.1747×10^{-1}
Y_{O_2}	0.3699×10^{-1}
Y_{OH}	0.1736×10^{-1}
Y_{Ar}	0.1280×10^{-1}
Inlet Angle θ_{in} [deg]	0.0
Exit Angle θ_{ex} [deg]	17.768

TABLE 8.5.1 **Group 2** nozzle input parameters: inlet conditions and wall angles.

	Case 1	Case 2	Case 3	Case 4	Case 5
Pressure	group 1			group 2	
Temperature					
Mach Number					
Composition					
Chemical Reaction State	<i>finite-rate</i>				
2 Walls: turn radius R_t [m]	0.800	0.100	0.001	0.100	0.001
turn begins x_1 [m]	0.000	0.000	0.000	0.000	0.000
turn at x_t [m]	0.107	0.0267	2.67×10^{-4}	0.0267	2.67×10^{-4}
turn ends x_2 [m]	0.214	0.0534	5.34×10^{-4}	0.0534	5.34×10^{-4}
Inlet Height [m]	0.2				
No. of Streamlines N	41				

TABLE 8.5.2 Input parameters for 5 Cases.

8.6 Case 1: A P_{inlet} of 1.0 atm and R_t of 0.8 m (i.e. 800 L_x)

The exact same case has been studied in section 7.5 using the former numerical method and some interesting features regarding the chemical behavior are found. However, that calculation is not accurate enough to allow a detail analysis of the chemistry. By comparing the plots of pressure and temperature shown in figures 8.6.1 and 8.6.2 with those in figures 7.5.2 and 7.5.3, the improvement achieved by the new method is clear. Most obvious are their smooth distributions along the wall streamline.

Chemical activity along the center streamline (#21) is indicated by the increasing pressure and temperature near the inlet. It is not as obvious along the wall following the turn. An increase in pressure is found only by examining the numerical data and the increase in temperature is barely noticeable from figure 8.6.2. The significance of these increases is that chemical energy is being released.

8.6.1 Species response to expansion

The response of hydrogen-air kinetic to an expansion is best described along the wall streamline since it is subjected to the highest rate of expansion. The responses along neighboring streamlines are also useful in describing the change in kinetic behavior upon progressively smaller rate of expansion toward the center streamline. The evolution of individual species composition along the half-nozzle streamlines (21) is plotted in figures 8.6.3 to 8.6.11. The mass fraction of Ar is not plotted since it is constant. Therefore, the figures only include Y_{H} , Y_{H_2} , $Y_{\text{H}_2\text{O}}$, Y_{N} , Y_{N_2} , Y_{NO} , Y_{O} , Y_{O_2} and Y_{OH} respectively. The observed behavior of the nine species is summarized as follows:

1. H : Prior to an expansion or after it has completed, Y_{H} drops. That is, H is being consumed whether (P, T) are at $\sim (1 \text{ atm}, 2800 \text{ K})$ or $\sim (0.15 \text{ atm}, 1800 \text{ K})$. However, as the expansion rate is large enough, such as along the early portion of the wall streamline ($x \lesssim 0.42 \text{ m}$) or along the latter portion of the center streamline ($x \gtrsim 0.4 \text{ m}$), the production rate of H overtakes the drop and results in a net rise. According to the pattern of figure 8.6.3, the level of Y_{H} immediately following a turn increases with the curvature of the turn.

2. H_2 : The composition of H_2 decreases slowly before expansion and rapidly during expansion. The decrease is reduced to a relatively much slower rate immediately after expansion. This change occurs at a higher value of Y_{H_2} when the rate of expansion is higher. This can be observed along the first three streamlines from the wall (lower part of figure 8.6.5) at the end of the nozzle.
3. H_2O : Along the initial portion of the center streamline, H_2O is produced; thus continuing the same processes as in the combustor. H_2O is also formed during and after expansion. The latter, however, occurs at a relatively slower rate. When the rate of expansion is high, less H_2O is formed before the slow down begins.
- 4-6. N, N_2, NO : The fraction of N is the smallest in the species set. N responds to pressure and temperature drops by reducing its composition to nearly zero. The change in Y_{N_2} is mainly due to the other radical NO . Since the formation of NO is frozen during expansion, so does the consumption of N_2 . Along the wall (lowest curve in figure 8.6.8), Y_{NO} has become constant at $x \simeq 0.15 m$ whereas the wall turn is not completed until $x \simeq 0.42 m$. The same freezing phenomenon is observed along the other streamlines. Note that the jaggedness of the Y_{N_2} curves is within the computational tolerances.
7. O : This radical is not very sensitive to small pressure changes since it evolves similarly along all streamlines despite of their different starting points and rates of expansion. This is only true up to the point where the rate of expansion is a maximum where the descending trend of Y_O accelerates according to the rate of expansion. This corresponds to the point $x \simeq 0.21 m$ on the wall and farther downstream on the other streamlines. The accelerated descend comes to a stall when the expansion is completed. There is more O left at this point if the expansion rate is high. Y_O continues to drop afterward but at a much slower rate.
8. O_2 : The behavior of Y_{O_2} is similar to that of Y_H . Along the center streamline where no expansion is felt initially, O_2 is consumed in the combustion process. However, along the wall where expansion is immediate, the consumption is soon reverse to a net production. The species is again being consumed after the expansion has completed. The highest level of Y_{O_2} achieved during its rise and fall along a streamline is directly related to the expansion rate on that streamline.
9. OH : While a resemblance is found between the behavior of H and O_2 , there is also a resemblance between the behavior of OH and H_2 . Without the effect of expansion as is true along the center streamline initially, OH is slowly being used up in combustion.

Its consumption is much more rapid during expansion. Afterward, the drop in Y_{OH} slows down to nearly a constant. In addition, the drop even reverses to a slow rise along the wall. As in the case of H_2 , the first few streamlines indicate that there is more left over OH following a higher rate of expansion.

According to the behavior observed, the rate of wall turn in this example appears to be large enough to allow most combustion reactions to follow the expansion process. In other words, the chemical time scale is of the same or smaller order as the residence time over the expansion. Freezing is not clearly observed except for N_2 and NO . Nevertheless, some ideas regarding the dominant chemical processes before expansion, during expansion and after expansion can be drawn.

(1) Before or without expansion —

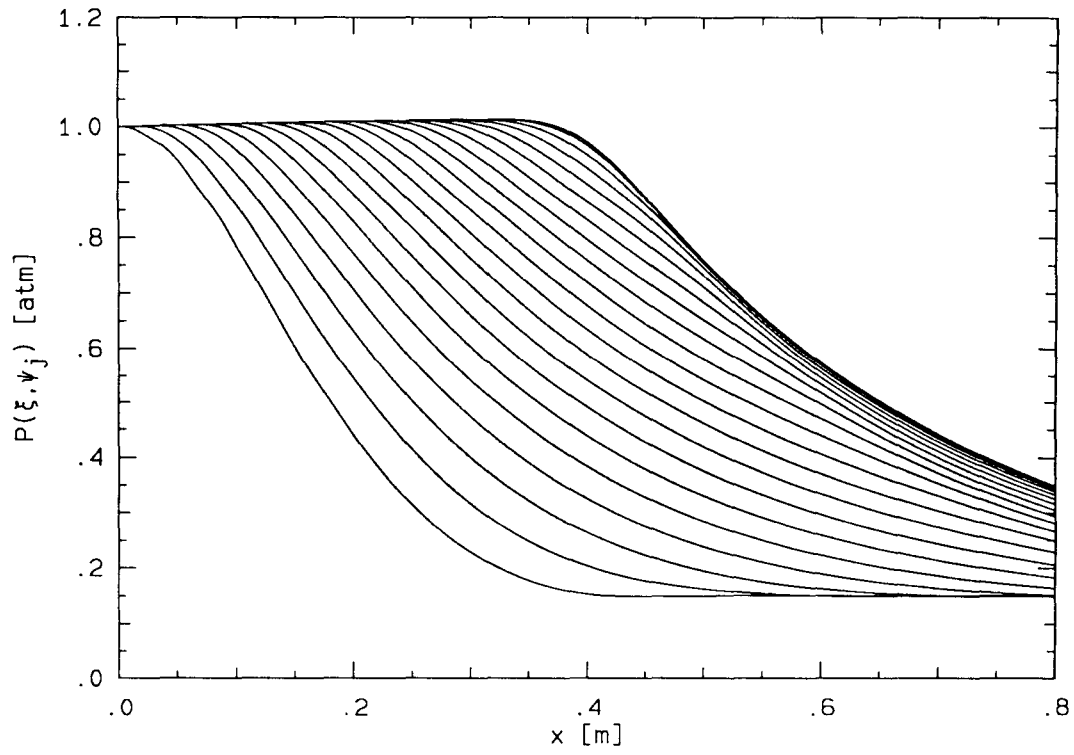
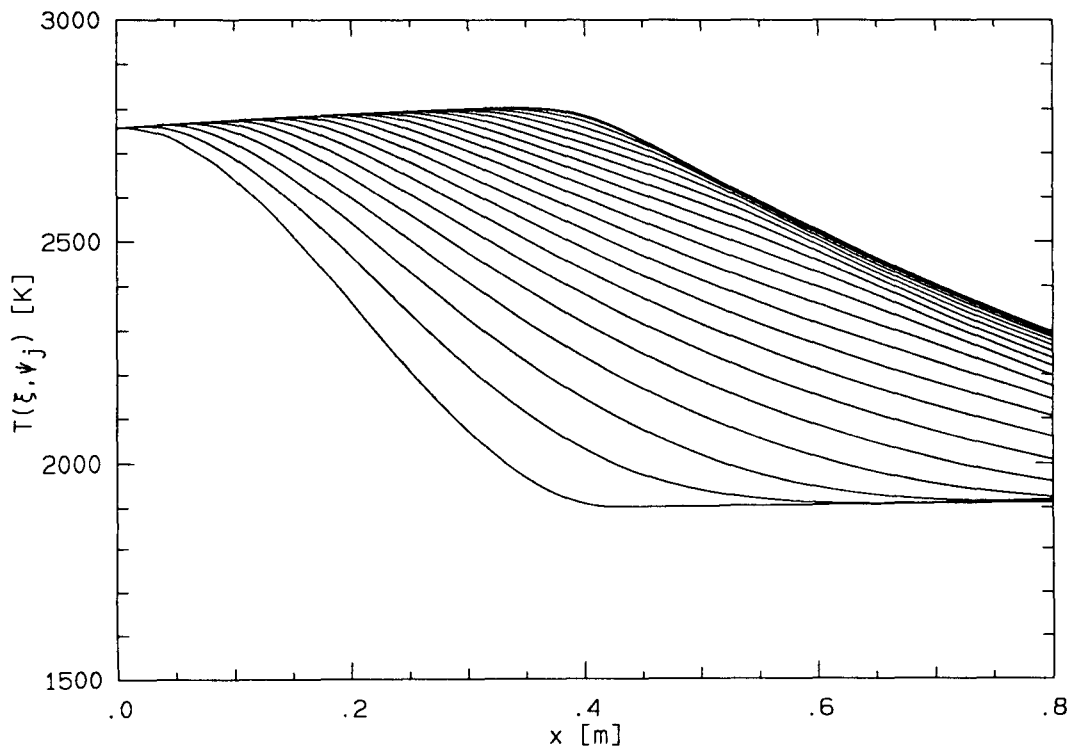
H_2 and O_2 and other combustion related radicals are being consumed overall to release thermo-energy. Pressure and temperature increase while part of the chemical energy is being trapped in the formation of radicals, including NO .

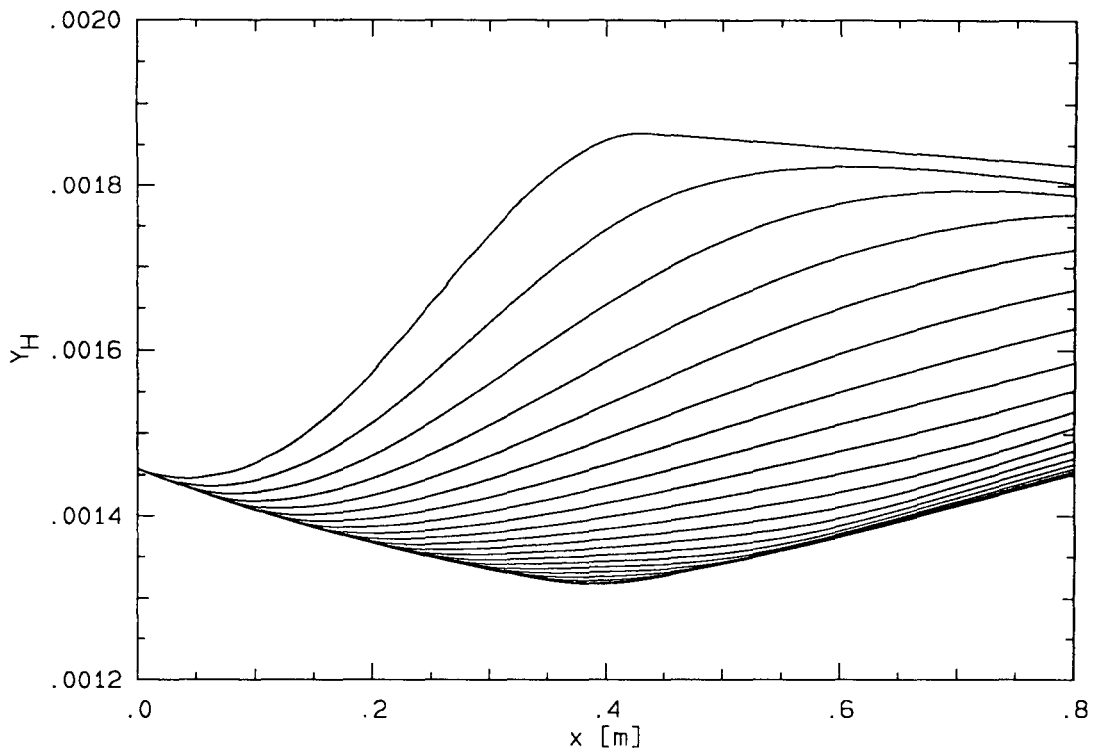
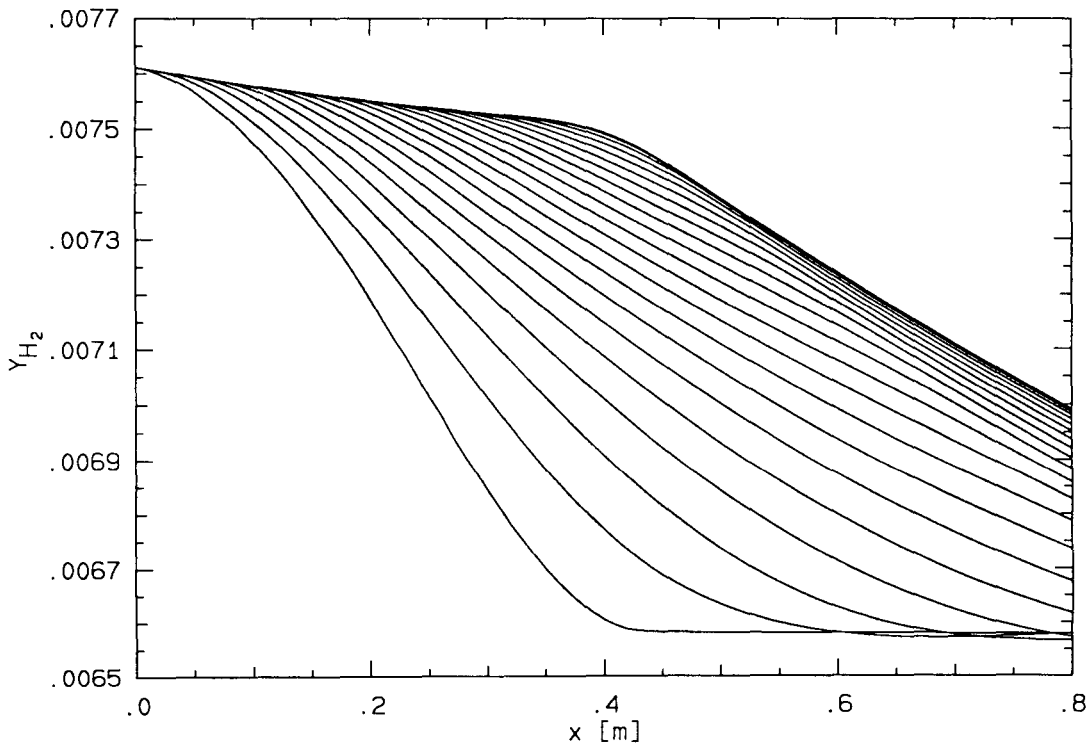
(2) During expansion —

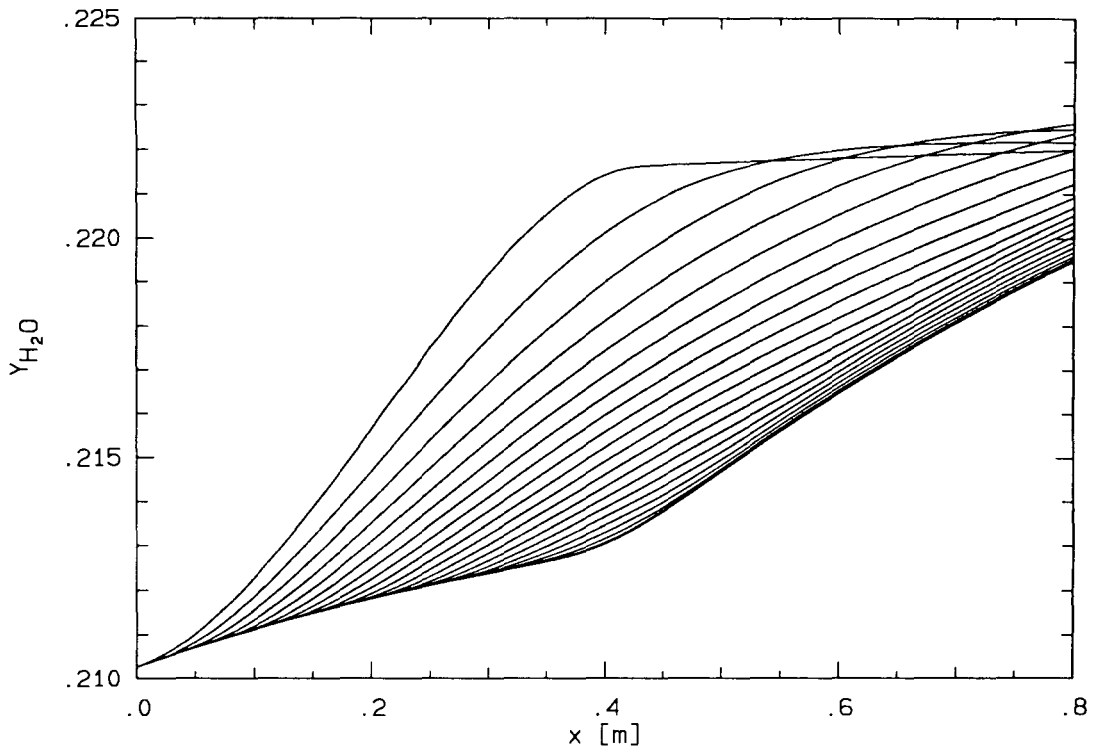
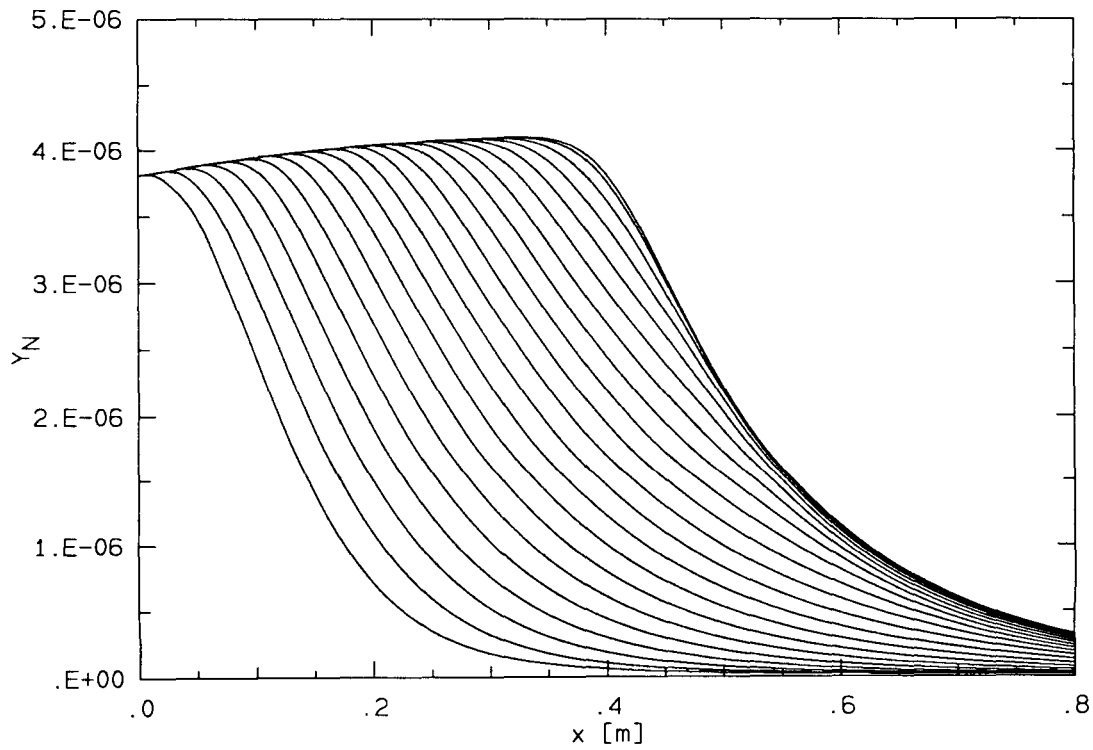
Combustion processes continue to produce H_2O , but the active participants are mostly radicals. Of prime importance is OH . It combines with H_2 to produce water and H . Note that the amount of OH consumed closely corresponds to the amount of H_2O produced (by weight as in mass fraction). The disappearance of O is attributed to its recombination to form O_2 . These processes appear to occur at a rate much faster than the expansion rate since their response is synchronized with the expansion. This is not unlikely because the temperature throughout the expansion is sufficiently high (from 2800 to 1800 K) and the reaction between H_2 and OH is extremely fast. On the other hand, the other NO_x radical, NO , is frozen after a certain degree of expansion.

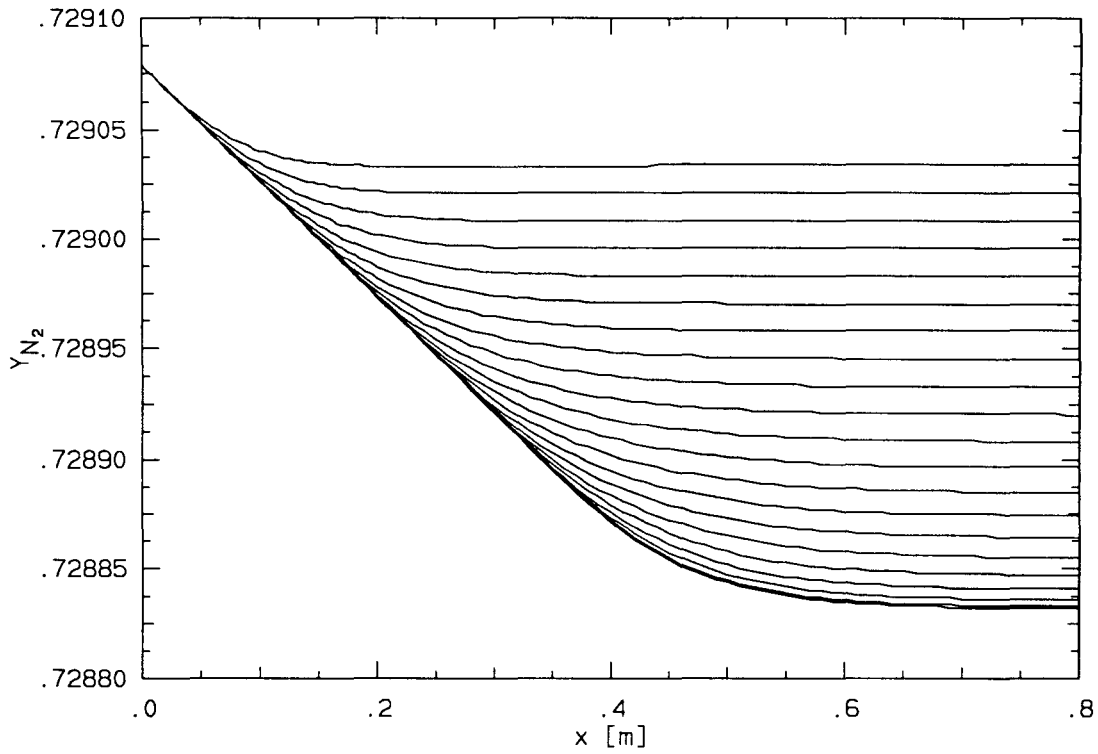
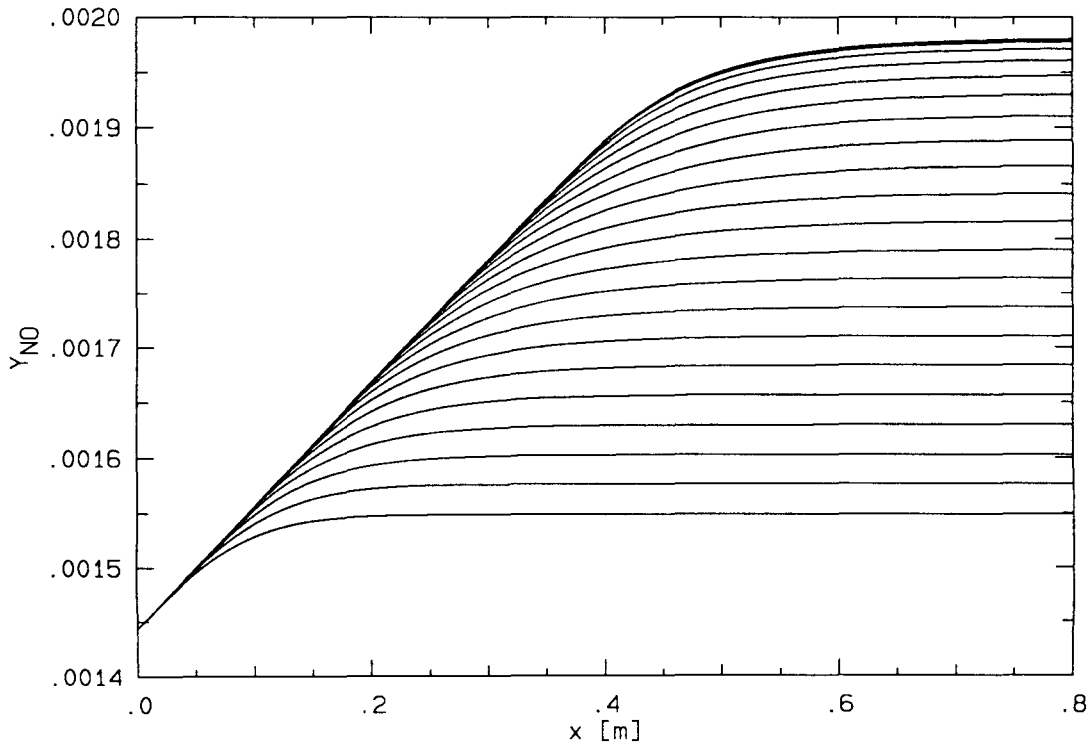
(3) After expansion —

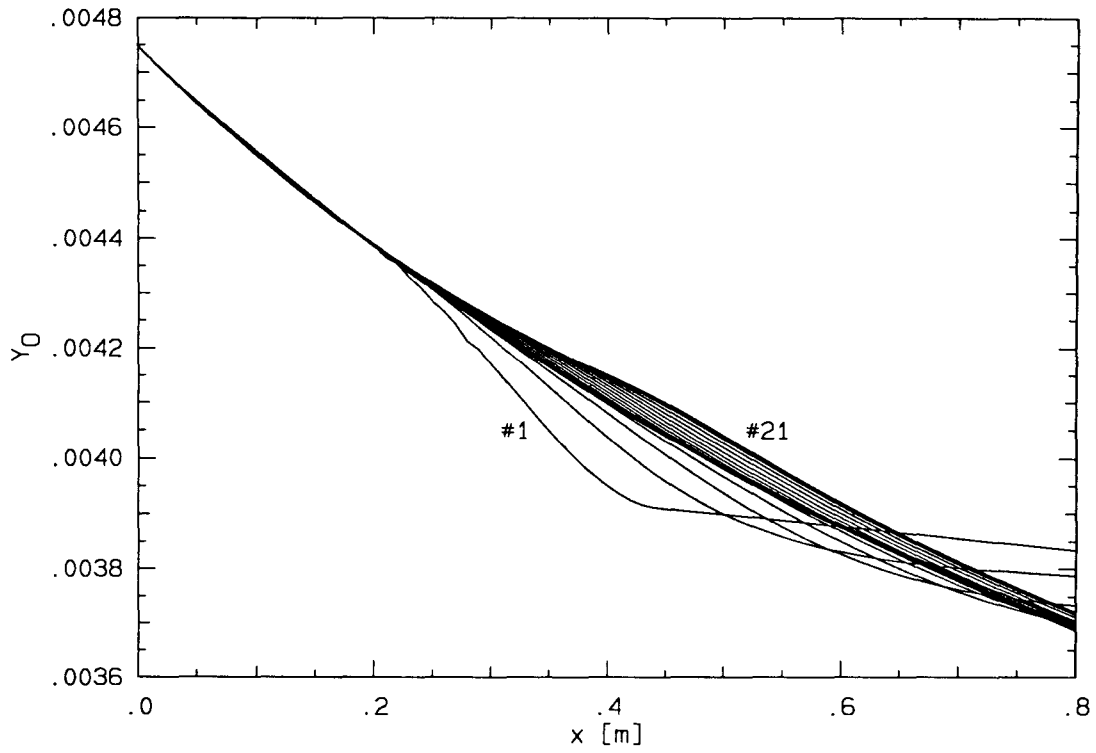
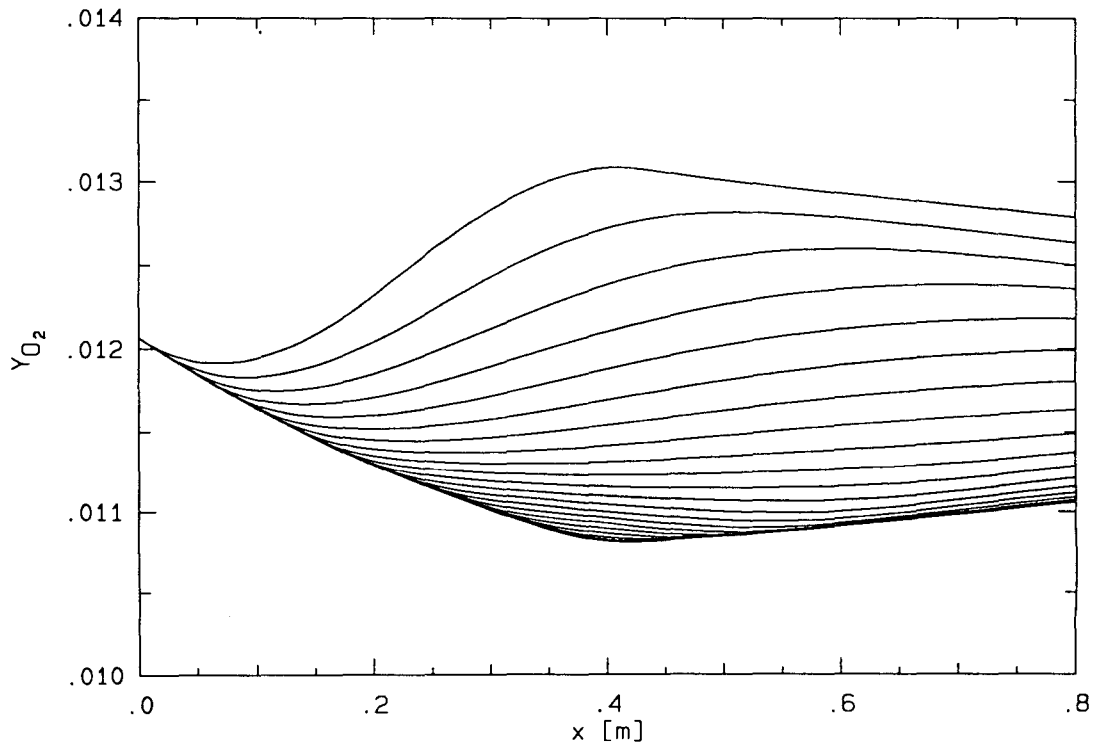
The kinetics of the radical H and the species O_2 dominate the production of H_2O . The pressure and temperature have become nearly constant and the excessive amount of H is no longer needed to adapt for the pressure drop. Radical O and species H_2 also participate with lesser contribution.

FIG. 8.6.1 Pressure along ψ_j , $j = 1, 21$ (bottom to top).FIG. 8.6.2 Temperature along ψ_j , $j = 1, 21$ (bottom to top).

FIG. 8.6.3 Mass fraction of H along ψ_j , $j = 1, 21$ (top to bottom).FIG. 8.6.4 Mass fraction of H_2 along ψ_j , $j = 1, 21$ (bottom to top).

FIG. 8.6.5 Mass fraction of H_2O along ψ_j , $j = 1, 21$ (top to bottom).FIG. 8.6.6 Mass fraction of N along ψ_j , $j = 1, 21$ (bottom to top).

FIG. 8.6.7 Mass fraction of N_2 along ψ_j , $j = 1, 21$ (top to bottom).FIG. 8.6.8 Mass fraction of NO along ψ_j , $j = 1, 21$ (bottom to top).

FIG. 8.6.9 Mass fraction of O along ψ_j , $j = 1, 21$.FIG. 8.6.10 Mass fraction of O_2 along ψ_j , $j = 1, 21$ (top to bottom).

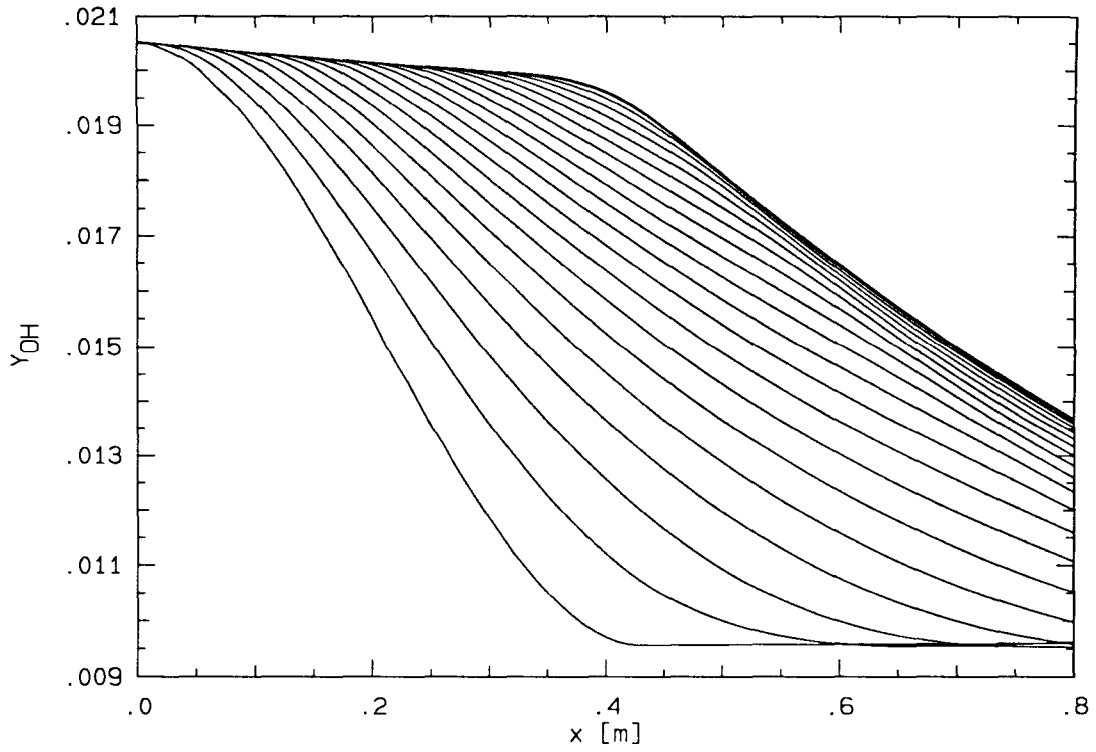


FIG. 8.6.11 Mass fraction of OH along ψ_j , $j = 1, 21$ (bottom to top).

8.7 Case 2: A P_{inlet} of 1.0 atm and R_t of 0.1 m (i.e. 100 L_x)

Very little indication of freezing is found in the last example. Therefore, a wall turn radius of $1/8$ the previous one is imposed here to produce a higher rate of pressure and temperature drops. The effect is to be observed along the wall since the behavior along streamlines close to the centerline is identical to that in case 1.

The half nozzle streamline pattern is shown in figure 8.7.1 to depict the turning rates along the wall and the interior streamlines. The nozzle length calculated is 0.2 m which is two times the wall turn radius. The pressure and temperature distributions along the half-nozzle streamlines are shown in figures 8.7.2 and 8.7.3. Note that their levels following the turn on the wall are very close to those in the previous case. This is the expected result because the two cases are only differed by their wall turn curvatures. Any difference in the levels of P_{wall} and T_{wall} following the turn can only be explained by the progress of chemical reaction around the turn.

The species composition calculated in this case is compared with the previous one to determine the effect of expansion rate on chemistry. The mass fractions of only seven species are plotted this time: Y_{H} , Y_{H_2} , $Y_{\text{H}_2\text{O}}$, Y_{NO} , Y_{O} , Y_{O_2} and Y_{OH} . They are shown in figures 8.7.4 to 8.7.10. The two species left out are N and N_2 ; they behave exactly the same as before and are of little significance.

After examining the figures, all species are found to evolve in the way predictable from the patterns of the composition plots in the section 8.6. The following is a comparison between the levels of the seven species achieved on the wall after the expansion in this case and in the previous case:

1. H : More H is formed or remains following the expansion. It can be deduced from the behavior of the other species that the increased level is rather a result of reduced consumption.
2. H_2 : The level of H_2 is higher.
3. H_2O : The final composition of H_2O is lower by approximately 1%.
- 4-6. N, N_2 , NO : The amount of N left remains in $\mathcal{O}(10^{-7})$. The composition of NO is frozen at a lower level and the level of N_2 is altered according to that of NO.
7. O : More O remains.

8. O_2 : A higher value is reached before decreasing.
9. OH : The level of OH is higher.

All these findings agree with the trends predicted in the last example. The two cases are therefore dominated by the same set of kinetics and the description in section 8.6.1 applies. Furthermore, the rate of wall turn in this case must still be similar to or slower than the dominant reaction rates. A yet sharper turn must be imposed to determine the limiting behavior.

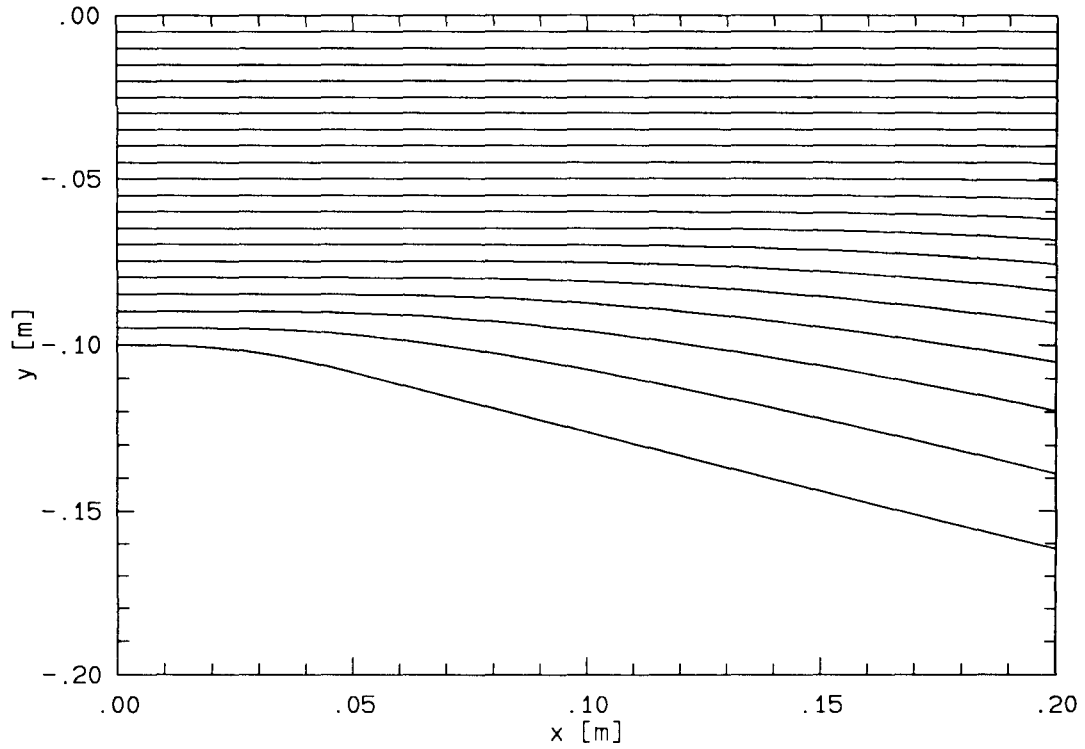


FIG. 8.7.1 Streamline pattern for a Re of 0.10 m.

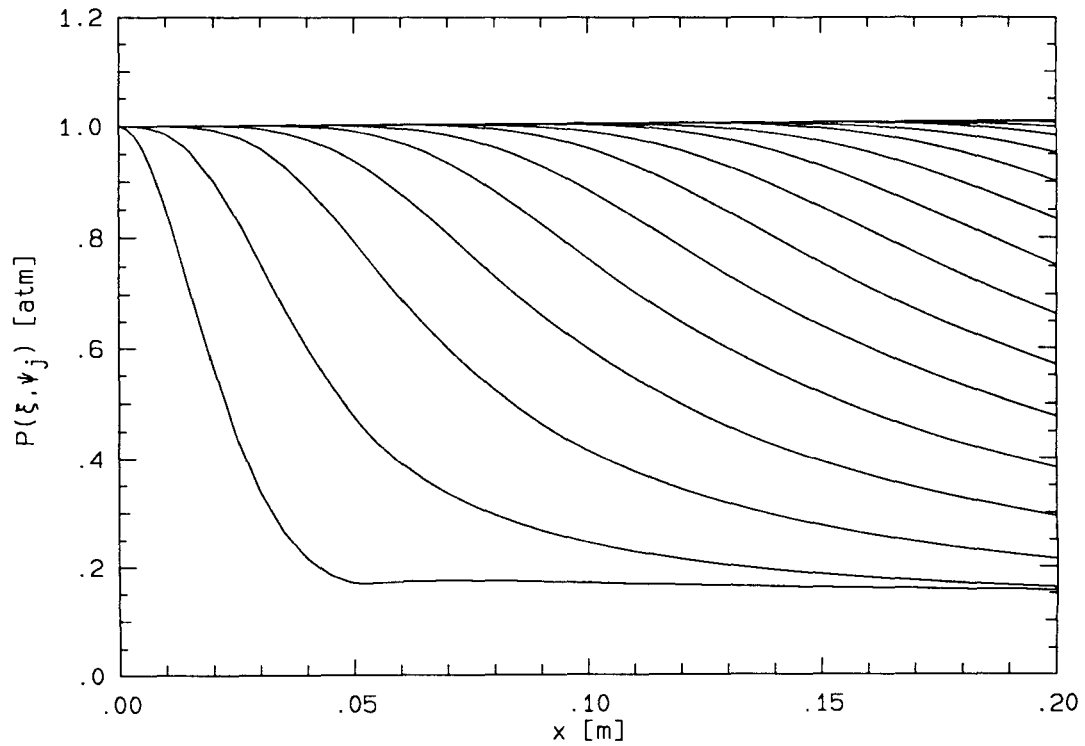
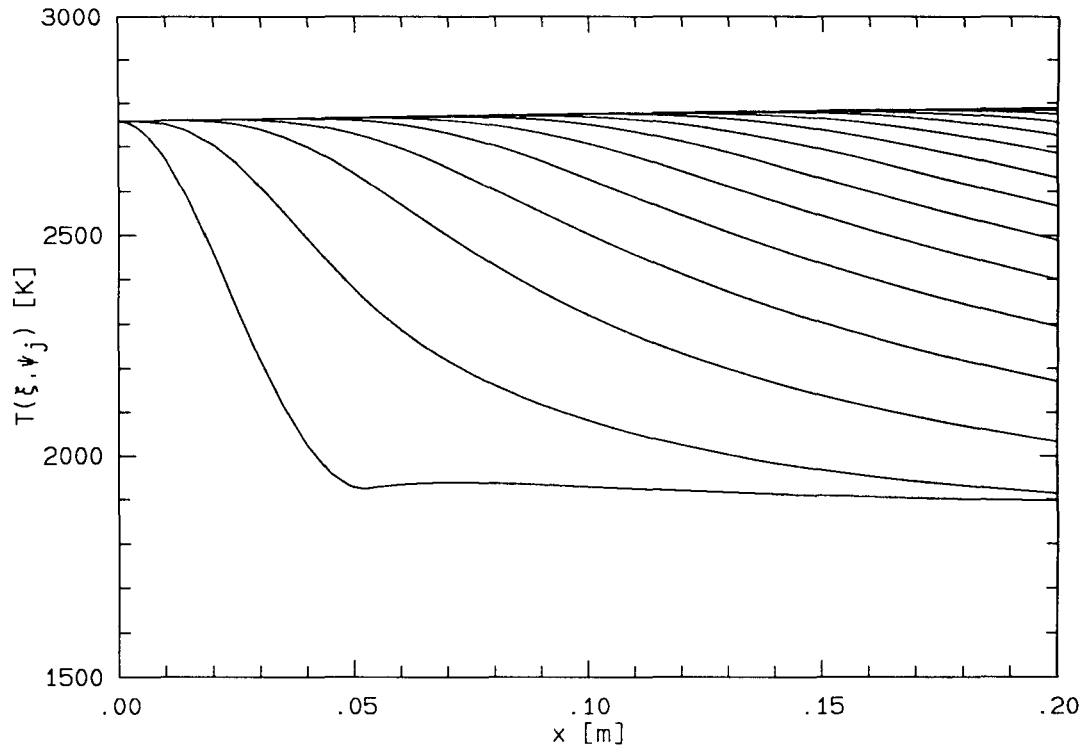
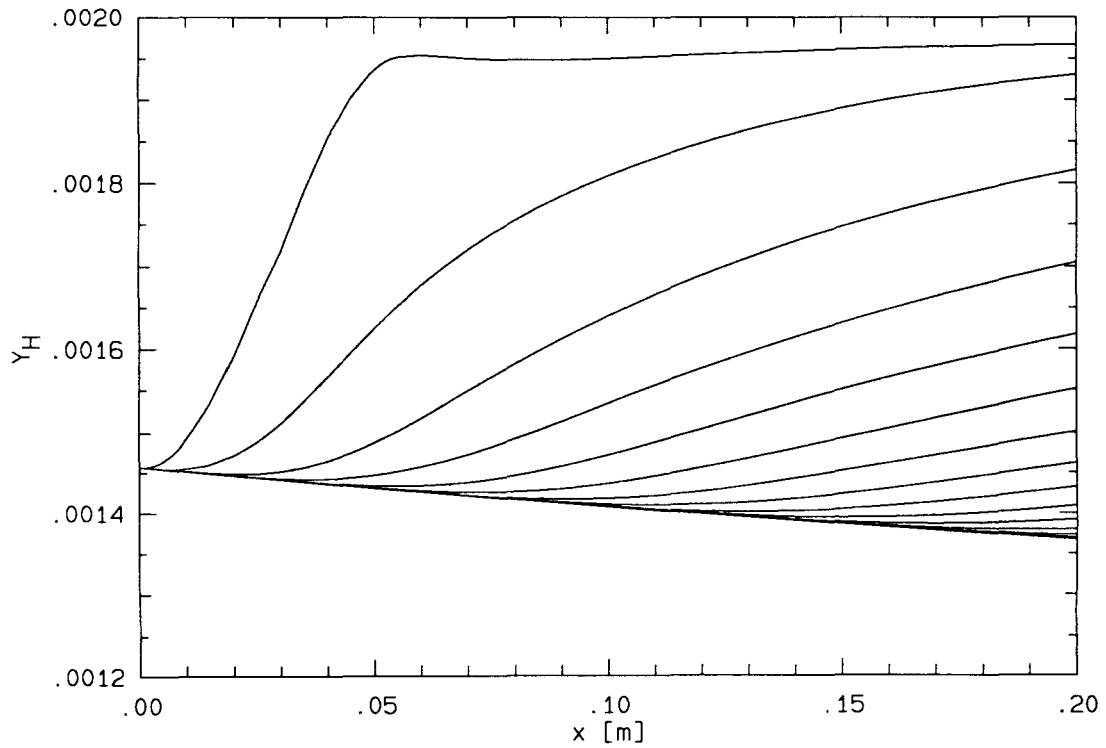
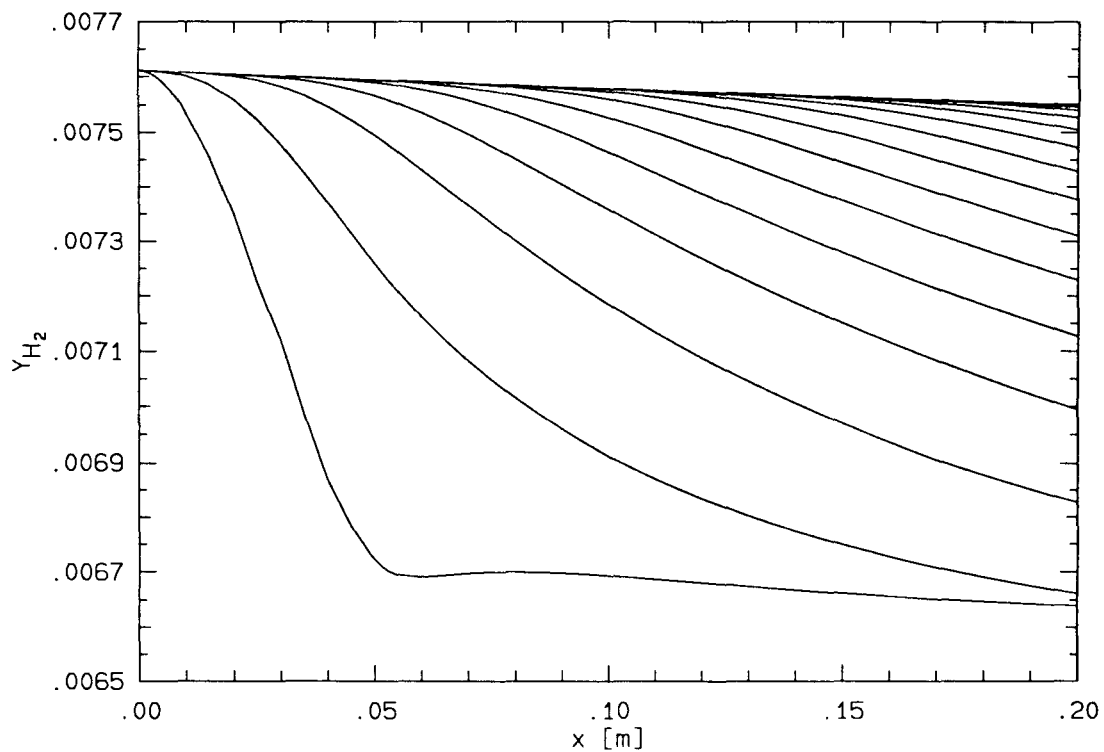
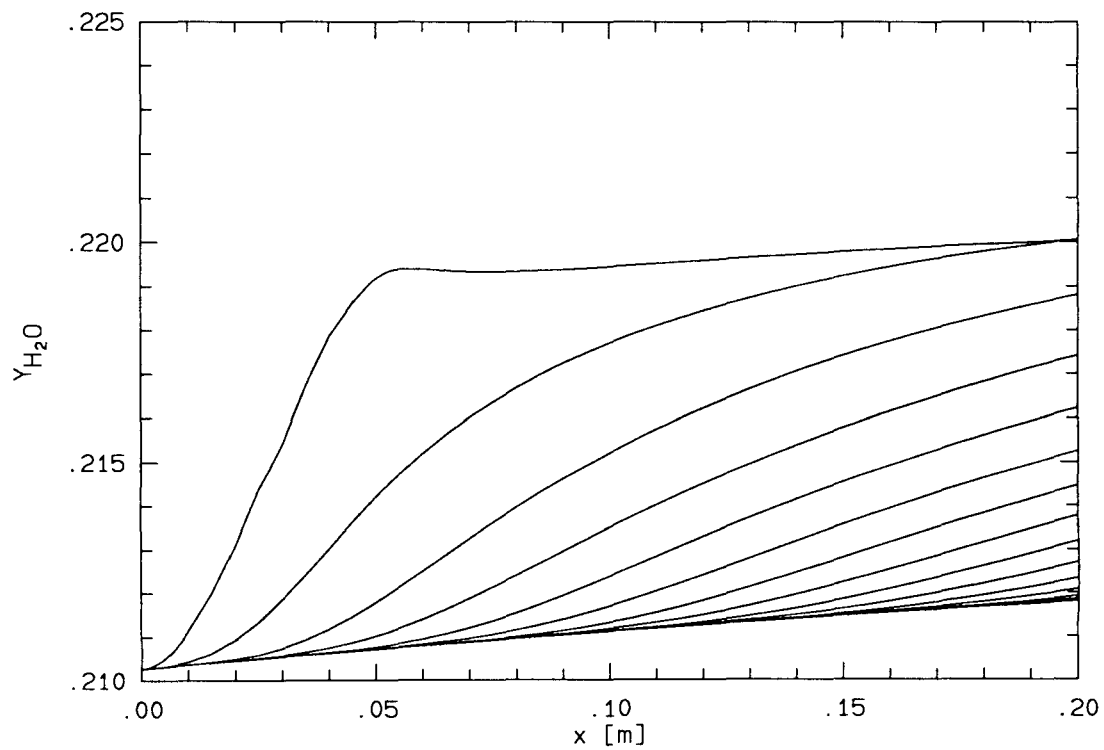
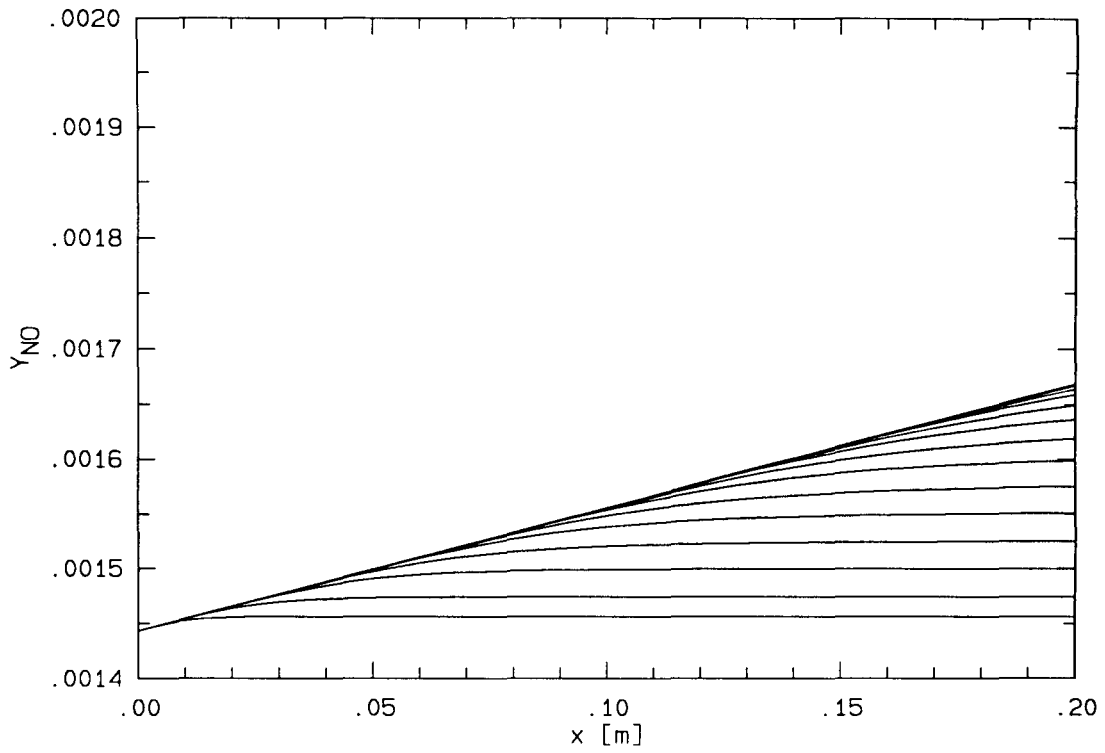
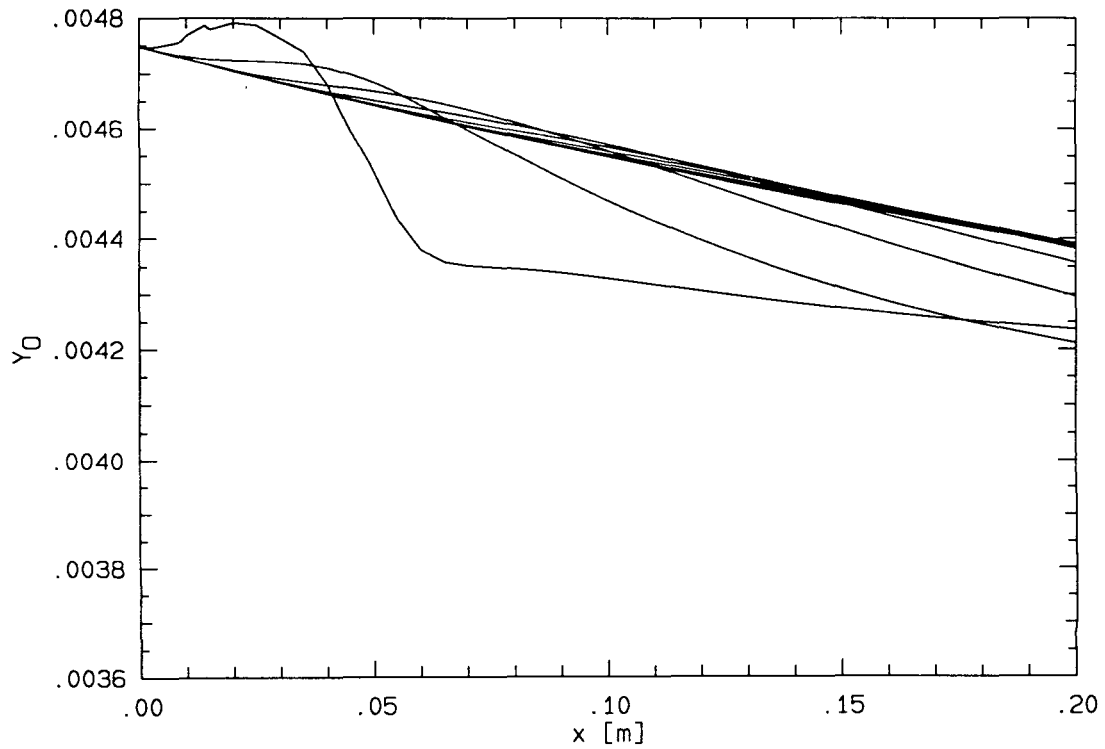
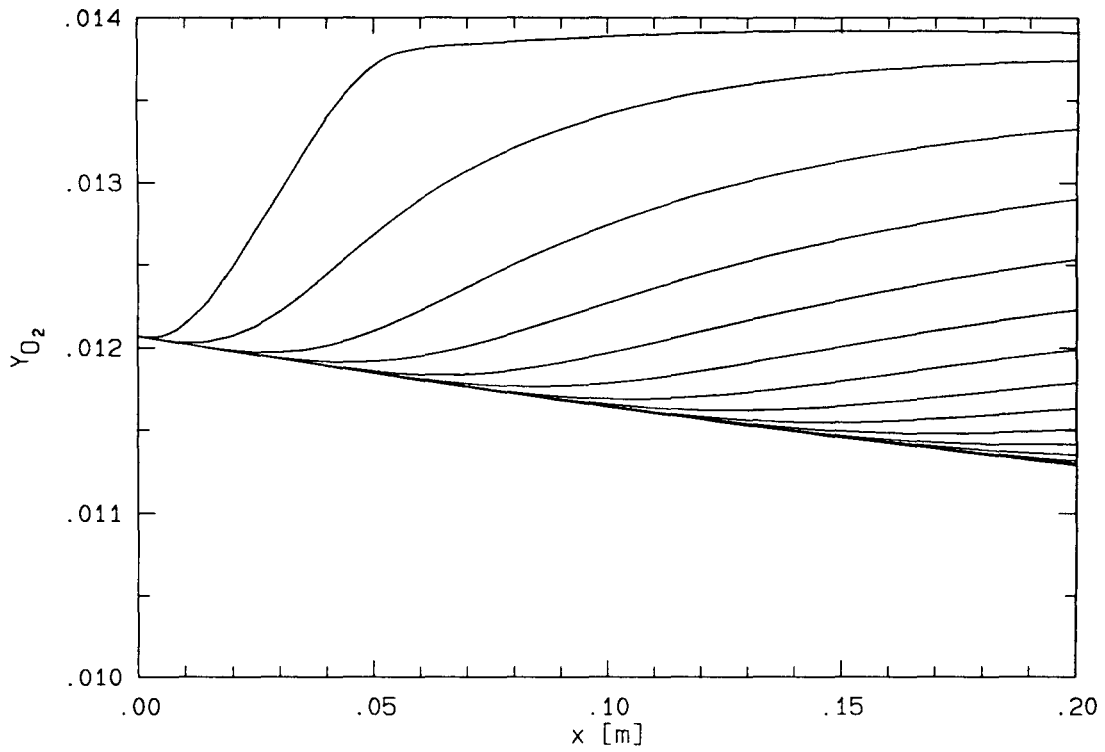
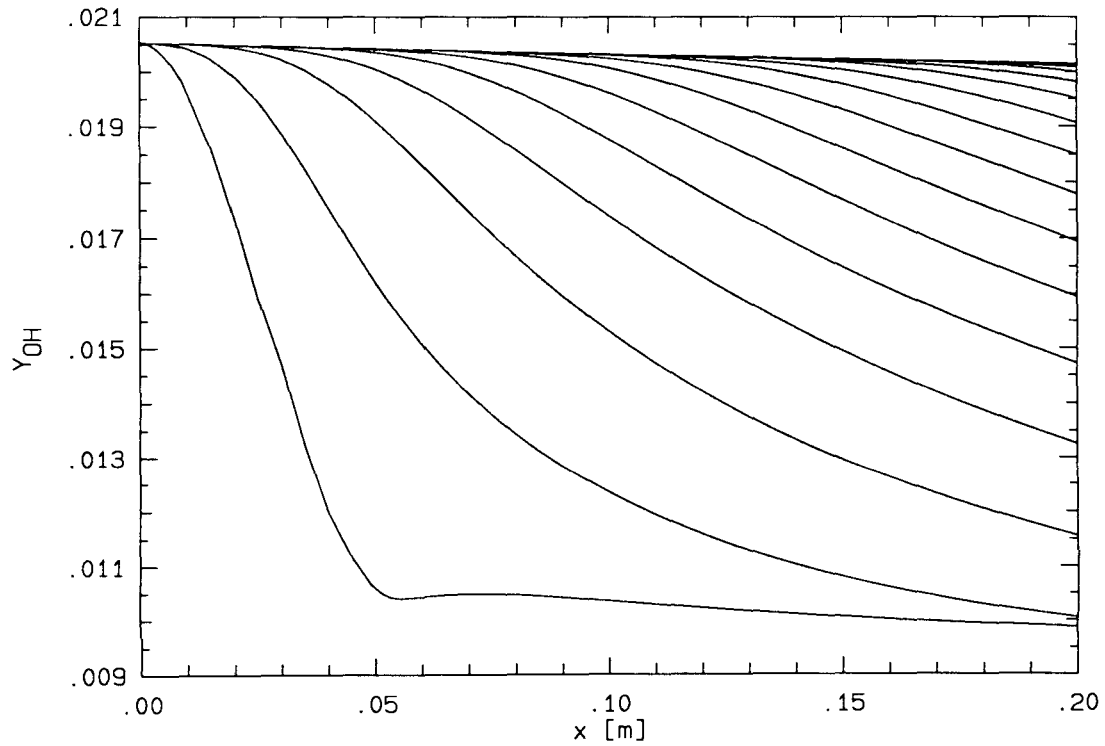


FIG. 8.7.2 Pressure along ψ_j , $j = 1, 21$ (bottom to top).

FIG. 8.7.3 Temperature along ψ_j , $j = 1, 21$ (bottom to top).FIG. 8.7.4 Mass fraction of H along ψ_j , $j = 1, 21$ (top to bottom).

FIG. 8.7.5 Mass fraction of H₂ along ψ_j , $j = 1, 21$ (bottom to top).FIG. 8.7.6 Mass fraction of H₂O along ψ_j , $j = 1, 21$ (top to bottom).

FIG. 8.7.7 Mass fraction of NO along ψ_j , $j = 1, 21$ (bottom to top).FIG. 8.7.8 Mass fraction of O along ψ_j , $j = 1, 21$.

FIG. 8.7.9 Mass fraction of O_2 along ψ_j , $j = 1, 21$ (top to bottom).FIG. 8.7.10 Mass fraction of OH along ψ_j , $j = 1, 21$ (top to bottom).

8.8 Case 3: A P_{inlet} of 1.0 atm and R_t of 0.001 m (i.e. $\sim L_x$)

The geometry in this case has a minimum radius of curvature of the same order as the estimated chemical length scale L_x (c.f. section 7.2.3). The variables examined in the case where R_t equals $100 L_x$ are again plotted along the half-nozzle streamlines. These include the streamline pattern, P , T , Y_H , Y_{H_2} , Y_{H_2O} , Y_{NO} , Y_O , Y_{O_2} and Y_{OH} which are shown in figures 8.8.1 to 8.8.10 respectively. The results obtained are not as accurate as before since the same number of discrete streamlines (41 for the symmetric nozzle) is used while the wall turn is much sharper. The maximum error is approximately 5.5% according to figure 8.4.1. This accounts for the overshoot appearance in the variables along the wall immediately following the turn.

Comparing the current results with the ones calculated for wall geometries having turn radii 100 times and 800 times larger, all the variables are found to follow the expected trends. For example, the pressure and temperature drop even faster on the wall according to the higher rate of turn; the mass fraction of each species increases or decreases the same way during expansion; the amount of each species achieved or left following expansion is higher or lower according to the descriptions in section 8.7 (items 1 through 9) and 8.6.1.

Despite the similarity in the patterns of the plots in this section and the previous two, they present an important feature that has not yet been observed. It is revealed by comparing the pressure or temperature plot with the composition plots. At the $x \sim 0.00053 m$, the wall turn has completed; P and T have reached their minimum points and become nearly constant** along the wall. The species composition, however, evolves with a delayed action. Except for the nitrogen related species and Ar, the other species continue to react rapidly along the wall when P and T are nearly constant and do not slow down until some distance downstream ($x \sim 0.005 m$). Therefore, the turning rate must be faster than the combustion rate. This is not so in the last two cases since the change in composition along the wall slows down at approximately the same point where P and T become nearly constant. In a simple model, the current situation is like having the wall pressure and temperature following the turn imposed directly at the inlet; the species are then allowed to relax toward their equilibrium state. The composition in the previous cases approaches equilibrium at approximately the same rate as or at a higher rate than the expansion.

Although the relaxation toward equilibrium is slower than the turning rate, the combustion reaction nevertheless proceeds at a appreciable rate. In other words, the composition

** The numerical error is neglected for the sake of analysis.

becomes nearly constant within a reason length along the nozzle — approximately $10^{-2} m$. The forward and reverse rates of the reactions must both be very high at the inlet so that the perturbed chemical system can response quickly. Along the center streamline, the species composition changes slowly. This only implies that the forward and reverse steps nearly balance each other since the inlet state is close to equilibrium. It is the result along the wall that leads to the conclusion of high forward and reverse rates. Quantitatively, the amount of each species downstream of the turn only differs from that in case 2 by a small percentage ($\lesssim 10\%$) even though the turn radius is a hundred times smaller. There are two major reasons for the difference: the change in the flow residence time over the turn and the change in reaction rates due to drop in pressure and temperature. Since the residence time is roughly proportional to the turn radius, the finding then implies that the reaction rates must be different. Consider now the overall production rate (*c.f.* equation 2.3.2.2); it must be larger in this case because of the shorter residence time. The Arrhenius rate coefficients and the products of concentrations are, however, smaller for both steps as P and T drop to their lower levels almost instantaneously. Then the appreciable production rate can only be the resulting difference between two fast steps.

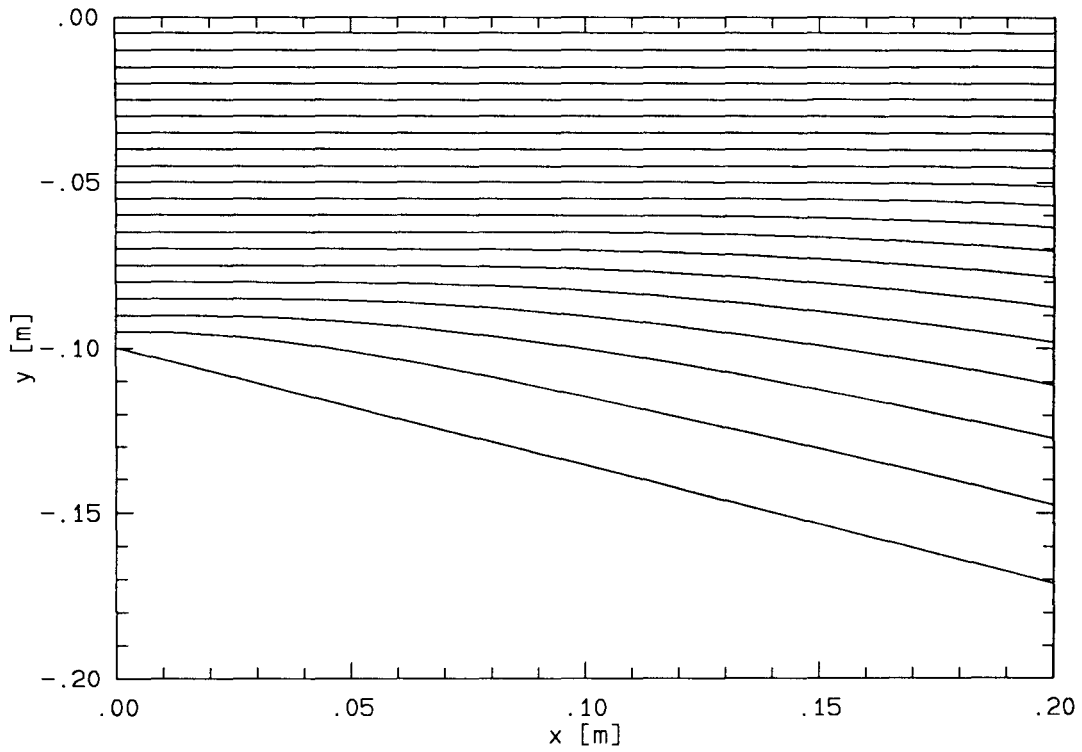


FIG. 8.8.1 Streamline pattern for a Re of 0.10 m.

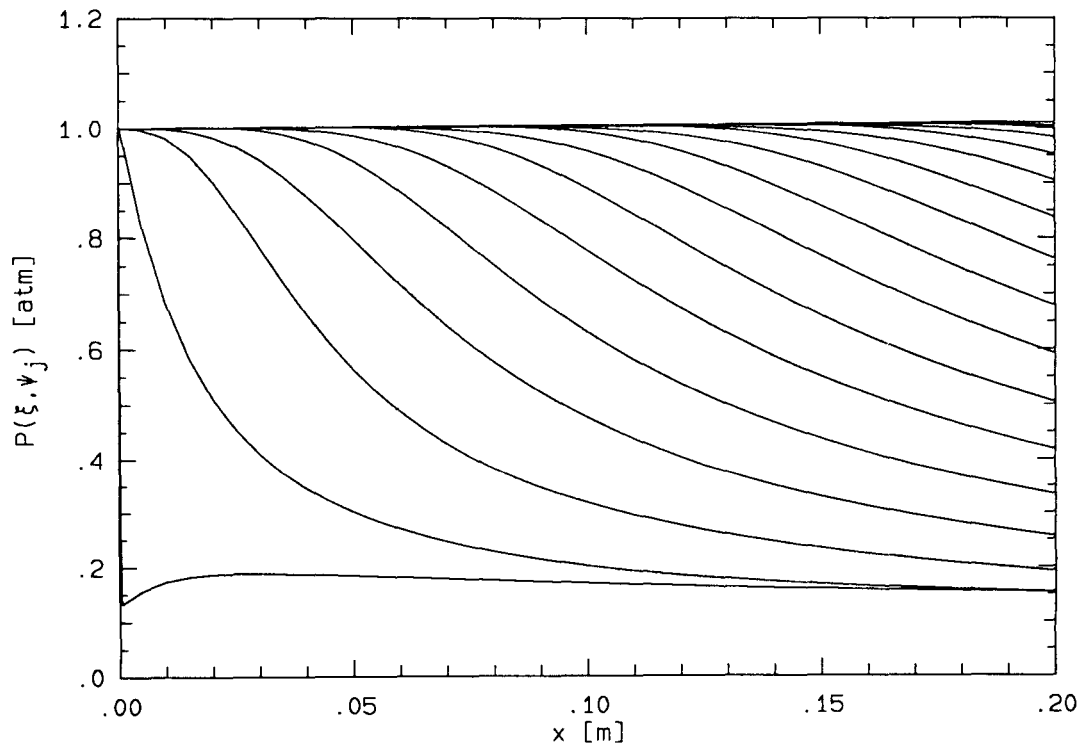
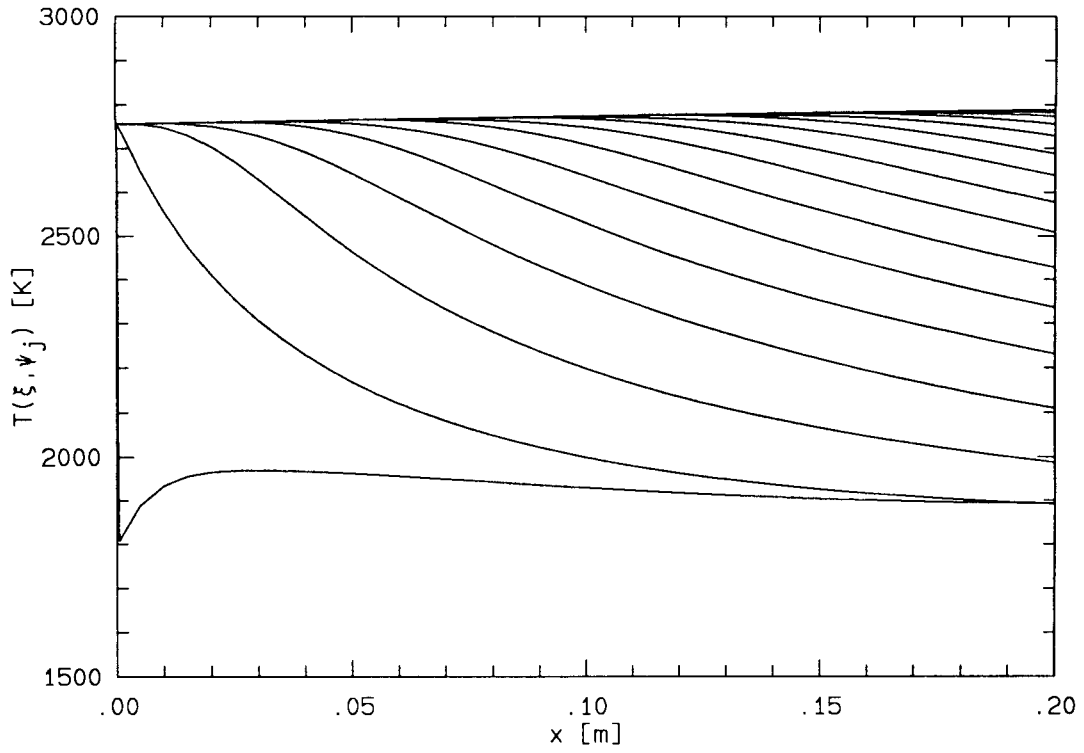
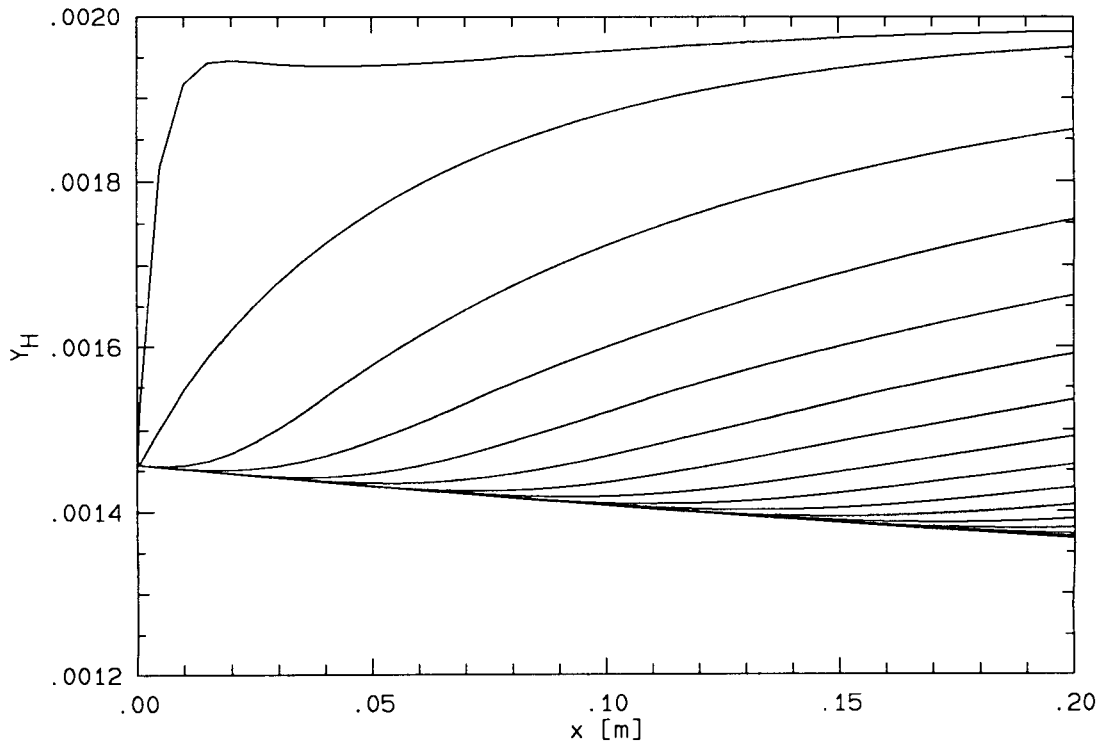
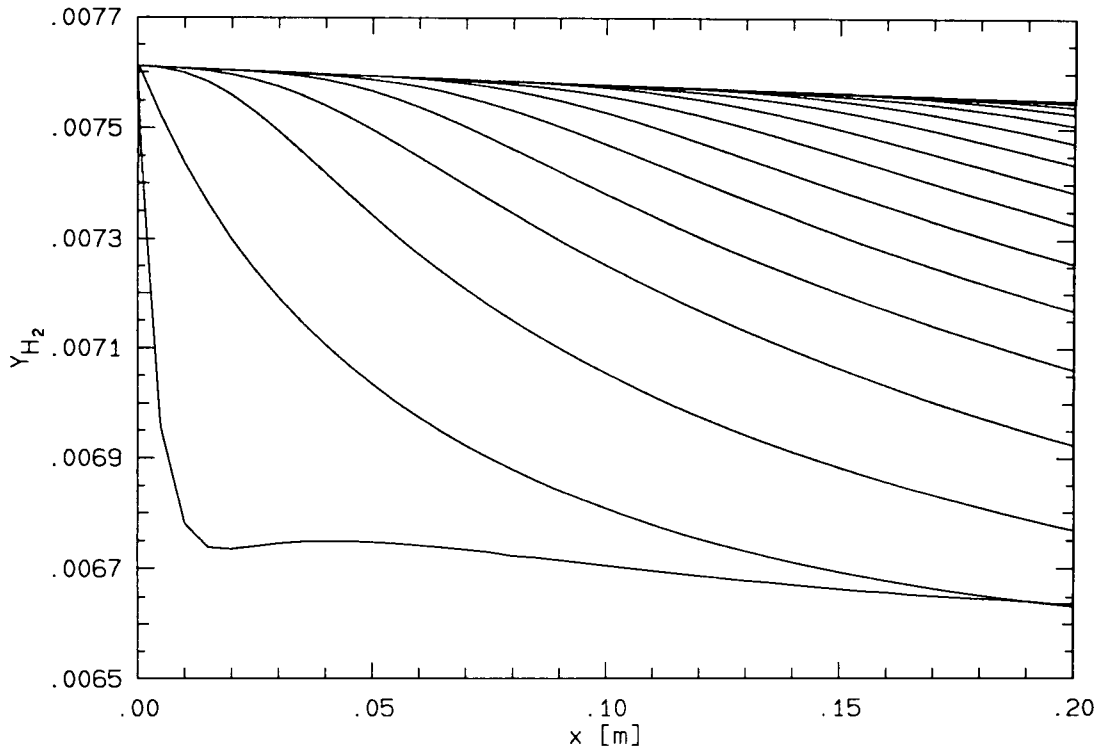
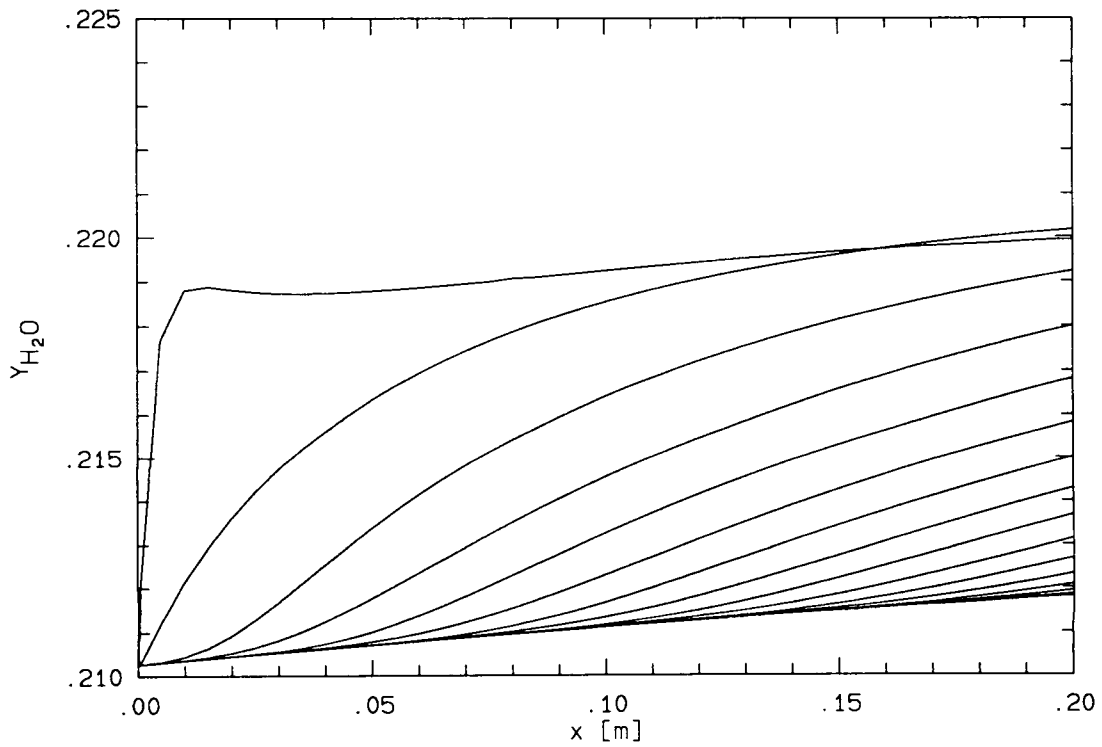
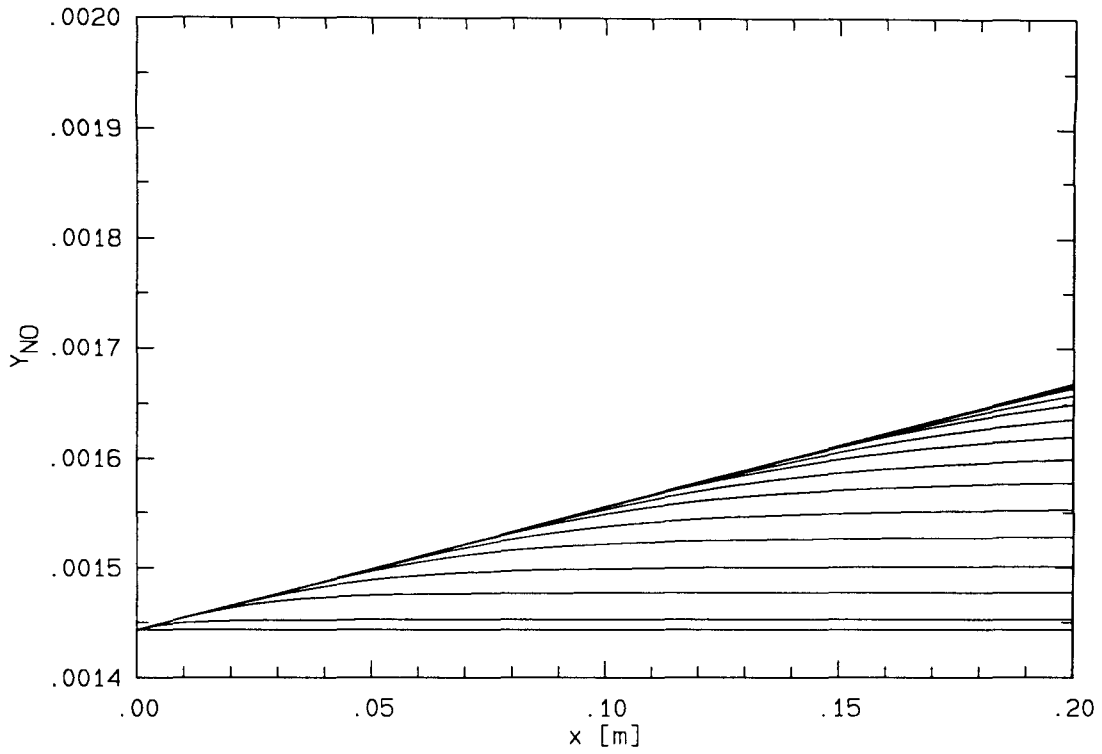
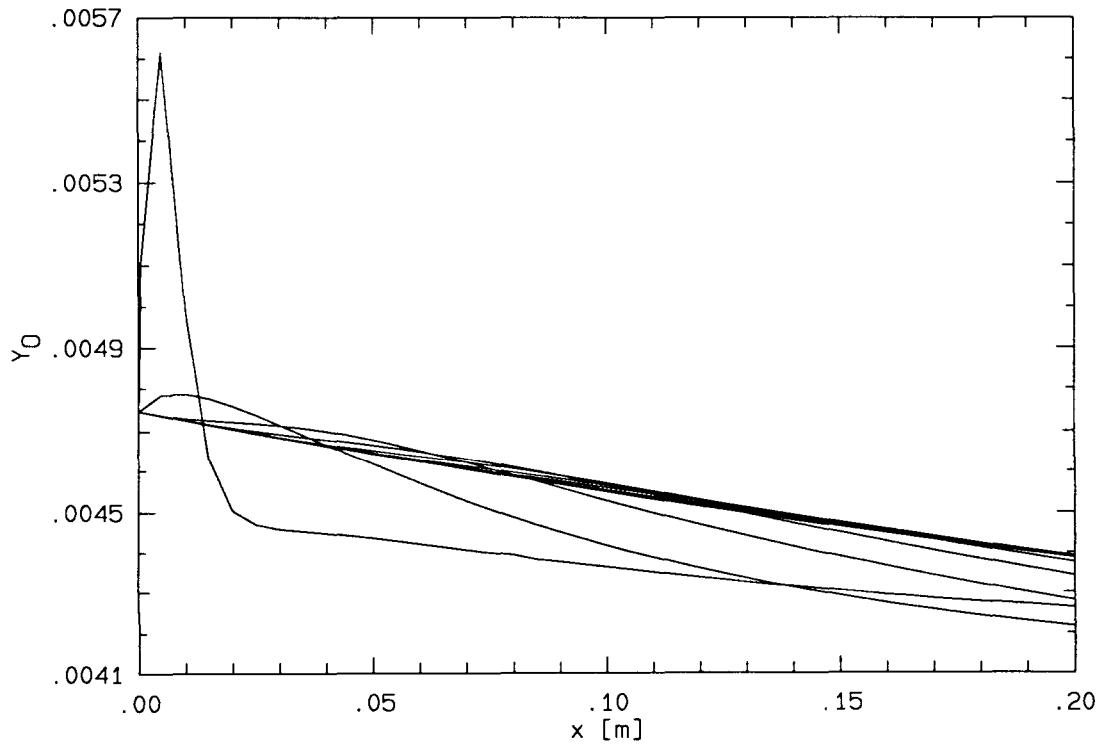
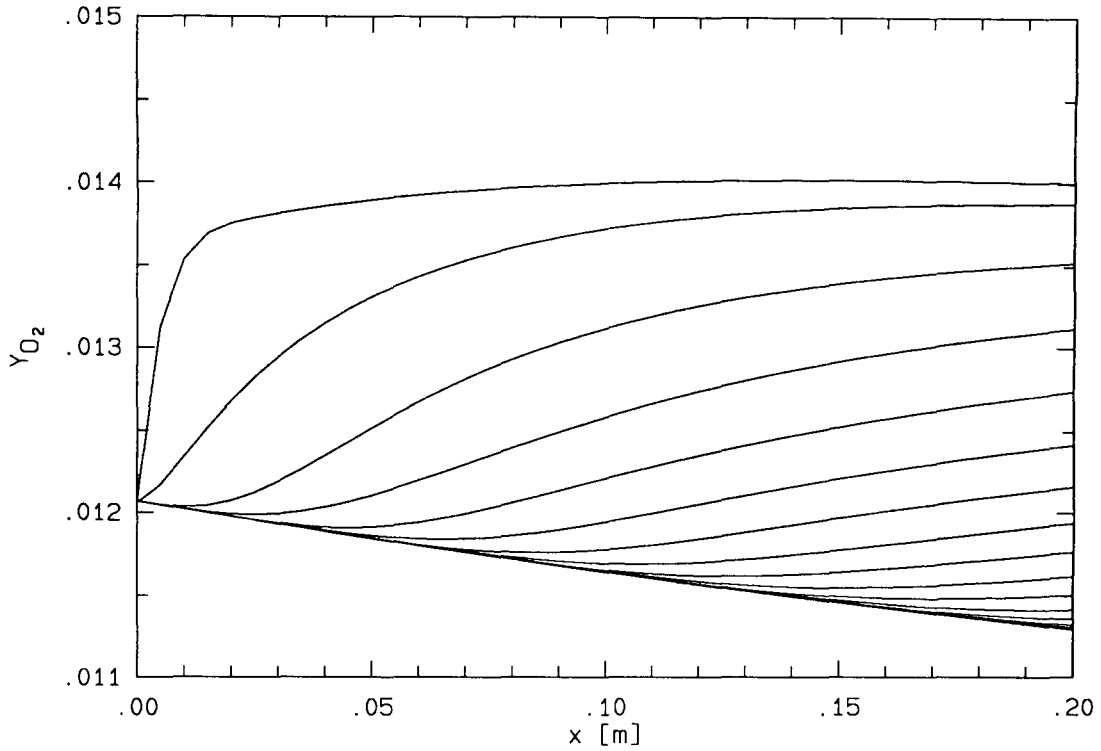
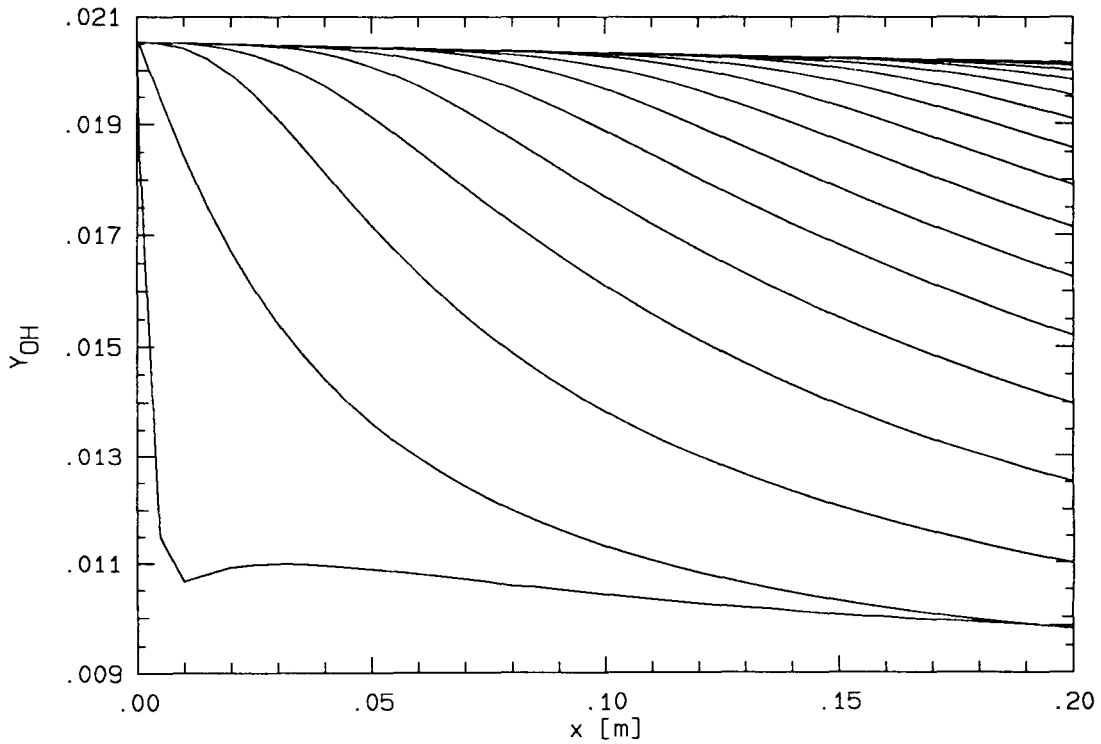


FIG. 8.8.2 Pressure along ψ_j , $j = 1, 21$ (bottom to top).

FIG. 8.8.3 Temperature along ψ_j , $j = 1, 21$ (bottom to top).FIG. 8.8.4 Mass fraction of H along ψ_j , $j = 1, 21$ (top to bottom).

FIG. 8.8.5 Mass fraction of H₂ along ψ_j , $j = 1, 21$ (bottom to top).FIG. 8.8.6 Mass fraction of H₂O along ψ_j , $j = 1, 21$ (top to bottom).

FIG. 8.8.7 Mass fraction of NO along ψ_j , $j = 1, 21$ (bottom to top).FIG. 8.8.8 Mass fraction of O along ψ_j , $j = 1, 21$.

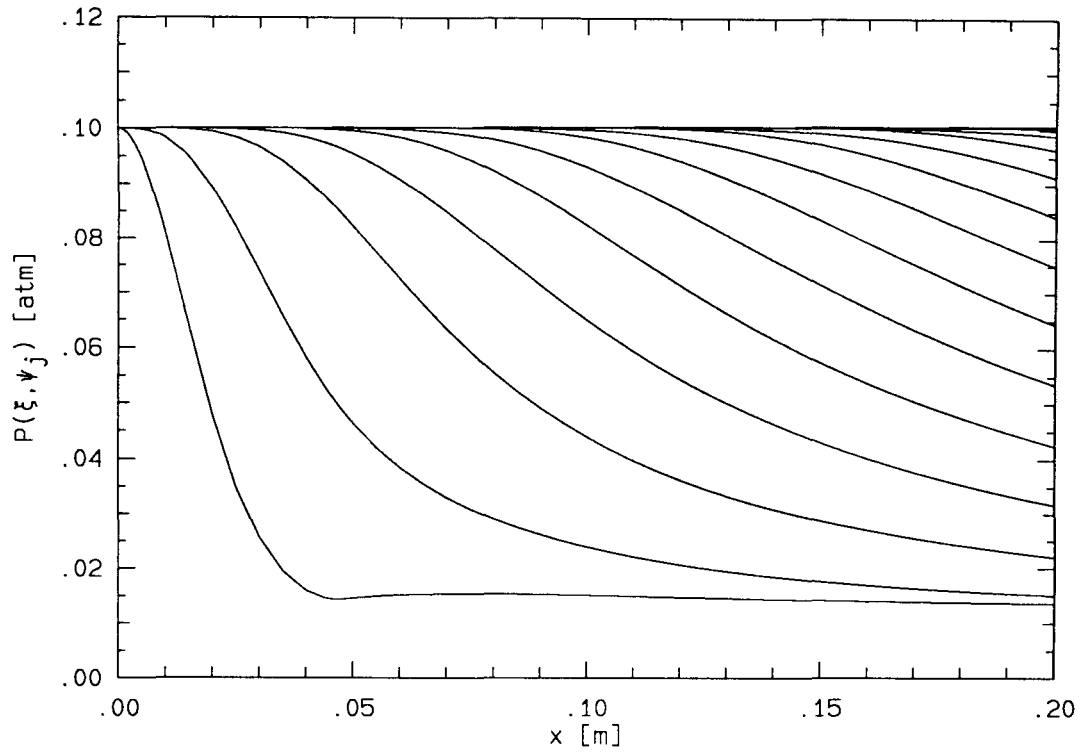
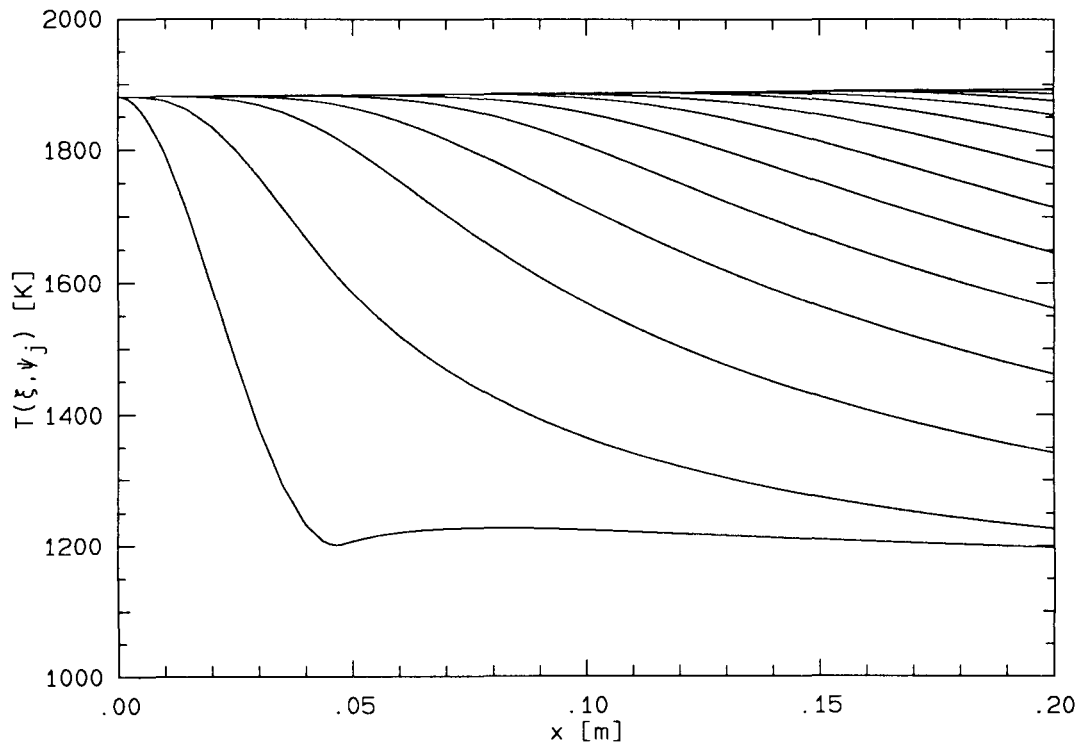
FIG. 8.8.9 Mass fraction of O_2 along ψ_j , $j = 1, 21$ (top to bottom).FIG. 8.8.10 Mass fraction of OH along ψ_j , $j = 1, 21$ (top to bottom).

8.9 Case 4: A P_{inlet} of 0.1 atm and R_t of 0.1 m (i.e. 100 L_x)

The fast chemical response in the previous cases is the result of high inlet pressure and temperature. A pressure $1/10$ of the previous one is used here with a mild wall turn curvature. Note that the inlet temperature is also lower according to the diffuser-combustor calculation. The inlet conditions for this calculation belong to **group 2** described in table 8.5.1.

The resulting distributions of P , T , M_f , q , Y_H , Y_{H_2} , Y_{H_2O} , Y_O , Y_{O_2} and Y_{OH} along the half-nozzle streamlines (21) are shown in figures 8.9.1 to 8.9.10. The frozen Mach number and speed shown are representative of the **group 2** inlet conditions. Most obvious of all is the behavior along the center streamline where the pressure, temperature, and the amount of H_2O only increase with extreme slowness due to the low inlet pressure and temperature. The kinetics along the wall, however, do not agree with the assumption of a *mild* expansion. The behavior is an exaggerated version of case 3 where the chemical time is too slow to catch up with the expansion rate.

In figures 8.9.5 to 8.9.10, all species along the wall evolve slowly independent of the expansion rate. As far as the chemical reactions are concerned, the pressure and temperature at the inlet can be assumed to have dropped to the values following the turn instantaneously. The chemical behavior displayed is merely a relaxation toward the equilibrium at the new pressure and temperature. The response of each species during expansion is the same as in cases 1 to 3. For example, the mass fractions of H, O_2 and H_2O increase during expansion while those of H_2 , O and OH decrease. The difference in the behavior of O along different streamlines can be attributed to its sensitivity to different expansion rates. It is more significant than in the previous cases because of a much larger inlet concentration of O. The composition of N, N_2 and NO are not plotted since the change in their mass fractions is less than $\mathcal{O}(10^{-6})$ throughout the nozzle.

FIG. 8.9.1 Pressure along ψ_j , $j = 1, 21$ (bottom to top).FIG. 8.9.2 Temperature along ψ_j , $j = 1, 21$ (bottom to top).

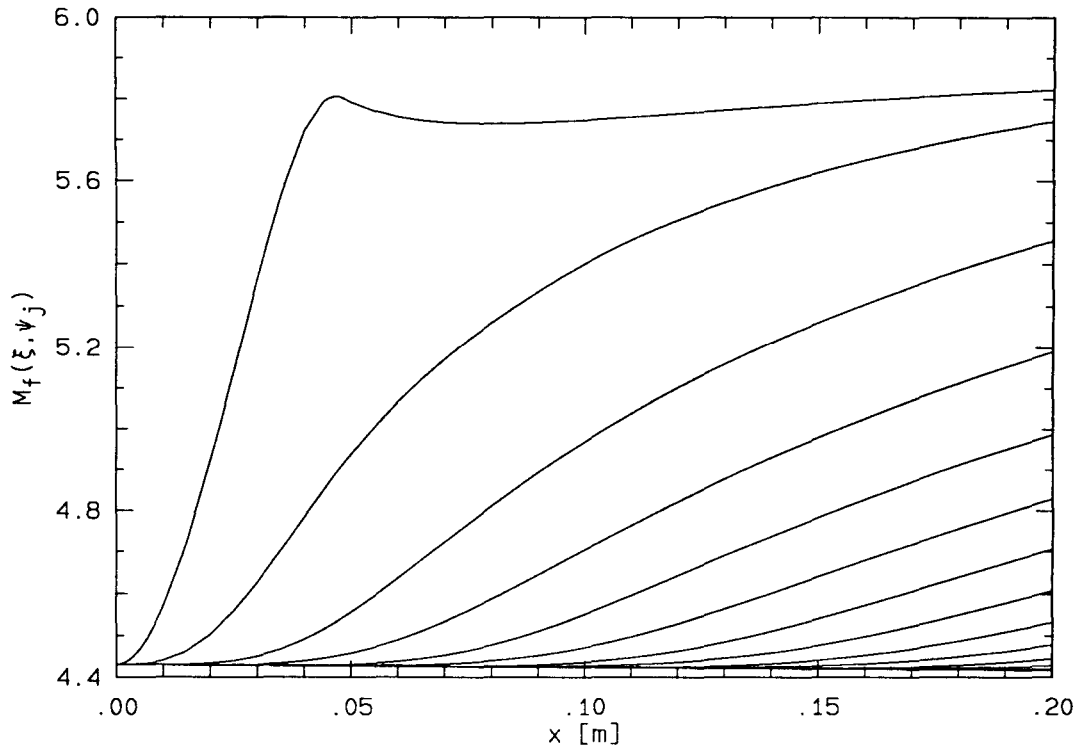


FIG. 8.9.3 Frozen Mach number along ψ_j , $j = 1, 21$ (top to bottom).

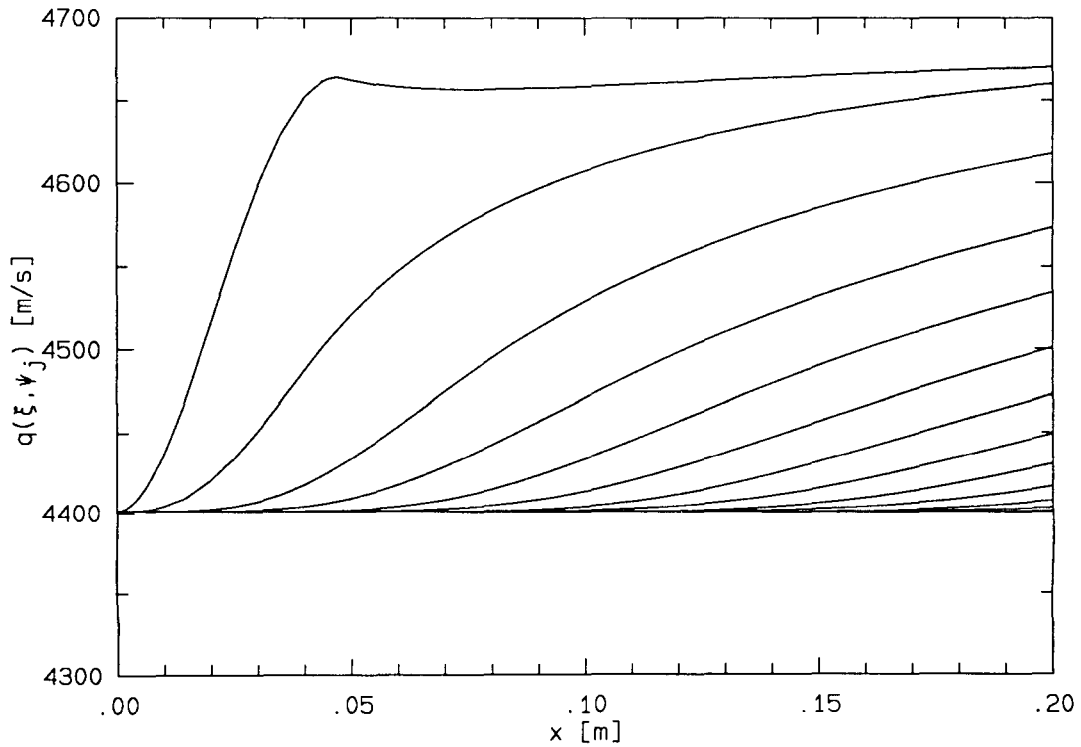
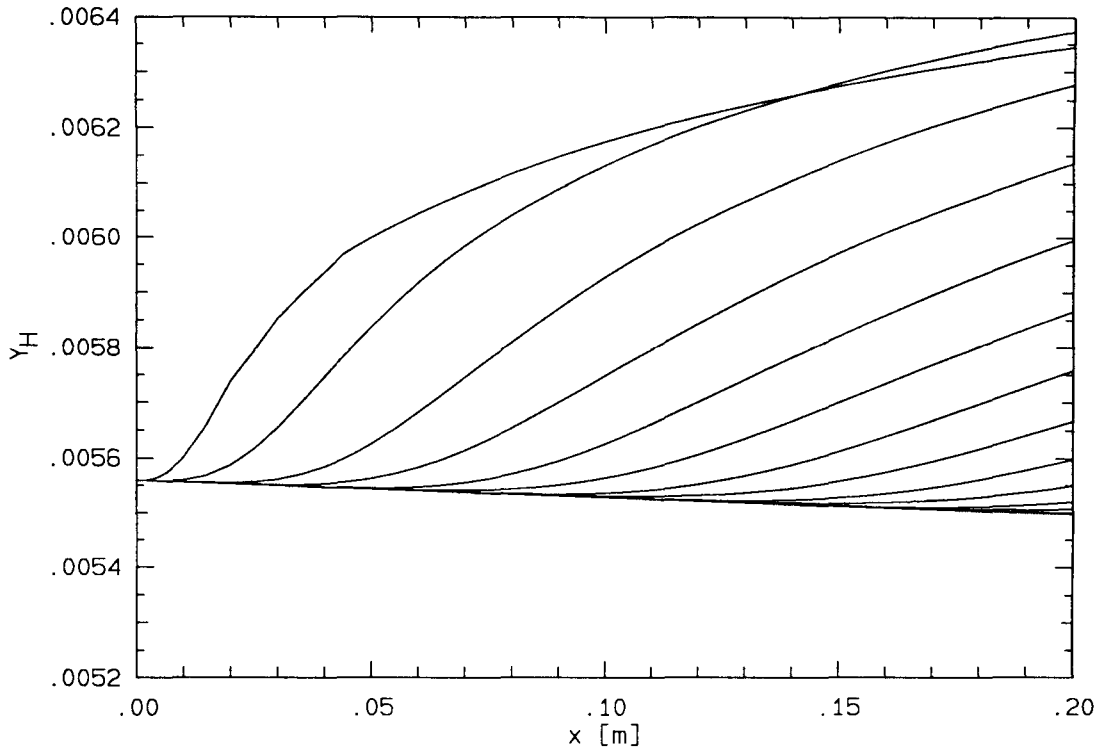
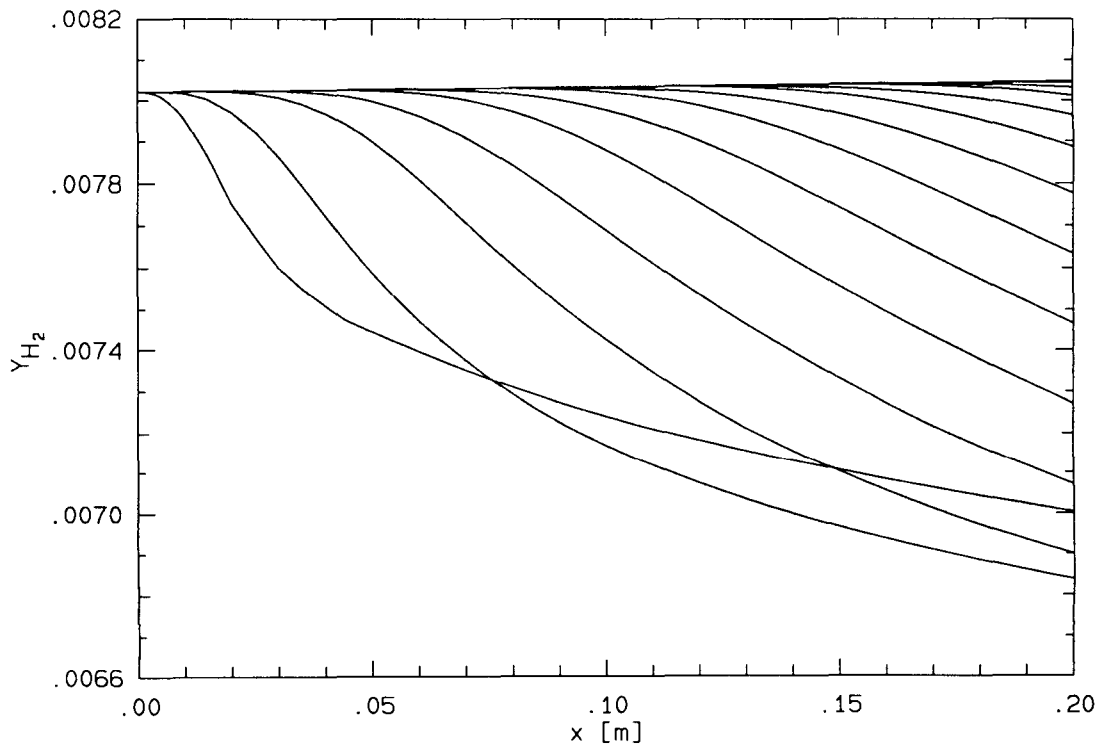
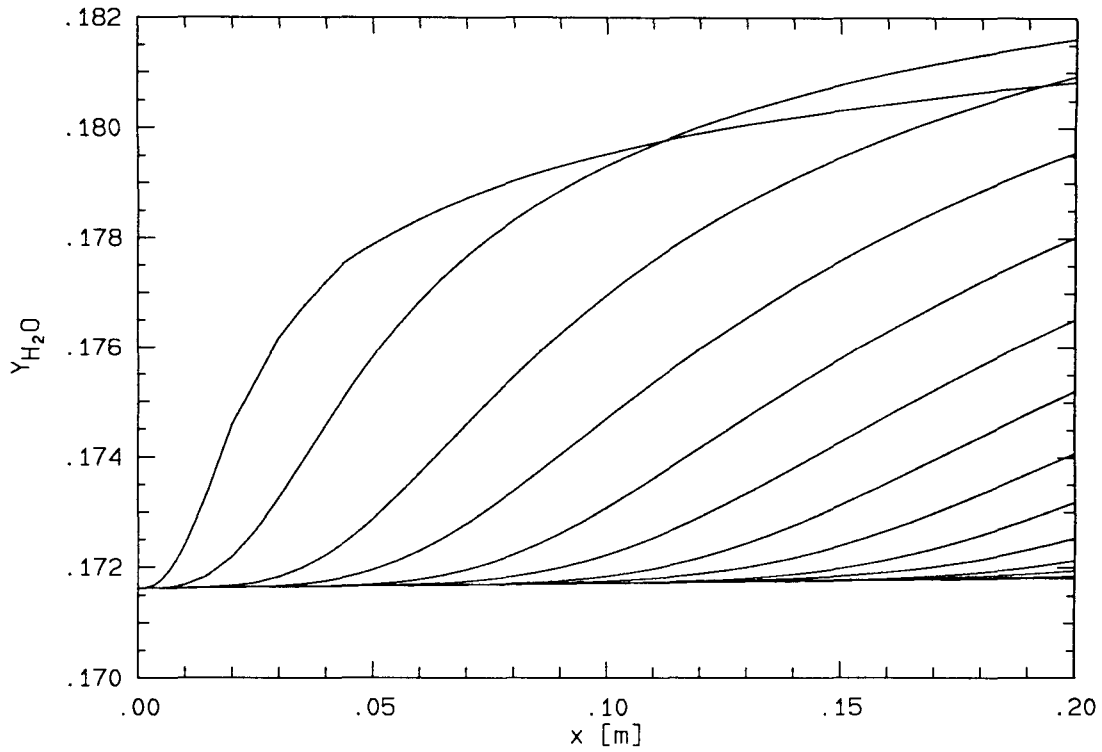
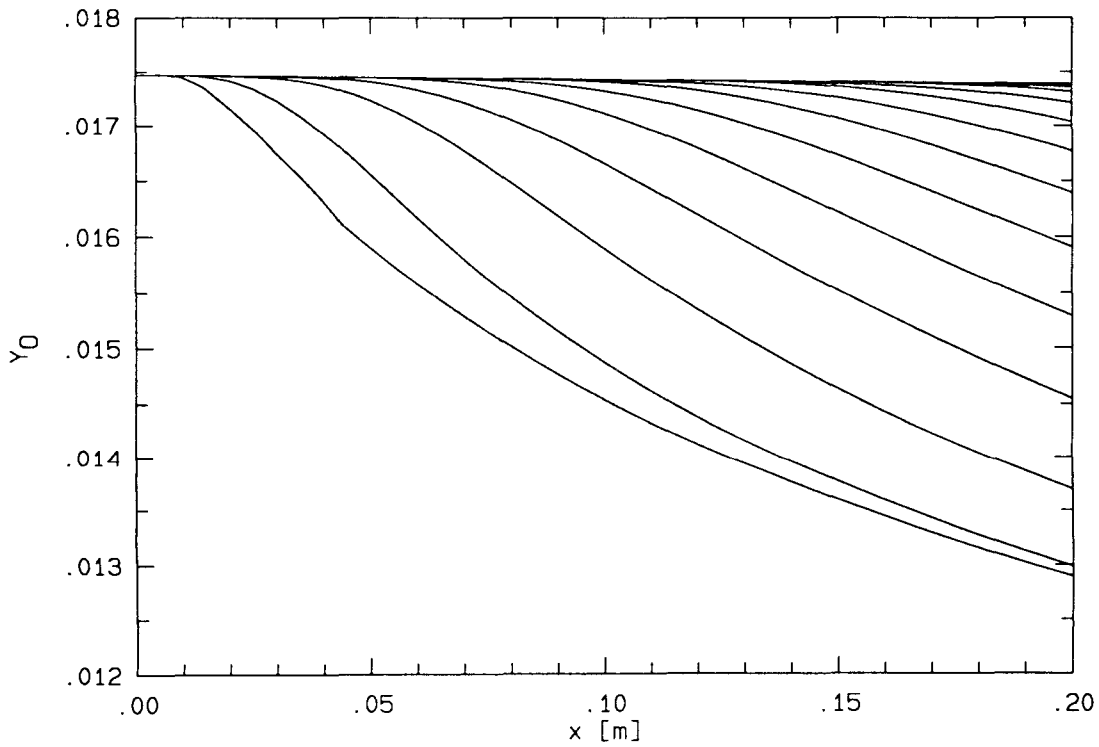
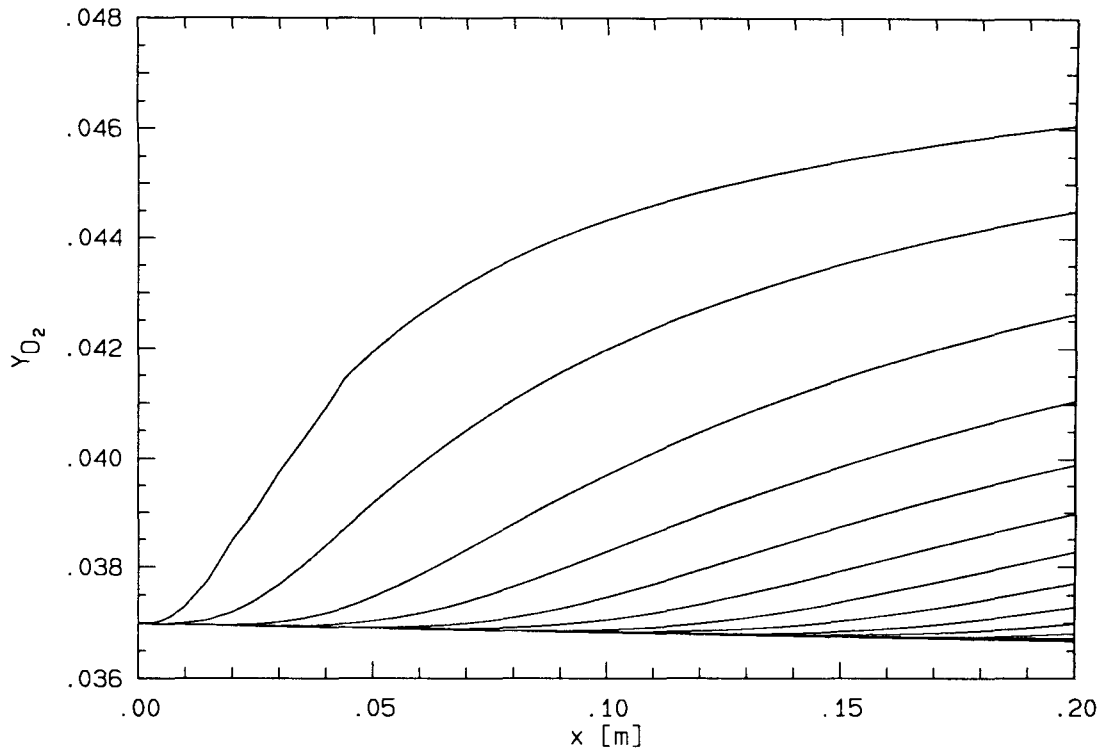
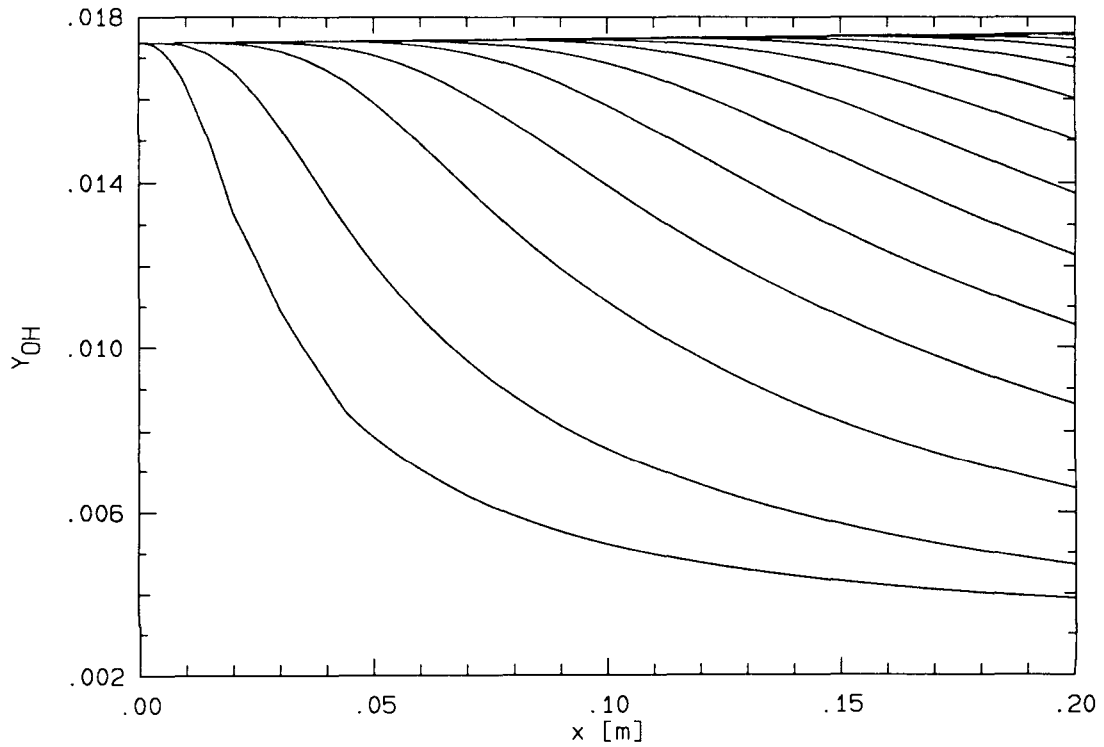


FIG. 8.9.4 Speed along ψ_j , $j = 1, 21$ (top to bottom).

FIG. 8.9.5 Mass fraction of H along ψ_j , $j = 1, 21$ (top to bottom).FIG. 8.9.6 Mass fraction of H_2 along ψ_j , $j = 1, 21$ (bottom to top).

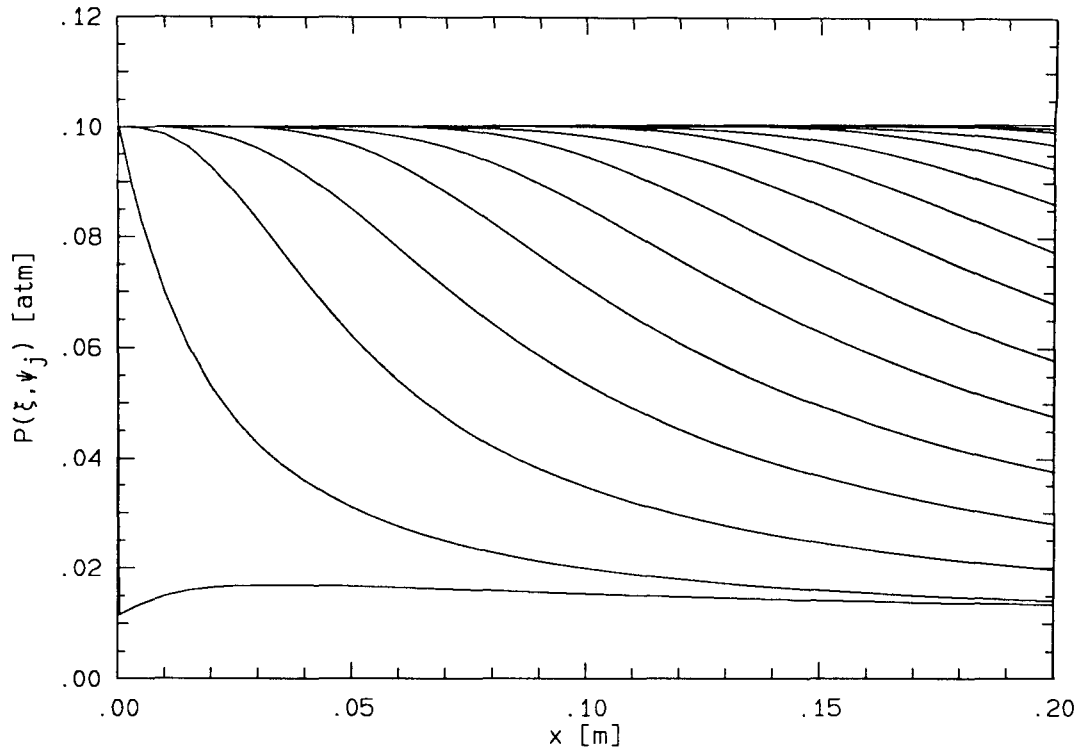
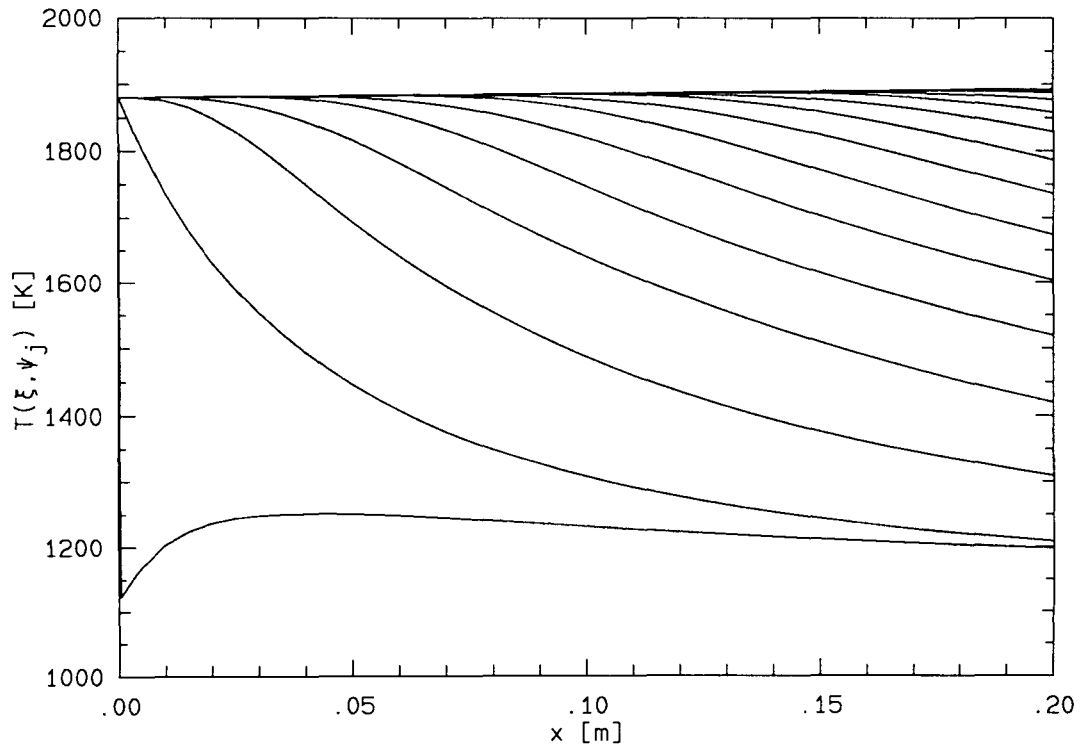
FIG. 8.9.7 Mass fraction of H₂O along ψ_j , $j = 1, 21$ (top to bottom).FIG. 8.9.8 Mass fraction of O along ψ_j , $j = 1, 21$.

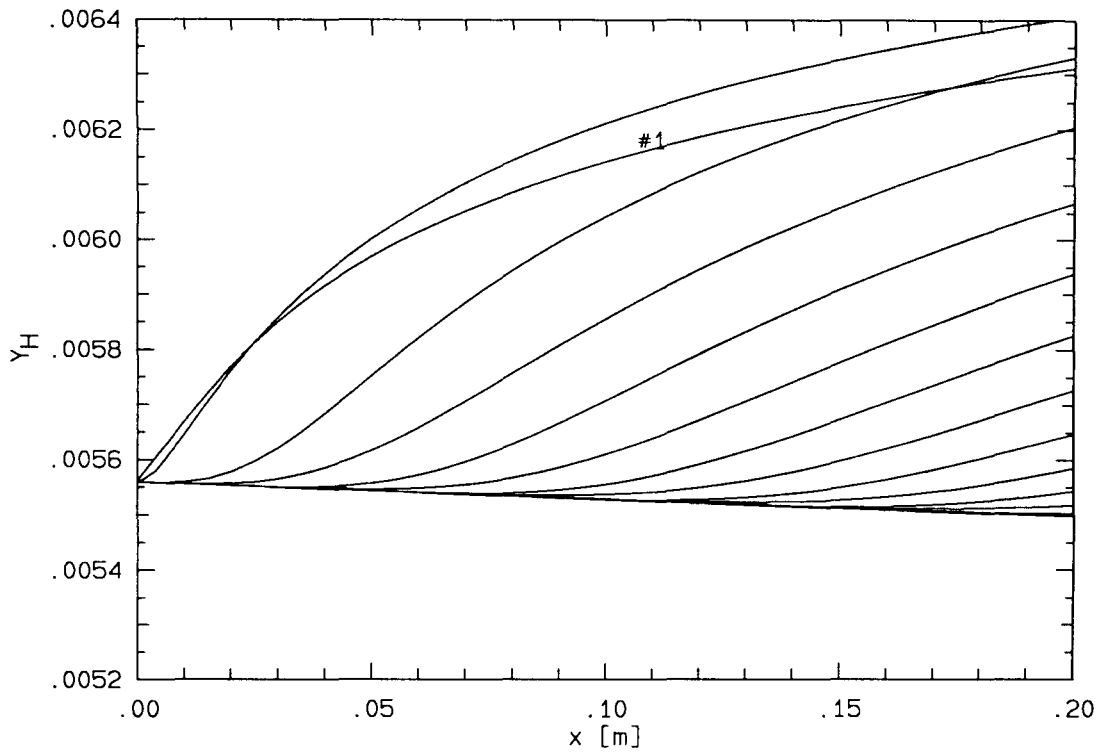
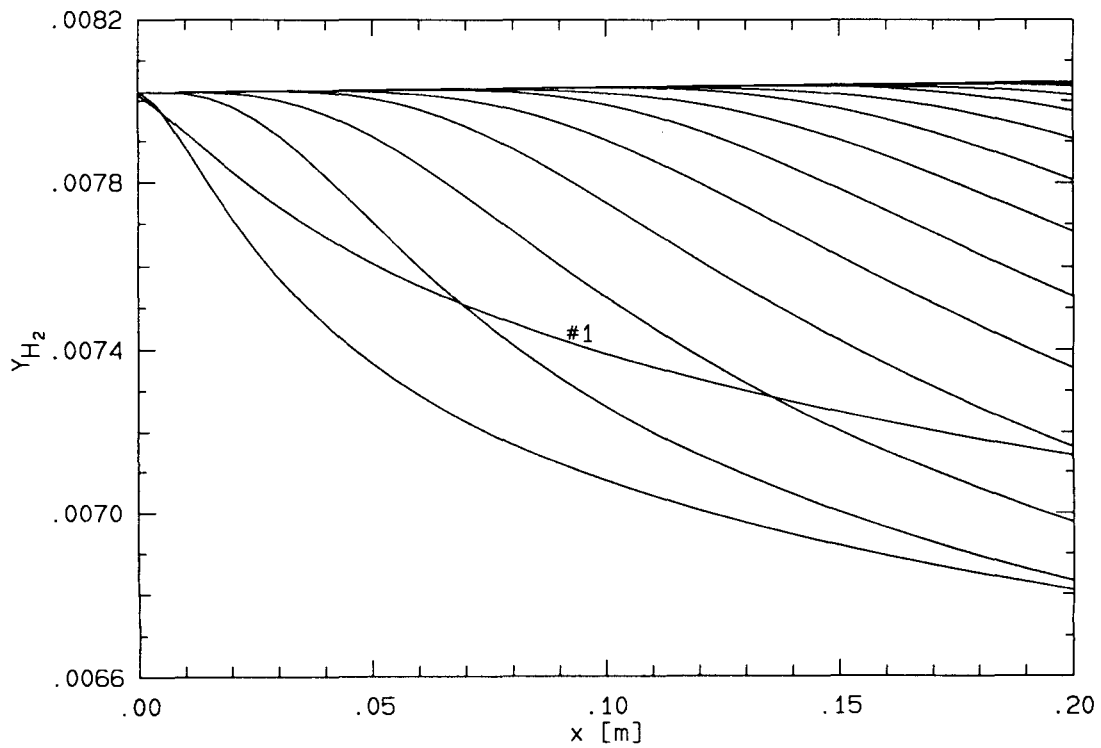
FIG. 8.9.9 Mass fraction of O_2 along ψ_j , $j = 1, 21$ (top to bottom).FIG. 8.9.10 Mass fraction of OH along ψ_j , $j = 1, 21$ (top to bottom).

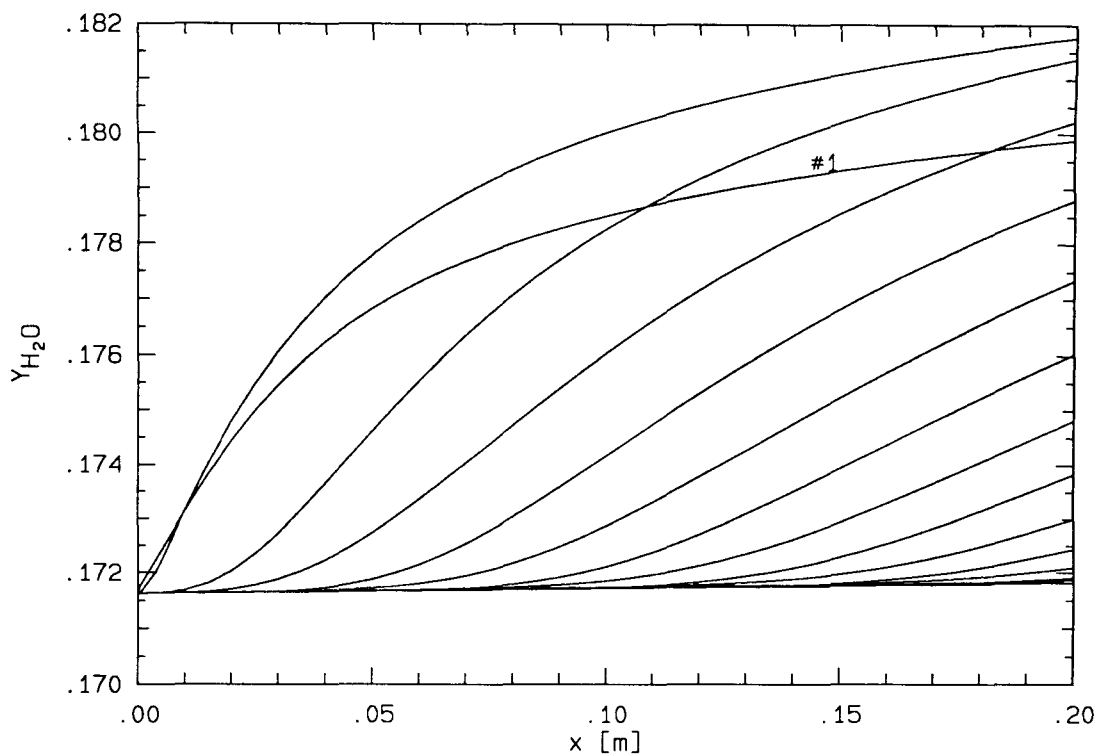
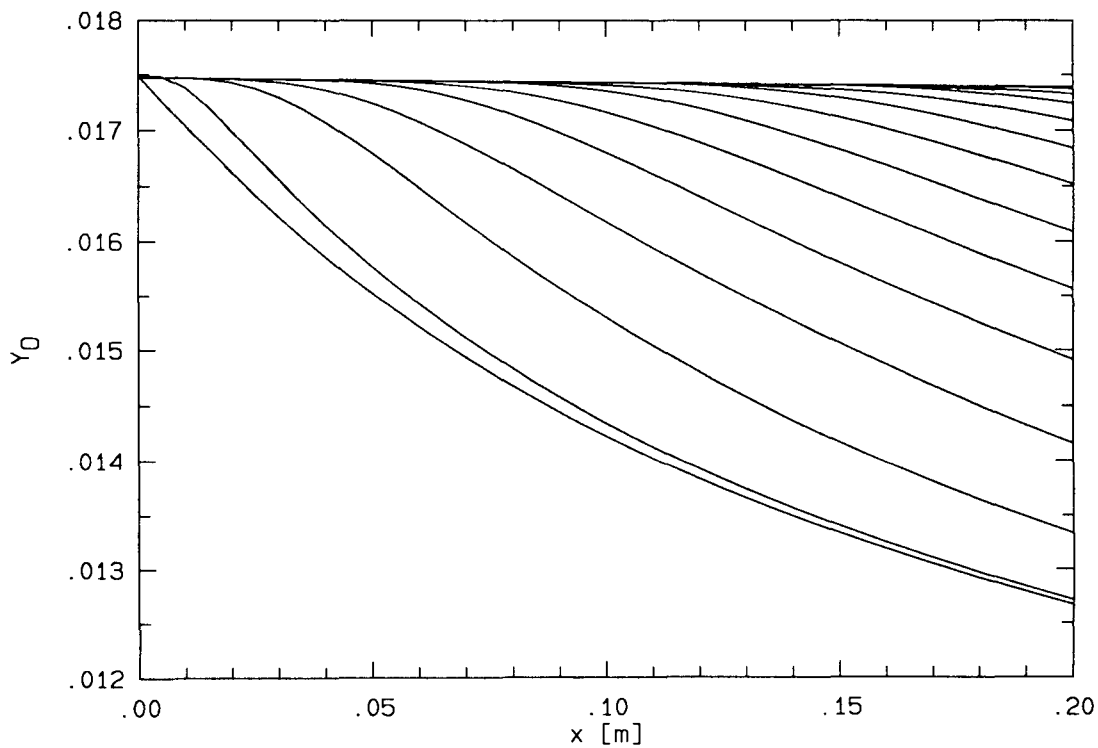
8.10 Case 5: A P_{inlet} of 0.1 atm and R_t of 0.001 m (i.e. L_x)

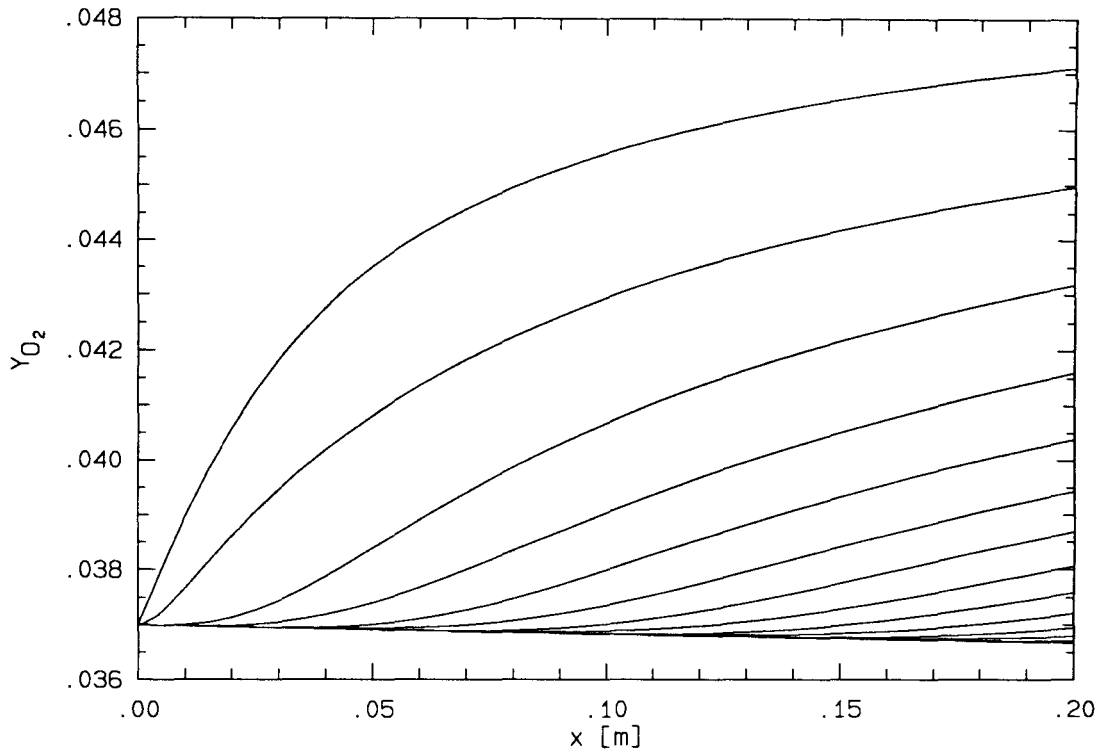
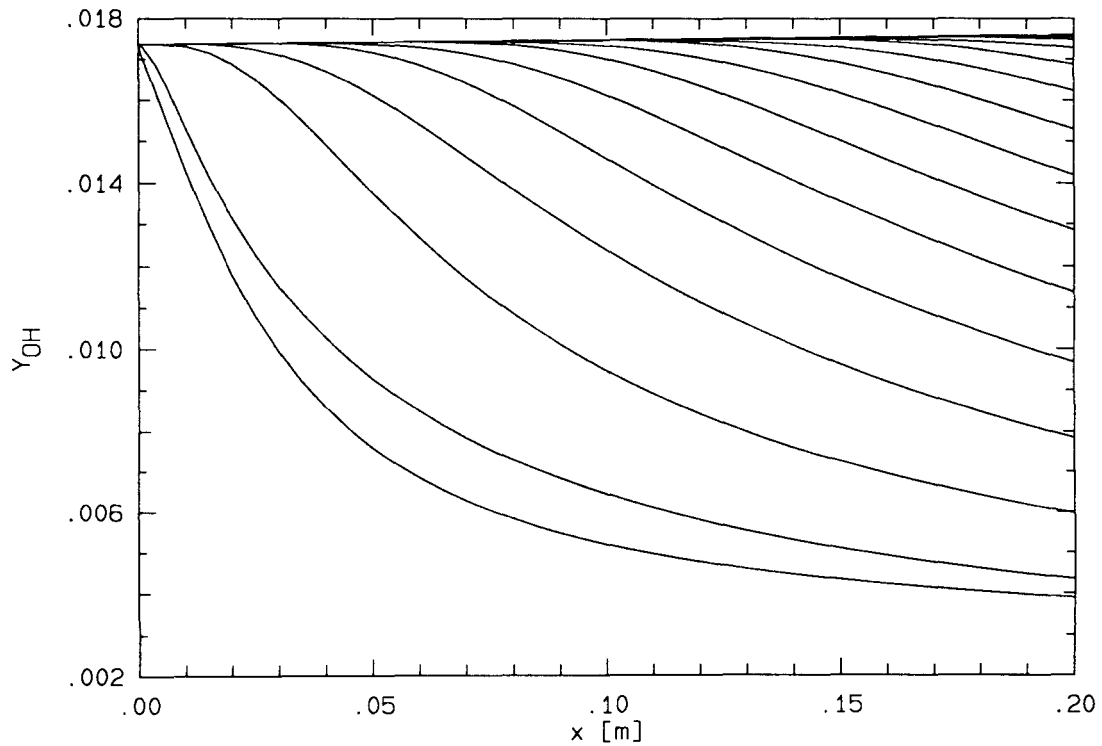
This case is mainly presented to support an argument made in the last two sections: the combustion of hydrogen and oxygen are capable of relaxing toward equilibrium at a appreciably high rate or within a reasonably short distance even though P and T drop to much lower values almost instantaneously at the inlet. That is, the combustion reaction cannot be assumed *frozen* for a nozzle with a length in the order of 1 m. The same inlet conditions as in case 4 is used except that the wall turn is a hundred times sharper.

Shown in figures 8.10.1 to 8.10.8 are again the distributions of P , T , Y_{H} , Y_{H_2} , $Y_{\text{H}_2\text{O}}$, Y_{O} , Y_{O_2} and Y_{OH} along the half-nozzle streamlines. Although P and T drop drastically faster than the last case, comparing the composition plots reveals little difference. The change in species composition is nearly unaltered by the much higher rate of expansion.

FIG. 8.10.1 Pressure along ψ_j , $j = 1, 21$ (bottom to top).FIG. 8.10.2 Temperature along ψ_j , $j = 1, 21$ (bottom to top).

FIG. 8.10.3 Mass fraction of H along ψ_j , $j = 1, 21$ (top to bottom).FIG. 8.10.4 Mass fraction of H_2 along ψ_j , $j = 1, 21$ (bottom to top).

FIG. 8.10.5 Mass fraction of H_2O along ψ_j , $j = 1, 21$ (top to bottom).FIG. 8.10.6 Mass fraction of O along ψ_j , $j = 1, 21$.

FIG. 8.10.7 Mass fraction of O_2 along ψ_j , $j = 1, 21$ (top to bottom).FIG. 8.10.8 Mass fraction of OH along ψ_j , $j = 1, 21$ (top to bottom).

8.11 Discussion

In the five cases presented, P , T , q and so on agree closely with those obtained from a simple wave approximation. In other words, the effects of chemistry is secondary to expansion. Nevertheless, interesting kinetic behavior is observed. The accelerated production of H_2O during an expansion is a particular example. But recall from chapter 5 that this behavior has already been observed when a fluctuating pressure is imposed on a static hydrogen-air mixture. It has been suggested that when the mixture is close enough to equilibrium, a pressure drop would favour the production of H_2O (*c.f.* figures 5.3.2 to 5.3.6). The situation here is slightly different. The nozzle inlet mixture is not yet at equilibrium, but there is an abundance of radicals in the mixture. To show that the production of H_2O is not unnatural, the inlet conditions for case 1 is used as the initial conditions for a fluctuating pressure calculation. In case 1, the inlet pressure is 1.0 atm and the pressure drops to approximately 0.15 atm following the expansion along the wall; therefore, the average pressure is set at 1.0 atm with an amplitude of fluctuation of -0.85 atm (*c.f.* section 5.3). The amplitude has a negative sign because a falling pressure is desired initially. A frequency of $2 \times 10^4 \text{ Hz}$ is used to simulate a turn radius of $\sim 0.2 \text{ m}$. The resulting evolution of $Y_{\text{H}_2\text{O}}$ is shown in figure 8.11.2. It can be seen that the initial amount of H_2O increases during the pressure drop. The pressure profile is shown in figure 8.11.1. Other species considered before are also plotted. These include H , H_2 , O and OH for which the mass fractions are shown in figures 8.11.3 to 8.11.6 respectively. Comparison of these figures with those in case 1 to 3 reveals the similarity in kinetic behavior during a pressure drop. Although not encountered in the nozzle calculation, this fluctuating pressure calculation clearly shows that a compression do not favor to the production of H_2O .

Another significant characteristic of the hydrogen-air kinetic is its intrinsic time scale. At high initial pressure and temperature, the time scale is very short. For the **group 1** conditions where $P \sim 1.0 \text{ atm}$ and $T \sim 2800 \text{ K}$, the chemical time is in the *microsecond* scale. But for the **group 2** conditions where $P \sim 0.1 \text{ atm}$ and $T \sim 1800 \text{ K}$, the time scale is at least three orders longer. Therefore, it is always advantageous to have high pressure and temperature at the combustor exit or the nozzle inlet. Unfortunately, it is not practical to have high pressure in a combustor since this would impose higher loss in the diffuser. It would also require an unrealistically long nozzle to expand the combustor product to ambient pressure. Higher combustor exit temperature does not have these mal-effects. In fact, temperature has been found in chapter 4 to have a stronger influence on the chemical time. To achieve this, the combustor must be highly efficient. The methods discussed in chapter 5 for enhanced combustor performance can be of assistance.

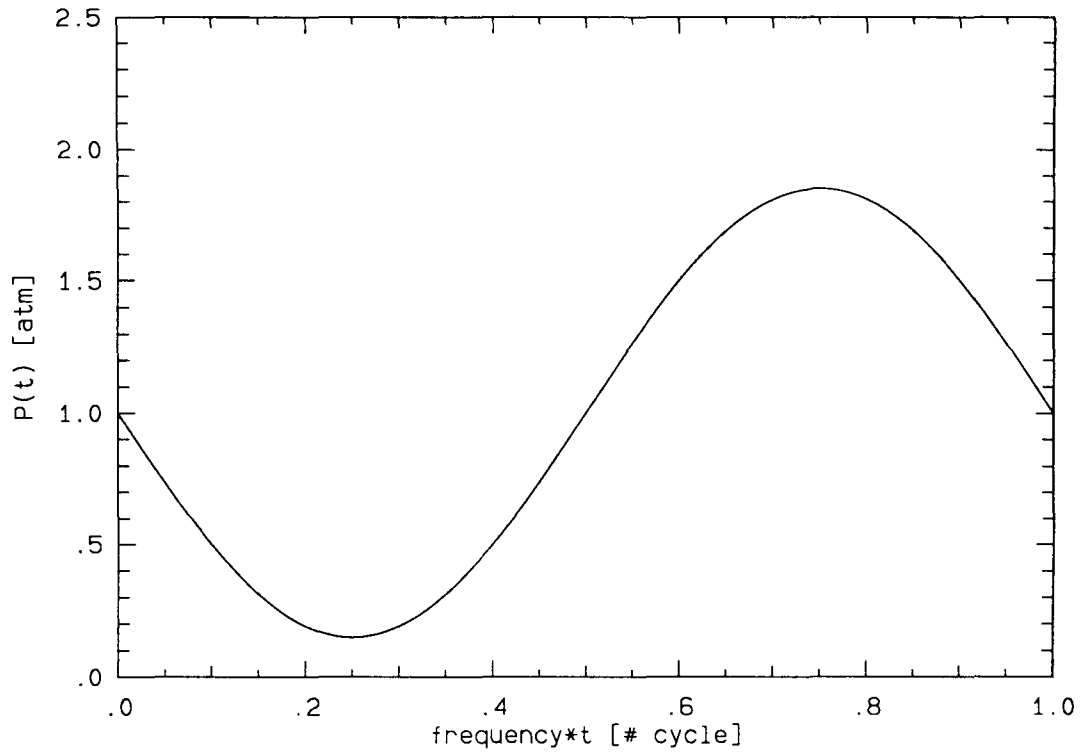


FIG. 8.11.1 Fluctuating pressure profile for a frequency of 2×10^4 Hz.

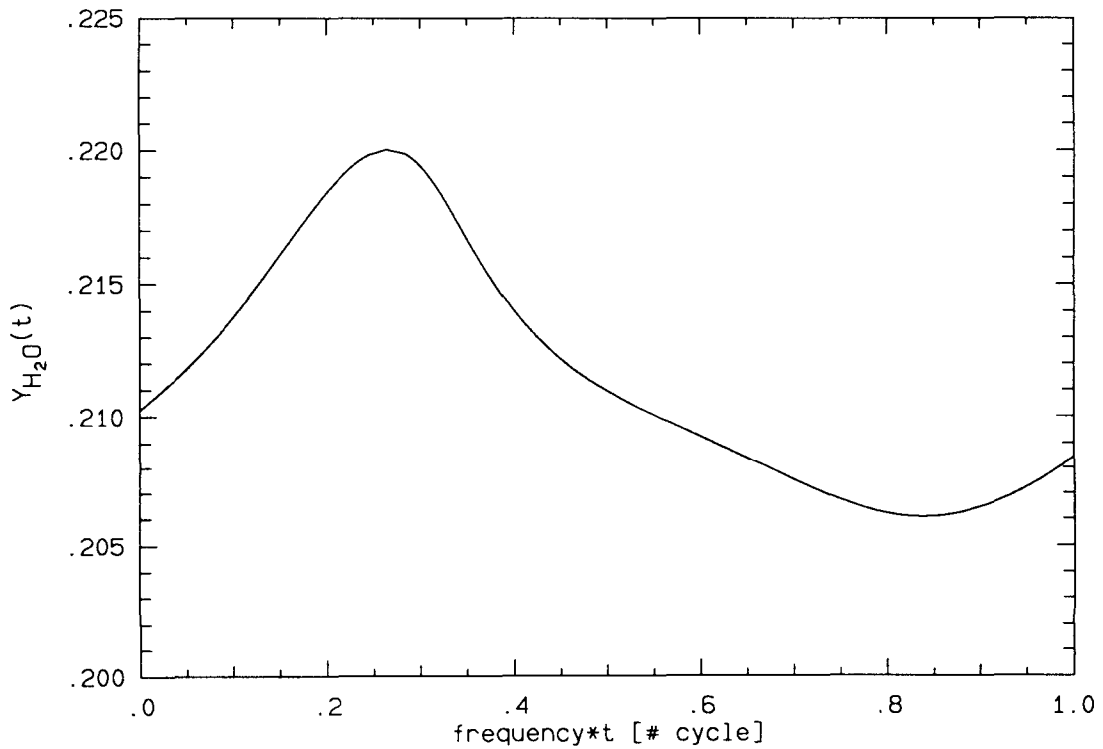


FIG. 8.11.2 Mass fraction of H_2O in one pressure cycle.

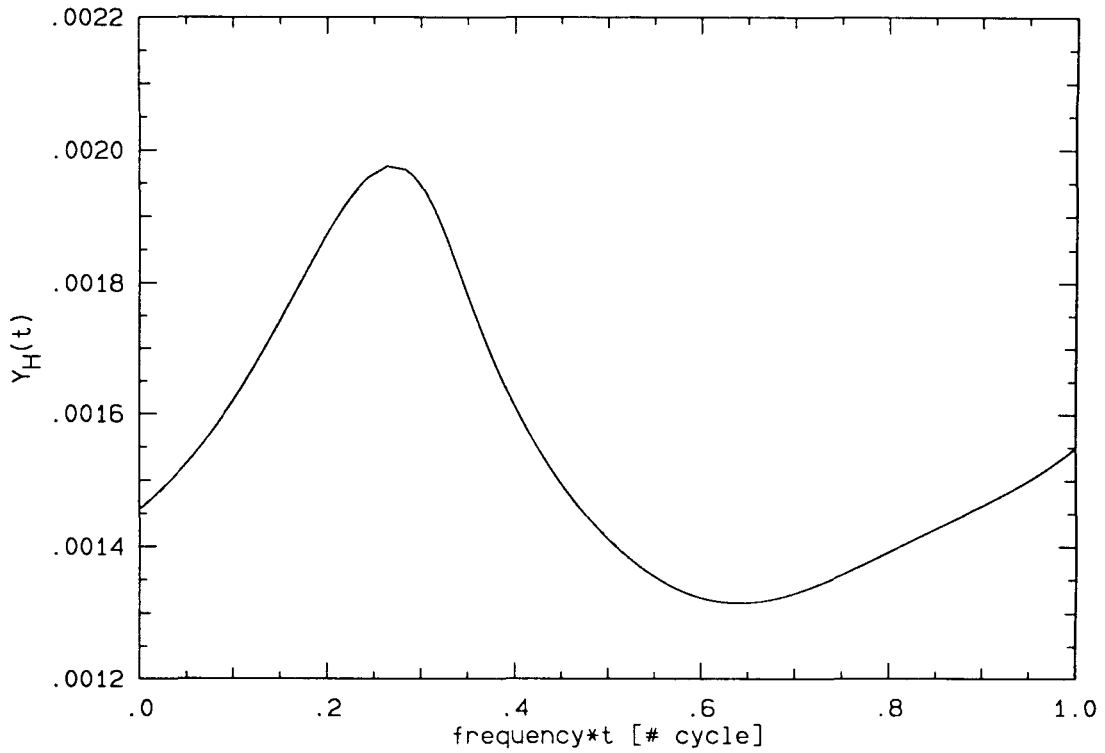
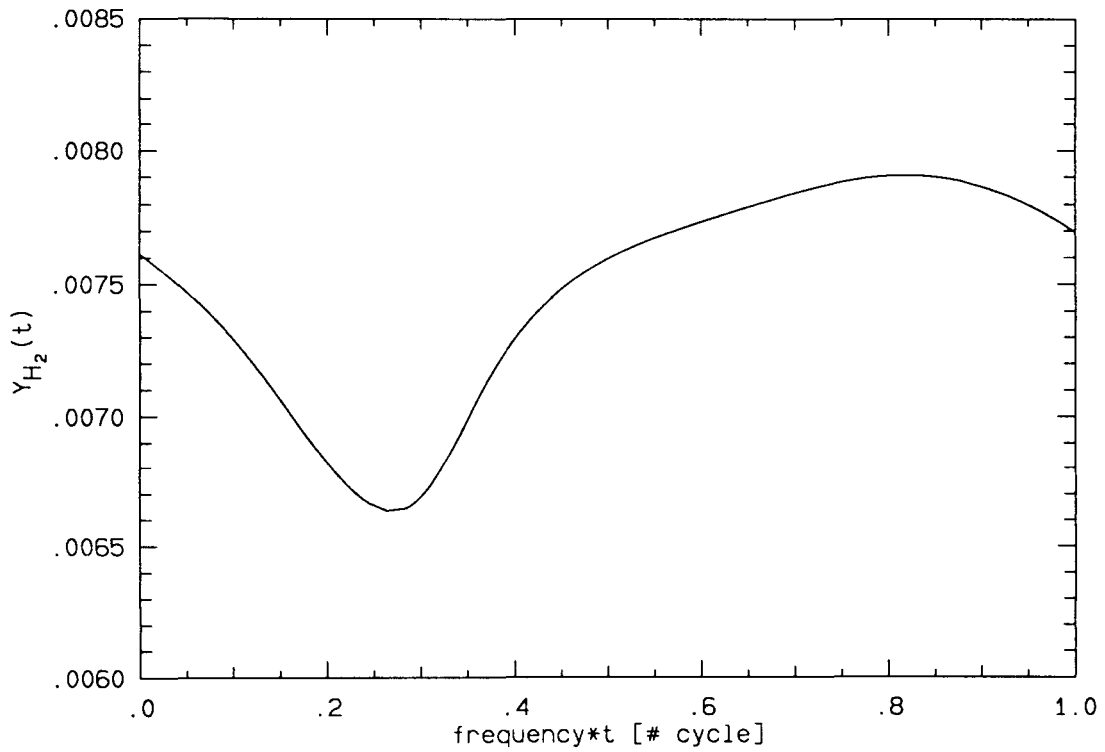


FIG. 8.11.3 Mass fraction of H in one pressure cycle.

FIG. 8.11.4 Mass fraction of H_2 in one pressure cycle.

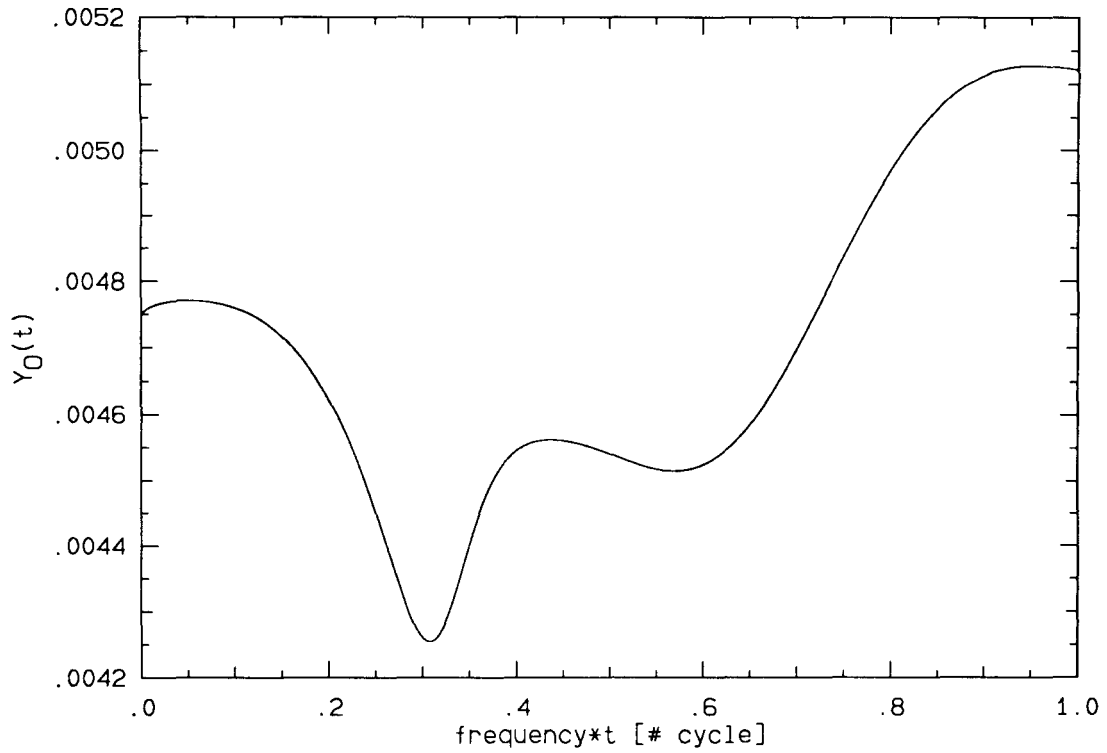


FIG. 8.11.5 Mass fraction of O in one pressure cycle.

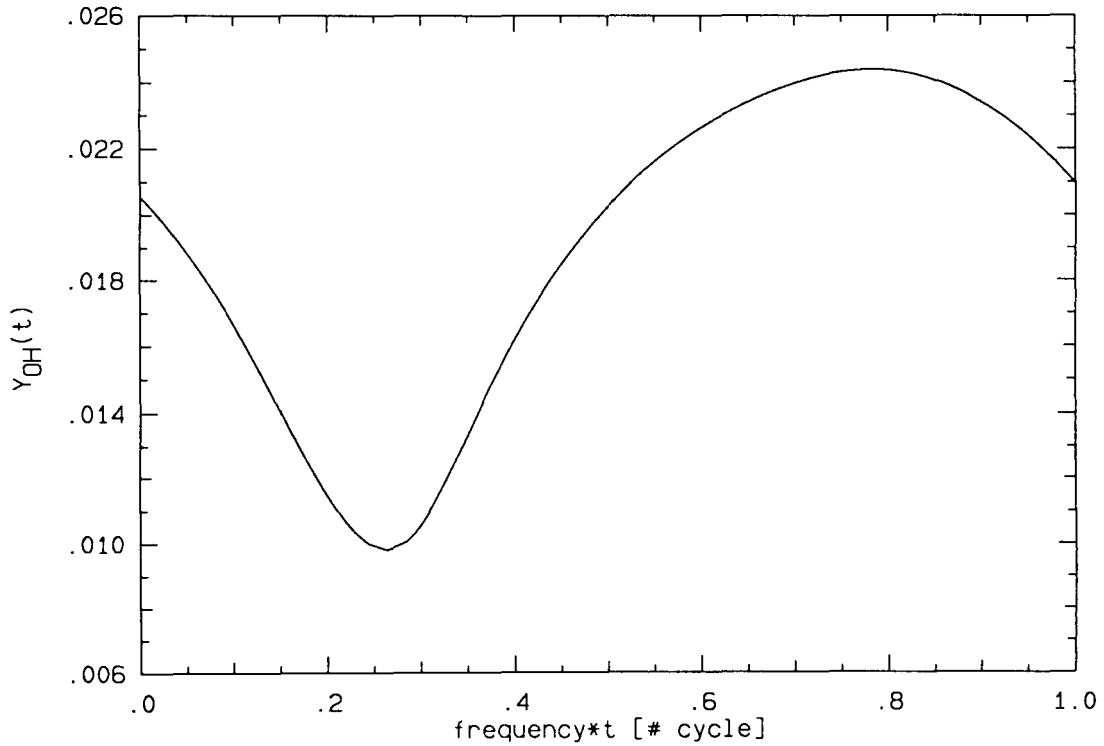


FIG. 8.11.6 Mass fraction of OH in one pressure cycle.

CHAPTER 9

Recommendation for Future Work

9.1 Chemical Kinetics

Most of the studies in this work have been conducted with finite-rate chemical reactions. Although the reduced chemical system only contains 13 species and 27 reactions, to study the kinetics in depth is extremely difficult. A close look at the reaction mechanisms and the dependence of their production rates on temperature, pressure and composition is required. This has been attempted in the combustor calculation with some success. However, that analysis is in no way completed. Some rate-determining reactions have been deduced under the conditions specified in that study. There remains the question of what would happen if those conditions are perturbed and why does the system respond as such. These questions arise when two seemingly unimportant reactions which are competing against each other at equal rate are perturbed so that one of the reactions becomes much more important. This situation has been suggested to explain the kinetic behavior observed in the fluctuating pressure calculation and the nozzle calculation during rapid expansion. To prove this, one must analyze the sensitivity of each reaction to any perturbation.

A phenomenon that this work fails to observe is the freezing of several high energy radicals during rapid expansion. It has been suspected that radicals such as OH would render inactive under this circumstance; instead, it has been found to be the species responsible for the production of H₂O during an expansion. The analysis suggested above may again help to explain the behavior. A subject related to the phenomenon of freezing is the chemical energy locked up in various radicals. Freezing is an adverse behavior since it prevents the release of such energy. But the opposite might not always be favorable. For example, the formation of H₂O during an expansion is accompanied by the creation of H. It is then necessary to examine the heat of formation in the radicals rather than the phenomenon of freezing.

There are yet many interesting calculations that may be conducted using the combustor and the nozzle models developed in this work. Of particular interest are some nozzle calculations with different inlet compositions. The kinetic behavior observed in the nozzle is in part due to the abundance of active radicals from the inlet. A very different behavior is expected when some of those radicals are removed. Therefore, it is informative to find out whether this is the case and, if so, what are the species involved. The suggested role of OH in the process can also be confirmed in this manner. Furthermore, it is also desirable to extend the range of the nozzle calculation so that the behavior farther downstream can be examined. Only case 1 in chapter 8 has been calculated until the center streamline begins to interact with the wall disturbance. But even in that case, the nozzle pressure at the end of the calculation is far from the ambient. More importantly, an extended calculation would reveal whether the end mixture is at equilibrium or not — if the inlet conditions are uniform, the exit composition must be identical on all streamlines when equilibrium is reached.

9.2 Numerical

In the one-dimensional combustor calculations, very tight tolerances and small step-size have been used. This is because the number of differential equations to be solved are relatively small. As a result, very high accuracy can be achieved while the computational efficiency is still satisfactory. For a typical case shown in chapter 4, a CPU time of $\mathcal{O}(1)$ minute is required on a VAX machine. Computation of the nozzle model is much more expensive. Since there are two dimensions in the problem, two resolutions are desired. The number of differential equations to be solved depends on the cross-stream resolution or the number of streamlines. In several of the cases studied, the cross-stream resolution is very low so that the numerical error is significant. These include cases 3 and 5 in chapter 8. The typical run time for a reacting case using the characteristic boundary treatment is of $\mathcal{O}(10)$ CPU minutes on a CRAY Y-MP2E/116 machine.

To improve the efficiency of the nozzle code, and hence to achieve higher accuracy, the chemical kinetic handling procedures must be customized. Consider the run time for a non-reacting case where the reaction rates are not evaluated and are set to zero, it is only $1/5$ of the reacting counter part. CHEMKIN is a very convenient tool in developing a kinetic code, but many calculations are repeated in different routines. Customizing the kinetic calculations may eliminate this loss.

The performance of the nozzle program may also be improved slightly by using a combination of the methods developed in chapters 6 and 8. The interpolation and extrapolation scheme of chapter 6 is approximately 30% more efficient than the characteristic boundary treatment of chapter 8. However, the accuracy of the former scheme is much more sensitive to wall geometry. Depending on the case to be studied, it is possible to apply the faster scheme when the geometry is mild and apply the more accurate scheme only when the geometry is acute. This arrangement is tested in case 1 of chapter 8. The nozzle is manually broken into two sections; the exit conditions in the first section is used as the inlet conditions of the second. The combined CPU time is about 5% shorter than when using the characteristic method alone while the accuracy is identical. Although the gain is small in the test, it can be improved with a more sophisticated switching scheme.

APPENDIX I

Thermodynamic Equations for a Calorically Imperfect Gas

In order to represent a multi-component chemical system accurately, the dependence of a species' thermodynamic properties on its state must be taken into account. The standard state properties of most commonly encountered chemical species are available from many sources such as the JANAF thermochemical tables^[1] and the NASA combustion database. These basic properties are only functions of temperature and, therefore, can be conveniently used to derive more specific relations. There are two thermodynamic quantities encountered in this work that need to be clarified: the *absolute entropy* and the *frozen speed of sound*.

I.1 The Absolute Entropy

The absolute entropy is usually needed when the isentropic condition is involved. It must be obtained by combining the standard state entropy, $S_k^\circ(T)$, with the pressure term. Let S_k be the absolute entropy for the k^{th} species. Then according to the 1st and 2nd laws of thermodynamics,

$$TdS_k = dh_k^\circ - \frac{dP_k}{\rho_k} .$$

But the partial pressure and density are given by

$$P_k = X_k P \quad \text{and}$$

$$\rho_k = Y_k \rho$$

such that by applying the gas law for a mixture of perfect gases and the relationship between the mole fraction X_k and the mass fraction Y_k ,

$$\rho_k = \frac{m_k}{R_u} P_k .$$

The differential relation can now be integrated from the reference standard state to a particular state. In most thermodynamic database, S_k° is zero at the reference state of 1.0 atm and 298.14 K. Let S_k be zero at at the same state, then

$$S_k(P, T, X_k) = S_k^\circ(T) - \frac{R_u}{m_k} \log \left(X_k \frac{P}{P_a} \right) , \quad (\text{I.1.1})$$

where P_a is the atmospheric pressure.

The mass weighted absolute entropy is often more useful. It is defined as

$$\bar{S} = \sum_{k=1}^K S_k Y_k .$$

The result is

$$\bar{S}(P, T, X_j) = \sum_{k=1}^K S_k^{\circ} \frac{X_k m_k}{\bar{m}} - \frac{R_u}{m_k} \sum_{k=1}^K X_k \log X_k - \frac{R_u}{m_k} \log \frac{P}{P_a} . \quad (\text{I.1.2})$$

The conversion formula,

$$Y_k = \frac{X_k m_k}{\bar{m}}$$

has been used so that \bar{S} depends on mole fractions. Alternatively, the result can be written in terms of mass fractions.

I.2 The frozen Speed of Sound

In a calorically perfect and non-reacting gas, the speed of sound is found to be of great significance in the behavior of compressible gas dynamics, especially when in the supersonic regime. The equivalent quantity in a calorically imperfect and reacting gas is the frozen speed of sound. Its significance was pointed out by Einstein in 1920 and proven experimentally by Wegener and Cole^[16] in 1960. In this work, it has appeared in two occasions – chapter 6 and 8 – where upon manipulation of the flow equations, the quantity is found to take the role of the ordinary speed of sound*. Without referring to those studies, the frozen speed of sound can be derived with the following definition:

$$a_f^2 \equiv \left(\frac{\partial P}{\partial \rho} \right)_{\bar{S}, Y_k} . \quad (\text{I.2.1a})$$

The composition is kept constant in the partial derivative, hence, the frozen aspect of the quantity. This definition can also be expressed in another form^[14], namely,

$$a_f^2 \equiv \left(\frac{\frac{\partial \bar{h}}{\partial \rho}}{\frac{1}{\rho} - \frac{\partial \bar{h}}{\partial \rho}} \right)_{\bar{S}, Y_k} , \quad (\text{I.2.1b})$$

* In the characteristic formulation of chapter 8, the form of the frozen speed of sound is derived by Vincenti^[14].

where \bar{h} is the mass weighted specific enthalpy given by

$$\bar{h} = \sum_{k=1}^K h_k Y_k .$$

The first definition is used in the following derivation. Differentiating the expression for absolute entropy (equation I.1.1) with respect to ρ while holding S and Y_k constant, a relation involving $(P/\rho)_{\bar{S}, Y_k}$ is obtained:

$$\sum_{k=1}^K Y_k \frac{dS_k^\circ}{dT} \left(\frac{\partial T}{\partial P} \frac{\partial P}{\partial \rho} + \frac{\partial T}{\partial \rho} \right)_{\bar{S}, Y_k} - \frac{R_u}{\bar{m}} \left(\frac{1}{P} \frac{\partial P}{\partial \rho} \right)_{\bar{S}, Y_k} = 0 .$$

With the gas law for a mixture of perfect gases,

$$T = \frac{\bar{m}P}{R_u \rho} \quad \Rightarrow \quad \begin{cases} \frac{\partial T}{\partial P} = \frac{T}{P} \\ \frac{\partial T}{\partial \rho} = -\frac{T}{\rho} \end{cases}$$

and that

$$\frac{dS_k^\circ}{dT} = \frac{C_{pk}^\circ}{T} ,$$

the result becomes

$$\left(\frac{\partial P}{\partial \rho} \right)_{\bar{S}, Y_k} = \frac{P}{\rho} \frac{\sum_{k=1}^K C_{pk}^\circ Y_k}{\sum_{k=1}^K C_{pk}^\circ Y_k - \frac{R_u}{\bar{m}}} .$$

Since the standard state heat capacity at constant pressure, C_{pk}° , is equivalent to the specific C_{pk} and

$$\frac{R_u}{m_k} = C_{pk} - C_{vk} \quad \text{and}$$

$$\sum_{k=1}^K \frac{Y_k}{m_k} = \frac{1}{\bar{m}} ,$$

the frozen speed of sound is then

$$a_f = \sqrt{\frac{\bar{C}_p P}{\bar{C}_v \rho}} = \sqrt{\bar{\gamma} \frac{P}{\rho}} \quad (\text{I.2.2})$$

where

$$\begin{cases} \bar{C}_p = \sum_{k=1}^K C_{pk} Y_k \\ \bar{C}_v = \sum_{k=1}^K C_{vk} Y_k \end{cases} \quad \text{and } \bar{\gamma} \equiv \frac{\bar{C}_p}{\bar{C}_v}$$

are the mass weighted specific heat at constant pressure and at constant volume and the ratio of mean specific heat. The resemblance between the frozen and the ordinary speed of sound is obvious.

APPENDIX II

A One-Dimensional Diffuser Model

The results of both the combustor calculation of chapter 4 and the nozzle calculations of chapter 7 and 8 are based extensively on the diffuser exit conditions. This is to ensure the use of practical inlet conditions for the combustor and the nozzle. The chemical composition at those points are not entirely arbitrary and neither are the pressure, temperature and flow speed. They are very much related and the key to their relationship is in the upstream component, the diffuser. In this appendix, the construction of a one-dimensional diffuser based on frozen or equilibrium chemistry is described. Because of the type of kinetic chosen, there is no need for any length scale and the calculation becomes one of matching between the inlet and the exit. Three major constraints has been imposed on the present diffuser model:

- i) diffuser inlet conditions are equivalent to ambient conditions which correspond to standard atmospheric conditions;
- ii) diffuser is characterized by an inherent loss, quantified by a kinetic energy efficiency η_{eff} or a fractional entropy rise; and
- iii) diffuser chemistry is frozen or equilibrium.

A diffuser of similar design has been analyzed by Ikawa^[5].

According to the standard atmospheric conditions*, the inlet temperature, pressure and air composition are fixed quantities at a given altitude. In other words,

$$T_{\infty} = T_{\infty}(H), \quad P_{\infty} = P_{\infty}(H), \quad \rho_{\infty} = \rho_{\infty}(H), \quad \dots ,$$

and so on. With the above information in mind, a diffuser may be described by the following four parameters:

- i) free-stream Mach number, M_{∞} ;
- ii) diffuser exit (\sim combustor inlet) Mach number, M_c or flight altitude H ;
- iii) diffuser exit (\sim combustor) pressure, P_c or temperature T_c ; and,
- iv) diffuser inherent loss, η_{eff} or a fractional entropy rise.

* For example, see the *Standard U.S. Atmosphere, 1976*.

It is more convenient to choose the combustor pressure P_c as an input rather than the inlet temperature because the type of combustor considered in this work is of constant pressure. Furthermore, for reasons which will become clear later, M_c and η_{eff} are also the preferred parameters in the problem. The latter quantity is to represent grossly the loss in a diffuser. It is defined as

$$\eta_{\text{eff}} \equiv \frac{\text{kinetic energy available by expanding diffuser exit flow to ambient pressure}}{\text{kinetic energy of diffuser inlet flow}} \\ \equiv \frac{U_{\text{eff}}^2}{U_{\infty}^2} . \quad (\text{II.1})$$

For a well designed diffuser inlet, η_{eff} is nearly constant over a wide range of flight speed and inlet conditions.

Having decided on the input parameters, the diffuser model can be formulated in the following manner. First, consider the hypothetical 'eff' state. From the definition of η_{eff} ,

$$U_{\text{eff}}^2 = \eta_{\text{eff}} U_{\infty}^2 = \eta_{\text{eff}} M_{\infty}^2 a_{f\infty}^2 .$$

The expression for the frozen speed of sound a_f can be found in appendix I. According to the conservation of energy,

$$\sum_{k=1}^K h_k Y_k + \frac{1}{2} U^2 = \sum_{k=1}^K h_k(T_{\infty}) Y_{k\infty} + \frac{1}{2} U_{\infty}^2 = h_t (\text{constant}) ;$$

therefore,

$$\sum_{k=1}^K h_k(T_{\text{eff}}) Y_{k\text{eff}} = \sum_{k=1}^K h_k(T_{\infty}) Y_{k\infty} + \frac{1 - \eta_{\text{eff}}}{2} M_{\infty}^2 a_{f\infty}^2 . \quad (\text{II.2})$$

Note that on the right-hand side of the expression, T_{∞} , $Y_{k\infty}$ and $a_{f\infty}$ are functions of the altitude H only. Now consider the connection between the diffuser exit state, denoted by the subscript 'c', and the 'eff' state. The entropies, \bar{S} , at the two points must be identical since the expansion is hypothetically ideal; it is also known that the pressure after the expansion is equal to the ambient pressure. That is,

$$\bar{S}(P_{\infty}, T_{\text{eff}}, Y_{k\text{eff}}) = \bar{S}(P_c, T_c, Y_{kc}) , \quad (\text{II.3})$$

where \bar{S} is defined in appendix I. Energy must also be conserved at both states such that

$$\sum_{k=1}^K h_k(T_c) Y_{kc} + \frac{1}{2} M_c^2 a_{fc}^2 = \sum_{k=1}^K h_k(T_{\infty}) Y_{k\infty} + \frac{1}{2} M_{\infty}^2 a_{f\infty}^2 . \quad (\text{II.4})$$

The unknowns in equations II.2 to II.4 are the flight altitude H , the diffuser exit conditions T_c and Y_{kc} , and the 'eff' conditions T_{eff} and $Y_{k\text{eff}}$.

In the case with frozen chemistry, the composition remains at $Y_{k\infty}$ which only depends on H . Then the three equations are sufficient to solve for the three unknowns H , T_c and T_{eff} .

In the case with equilibrium chemistry, the addition 2 K equations necessary to describe the compositions at the 'eff' and 'c' states are provided by the equilibrium conditions:

$$Y_{k\text{eff}} = Y_{k\text{eff,eq}}(P_{\text{eff}}, U_{\text{eff}}; h_t) = Y_{k\text{eff,eq}}(P_{\infty}, U_{\text{eff}}; h_t) \quad \text{and}$$

$$Y_{kc} = Y_{kc,\text{eq}}(P_c, M_c; h_t).$$

Thus the description is completed.

The formulation is exactly the same if the flight altitude H had been specified instead of M_c or T_c instead of P_c . However, if a fractional increase in entropy through the diffuser is used in place of η_{eff} , the hypothetical 'eff' state can be eliminated while an entropy equation relating the diffuser inlet and exit must be added.

There is a very important difference between setting a diffuser exit Mach number and setting a flight altitude. In the first case, the diffuser exit (\sim combustor inlet) temperature is only found to vary within a few hundred K when imposing a constant M_c and P_c over a wide range of flight Mach number M_{∞} **. This is often desirable so that the combustor can operate near its optimal point under most conditions. Such an approach is also useful in defining a *flight path*. In short, a flight path plots out the flight conditions at which the vehicle performance is optimized. It is generally specified in terms of flight Mach number or speed:

$$M_{\infty}(H) \quad \text{or} \quad U_{\infty}(H).$$

In choosing a M_c ,

$$M_c \quad \longrightarrow \quad H(M_{\infty}; M_c, P_c, \eta_{\text{eff}}) \xrightarrow{P_c, M_c, \eta_{\text{eff}} = \text{constant}} H(M_{\infty})$$

so that

$$T_{\text{diffuser exit}} \sim \text{constant} \quad \text{for all } M_{\infty} \quad \text{along } H(M_{\infty}; M_c).$$

It is extremely difficult to achieve the same result by selecting H arbitrarily. The diffuser exit may often become too low ($< 850 K$, lower limit for the combustor temperature) or too high ($> 5000 K$, upper limit for species properties).

** The significance of the combustor inlet temperature is shown in section 4.4.

APPENDIX III

Kinetic Data for Hydrogen-Air Reactions

III.1 Compiled Kinetic Data

A set of seven combustion reports has been surveyed to obtain the relevant reaction steps and species for a hydrogen-air system. Although the first six references are mostly concerned with hydrocarbon-oxygen combustion, their kinetic data also include those for hydrogen-oxygen combustion. The relevant reactions are collected in table III.1a. Some important nitrogenous reactions involving hydrogen are found in reference 2 in a study of “*Hydrocarbon/Nitric Oxide Interaction ...*”. They are listed independently in table III.1b. A more complete collection of nitric oxide reactions is provided by reference 7. These reactions are listed in table III.1c. In the tables, a forward step is appended with an ‘a’ following the reaction number. A reverse step, if available, is appended by a ‘b’. Since most of the reactions appear in several sources, the reaction steps are tabulated with their respective source numbers and rate coefficients. The sources are numbered according to the list in section III.1.

The rate coefficients shown are defined according to the Arrhenius equation:

$$k(T) = AT^\beta \exp\left(\frac{E_a}{R_u T}\right),$$

where A is the pre-exponent constant, β the temperature exponent and E_a the activation energy. The units of k and A are in molar and second; their exact combinations depend on individual reaction. The symbol M appeared in some reactions represents a third body. The enhanced third body coefficients * is assumed to be 1 in such cases.

* The *enhanced coefficient* is a multiplicative constant for the reaction rate.

It is clear from table III.1a that while most coefficients from the references agree except for minor differences in the activation energy, there are occasions where the differences are not negligible. For example, in reactions 3a and 3b of table III.1a, the pre-exponent constant varies over two order of magnitude, the temperature exponent varies from ~ -1 to 0 and the activation energy varies from ~ 0 to $\sim 10^4$. Most of the coefficients may be rooted to certain experimental investigations as shown in reference 4. However, some are approximated by incorporating theoretical expressions with experimental values as was done in reference 3: experimental values obtained over a smaller temperature range were fitted into theory to produce values for a wider range. Non-linearity of the Arrhenius equation also accounts for some discrepancies in the fitted coefficients.

	Reaction Mechanism (forward and reverse steps)	Reference					$k_f = AT^\beta \exp\left(-\frac{E_a}{R_u T}\right)$			
		1	2	3	4	5	6	A	β	E_a [cal/mol]
1a	$\text{H}_2 + \text{O}_2 \longrightarrow \text{OH} + \text{OH}$	•	•	•				1.70×10^{13}	0.0	47780.0
1b	$\text{OH} + \text{OH} \longrightarrow \text{H}_2 + \text{O}_2$			•				4.79×10^{11}	0.0	29460.0
2a	$\text{H}_2 + \text{OH} \longrightarrow \text{H}_2\text{O} + \text{H}$	•	•	•				1.17×10^9	1.3	3626.0
						•	•	1.00×10^8	1.6	3303.0
2b	$\text{H}_2\text{O} + \text{H} \longrightarrow \text{H}_2 + \text{OH}$			•				5.62×10^9	1.3	18840.0
					•	•		4.60×10^8	1.6	18593.0
					•	•		4.62×10^8	1.6	18521.3
3a	$\text{O}_2 + \text{H} \longrightarrow \text{OH} + \text{O}$	•	•	•				5.13×10^{16}	-0.816	16507.0
					•			1.42×10^{14}	0.0	16394.4
						•	•	1.20×10^{17}	-0.91	16530.6
3b	$\text{OH} + \text{O} \longrightarrow \text{O}_2 + \text{H}$			•				3.24×10^{15}	-0.816	60.0
						•		1.40×10^{13}	0.0	764.8
							•	1.80×10^{13}	0.0	0.0
4a	$\text{H}_2 + \text{O} \longrightarrow \text{OH} + \text{H}$	•	•	•				1.82×10^{10}	1.0	8826.0
					•	•	•	1.50×10^7	2.0	7563.9
4b	$\text{OH} + \text{H} \longrightarrow \text{H}_2 + \text{O}$			•				8.13×10^9	1.0	6960.0
						•		6.73×10^6	2.0	5341.3
							•	6.70×10^6	2.0	5573.1
5a	$\text{O}_2 + \text{H} + \text{M} \longrightarrow \text{HO}_2 + \text{M}$	•	•	•				2.10×10^{18}	-1.0	0.0
					•	•	•	2.00×10^{18}	-0.8	0.0
5b	$\text{HO}_2 + \text{M} \longrightarrow \text{O}_2 + \text{H} + \text{M}$			•				2.69×10^{18}	-1.0	51390.0
							•	2.77×10^{18}	-0.8	46697.6
6a	$\text{O}_2 + \text{H} + \text{O}_2 \longrightarrow \text{HO}_2 + \text{O}_2$	•	•	•				6.76×10^{19}	-1.42	0.0
6b	$\text{HO}_2 + \text{O}_2 \longrightarrow \text{O}_2 + \text{H} + \text{O}_2$			•				8.51×10^{19}	-1.42	51390.0
7a	$\text{O}_2 + \text{H} + \text{N}_2 \longrightarrow \text{HO}_2 + \text{N}_2$	•	•	•				6.76×10^{19}	-1.42	0.0
7b	$\text{HO}_2 + \text{N}_2 \longrightarrow \text{O}_2 + \text{H} + \text{N}_2$			•				8.51×10^{19}	-1.42	51390.0
8a	$\text{OH} + \text{HO}_2 \longrightarrow \text{O}_2 + \text{H}_2\text{O}$	•	•	•				5.01×10^{13}	0.0	1000.0
					•	•	•	2.00×10^{13}	0.0	0.0
8b	$\text{O}_2 + \text{H}_2\text{O} \longrightarrow \text{OH} + \text{HO}_2$			•				7.07×10^{14}	0.0	69000.0
9a	$\text{H} + \text{HO}_2 \longrightarrow \text{OH} + \text{OH}$	•	•	•				2.51×10^{14}	0.0	1900.0
					•	•	•	1.50×10^{14}	0.0	1001.3
9b	$\text{OH} + \text{OH} \longrightarrow \text{H} + \text{HO}_2$			•				2.04×10^{13}	0.0	36370.0
10a	$\text{O} + \text{HO}_2 \longrightarrow \text{O}_2 + \text{OH}$	•	•	•				4.79×10^{13}	0.0	1000.0
					•			2.00×10^{13}	0.0	0.0
10b	$\text{O}_2 + \text{OH} \longrightarrow \text{O} + \text{HO}_2$			•				6.31×10^{13}	0.0	51920.0

(TABLE III.1a continues on next page)

	Reaction Mechanism (forward and reverse steps)	Reference					$k_f = AT^\beta \exp\left(-\frac{E_a}{R_u T}\right)$			
		1	2	3	4	5	6	A	β	E_a [cal/mol]
11a	$\text{OH} + \text{OH} \longrightarrow \text{H}_2\text{O} + \text{O}$	•	•	•				6.03×10^8	1.3	0.0
						•		1.50×10^9	1.14	100.4
							•	1.50×10^9	1.14	0.0
11b	$\text{H}_2\text{O} + \text{O} \longrightarrow \text{OH} + \text{OH}$			•				6.46×10^8	1.3	17080.0
					•			1.50×10^{10}	1.14	17302.5
						•		1.49×10^{10}	1.14	17001.4
						•		1.50×10^{10}	1.14	17281.0
12a	$\text{H}_2 + \text{M} \longrightarrow \text{H} + \text{H} + \text{M}$	•	•					2.24×10^{12}	0.5	92600.0
12b	$\text{H} + \text{H} + \text{M} \longrightarrow \text{H}_2 + \text{M}$		•					1.00×10^{18}	-1.0	0.0
				•				6.31×10^{11}	0.5	-11430.0
					•			4.50×10^{18}	-1.0	0.0
13a	$\text{O}_2 + \text{M} \longrightarrow \text{O} + \text{O} + \text{M}$	•	•	•				1.86×10^{11}	0.5	95560.0
13b	$\text{O} + \text{O} + \text{M} \longrightarrow \text{O}_2 + \text{M}$			•				5.50×10^{10}	0.5	-18110.0
14a	$\text{H} + \text{HO} + \text{M} \longrightarrow \text{H}_2\text{O} + \text{M}$	•	•	•				7.59×10^{23}	-2.6	0.0
					•			4.40×10^{23}	-2.0	0.0
						•		2.15×10^{22}	-2.0	0.0
14b	$\text{H}_2\text{O} + \text{M} \longrightarrow \text{H} + \text{HO} + \text{M}$			•				1.32×10^{24}	-2.6	113650.0
						•		3.87×10^{23}	-2.0	119387.2
15a	$\text{H} + \text{HO}_2 \longrightarrow \text{H}_2 + \text{O}_2$	•	•	•				2.52×10^{13}	0.0	700.0
					•	•	•	2.50×10^{13}	0.0	690.7
15b	$\text{H}_2 + \text{O}_2 \longrightarrow \text{H} + \text{HO}_2$			•				7.24×10^{13}	0.0	53490.0
					•			1.00×10^{13}	0.0	1075.4
						•		3.00×10^{13}	0.0	1720.7
16a	$\text{HO}_2 + \text{HO}_2 \longrightarrow \text{H}_2\text{O}_2 + \text{O}_2$	•	•	•				2.00×10^{12}	0.0	0.0
16b	$\text{H}_2\text{O}_2 + \text{O}_2 \longrightarrow \text{HO}_2 + \text{HO}_2$			•				1.38×10^{13}	0.0	33010.0
17a	$\text{H}_2\text{O}_2 + \text{M} \longrightarrow \text{OH} + \text{OH} + \text{M}$	•	•	•				1.29×10^{17}	0.0	45500.0
17b	$\text{OH} + \text{OH} + \text{M} \longrightarrow \text{H}_2\text{O}_2 + \text{M}$			•				1.23×10^{15}	0.0	-4430.0
18a	$\text{H}_2\text{O}_2 + \text{H} \longrightarrow \text{H}_2 + \text{HO}_2$	•	•	•				1.59×10^{12}	0.0	3800.0
18b	$\text{H}_2 + \text{HO}_2 \longrightarrow \text{H}_2\text{O}_2 + \text{H}$			•				6.76×10^{11}	0.0	23570.0
19a	$\text{H}_2\text{O}_2 + \text{OH} \longrightarrow \text{H}_2\text{O} + \text{HO}_2$	•	•	•				1.00×10^{13}	0.0	1800.0
19b	$\text{H}_2\text{O} + \text{HO}_2 \longrightarrow \text{H}_2\text{O}_2 + \text{OH}$			•				2.04×10^{13}	0.0	3670.0
20	$\text{H} + \text{H} + \text{H}_2 \rightleftharpoons \text{H}_2 + \text{H}_2$	•						9.20×10^{16}	-0.6	0.0
21	$\text{H} + \text{H} + \text{H}_2\text{O} \rightleftharpoons \text{H}_2 + \text{H}_2\text{O}$	•						6.00×10^{17}	-1.25	0.0

TABLE III.1a Hydrogen-Oxygen reactions from references 1-6.

	Reaction Mechanism (forward and reverse steps)	Reference	$k_f = AT^\beta \exp\left(-\frac{E_a}{R_u T}\right)$		
			2	A	β
1	$\text{NO} + \text{HO}_2 \rightleftharpoons \text{NO}_2 + \text{OH}$	•	2.11×10^{12}	0.0	-479.0
2	$\text{NO}_2 + \text{H} \rightleftharpoons \text{NO} + \text{OH}$	•	3.50×10^{14}	0.0	1500.0
3	$\text{NH} + \text{O}_2 \rightleftharpoons \text{HNO} + \text{O}$	•	1.00×10^{13}	0.0	12000.0
4	$\text{NH} + \text{O}_2 \rightleftharpoons \text{NO} + \text{OH}$	•	1.40×10^{11}	0.0	2000.0
5	$\text{NH} + \text{NO} \rightleftharpoons \text{N}_2\text{O} + \text{H}$	•	4.33×10^{14}	-0.5	0.0
6	$\text{N}_2\text{O} + \text{H} \rightleftharpoons \text{N}_2 + \text{OH}$	•	7.60×10^{13}	0.0	15200.0
7	$\text{NH} + \text{OH} \rightleftharpoons \text{HNO} + \text{H}$	•	2.00×10^{13}	0.0	0.0
8	$\text{NH} + \text{OH} \rightleftharpoons \text{N} + \text{H}_2\text{O}$	•	5.00×10^{11}	0.5	2000.0
9	$\text{NH} + \text{N} \rightleftharpoons \text{N}_2 + \text{H}$	•	3.00×10^{13}	0.0	0.0
10	$\text{NH} + \text{H} \rightleftharpoons \text{N} + \text{H}_2$	•	3.00×10^{13}	0.0	0.0
11	$\text{NH}_2 + \text{O} \rightleftharpoons \text{HNO} + \text{H}$	•	6.63×10^{14}	-0.5	0.0
12	$\text{NH}_2 + \text{O} \rightleftharpoons \text{NH} + \text{OH}$	•	6.75×10^{12}	0.0	0.0
13	$\text{NH}_2 + \text{OH} \rightleftharpoons \text{NH} + \text{H}_2\text{O}$	•	4.50×10^{12}	0.0	2200.0
14	$\text{NH}_2 + \text{H} \rightleftharpoons \text{NH} + \text{H}_2$	•	6.92×10^{13}	0.0	3650.0
15	$\text{NH}_2 + \text{NO} \rightleftharpoons \text{NNH} + \text{OH}$	•	8.82×10^{15}	-1.25	0.0
16	$\text{NH}_2 + \text{NO} \rightleftharpoons \text{N}_2 + \text{H}_2\text{O}$	•	3.78×10^{15}	-1.25	0.0
17	$\text{NH}_3 + \text{OH} \rightleftharpoons \text{NH}_2 + \text{H}_2\text{O}$	•	2.04×10^6	2.04	566.0
18	$\text{NH}_3 + \text{H} \rightleftharpoons \text{NH}_2 + \text{H}_2$	•	6.36×10^5	2.39	10171.0
19	$\text{NH}_3 + \text{O} \rightleftharpoons \text{NH}_2 + \text{OH}$	•	2.10×10^{13}	0.0	9000.0
20	$\text{NNH} + \text{M} \rightleftharpoons \text{N}_2 + \text{H} + \text{M}$	•	2.00×10^{14}	0.0	20000.0
21	$\text{NNH} + \text{NO} \rightleftharpoons \text{N}_2 + \text{HNO}$	•	5.00×10^{13}	0.0	0.0
22	$\text{NNH} + \text{H} \rightleftharpoons \text{N}_2 + \text{H}_2$	•	3.70×10^{13}	0.0	3000.0
23	$\text{HNO} + \text{M} \rightleftharpoons \text{NO} + \text{H} + \text{M}$	•	1.50×10^{16}	0.0	48680.0
24	$\text{HNO} + \text{OH} \rightleftharpoons \text{NO} + \text{H}_2\text{O}$	•	3.60×10^{13}	0.0	0.0
25	$\text{HNO} + \text{H} \rightleftharpoons \text{NO} + \text{H}_2$	•	5.00×10^{12}	0.0	0.0
26	$\text{N} + \text{OH} \rightleftharpoons \text{NO} + \text{H}$	•	3.80×10^{13}	0.0	0.0

TABLE III.1b Nitric-Oxide & Hydrogen reactions from reference 2.

	Reaction Mechanism (forward and reverse steps)	Reference		$k_f = AT^\beta \exp\left(-\frac{E_a}{R_u T}\right)$		
		2	7	A	β	E_a [cal/mol]
1	$N_2 + M \rightleftharpoons N + N + M$		•	3.72×10^{21}	-1.6	224928.0
2a	$N_2 + O \rightarrow NO + N$		•	1.82×10^{14}	0.0	76241.0
2b	$NO + N \rightarrow N_2 + O$	•		3.27×10^{12}	0.3	0.0
3	$NO + M \rightleftharpoons N + O + M$		•	3.98×10^{20}	-1.5	150000.0
4a	$NO + O \rightarrow N + O_2$		•	3.80×10^9	1.0	41369.0
4b	$N + O_2 \rightarrow NO + O$	•		6.40×10^9	1.0	6280.0
5	$NO_2 + M \rightleftharpoons NO + O + M$		•	1.10×10^{16}	0.0	65571.0
6	$NO_2 + O \rightleftharpoons NO + O_2$	•	•	1.00×10^{13}	0.0	596.0
7	$NO_2 + N \rightleftharpoons NO + NO$		•	3.98×10^{12}	0.0	0.0
8	$NO_2 + NO_2 \rightleftharpoons NO + NO + O_2$		•	2.00×10^{12}	0.0	26825.0
9*	$O_2 + M \rightleftharpoons O + O + M$		•	1.82×10^{11}	-1.0	117988.0

* (reaction repeated in table III.1a)

TABLE III.1c Nitric-Oxide reactions from references 2 & 7.

Considering the interactions of hydrogen, oxygen and nitrogen with a third body argon, the list of reactions in tables III.1a to III.1c should sufficiently describe the hydrogen-air system at interest. The element set consists of 4 components:

$$\left\{ \begin{array}{l} N \\ O \\ H \\ Ar \end{array} \right.$$

while the species set consists of 19 components:

$$\left\{ \begin{array}{l} N \quad N_2 \quad NO \quad NO_2 \quad N_2O \quad NH \quad NH_2 \quad NH_3 \quad N_2H \\ O \quad O_2 \quad OH \\ H \quad H_2 \quad HNO \quad HO_2 \quad H_2O \quad H_2O_2 \\ Ar . \end{array} \right.$$

The absence of carbon-dioxide in the assumed air has largely simplified the list. However, its importance must be re-evaluated according to individual studies, especially when pollution is concerned.

III.2 References for Kinetic Data

1. Smooke, M. D., *Solution of Burner-Stabilized Premixed Laminar Flames by Boundary Value Methods*, **Journal of computational Physics**, Vol. 48, 1982.
2. Hennessy, R. J., Robinson, C. & Smith, D. B., *Methane and Ethane Flame Chemistry*, **21st Symposium on Combustion/The Combustion Institute**, 1986.
3. Thorne, L. R., Branch, M. C., Chandler, D. W., Kee, R. J. & Miller, J. A., *Hydrocarbon/Nitric Oxide Interactions in Low Pressure Flames*, **21st Symposium on Combustion/The Combustion Institute**, 1986.
4. Seshadri, K., *Asymptotic Structure and Extinction of Methane-Air Diffusion Flames*, **Combustion and Flame**, Vol. 73, pp.23-44, 1988.
5. Rogg, B., *Response & Flamelet Structure of Stretched Premixed Methane-Air Flames*, **Combustion and Flame**, Vol. 73, pp.45-46, 1988.
6. Brown, R. C., *Simulation of Ionic Structure in Lean and Close-to-Stoichiometric Acetylene Flames*, **Combustion and Flame**, Vol. 73, pp.1-21, 1988.
7. Gardiner, W. C., *Combustion Chemistry*, Springer-Verlag, 1984.

APPENDIX IV

Governing Equations for a Two-Dimensional Nozzle

The governing equations in the physical x - y plane have been discussed in detail in section 6.3. The transformed equations in terms of the ξ - ψ coordinates have also been outlined in section 6.5. There only remains the task of writing the set *explicitly* in the form

$$\frac{\partial \mathbf{Z}}{\partial \xi} = \mathbf{F} \left(\mathbf{Z}, \frac{\partial \mathbf{Z}}{\partial \psi} \right)$$

for the $(K + 4)$ variable set

$$\mathbf{Z} \equiv [Y_k, P, T, q, \theta]^T .$$

After some algebraic manipulations, the following set is obtained:

$$\frac{\partial Y_k}{\partial \xi} = \frac{m_k \dot{\omega}_k}{\rho q \cos \theta} \quad \text{for } k = 1, K \quad (.1)$$

where $\dot{\omega}_k$ is the molar production rate previously described in section 2.3;

$$\begin{aligned} \frac{\partial P}{\partial \xi} = & \left\{ \frac{q \cos \theta}{1 - q^2 \cos^2 \theta \left(\frac{\rho}{P} - \frac{1}{\bar{C}_p T} \right)} \right\} \left[-\bar{m} \sum_{k=1}^K \dot{\omega}_k + \frac{1}{\bar{C}_p T} \sum_{k=1}^K h_k m_k \dot{\omega}_k \right. \\ & \left. + \frac{\rho}{\rho_0} \tan \theta \frac{\partial P}{\partial \psi} + \frac{\rho}{\rho_0} \rho q^2 \frac{\partial \theta}{\partial \psi} \right], \quad (.2) \end{aligned}$$

$$\begin{aligned} \frac{\partial T}{\partial \xi} = & \frac{1}{\rho \bar{C}_p} \left\{ \frac{q \cos \theta}{1 - q^2 \cos^2 \theta \left(\frac{\rho}{P} - \frac{1}{\bar{C}_p T} \right)} \right\} \left[-\bar{m} \sum_{k=1}^K \dot{\omega}_k \right. \\ & \left. + \left(\frac{\rho}{P} - \frac{1}{q^2 \cos^2 \theta} \right) \sum_{k=1}^K h_k m_k \dot{\omega}_k \right. \\ & \left. + \frac{\rho}{\rho_0} \tan \theta \frac{\partial P}{\partial \psi} + \frac{\rho}{\rho_0} \rho q^2 \frac{\partial \theta}{\partial \psi} \right], \quad (.3) \end{aligned}$$

$$\frac{\partial q}{\partial \xi} = -\frac{1}{\rho q} \left\{ \frac{q \cos \theta}{1 - q^2 \cos^2 \theta \left(\frac{\rho}{P} - \frac{1}{\bar{C}_p T} \right)} \right\} \left[-\bar{m} \sum_{k=1}^K \dot{\omega}_k + \frac{1}{\bar{C}_p T} \sum_{k=1}^K h_k m_k \dot{\omega}_k + \frac{\rho}{\rho_0} \tan \theta \frac{\partial P}{\partial \psi} + \frac{\rho}{\rho_0} \rho q^2 \frac{\partial \theta}{\partial \psi} \right], \quad (4)$$

$$\frac{\partial \theta}{\partial \xi} = \left\{ \frac{q \cos \theta}{1 - q^2 \cos^2 \theta \left(\frac{\rho}{P} - \frac{1}{\bar{C}_p T} \right)} \right\} \left[\frac{\tan \theta}{\rho q^2} \left(-\bar{m} \sum_{k=1}^K \dot{\omega}_k + \frac{1}{\bar{C}_p T} \sum_{k=1}^K h_k m_k \dot{\omega}_k \right) - \frac{\rho}{\rho_0} \frac{1}{\rho q^2} \left(1 - q^2 \left(\frac{\rho}{P} - \frac{1}{\bar{C}_p T} \right) \right) \frac{\partial P}{\partial \psi} + \frac{\rho}{\rho_0} \tan \theta \frac{\partial \theta}{\partial \psi} \right], \quad (5)$$

in which ρ is given in terms of the elements of \mathbf{Z} by the state equation:

$$\rho = P \frac{\bar{m}}{R_u T} \quad ; \quad \bar{m} = \frac{1}{\sum_{k=1}^K \frac{Y_k}{m_k}}. \quad (6)$$

In section 6.6, the two conditions relating $\partial P/\partial \psi$ and $\partial \theta/\partial \psi$ at the wall boundaries are obtained by noting that

$$\left\{ \begin{array}{l} \frac{\partial \theta}{\partial \xi} \Big|_{\psi_l} = \frac{d\theta_l}{d\xi} = \cos^2 \theta_l \frac{d^2 B_l}{d\xi^2} \\ \frac{\partial \theta}{\partial \xi} \Big|_{\psi_u} = \frac{d\theta_u}{d\xi} = \cos^2 \theta_u \frac{d^2 B_u}{d\xi^2} \end{array} \right. \quad \text{and}$$

and applying these results to the θ -differential equation. B_l and B_u are the wall geometries defined in equation 6.4.13. The relations are written in full as

$$\left[\frac{1 - q^2 \cos^2 \theta \left(\frac{\rho}{P} - \frac{1}{\bar{C}_p T} \right)}{q \cos \theta} \right]_{\psi_l} \cos^2 \theta_l \frac{d^2 B_l}{d\xi^2} - \left[\frac{\tan \theta}{\rho q^2} \left(-\bar{m} \sum_{k=1}^K \dot{\omega}_k + \frac{1}{\bar{C}_p T} \sum_{k=1}^K h_k m_k \dot{\omega}_k \right) \right]_{\psi_l} \\ = \left[\frac{\rho}{\rho_0} \frac{1}{\rho q^2} \left(q^2 \left(\frac{\rho}{P} - \frac{1}{\bar{C}_p T} \right) - 1 \right) \right]_{\psi_l} \frac{\partial P}{\partial \psi} \Big|_{\psi_l} + \left[\frac{\rho}{\rho_0} \tan \theta \right]_{\psi_l} \frac{\partial \theta}{\partial \psi} \Big|_{\psi_l} \quad (7a)$$

and

$$\begin{aligned}
 & \left[\frac{1 - q^2 \cos^2 \theta \left(\frac{\rho}{P} - \frac{1}{\bar{C}_p T} \right)}{q \cos \theta} \right]_{\psi_u} \cos^2 \theta_u \frac{d^2 B_u}{d\xi^2} - \left[\frac{\tan \theta}{\rho q^2} \left(-\bar{m} \sum_{k=1}^K \dot{\omega}_k + \frac{1}{\bar{C}_p T} \sum_{k=1}^K h_k m_k \dot{\omega}_k \right) \right]_{\psi_u} \\
 & = \left[\frac{\rho}{\rho_0} \frac{1}{\rho q^2} \left(q^2 \left(\frac{\rho}{P} - \frac{1}{\bar{C}_p T} \right) - 1 \right) \right]_{\psi_u} \frac{\partial P}{\partial \psi} \Big|_{\psi_u} + \left[\frac{\rho}{\rho_0} \tan \theta \right]_{\psi_u} \frac{\partial \theta}{\partial \psi} \Big|_{\psi_u}
 \end{aligned} \tag{.7b}$$

at the lower and upper walls respectively.

References

1. Chase, M. W. et al., *JANAF Thermochemical Tables*, National Bureau of Standards, 3th Ed., 1986.
2. Gordon, S. & McBride, B. J., *Computer Program of Calculation of Complex Chemical Equilibrium Compositions, Rocket Performance, Incident and Reflected Shocks and Chapman-Jauguet Detonations*, NASA, SP-273, 1971.
3. Hilsenrath, J. & Klein, M., *Tables of Thermodynamic Properties of Air in Chemical Equilibrium Including Second Virial Corrections from 1,500 K to 15,000 K*, National Bureau of Standards, AEDC-TC65-85, 1965.
4. Hindmarsh, A. C., *ODEPACK: A Systemize Collection of ODE Solvers*, **IMACS Trans. on Scientific Computation** (North-Holland, Amsterdam), Vol. 1, 1983.
5. Ikawa, H., *Rapid Methodology for Design and Performance Prediction of Integrated SCRAMJET/Hypersonic Vehicle*, **AIAA**, 25th Joint Propulsion Conference, AIAA-89-2682, 1989.
6. Kee, R. J., Miller, J. A. & Jefferson, T. H., *CHEMKIN: A General Purpose, Problem-Independent, Transportable FORTRAN Chemical Kinetic Code Package*, Sandia National Laboratory, Livermore, SAND80-8003, 1980.
7. Kerrebrock, J. L., *Some Readily Quantifiable Aspects of SCRAMJET Engine Performance*, to be published.
8. Kubota, T. & Ko, D. R. S., *A Second-Order Weak Interaction Expansion for Moderately Hypersonic Flow Past a Flat Plate*, **AIAA Journal**, Vol. 5, 1967.
9. Kuo, K. K., *Principles of Combustion*, New York, Wiley, 1986.
10. Mikolatis, D. W., *An Asymptotic Analysis of the Induction Phases of Hydrogen-Air Detonations*, **Combustion Science & Technology**, Vol. 52, 1987.
11. Ralston, A. & Rabinowitz, P., *A First Course in Numerical Analysis*, New York, McGraw-Hill. 2nd Ed., 1978

12. Rossini, F. D., *Chemical Thermodynamics*, New York, Wiley, 1950.
13. Serdengecti, S., *The "SCRAMJET" Program*, unpublished; personal communication.
14. Vincenti, W. G., *Introduction to Physical Gas Dynamics*, New York, Wiley, 1965.
15. Waitz, I, *An Investigation of Contoured Wall Injectors for Hypervelocity Mixing Augmentation*, **Ph.D. Thesis**, California Institute of Technology, Pasadena, California, 1991.
16. Wegener, P. P. & Cole, J. D., *Experiments on Propagation of Weak Disturbances in Stationary Supersonic Nozzle Flow of Chemically Reacting Gas Mixtures*, 8th Symposium (International) on Combustion, 1960.
17. Yang, J, *An Analytical and Computational Investigation of Shock-Induced Vortical Flows with Applications to Supersonic Combustion*, **Ph.D. Thesis**, California Institute of Technology, Pasadena, California, 1991.